Introduction

Dynamic changes resulting from a variety of causes (e.g. structural damage or nonlinearity onset) may disturb or threaten the normal working conditions of a system. The capacity to estimate the mechanical health condition of a structure using remote non-destructive techniques constitutes a substantial plan which allows to reduce maintenance costs and to ensure safety. Hence, questions such as the detection of those events have attracted the attention of countless researchers in recent times.

A well-known classification for damage detection, presented in Rytter (1993)[109], defines four levels in increasing order of complexity:

- Level 1: Damage *detection*: inspection of the presence of damage in the structure
- Level 2: Damage *localization*: determination of geometrical location of the damage
- Level 3: *Assessment* of the severity of the damage
- Level 4: Prediction of the *remaining lifetime* of the structure

Damage detection can be implemented by visual inspection or by using localized methods such as acoustic and ultrasonic techniques, magnet field methods, radiography, penetrant liquids, eddy-current methods and thermal field methods. However, such methods require the accessibility of the zone where damage is located.

"Smart structure" is a popular expression in modern engineering that relates to vibration monitoring. It consists in a structure instrumented by sensors measuring vibration responses of the structures in real time, for the purpose of structural health monitoring (SHM). Nowadays, this kind of approach is widely used because vibration monitoring systems is well developed. Efficient and reliable vibration analysis tools allow to detect the occurrence of damage, to assess its severity and to predict the residual life of the structure. By acting before the apparition of a serious fault, the cost of maintenance and reparation may be considerably reduced and at the same time, the security may be improved. Vibration analysis is based on the assumption that the dynamical behavior of a structure, observed by measured responses, relates directly to system features as stiffness, mass and damping distribution. A fault in a dynamic system may be shown by changes in the dynamic properties of the structure, namely the eigenfrequencies, the mode shapes/deformation shapes, the modal damping ratios and/or the transfer functions. So, identification of those quantities is also of primary importance for the diagnosis problem.

Nowadays identification methods of linear systems are rather powerful, but they are based on stationarity and linearity assumptions, which is not always the case in real-life applications. For example, nonlinearity may be induced by environmental factors such as temperature, humidity, wind or comes from physical factors related to geometric effects or to material behavior, etc. Furthermore, as reported in Farrar *et al.* (2007)[25], there are many types of damage that make an initially linear structural system respond in a nonlinear manner. For example, cracks subsequently open and close under operational condition. Other common

damages that produce nonlinear system responses come from loose connections, delamination in bonded, layered materials under dynamic loading or material nonlinearities. The new response characteristics induced by the nonlinearity can be considered as indicators of damage. However, accurate determination of these quantities should be assured so that they can be utilized for indicators of damage. And so, the detection problem necessitates methods that are able to study nonlinear systems.

The objective of this thesis is to identify changes in the dynamical behaviour of a mechanical system through the development of identification, detection and model updating techniques. Damage or nonlinearity onset is considered responsible for the changes. According to the classification of damage identification presented above, the diagnosis problem in the present work is addressed for the first three levels, i.e. detection, localization and assessment. The identification of damages and nonlinearity onset is always based on the comparison between a current and the reference (normal) states.

The layout of the dissertation is as follows:

Chapter 1 presents a literature review on modal identification and detection methods. This part describes some main features of nonlinear systems and also the challenges that the nonlinearity presents. Localization and evaluation problems are next discussed separately.

Chapters 2, 3 and 4 focus on the detection of fault, namely nonlinearity onset or damage occurrence by three methods respectively: the Wavelet Transform (WT), the Second Order Blind Identification (SOBI) method and the Kernel Principal Component Analysis (KPCA) method. Output-only measurements are used for signal processing. The first two methods achieve health monitoring through a process of modal identification while the last method works directly in the characteristic spaces determined by a chosen kernel function. The detection can be performed by means of the concept of subspace angle or be based on statistics.

The robustness of the methods is illustrated on a clamped beam structure with a geometrical nonlinearity at the end; this benchmark was studied in the framework of the European COST Action F3. Other examples are considered such as an aircraft mock-up with different levels of damage and two industrial applications with the aim of performing quality control on a set of electro-mechanical devices and on welded joints.

Chapter 5 aims at damage localization based on sensitivity analysis of Principal Component Analysis (PCA) results in the frequency domain. The localization is performed through comparison of the principal component sensitivities between the reference (healthy) and the damaged states. Only measured responses, e.g. frequency response functions (FRFs) are needed for this purpose.

Following the sensitivity analysis in Chapter 5, *Chapter 6* addresses the evaluation of parameters, namely assessment of damages. For this purpose, a model updating procedure is performed. This procedure requires to build an analytical model of the structure.

The sensitivity analysis for damage detection is illustrated by both numerical and experimental data in mass-spring systems and in beam structures. A real-life structure i.e. the I-40 bridge in New Mexico that was destroyed in 1993 is also examined.

Finally, conclusions are withdrawn based on the realized work and some perspectives are given for the continuation of this research.

Chapter 1

Literature review

1.1 Introduction

The detection problem is often achieved by comparing dynamic properties of a system between its initial state and a current state. The dynamic properties, namely the natural frequencies, the mode shapes and the damping ratios, can be determined by modal identification methods so that modal identification can be seen as an important tool for the purpose of detection. This chapter gives a brief overview on common methods used for modal identification, detection, localization and parameter evaluation, respectively.

As noted previously, nonlinear features give rise to many challenges when inspecting mechanical systems owing to the main following reasons:

- The superposition principle that forms the basis of modal analysis in linear systems is no longer valid. The resolution of nonlinear equations requires more advanced mathematical techniques.
- The Maxwell's reciprocity theorem is not verified for a nonlinear system.
- The nonlinearity can originate from different sources: nonlinear material behavior, frictional contact, geometrical nonlinearity, energy loss mechanism, open-close crack ...
- In nonlinear dynamics, the responses are much more complex and sometimes, may not be forecasted. Even with a deterministic input, the output dynamics can become rich or even chaotic. In a system with nonlinear stiffness, resonant frequencies do not keep constant but show time varying features. Other phenomena that are not observed in linear systems may also occur, namely: bifurcations, harmonics, limit cycles, modal interactions (internal resonances, inter modulation)… The presence of the above phenomena depends on the type of excitation, as well as on the initial conditions. So, the number of nonlinear normal modes (NNMs) may be greater than the number of degrees of freedom of the system. NNMs can be stable or unstable.

Such nonlinear behaviors render inadequate identification and detection methods, as well as updating techniques developed for linear models. Since there is not a single method to model and identify all types of nonlinearities, the elaboration of a nonlinear identification and damage detection toolbox raises a lot of challenges.

In the following, linear systems are first studied. Then nonlinear systems are considered with the aim of detecting the onset of nonlinearity in the dynamic behaviour.

1.2 Modal identification methods

To evaluate modal parameters of a structure, two paths can be followed: a theoretical approach and an experimental approach as presented in Figure 1.1. Because a mathematical model of an existing structure is not always available, the experimental modal analysis approach is particularly interesting. It is based on the exploitation of system responses and requires identification techniques to extract modal parameters.

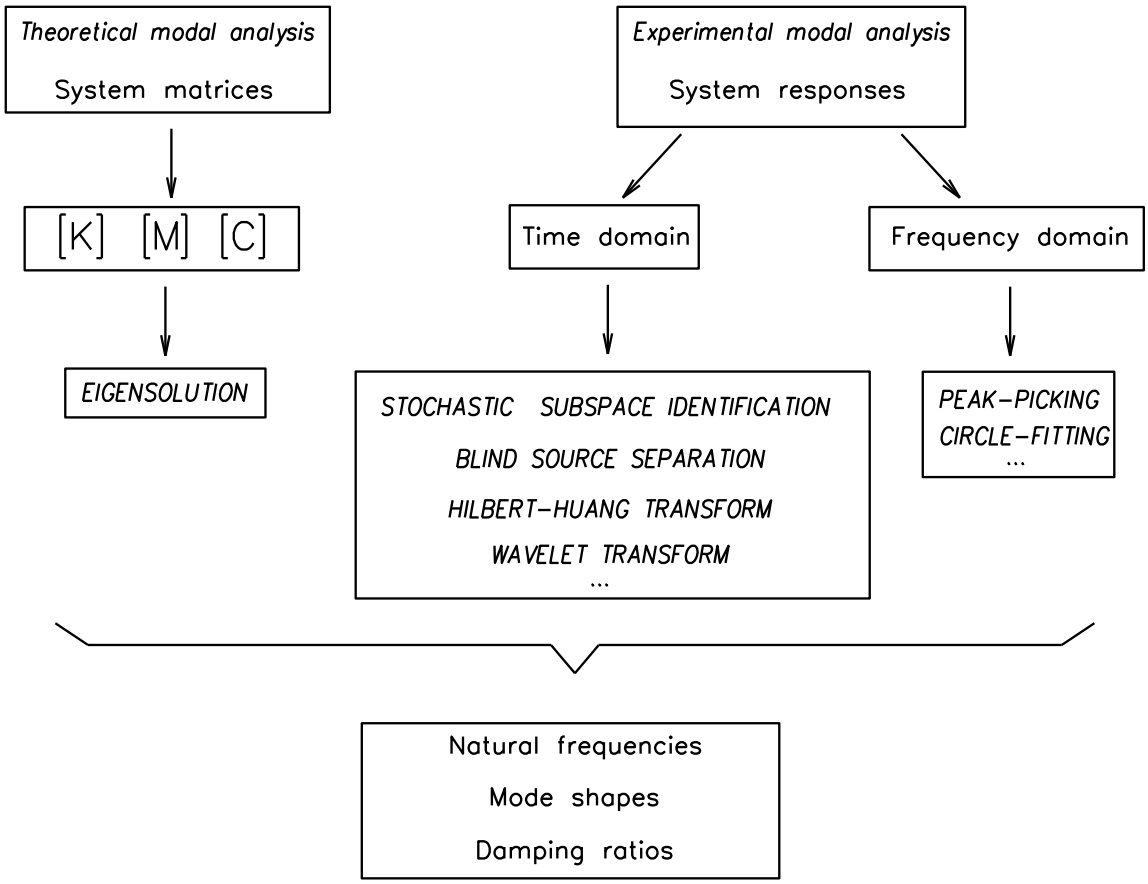

Figure 1.1: Classification of modal analysis methods

Modal identification methods may be classified into two categories depending on whether they are carried out in the frequency domain (e.g. using frequency response functions - FRFs) or in the time domain (e.g. using time signals). Several well established techniques are reported in the literature e.g. Maia *et al.* (1997)[75]. As the goal of this work is not to describe all the methods in details, we have limited the presentation to some typical time-domain methods proposed in the last decade and that are the most relevant for our work.

- **Stochastic Subspace Identification - SSI**

The main advantage of the SSI method is that it does not need the measurement of the excitation as long as it can be assumed as a combination of uncorrelated random signals. The discretized state-space model at sampling step k can be written as:

$$\mathbf{r}_{k+1} = \mathbf{A}\,\mathbf{r}_k + \mathbf{w}_k \tag{1.1}$$

$$\mathbf{y}_k = \mathbf{B}\,\mathbf{r}_k + \mathbf{v}_k \tag{1.2}$$

where matrices **A** and **B** are the state space and output matrices, respectively. $\mathbf{r}_k \in \Re^m$ represents the state vector and $\mathbf{y}_k \in \Re^m$ the time series. $\mathbf{w}_k$ and $\mathbf{v}_k$ represent the process and measurement noises, respectively. Those last vectors are assumed to be zero-mean white Gaussian noise processes.

Based on the definition of the block Hankel matrix, either in the covariance-driven form or in the data-driven form, the SSI method aims at determining the state space and output matrices **A** and **B**. Then the modal features may be deduced in a straightforward manner from those matrices.

For linear systems, SSI has proven to be efficient for modal identification and damage detection (Peeters and De Roeck (2001)[98], Yan *et al.* (2004)[132]). The method has also been used by several authors for other purposes. For example, to handle a multi-patch measurements setup with uncontrolled and non-stationary excitation, the covariance normalization is proposed in Mevel *et al.* (2002)[81] in order to neglect the influence of excitation. For the identification of nonlinear vibrating structures, the perspective of nonlinearities is adopted as internal feedback forces in Marchesiello and Garibaldi (2008)[78].

- **Blind Source Separation – BSS**

The multidimensional observations can be represented in the following form:

$$\mathbf{x}(t) = \mathbf{y}(t) + \boldsymbol{\sigma}(t) = \mathbf{A}\mathbf{s}(t) + \boldsymbol{\sigma}(t) \tag{1.3}$$

where $\mathbf{x}(t)$ is considered as an instantaneous linear mixture of source signals and noise.

$\mathbf{s}(t) = \left[s_1(t), ..., s_m(t)\right]^{\mathrm{T}}$ contains the signals issued from *m* sources of narrow frequency range.

$\mathbf{y}(t) = \left[y_1(t), ..., y_m(t)\right]^{\mathrm{T}}$ contains the assembly of sources at a time *t*.

A is the transfer matrix or the mixing matrix between sensors.

$\boldsymbol{\sigma}(t)$ represents the noise vector.

Blind source separation consists in retrieving the source signals $\mathbf{s}(t)$ from their observed mixtures $\mathbf{x}(t)$. BSS attempts to separate a set of signals, without the knowledge (or with very little information) about the source signals or the mixing process. In most cases, vectors found in the mixing matrix **A** can describe vibration modes of the system and the sources in $\mathbf{s}(t)$ allows determining natural frequencies and damping.

Among the methods in the BSS family, one can cite for example Principal Component Analysis (PCA) or Proper Orthogonal Decomposition (POD), Smooth Orthogonal Decomposition (SOD), Independent Component Analysis (ICA) and Second-Order Blind Identification (SOBI). All of them have been exploited in many engineering applications owing to their versatility and their simplicity of practical use. Each method presents some advantages and drawbacks. For instance, natural frequencies can be estimated through the investigation of smooth orthogonal coordinates (in SOD) and sources (in ICA and SOBI). PCA involves a knowledge of the system's mass matrix for modal identification while SOD is able to overcome this drawback (Chelidze and Zhou (2006)[13]). In the PCA and SOD methods, the modes are orthogonal while in the ICA method, they are linearly independent. PCA may show some limitations when the data is not Gaussian or multi-modal Gaussian,

because in those cases, PCA simply gives uncorrelated variables which are not guaranteed statically independent. On the contrary, ICA consists in separating non-Gaussian source signals that are mutually statistically independent. The ICA method requires that at most one of the sources is Gaussian. Regarding to the SOBI method, the statistical independence is not required, but some degree of unrelatedness among the sources is required for source separation (Tang *et al.* (2005)[120]). SOBI considers the temporal relationship between components at multiple time delays by second-order statistics and makes it still possible to separate temporally correlated sources (Belouchrani *et al.* (1993)[8], (1997)[9]). Hazra and Narasimhan (2009)[39] remarked that SOBI-based methods show significant improvement over ICA methods in systems with high levels of damping because SOBI utilizes the inherent time structures of the sources.

The two families of methods cited above are based on the assumption of stationarity of the signals and lead to the identification of a unique set of 'modal' features. Time-frequency decompositions are helpful to capture transient dynamic features that appear during operation. Non-stationary signals can be more adequately inspected by time-frequency analysis using for instance Short-Time Fourier Transform (STFT), Wigner-Ville distribution, Wavelet Transform (WT), Hilbert-Huang Tranform (HHT)… For the sake of conciseness, we will focus on the last two methods, which allow extracting instantaneous features and have interested countless of researchers in recent time.

- **Wavelet Transform - WT**

A wavelet is a wave-like oscillation that is very useful for signal processing. Through the convolution operation on portions of an unknown signal, wavelets allow us to get information about the signal. Such process where the wavelets are scaled and translated is called the Wavelet transform. The WT shows advantages over the Fourier transform (FT) and the short-term Fourier transform (STFT) for analyzing signals that have discontinuities and sharp peaks and/or for analyzing non-periodic and non-stationary signals. The FT is localized in frequency and is unable to describe time-shifting frequency components. The STFT allows localization in both time and frequency but induces a frequency-time resolution trade-off (Mallat (1999)[76]) because the signal is observed by a window of constant size. Restrictions of the FT and STFT can be overcome by the WT thanks to the balanced resolution at any time and frequency with scaled and translated windows.

The WT in its discrete or continuous form has been used in many applications in various domains. The wavelet family comprises a lot of analyzing functions. Using Morlet wavelet, Kijewski and Kareem (2003)[56] dealt with system identification in civil engineering and Staszewski (1998)[118] with identification of systems with cubic stiffness nonlinearity. Argoul, Le and Erlicher [2, 68 and 21] used the continuous Cauchy wavelet transform as a tool for modal identification in linear and nonlinear systems. By combining with the capabilities of the bootstrap distribution in statistical estimation, the WT was used to consider the uncertainty effect on modal parameters of output-only system in Yan *et al.* (2006)[138]. In Lilien *et al.* (2006) [70], the WT was used to filter noisy data and then to identify frequency contents for the purpose of real time monitoring of electric line ampacity. Recently, Hazra and Narasimhan (2009)[39] proposed to use the WT for pre-processing in a SOBI-based technique. The technique was illustrated with civil structures under wind and earthquake excitations.

The use of the WT to detect nonlinearity onset in a dynamical system is described in details in Chapter 2.

- **Hilbert-Huang Transform - HHT**

The Hilbert-Huang Transform is basically an Empirical Mode Decomposition (EMD) technique. Huang *et al*. (1998)[44] proposed the EMD for decomposing a measured response $x(t)$ in m intrinsic mode functions (IMFs).

$$x(t) = \sum_{i=1}^{m} c_i(t) + r_m(t) \tag{1.4}$$

in which $c_i(t)$ (i = 1, 2, …, m) are IMFs of $x(t)$ and $r_m(t)$ is a residue that can be the mean trend of the signal or a constant.

An IMF is a mono-component which admits well-behaved Hilbert transforms. The EMD is applicable to nonstationary signals. The method achieves a sifting procedure consisting in subtracting the signal from the average of the upper and lower envelopes of the signal until the resulting signal becomes mono-component (IMF). The original signal is then subtracted from the IMF and the sifting procedure is repeated to the remaining signal to acquire another IMF. The IMFs c_1, c_2, …, c_m are frequency components arranged in decreasing order.

In the EMD, the envelopes are constructed by spline-fitting technique and the method is intuitive. Problems of smoothing can appear at the extremities of the signal, which requires several techniques to smooth the edges.

Let us consider a general signal noted $x(t)$. The Hilbert transform of $x(t)$ allows to determine a single set of value for amplitude, phase and frequency at any time t. For a meaningful composition of a signal in the frequency-time domain, Huang *et al*. (1998)[44] proposed to process the Hilbert transform to each IMF in order to obtain different frequency components at any time t. So we can acquire m spectral components from m IMFs resulting from the EMD procedure. The determination of damping ratios was described in [44]. Mode shapes can be deducted from the HHT achievement in the ensemble of DOFs of the system. However, it is important to mention the following particularities of the method:

- each IMF contains intrinsic characteristics of the signal $x(t)$;
- neighbouring components may contain oscillations of the same frequency, but they never occur at the same time in two different IMF components. An IMF has not the same frequency as the previous IMF at the same moment t;
- the HHT is applicable for non-stationary signals and for nonlinear dynamic behaviours;
- if one considers a linear combination of two sinusoidal oscillations of close frequencies, the EMD method can extract the two components and their instantaneous frequencies overlap. The key problem of the HHT is the use of splines as it seems to be the main factor of limitation of the method;
- problems of smoothing at signal extremities produce unexpected large oscillations. This boundary effect is due to the spline smoothing and to the Hilbert transform.

The HHT has been used successfully in the last decade for the analysis of non-stationary and/or nonlinear signals. The method has been recently improved by countless researchers so that its application becomes more friendly and accurate. For example, Flandrin *et al.*

(2005)[28] used added noise to overcome one of the difficulties of the original EMD method. Wu and Huang (2009)[131] proposed a new Ensemble Empirical Mode Decomposition that sifts an ensemble of white noise-added signal and treats the mean as the final true result. Huang *et al*. (2009)[45] proposed two new methods to overcome the difficulties of computing instantaneous frequency: the direct quadrature and the normalized Hilbert transform.

Nowadays, as mentioned previously, identification of nonlinear systems presents many challenges with respect to linear systems. There is a big interest in the identification of nonlinear structures both in the frequency and time domains. The NARMAX (Nonlinear Auto Regressive Moving Average with eXogenous outputs) model is an example; it was fitted using modal coordinates in Thouverez and Jezequel (1996)[122] to identify nonlinear systems. Adams and Allemang (2000)[1] proposed a method in the frequency domain called Nonlinear Identification through Feedback of the Output. Artificial neural networks have received lot of attention in identifying nonlinear systems (Le Riche *et al.* (2001)[66], Pei *et al.* (2004)[100]). In the period of 1997-2001, in the framework of the European Cooperation in the field of Scientific and Technical Research - COST Action F3 Structural Dynamics, the identification of nonlinear systems was addressed by a specific working group (Golinval *et al.* (2003)[34]). Two main benchmarks were studied using different methods: for example, the condition reserve path method in the frequency domain, the restoring force surface method in the time domain, some modal methods based on the definition of nonlinear normal modes (NNMs), the proper orthogonal decomposition (POD), the wavelet transform (WT) and model updating techniques. More recently, Arquier *et al.* (2006)[3] presented the time integration periodic orbit method and the modal representation method for undamped nonlinear mechanical systems. Marchesiello and Garibaldi (2008)[78] identified nonlinear vibrating structures by subspace methods. Peeters *et al.* (2009)[99] developed a technique for determining the NNMs of nonlinear mechanical systems based on a shooting procedure and a method for the continuation of NNM motions. They also proposed a phase resonance appropriation technique to identify NNMs experimentally. Da Silva *et al.* (2010)[15] proposed a method to identify localized nonlinear parameters based on the identification of Wiener kernels through model updating. Rainieri and Fabbrocino (2010)[105] discussed the identification from non-stationary signals by comparing the results of the automated output-only modal identification algorithm LEONIDA and some other methods. Their applications are achieved through data recorded in operational conditions and during ground motions induced by the recent L'Aquila earthquake.

All these methods of identification provide us better comprehension of mechanical systems. Furthermore, they can provide useful tools for detection problem, as presented in the next section.

1.3 Methods of detection

Detection of changes in the dynamic state of structures is an important issue in the field of Structural Health Monitoring (SHM). It may be caused by the occurrence of damage but also by the onset of a nonlinear behaviour.

Detection methods that use mathematical models include parametric and non-parametric techniques. Parametric methods require the construction of a structural model and are based on model updating techniques (Friswell *et al.* (2001)[31], Titurus *et al.* (2003)[124, 125]). A precise model is of primary importance in this case; it offers the advantage to allow damage location and possibly remaining lifetime calculation but it generally needs a lot of modelling and computation time. Non-parametric methods do not require a structural model. Based on

vibration measurements only, those methods attempt to extract features, which are sensitive to changes in the current dynamic state of the monitored structure. They may be based on the direct use of modal parameters (eigenfrequencies and mode shapes), or stiffness and flexibility matrices. There exists a large amount of damage detection methods using eigenfrequency changes (Messina *et al.* (1998)[82], Yang *et al.* (2004)[140]). The techniques using only eigenfrequencies are simple; however it is necessary to distinguish damage from the influence of environmental and operational conditions (Yan *et al.* (2005)[134, 135], Deraemaeker *et al.* (2008)[19]). The main drawbacks of those techniques are that sometimes unrealistic damage patterns are found, and the number of measured eigenfrequencies is generally lower than the number of unknown model parameters, resulting in a non-unique solution (Maeck (2003)[74]). Alternatively, the monitoring of mode-shape changes is a useful approach for detection. A common measure used to evaluate the correlation between two families of modes $\phi^{\{A\}}$ and $\phi^{\{B\}}$ is the Modal Assurance Criterion - MAC:

$$\mathrm{MAC}\left(\phi_i^{\{A\}}, \phi_j^{\{B\}}\right) = \frac{\left(\phi_i^{\{A\}^{\mathrm{T}}} \phi_j^{\{B\}}\right)^2}{\left\|\phi_i^{\{A\}}\right\| \left\|\phi_j^{\{B\}}\right\|} \tag{1.5}$$

where $\phi_i^{\{A\}}, \phi_j^{\{B\}}$ denote modes *i* and *j* of two different states *A* and *B* respectively (e.g. normal and faulty states). The MAC value between two modes can vary from 0 to 1; the value of 0 means no correlation and 1 means perfect correlation. The deviation from unity can reflect a faulty state.

Damage detection can also be based on the dynamically measured flexibility matrix, which is just the inverse of the stiffness matrix. The measured flexibility matrix **F** is estimated from the mass-normalized mode shapes and frequencies as:

$$\mathbf{F} = \mathbf{\Phi}\mathbf{\Omega}^{-1}\mathbf{\Phi} = \sum_{i=1}^{m} \frac{1}{\omega_i^2} \phi_i \phi_i^{\mathrm{T}} \tag{1.6}$$

where the mode-shape vectors have been mass-normalized such that $\mathbf{\Phi}^{\mathrm{T}}\mathbf{M}\mathbf{\Phi} = \mathbf{I}$, $\mathbf{\Omega} = \mathrm{diag}\left(\omega_i^2\right)$ ($i = 1,\ldots, m$) is the spectral matrix containing the *m* eigen-frequencies. In Yan and Golinval (2005)[133], the flexibility matrix was assembled from mode shapes identified by the stochastic subspace method (SSI), which permits to deduce the corresponding stiffness matrix by a pseudo-inversion. Koo *et al.* (2009)[61] proposed a damage detection method based on the damage-induced chord-wise deflections which were estimated using the modal flexibility matrices.

Furthermore, several other methods exist. They perform the detection based on the ensemble of extracted modal features, e.g. a subspace built by mode shapes. Other indexes are used to indicate detection. For example, some damage detection techniques are based on principal component analysis (PCA) of vibration measurements (De Boe and Golinval (2003)[16], Yan *et al.* (2005)[134]) where damage indexes are based on the concept of subspace angle and/or on statistics using the Novelty Index analysis. In Zang *et al.* (2004)[141], independent component analysis (ICA) was combined with neural networks for structural damage detection. Without modal identification, null subspace analysis (NSA) based on the definition of Hankel matrices (Yan and Golinval (2006)[137]) allows detecting damages efficiently. Several other BSS methods are attractive for fault detection, namely: the mean field independent component analysis (Pontoppidan *et al.* (2005)[102]); the fourth-order cumulant-based decorrelation method (Jianping and Guang (2009)[49]).

PCA is known as an efficient method to compress a set of random variables and to extract the most important features of a dynamical system. However, this method is based on the assumption of linearity. To some extent, many systems show a certain degree of nonlinearity and/or non-stationarity, and PCA may then overlook useful information on the nonlinear behavior of the system. Therefore, detection problem may necessitate methods which are able to study nonlinear systems.

Efforts have been made to develop nonlinear damage detection methods based on PCA. For example, the nonlinear PCA method proposed in Kramer (1999)[62], Sohn *et al.* (2001)[117] used artificial neural network training procedures which are able to generate nonlinear features. In Reference Yan *et al.* (2005)[135], local PCA is used to perform piecewise linearization in the cluster of nonlinear data in order to split it into several regions, and then to carry out PCA in each sub-region.

Alternatively, Kernel Principal Component Analysis (KPCA) is a nonlinear extension of PCA built to authorize features such that the relation between variables is nonlinear. Lee *et al.* (2004)[69] used KPCA to detect fault in the biological wastewater treatment process by means of statistics charts. Sun *et al.* (2007)[119] achieved fault diagnosis in a large-scale rotating machine through classification techniques. Widodo and Yang (2007)[130] extracted nonlinear feature in support vector machines (SVM) to classify the faults of induction motor. He *et al.* (2007)[40] monitored gearbox conditions by extracting the nonlinear features with low computational complexity based on subspace methods. Cui *et al.* (2008)[14] reduced the computational complexity of KPCA in the fault detection by a feature vector selection scheme. At the same time, they improved the KPCA detection by adopting a KPCA plus Fisher discriminant analysis. Chang and Sohn (2009)[12] detected damage in the presence of environment and operational variations by basing on unsupervised support vector machines. Ge *et al.* (2009)[32] improved the KPCA monitoring in nonlinear processes when the Gaussian assumption is violated by proposing a new joint local approach-KPCA.

On the other hand, time-frequency decompositions prove to be effective for studying systems in which responses are non-stationary or/and nonlinear. The Hilbert-Huang transform (HHT) has been exploited to evaluate damage in Yang *et al.* (2002)[139] and to determine the time of occurrence of damage in Yang *et al.* (2004)[140]. The detection and identification of nonlinearities were performed on the basis of HHT and perturbation analysis by Pai and Palazotto (2008)[95]. One of the main drawbacks of the HHT method relies in its empirical formulation. Conversely, the theoretical basis of the Wavelet Transform (WT) makes it more appropriate for non-stationary data analysis. Gurley and Kareem (1999)[37] used both the continuous and discrete WT for identification and characterization of transient random processes involving earthquakes, wind and ocean engineering. Messina (2004)[83] discussed and compared the continuous WT with differentiator filters for detecting damage in transversally vibrating beam. Yan and Gao (2005)[136] proposed an approach based on the Discrete Harmonic Wavelet packet transform to machine health diagnosis. The WT was also combined with auto-associative neural network in Sanz *et al.* (2007)[114] for monitoring the condition of rotating machinery; with outlier analysis in Rizzo *et al.* (2007)[108] for structural damage detection. In Argoul and Le (2003)[2], four WT instantaneous indicators are proposed to facilitate the characterization of the nonlinear behaviour of a structure.

To detect the onset of nonlinearity, other nonlinear indicator functions can be used as reported in Farrar *et al.* (2007)[25]. Basic signal statistics are commonly adopted; they are cited in Table 1.1. In He *et al.* (2007)[40], statistics in time and frequency domains were exploited for detecting nonlinear damage; these statistics allow to avoid the use of raw time series data. Nonlinearity can also be observed by checking linearity and reciprocity.

Nonlinearity onset was detected by comparing the FRF and coherence functions or PCA subspaces (Thouverez (2002)[123], Kerschen (2003)[52], Hot *et al*. (2010)[41]). Harmonic or waveform distortion is also one of the clearest indicators of the nonlinearity onset (Qiao and Cao (2008)[104], Nguyen *et al.*, (2010)[87], Da Silva *et al.* (2010)[15]). Furthermore, NARMAX model represents an efficient tool in analysing nonlinear responses [72, 129]. Liu *et al.* (2001) [72] proposed a tool for interpreting and analysing nonlinear system with significant nonlinear effects, then it was applied for fault detection in the civil engineering domain. Wei *et al.* (2005)[129] assessed internal delamination in multi-layer composite plates by basing on the NARMAX model.

Table 1.1: Basic signal statistics

Mean ($\bar{x}$)	Peak amplitude (x_p)	Root mean square (RMS)	Square root value (R)	Standard deviation (σ)
$\bar{x} = \frac{1}{N}\sum_{i=1}^{N} x_i$	$x_p = \max\lvert x_i \rvert$	$\mathrm{RMS} = \sqrt{\frac{1}{N}\sum_{i=1}^{N} x_i^2}$	$\mathrm{R} = \left(\frac{1}{N}\sum_{i=1}^{N}\sqrt{\lvert x_i \rvert}\right)^2$	$\sigma = \sqrt{\frac{1}{N}\sum_{i=1}^{N}\left(x_i - \bar{x}\right)^2}$
Crest factor (C)	Shape factor (S)	Kurtosis (κ)	Skewness (S_k)	
$C = x_p/\mathrm{RMS}$	$S = \mathrm{RMS}/\lvert\bar{x}\rvert$	$\kappa = \frac{\frac{1}{N}\sum_{i=1}^{N}\left(x_i - \bar{x}\right)^4}{\sigma^4}$	$S_k = \frac{\frac{1}{N}\sum_{i=1}^{N}\left(x_i - \bar{x}\right)^3}{\sigma^3}$	

1.4 Methods for localization and evaluation

The methods cited above provide effective tools to detect the presence of faults. Furthermore, the problem of damage localization and assessment has been approached from many directions in the last decade. Often based on the monitoring of modal features, these processes can be achieved by using an analytical model and/or promptly by measurements. The methods may be used for one or both purposes: localization/ assessment.

Damage can cause change in structural parameters, involving the mass, damping and stiffness matrices of the structure. Thus many methods deal directly with these system matrices. The Finite Element Method is an efficient tool in this process (Huynh *et al.* (2005)[46], Michels *et al*. (2008)[85]). The problem of detection and localization may be resolved by this method through model updating or sensitivity analysis (Pascual (1999)[97]). For damage localization and evaluation, model updating is utilized to reconstruct the stiffness perturbation matrix (Koh and Ray (2003)[59]); to handle changes in the system matrices of nonlinear systems (D'Souza and Epureanu (2008)[20]). This may be combined with a genetic algorithm (Gomes and Silva (2008)[36]) or based on modal parameter sensitivity (Bakir *et al.* (2007)[4]). In model updating, an optimization procedure is established in order to minimize the differences between experimental and numerical modal data by adjusting uncertain model parameters (Maia *et al.* (1997)[75]).

Among sensitivity analyses, natural frequency sensitivity has been used considerably in localization problem. Messina *et al.* (1998)[82] estimated the size of defects in a structure

based on the sensitivity of frequencies with respect to damage locations where all the structural elements were considered as potentially damaged sites. Ray and Tian (1999)[106] discussed sensitivity of natural frequencies with respect to the location of local damage. In that study, damage localization involved the considering of mode shape change. Teughels and De Roeck (2004)[121] identified damage in a highway bridge by updating both Young's modulus and shear modulus using an iterative sensitivity based finite element model updating method. Other authors (Koh and Ray (2004)[60], Jiang (2007)[47]) have located damage by measuring natural frequency changes before and after the occurrence of damage. However, such methods require a well fitted numerical model to compare with the actual system. Jiang and Wang (2009)[48] removed that requirement by utilizing a mathematical model identified from experimental measurement data, where a closed-loop control is designed to enhance the frequency sensitivity for the sake of structural damage localization and assessment.

Methods based on measurements are also widely used because of their availability in practice. Yang *et al.* (2002)[139] estimated damage severity by computing the current stiffness of each element. They used Hilbert-Huang spectral analysis based only on acceleration measurements using a known mass matrix assumption. Yan and Golinval (2005)[133] achieved damage localization by analyzing flexibility and stiffness without system matrices, using time data measurements. Koo *et al*. (2009)[61] detected and localized low-level damage in beam-like structures using deflections obtained by modal flexibility matrices. Following localization, Kim and Stubbs (2002)[57] estimated damage severity based on the mode shape of a beam structure. Rucka and Wilde (2006)[111] decomposed measured frequency response functions (FRFs) by continuous wavelet transform (CWT) in order to achieve damage localization. Based also on CWT, Bayissa *et al.* (2008)[6] analyzed measured time responses to extract the principal structural response features. Then the combination with the zeroth-order moment allows detecting and localizing damage in a plate model and a full-scale bridge structure. For crack identification in beam-type structures, Hadjileontiadis *et al*. (2005)[38] used fractal dimension analysis; Qiao and Cao (2008)[104] explored waveform fractal dimension and applied it to mode shape without a requirement of a numerical or measured baseline mode shape. The damage in a 50-year old bridge (Reynders *et al.* (2007)[107]) was identified using model updating based on eigen-frequencies, mode-shape vectors and modal curvature vectors. In References Bakir *et al.* (2008)[5] and Fang *et al.* (2008)[22], damage localization and quantification were achieved in reinforced concrete frames by comparing eigen-frequencies and mode-shapes with different optimization techniques. Using static load tests and non-linear vibration characteristic, Waltering *et al*. (2008)[128] assessed damage in a gradually damaged prestressed concrete bridge. Deraemaeker and Preumont (2006)[18] suggested a way to distinguish global from local damage through modal filters and frequency deviation. Cao and Qiao (2009)[10] recently used a novel Laplacian scheme for damage localization. Other authors have located damage by comparing identified mode shapes (Ray and Tian (1999)[106]) or their second-order derivatives (Pandey *et al.* (1991)[96]) in varying levels of damage. Sampaio *et al*. (1999)[113] extended the method proposed in [96] through the use of measured FRFs. Considering only the FRFs in the low-frequency range, Liu *et al*. (2009)[73] use the imaginary parts of FRF shapes and normalizing FRF shapes for damage localization. Their method was illustrated by a numerical example of cantilever beam.

Beside the performance of damage assessment, methods for parameter estimation are also very helpful for characterizing nonlinear systems. For example, the condition reserve path method (Marchesiello *et al.* (2001)[77], Kerschen (2003)[52]) consists in separating the linear and nonlinear part of the system response and in constructing uncorrelated response components in the frequency domain. The restoring force surface method (Kerschen *et al.*

(2001)[51]) allows a direct identification for single-degree-of-freedom nonlinear systems and can be extended to multi-degree-of-freedom systems. The second order differential equations expressed in terms of linear modal co-ordinates was employed in Bellizi and Defilippi (2001)[7] to determine the linear stiffness and modal damping parameter as well as nonlinear parameters. The second order differential equations expressed in terms of physical co-ordinates allowed identifying physical parameters of an initial nonlinear model (Meyer *et al.* (2001)[84]). Besides, the NIFO method (Nonlinear Identification through Feedback of the Outputs) (Adams and Allemang (2000)[1]) provides a simple method to estimate the linear and nonlinear coefficients. In Lenaerts (2002)[64], the Proper Orthogonal Decomposition was combined with the Wavelet transform to estimate nonlinear parameters. More recently, the subspace methods in the time domain (Marchesiello and Garibaldi (2008)[78]) were proposed to estimate the coefficients of nonlinearities. Assessment of localized nonlinear parameters was achieved by identifying the first and second-order Wiener kernels through modal updating in Da Silva *et al.* (2010)[15].

1.5 Concluding remarks

In this chapter, a brief overview of the state of the art on modal identification and detection methods in linear and nonlinear mechanical systems was presented.

Based on this overview, some methods which appear to us to be very promising are considered in the development of our research and are studied in details in the next chapters.

Among time-frequency decompositions, the Wavelet transform is a mathematically rigorous method which, combined with other tools, turns out to be a very promising tool for the purpose of treating nonlinear and non-stationary signals.

Output-only-based methods are very attractive for identification and detection since no structural analytical model is needed. Several methods as PCA, ICA… are well known and have been widely used in detection problems. The SOBI method has been introduced recently for modal identification purposes in the literature but its use for damage detection in mechanical systems has not been yet well studied. As a nonlinear feature extractor, KPCA appears also as an interesting alternative to PCA in the processing of nonlinear signals.

Localization and evaluation questions are more problematic than detection. For this purpose, sensitivity analysis is an appropriate approach and has been considered by many authors. In this dissertation, the sensitivity of mode shapes is used to locate and evaluate damage in structures. It consists in a PCA-based sensitivity analysis developed in the frequency domain.

Chapter 2

Nonlinearity Detection Method Based on the Wavelet Transform

2.1 Introduction

As mentioned in the previous chapter, the Wavelet transform is well-appreciated for both identification and detection purposes. The aim of this chapter is to propose a method to detect nonlinearity using the Wavelet Transform and the concept of subspace angle. Morlet wavelet is considered here as the mother wavelet to extract instantaneous frequencies and amplitudes from time measurements at different locations on the structure. Deformation modes associated to instantaneous frequencies may then be extracted from the whole data set and assembled to build instantaneous observation matrices. Singular value decomposition of these matrices allows to determine the dimensionality of the system. Next, the retained deformation shapes are compared with reference mode-shapes using the concept of subspace angle. The objective pursued here is to provide an index able to detect the onset of the nonlinear behaviour of the structure. The proposed technique is illustrated on the example of a clamped beam which exhibits a geometric nonlinearity at one end. It shows a good sensitivity to small changes in the dynamic behaviour of the structure and thus may also be used for damage detection.

2.2 Preliminary bases

- **Fourier Transform**

The Fourier Transform (FT) analyses the "frequency content" of a signal. The FT $\hat{f}(\omega)$ of $f(t)$ is defined by:

$$\hat{f}(\omega) = \int_{-\infty}^{+\infty} f(t) e^{-j\omega t} dt \qquad \text{with} \qquad j = \sqrt{-1} \tag{2.1}$$

The signal $f(t)$ may be reconstructed by considering the inverse Fourier Transform:

$$f(t) = \frac{1}{2\pi} \int_{-\infty}^{+\infty} \hat{f}(\omega) e^{j\omega t} d\omega \tag{2.2}$$

Equation (2.1) shows that the FT $\hat{f}(\omega)$ is a global representation of the signal in the sense that it necessitates the knowledge of the signal in the whole time domain and the information

is mixed due to infinite support of the basic function $e^{j\omega t}$. That means the use of the FT is appropriate when the considered signal is stationary.

The main limitation of the FT is due to the fact that it ignores the time evolution of the signal frequency content. So the FT does not allow to analyze local frequency behavior of the signal, nor its local regularity. In this case, it is necessary to use local transforms, i.e. which permit to decompose the signal on a basis generated by functions localized in time and frequency.

- **Analytic signal**

In order to analyze the time evolution of frequency content of a signal, it is necessary to use the notion of analytic signal that allows to separate the phase and amplitude information of signals.

A signal $f_a(t)$ is called an analytic signal if it has no negative-frequency components. The analytic part $f_a(t)$ of a signal $f(t)$ is necessarily complex and is given by its FT (Mallat (1999)[76]).

$$\hat{f}_a(\omega) = \begin{cases} 2\hat{f}(\omega) & \text{if } \omega \geq 0 \\ 0 & \text{if } \omega < 0 \end{cases} \tag{2.3}$$

- **Instantaneous frequency**

A real signal $f(t)$ may be decomposed in an amplitude $a(t)$ modulated by a time-varying phase $\phi(t)$:

$$f(t) = a(t)\cos\left(\phi(t)\right) \qquad a(t) \geq 0 \tag{2.4}$$

The instantaneous frequency $\omega(t)$ is the non-negative derivative of the phase:

$$\omega(t) = \phi'(t) \qquad \phi'(t) \geq 0 \tag{2.5}$$

However it exists many possible choices for $a(t)$ and $\omega(t)$. A particular decomposition may be performed by means of the analytic part $f_a(t)$ of $f(t)$ of which the FT is defined in (2.3), this complex signal consists of the module and the complex phase:

$$f_a(t) = a(t)e^{j\phi(t)} \tag{2.6}$$

Since $f = \text{Real}[f_a]$, one has: $f(t) = a(t)\cos\left(\phi(t)\right)$.

$a(t)$ is called the analytic amplitude of $f(t)$ and $\phi'(t)$ is its instantaneous frequency, these quantities are uniquely defined.

Analytic amplitude and instantaneous frequency are of great importance in the synthesis of signals which have non-stationary frequency contents.

- **Time - frequency localization and Uncertainty Principle**

The FT may be seen as a representation of sine curve basis. These sine curves are very well localized in frequency, but not in time, as their support is infinite. It is a consequence of their periodicity.

If one wants to represent the frequency properties of a signal locally in time, they should be analyzed by signals localized *in time and frequency*. For example, we can use (if possible)

a basis consisting of functions with compact support in time and frequency, called *time-frequency atoms*. One associates them with a unitary norm function $\phi_\gamma(t)$ in which γ may be multi-index parameter characterizing an atom.

It is proven that inner products are conserved by the FT up to a factor of 2π, i.e.

$$\int_{-\infty}^{+\infty} f(t)\bar{g}(t)dt = \frac{1}{2\pi}\int_{-\infty}^{+\infty} \hat{f}(\omega)\bar{\hat{g}}(\omega)d\omega \tag{2.7}$$

Eq. (2.7) is called the Parseval formula, which allows to perform the signal transform $T(\gamma)$ in this set of time-frequency atoms:

$$T(\gamma) = \int_{-\infty}^{+\infty} f(t)\bar{\phi}_\gamma(t)dt = \frac{1}{2\pi}\int_{-\infty}^{+\infty} \hat{f}(\omega)\bar{\hat{\phi}}_\gamma(\omega)d\omega \tag{2.8}$$

where $\hat{\phi}_\gamma(\omega)$ is the FT of the atom $\phi_\gamma(t)$.

The "time-frequency localization" of a basic atom is represented as a "Heisenberg box" (Figure 2.1), placed in the time - frequency plan, that is a rectangle of dimensions σ_t and σ_ω, centered in the coordinates (u, ξ).

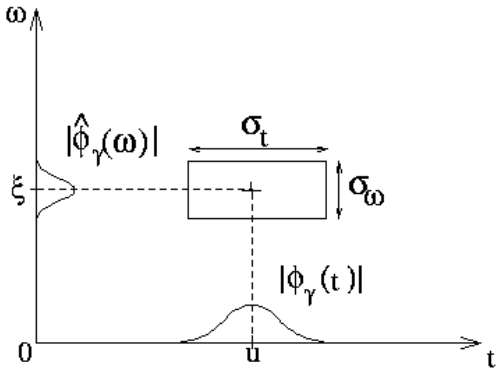

Figure 2.1: Heisenberg box of a time-frequency atom (Mallat (1999)[76])

The uncertainty principle proves that the area of this rectangle satisfies:

$$\sigma_t\sigma_\omega \geq \frac{1}{2} \tag{2.9}$$

This area is minimum when $\phi_\gamma(t)$ is a Gaussian, i.e. if it exists $\gamma = (u, \xi, a, b) \in \Re^2 \times \mathbf{C}^2$ such as $\phi_\gamma(t) = ae^{j\xi t - b(t-u)^2}$. In this case, the maximum resolution in time and frequency is achieved. For a Gaussian of type $\phi_\gamma(t) = \frac{1}{(\sigma^2\pi)^{1/4}} e^{-\frac{t^2}{2\sigma^2}}$ which is presented in terms of parameter σ, the spreads in time and frequency are $\sigma/\sqrt{2}$ and $1/(\sigma\sqrt{2})$, respectively.

- **Short-term Fourier Transform**

The short-term Fourier Transform (STFT), or alternatively short-time Fourier Transform of a signal $f(t)$ introduces a notion of time locality by multiplying the signal by a suitably

chosen window $g(t)$ (having good properties of localization) and by calculating the resulted product FT (Figure 2.2):

$$Sf(u,\xi) = \left\langle f, g_{u,\xi} \right\rangle = \int_{-\infty}^{+\infty} f(t) g(t-u) e^{-j\xi t} dt \tag{2.10}$$

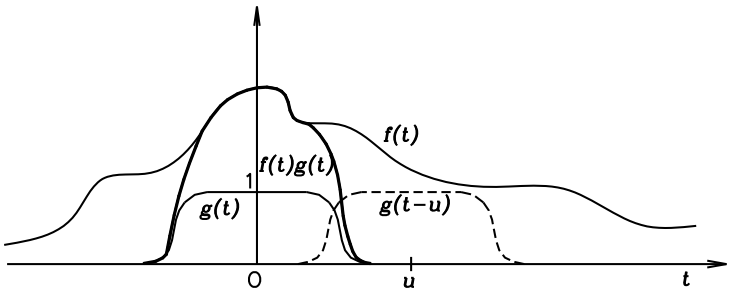

Figure 2.2: Time localization by the STFT

Considering a real, symmetric window with a unitary norm $g(t) = g(-t)$ of finite energy, it is translated by *u* and modulated by the frequency ξ :

$$g_{u,\xi}(t) = e^{j\xi t} g(t-u) \tag{2.11}$$

Its FT $\hat{g}_{u,\xi}(\omega)$ is given by:

$$\hat{g}_{u,\xi}(\omega) = \hat{g}(\omega-\xi) e^{-ju(\omega-\xi)} \tag{2.12}$$

The Parseval formula (2.7) permits to write:

$$Sf(u,\xi) = \frac{1}{2\pi} \int_{-\infty}^{+\infty} \hat{f}(\omega) \bar{\hat{g}}(\omega-\xi) e^{j\omega u} d\omega \tag{2.13}$$

Expressions (2.10) and (2.13) show that the window $g_{u,\xi}(t)$ allows the observation of the signal $f(t)$ around the time *t* = *u* and the frequency window $\hat{g}_{u,\xi}(\omega)$ allows the observation of the signal frequency spectrum $\hat{f}(\omega)$ around the frequency $\omega = \xi$. The STFT provides thus information on the content of $f(t)$ in the neighborhood of point *t* = *u* and $\omega = \xi$.

It is easy to prove that the spreads in time $\sigma_{t,g_{u,\xi}}$ and in frequency $\sigma_{\omega,g_{u,\xi}}$ are independent of the translation *u* and of the modulation ξ . Those resolutions are then equal to the spreads $\sigma_{t,g}$ and $\sigma_{\omega,g}$ of the mother window $g(t)$. It means that if the standard deviation in time is constant; the one in frequency is also constant. The family is thus obtained by translation in time and frequency of a single window with constant size (Figure 2.3*a*).

However, paving dimensions in the time-frequency plan depend on the chosen mother window. The choice of an adequate window is then of primary importance.

2.3 Wavelet transform

The Wavelet transform attempts to soften the main drawback of the STFT: a window of constant size does not allow to obtain an optimal time or frequency resolution. In fact, a small temporal window is adequate to localize a high frequency phenomenon whereas a larger window is necessary for a lower frequency phenomenon. The advantage of using wavelets is

to adapt the resolution to different components of the signal by its own nature. It results that the resolutions in time and frequency are variable in the time-frequency plan.

- **Definition**

In the same manner as the Fourier Transform may be defined as a projection on the complex exponential basis, the Wavelet Transform is introduced as the projection on the basis of wavelet functions (Mallat (1999)[76]):

$$Wf(u,s) = \frac{1}{\sqrt{s}} \int_{-\infty}^{+\infty} f(t) \bar{\psi}\left(\frac{t-u}{s} \right) dt \quad \text{with} \quad u,s \in \Re \tag{2.14}$$

A wavelet is a zero mean function $\psi(t) \in \mathcal{L}^2(\Re)$, with unitary norm (and so with finite energy) and centered in the neighborhood of t = 0. The functions $\psi_{u,s}(t)$ are obtained by dilating the mother wavelet by a scale factor s and translating it by u:

$$\psi_{u,s}(t) = \frac{1}{\sqrt{s}} \psi\left(\frac{t-u}{s} \right) \tag{2.15}$$

The last function is centered in the neighborhood of u, as the STFT atom. If the center frequency of $\psi(t)$ is ξ, then the center frequency of a dilated function is ξ / s. The wavelet coefficients $Wf(u,s)$ designate the similitude between the dilated (compressed)/ translated mother wavelet and the signal at the time t and at the scale (frequency) s.

- **Admissibility condition**

The function $\psi(t) \in \mathcal{L}^2$ must satisfy the condition:

$$C_\psi = \int_0^{+\infty} \frac{|\hat{\psi}(\omega)|^2}{|\omega|} d\omega < +\infty \tag{2.16}$$

This condition allows to analyze the signal and then to reconstruct it without loss of information according to the formula:

$$f(t) = \frac{2}{C_\psi} \text{Real} \left[\int_0^{+\infty} \int_{-\infty}^{+\infty} Wf(u,s) \psi_{u,s} du \frac{ds}{s^2} \right]$$

Moreover, the admissibility condition implicates that the FT of the wavelet must be zero at the frequency $\omega = 0$:

$$\hat{\psi}(\omega)\big|_{\omega=0} = 0 \tag{2.17}$$

It implies two important consequences: 1) the wavelets must have a band-pass spectrum; 2) the equivalence of the last equation under the form:

$$\int_{-\infty}^{+\infty} \psi(t) dt = 0 \tag{2.18}$$

shows $\psi(t)$ must be zero mean. $\psi(t)$ is thus a function of finite larger in time (time window) possessing an oscillation characteristic. One has then a small wave: a wavelet.

The time spread is proportional to s while the frequency spread is proportional to the inverse of s.

$$\Delta t = s\sigma_t \;; \quad \Delta\omega = \frac{\sigma_\omega}{s} \tag{2.19}$$

These quantities reflect the analysis quality; otherwise they represent the *resolutions in time and frequency*. Figure 2.3 compares Heisenberg box examples through STFT and wavelet atoms.

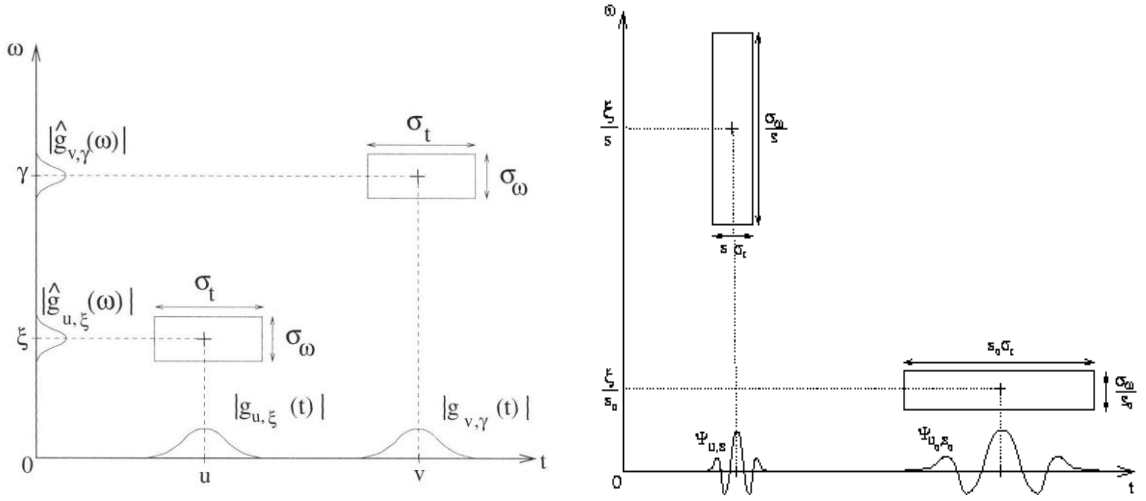

a) Short-term Fourier transform [76] *b) Wavelet transform [76]*

Figure 2.3: Comparison between STFT and WT windows

Note that the scale factor s is $s = \frac{\xi}{\omega}$, for a Gaussian window, the variances in (2.19) are represented in the form:

$$\Delta t = \frac{\xi}{\omega}\frac{\sigma}{\sqrt{2}} \;; \qquad \Delta\omega = \frac{\omega}{\xi}\frac{1}{\sigma\sqrt{2}} \;. \tag{2.20}$$

So, the wavelet shows a good precision in frequency for a low frequency and a good precision in time for a high frequency. This property is useful in signal analysis as at high frequencies, the precision in time is more important than the precision in frequency and vice-versa (Le (2003)[67]).

The contraction/dilatation property of wavelets is illustrated in Figure 2.4:

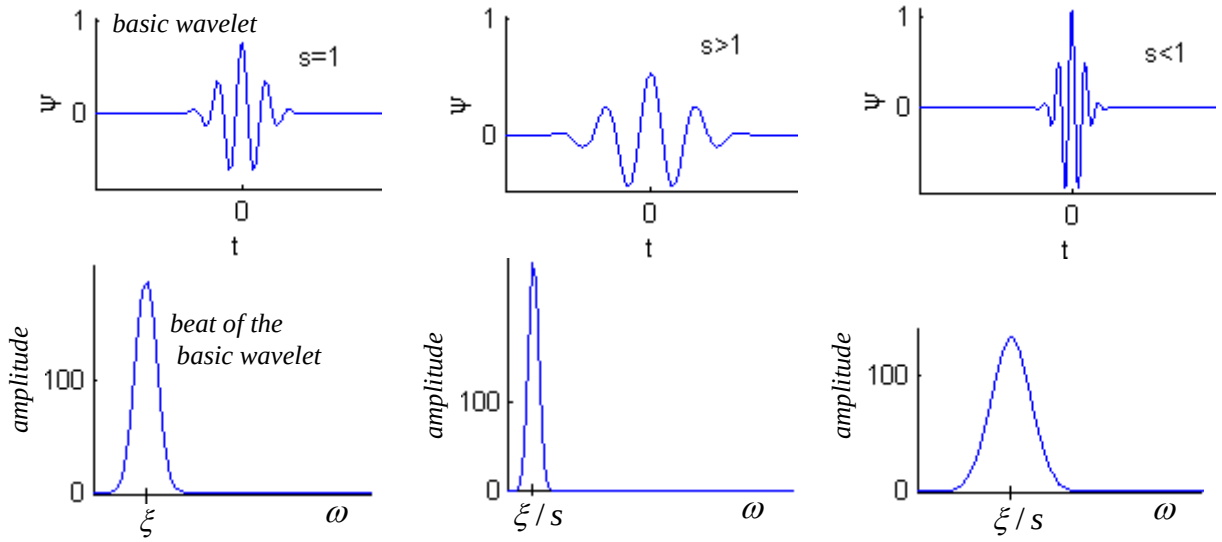

Figure 2.4: Wavelet localization in the time-frequency plan

In frequency analysis, the WT may be considered as a filter with the quality factor Q defined by the ratio between the center frequency ξ / s and the frequency band σ_ω / s [67]:

$$Q = \frac{\xi / s}{2\sigma_\omega / s} = \frac{\xi}{2\sigma_\omega} \tag{2.21}$$

This factor is independent of s and it depends only on characteristic parameters of the mother wavelet $\psi(t)$.

Using the Parseval formula (Eq. 2.7), the WT can be computed by the FT:

$$Wf(u,s) = \frac{\sqrt{s}}{2\pi} \int_{-\infty}^{+\infty} \hat{f}(\omega)\bar{\hat{\psi}}(s\omega)e^{j\omega u} d\omega \tag{2.22}$$

For each scale s, one computes the inverse transform of the product of signal $f(t)$ and the dilated versions $\hat{\psi}(s\omega)$ of the mother wavelet $\psi(t)$. In numerical applications, the WT computation is completed practically through the fast Fourier transform (FFT) algorithm.

- **Scalogram**

A bi-dimensional energy density is defined, the scalogram $P_W f(u,\omega)$ which measures the energy of $f(t)$ in the Heisenberg box of each wavelet $\psi_{u,s}$ centered at $(u, \omega = \xi / s)$:

$$P_W f(u,\omega) = |Wf(u,s)|^2 = \left| \int_{-\infty}^{+\infty} f(t)\bar{\psi}_{u,s}(t) dt \right|^2 \tag{2.23}$$

Or the normalized scalogram $P_w^{norm} f(u,\omega)$:

$$P_W^{norm} f(u,\omega) = \frac{1}{s} P_W f(u,\omega) = \frac{1}{s} |Wf(u,s)|^2$$

So, thanks to its ability to consider time and frequency resolutions at the same time, the WT is particularly well adapted to detect discontinuity or sharp signal transitions.

To separate amplitude and phase information of signals, one uses analytic complex wavelets, which have the property of progressiveness, i.e. $\hat{\psi}(\omega) = 0$ for $\omega < 0$. The progressiveness ensures the WT does not produce any interference between the past and future in the time domain. The energy of $\hat{\psi}(\omega)$ is then localized around a center frequency $\xi > 0$.

- **Choice of wavelet**

Many analytic wavelets are studied in the literature. The choice of mother wavelet depends on several analysis properties. The Morlet wavelet is very popular in the literature because its analogues to the FT are useful for harmonic analysis. It is the reason why it is chosen in this work. The Morlet wavelet is defined by the complete formula:

$$\psi(t) = c\left(e^{j\omega_0 t} - e^{-\frac{\omega_0^2 \sigma^2}{2}} \right) e^{-\frac{t^2}{2\sigma^2}}, \qquad c = \frac{1}{\sqrt[4]{\pi\sigma^2}} \left(1 - 2e^{-\frac{3\sigma^2\omega_0^2}{4}} + e^{-\sigma^2\omega_0^2} \right)^{-\frac{1}{2}} \tag{2.24}$$

where ω_0 and c are respectively the center frequency of $\hat{\psi}$ and the adequate normalization factor.

The term $e^{-\sigma^2\omega_0^2}$ is known as the correction term, as it verifies the admissibility condition and the zero-mean condition of the Morlet wavelet. In practice, for enough large value of product $\omega_0\sigma$, it is negligible. In this case, the Morlet wavelet becomes:

$$\psi_M(t) = g(t)e^{j\omega_0 t} \qquad \text{with} \qquad g(t) = \frac{1}{\sqrt[4]{\pi\sigma^2}} e^{-\frac{t^2}{2\sigma^2}} \tag{2.25}$$

This simplified Morlet wavelet is well-known in the literature and called the *Morlet wavelet* or the *standard Morlet wavelet*. The FT of the window $g(t)$ is $\hat{g}(\omega) = \left(4\pi\sigma^2\right)^{1/4} e^{-\sigma^2\omega^2/2}$. If $\sigma^2\omega_0^2 >> 1$, so $\hat{g}(\omega) \approx 0$ for $|\omega| > \omega_0$, the wavelet is considered as approximately analytical and admissible.

The analogues to FT of the Morlet wavelet are clear in the basic Morlet function: $\psi_M(t) = g(t)[\cos(\omega_0 t) + i\sin(\omega_0 t)]$. Essentially, this wavelet is a FT of Gaussian window, with oscillating sine and cosine at the center frequency ω_0. Dilatations of this temporally localized mother wavelet permit to discover harmonic components within the signal.

In the frequency domain, it is written:

$$\hat{\psi}_M(\omega) = \left(\sigma^2/\pi\right)^{\frac{1}{4}} e^{\frac{-\sigma^2}{2}(\omega-\omega_0)^2} \tag{2.26}$$

The relation between scale and frequency may be given prominence by considering the frequency formulation of the dilated Morlet wavelet:

$$\hat{\psi}_M(s\omega) = \left(\sigma^2/\pi\right)^{\frac{1}{4}} e^{\frac{-\sigma^2}{2}(s\omega-\omega_0)^2} \tag{2.27}$$

The function reaches the maximum at $s\omega = \omega_0$. As ω_0 is a fixed parameter that defines the wavelet, at a given scale *s*, the function is maximal at:

$$\omega = \frac{\omega_0}{s} \tag{2.28}$$

The last equation explains the relation between the instantaneous frequency and scale. It represents also the single relation between the dilatation parameter *s* and the frequency ω.

The standard Morlet wavelet does not verify exactly the zero mean in the admissibility condition. However, the simplified wavelet average is very small for high values of the product $\omega_0\sigma$ ($\omega_0\sigma \geq 5$ in practice) and the admissibility condition is nearly verified. For example, for $\omega_0 = 5$, $\sigma = 1$, one has $\left|\hat{\psi}_M(\omega)\big|_{\omega=0}\right| < 10^{-6}$; for $\omega_0\sigma = 10$, $\left|\hat{\psi}_M(\omega)\big|_{\omega=0}\right| < 10^{-22}$.

The center frequencies of the complete and standard Morlet wavelets are deduced from their frequency spectrum expressions. The relation between those values is described with the correction term:

$$\omega_c = \omega_{c,M}\left(1 + e^{-\sigma^2\omega_0^2}\right).$$

Then, the term $e^{-\sigma^2\omega_0^2}$ is the relative difference, if $\omega_0 = 5$, $\sigma = 1$, so $e^{-\sigma^2\omega_0^2} \approx 10^{-11}$ (as described in Figure 2.5*a*), the standard Morlet wavelet may be considered like the complete one.

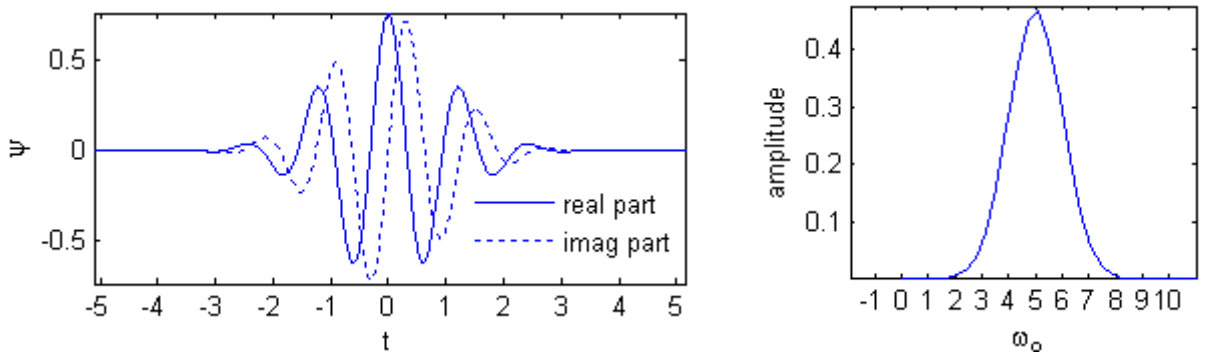

a) with $\omega_0 = 5, \sigma = 1$

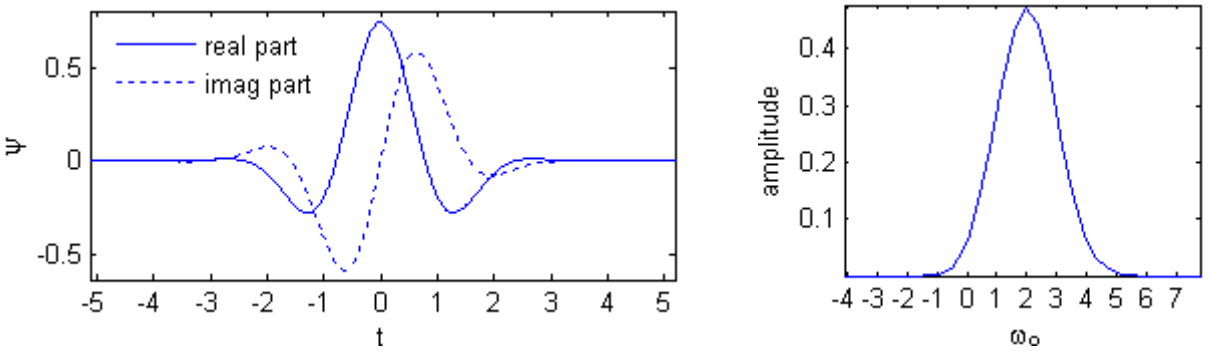

b) with $\omega_0 = 2, \sigma = 1$

Figure 2.5: Morlet wavelet in the time and frequency domains

For too small values of the product $\omega_0\sigma$, the admissibility condition is not verified as $\hat{\psi}(\omega)\big|_{\omega=0} \neq 0$ as illustrated in Figure 2.5*b*. One uses often a Gaussian envelop of unitary variance and the condition of enough high values for $\omega_0\sigma$ (which represents properly the factor *Q* in equation 2.21) comes down to enough high values for ω_0.

However, a wavelet employed in the WT must be a wave that is not lengthened, i.e. a really small wave. It implicates a wave of which the support is compact (the effective larger of the support is the smallest) or the decay is enough fast, to obtain the localization in time.

Practically, by choosing enough high values for $\omega_0\sigma$, one can use the standard Morlet wavelet even if the admissibility condition is not strictly verified. It is very adequate for the research of instantaneous frequencies and amplitudes of a signal. Moreover, the Gaussian window used in the Morlet wavelet is optimal, i.e. it shows the same resolution in both the time and frequency domains. It shows itself as a wavelet for which the time-frequency localization is very good.

2.3.1 Wavelet ridges

Different methods exist to define and to extract ridges (Staszewski (1998)[118], Carmona *et al.* (1999)[11] and Mallat (1999)[76]). The scalogram $P_W f(u,\omega)$ (expression 2.23) measures the energy of $f(t)$ in the time-frequency neighborhood of (u,ω). The ridge algorithm computes instantaneous frequencies of the signal from local maxima of the scalogram (Figure 2.6).

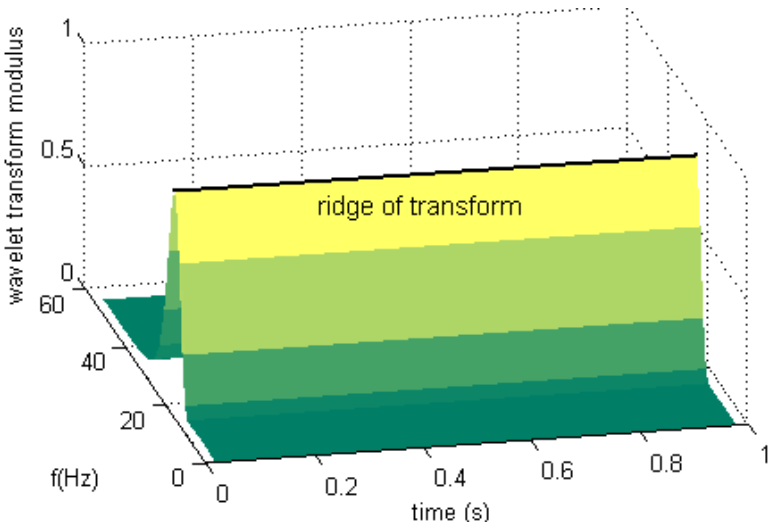

Figure 2.6: Instantaneous frequency identification in aid of wavelet ridge, WT of a signal of pure frequency $f(t) = e^{j\omega t}$

The ridge algorithm relies on the analytic wavelet transform. An analytic wavelet may be constructed by the product of a real and symmetric window $g(t)$ and an exponential complex:

$$\psi(t) = g(t)e^{j\omega_0 t} \tag{2.29}$$

The wavelet under the form of (2.29), called Gabor wavelet, may be determined from a normalized Gaussian window $g(t)$ as in Eq. (2.25). For enough high values of the product $\omega_0\sigma$ so that $\omega_0^2\sigma^2 \gg 1$, one has $\hat{g}(\omega) \approx 0$ for $|\omega| > \omega_0$. Since the center frequency is ω_0, the value $\hat{\psi}(0)$ is nearly zero, and such wavelet may be considered approximately analytic.

If $a(u)$ and $\phi(u)$ are respectively instantaneous amplitude and phase, the WT is given in [76]:

$$Wf(u,s) = \frac{\sqrt{s}}{2} a(u) e^{j\phi(u)} \left\{ \hat{g}\left[s\left(\omega - \phi'(u)\right)\right] + \varepsilon(u,\omega) \right\} \tag{2.30}$$

where $\varepsilon(u,\omega)$ is a corrective term. If this term is negligible, it is clear that (2.30) enables the measurement of $a(u)$ and $\phi'(u)$ from $Wf(u,s)$. The corrective term is negligible if $a(u)$ and $\phi'(u)$ have small variations over the support of $\psi_{u,s}$ and $\phi'(u) \geq \Delta\omega / s$, that $\Delta\omega$ is bandwidth of $\hat{g}$.

The scalogram reaches its maximum at $\omega(u) = \frac{\omega_0}{s(u)} = \phi'(u)$ and the points $(u, \omega(u))$ constitute the ridge. If $\Phi_W(u,\omega)$ is the complex phase of $Wf(u,s)$, at ridge points, the instantaneous frequency $\phi'(u)$ and the analytic amplitude $a(u)$ are given respectively by:

$$\phi'(u) = \omega = \frac{\partial \Phi_W(u,\omega)}{\partial u} \tag{2.31}$$

$$a(u) = \frac{2\sqrt{|Wf(u,s)|^2 / s}}{|\hat{g}(0)|} \tag{2.32}$$

When $\omega = \phi'(u)$, the corrective term $\varepsilon(u,\omega)$ is dominated by the second order, they are negligible if [76]:

$$\frac{\omega_0^2}{|\phi'(u)|^2}\frac{|a''(u)|}{|a(u)|} << 1 \quad \text{and} \quad \omega_0^2\frac{|\phi''(u)|}{|\phi'(u)|^2} << 1 \tag{2.33}$$

The presence of ϕ' in the denominator shows that a' and ϕ' may vary slowly if ϕ' is small but may vary much faster for larger instantaneous frequencies.

2.3.2 End effect

The spreads in time and frequency in the WT are non-zero; they depend on the mother wavelet characteristics and on the analysis scale. Despite the wavelet localization in time and frequency, the time window of localization spreads toward the past and future at a given time (Figure 2.7). As the signal has finite length and is sampled with a non-zero sample period, it exists an anomaly at the ends.

A simple solution for this problem is to extend the signal at the start and at the end and to leave the perturbed values due to the end effect outside the interest zone. The use of a zero-padding is simple but it introduces discontinuity at ends. A more adequate method is obtained by expanding the signal by reflection at its ends (Figure 2.8); in this way, the signal always keeps locally its frequency characteristics (Kijewski and Kareem (2002)[55]).

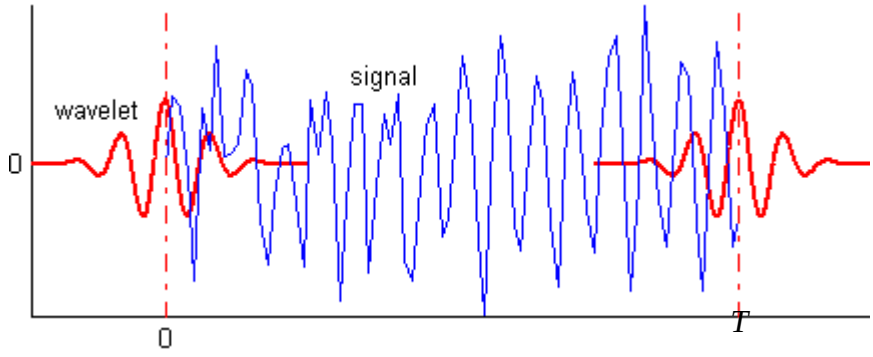

Figure 2.7: Wavelet spreads outside the finite signal

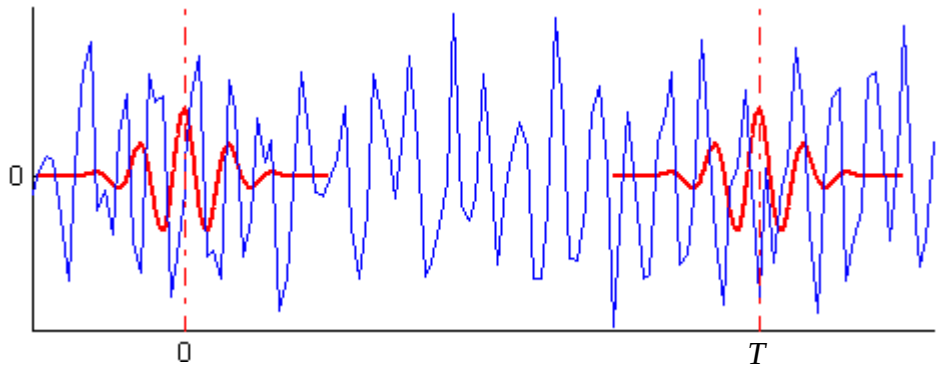

Figure 2.8: The generated signal by the reflection

$$\mathbf{x}_{initial} = [x_1 \quad x_2 \quad x_3 \quad \ldots \quad x_{N-2} \quad x_{N-1} \quad x_N] \tag{2.34}$$

$$\mathbf{x}_{generated} = [\ldots -x_2 \quad -x_1 \quad x_1 \quad x_2 \quad \ldots \quad x_{N-2} \quad x_{N-1} \quad x_N \quad -x_{N-1} \quad -x_{N-2} \quad \ldots] \tag{2.35}$$

The time length of the dilated window Δt_i for a frequency (scale) ω_i is given by (2.20): $\Delta t_i = \dfrac{\sigma\omega_0}{\omega_i\sqrt{2}}$.

The effectiveness of the end effect reduction is illustrated in Figure 2.9.

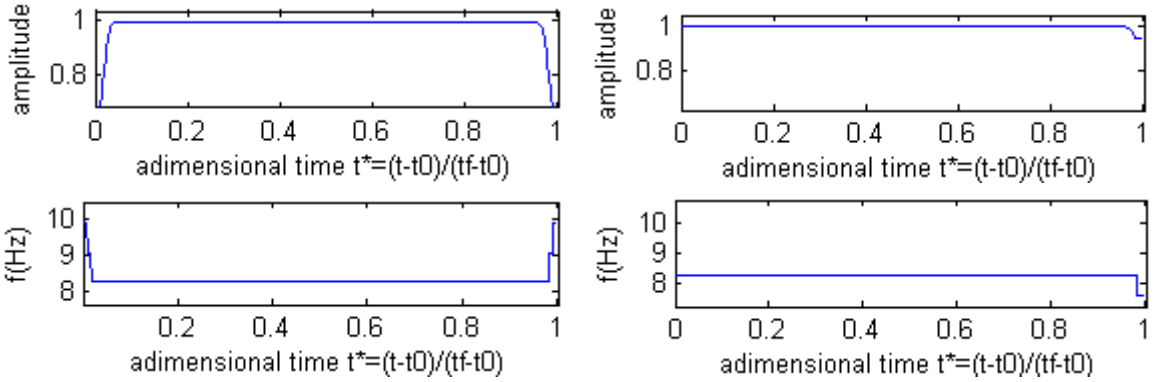

a) from the original signal *b) from the generated signal*

Figure 2.9: WT for $f(t) = \sin(2\pi ft)$ (measured in the time interval of [*t0*; *tf*])

An extension of the signal constructed by reflection is quite simple and adapts naturally to a signal with stable amplitude (e.g. responses to harmonic or random excitation). However, when the frequency varies depending on the amplitude size, such extension still induces discontinuity at the ends. It is illustrated in Figure 2.10*a* in the case of a nonlinear stiffness system when the free response has to be extended to the left. Another approach is proposed here to better adapt to the WT continuity.

- **Fitting padding**

The principal idea is: added part must have a form according to the global appearance of the original signal. A simple technique for signal generating is proposed below. It is described with the left extension as presented in Figure 2.10*b*.

a- Find the maximal absolute value of the signal $x_{\max}$, for free response; it stays usually at the start of the signal.

b- Determine a superior or inferior envelope at end. For simplicity, this envelope may be approximately shaped by finding a quadratic parabola passing three points early determined. For the inferior (superior) envelope, those three points are all minima (maxima) of which values are lowest (highest). Consider that the parabola passing those three points can describe tendency of the signal at the left end. Suppose that the signal will be extended until moment $-t_0$, then one can compute ordinate x_0 corresponding to abscissa $-t_0$ of the envelop.

c- The generated part is just a period staying in the interval [0, t_0] of the signal, amplified following the formula:

$$X_{padding} = X_{0,t_0}\frac{x_0}{x_{\max}}\alpha \qquad (2.36)$$

α is a fitting coefficient which ensures an entire harmonic appearance of the generated signal.

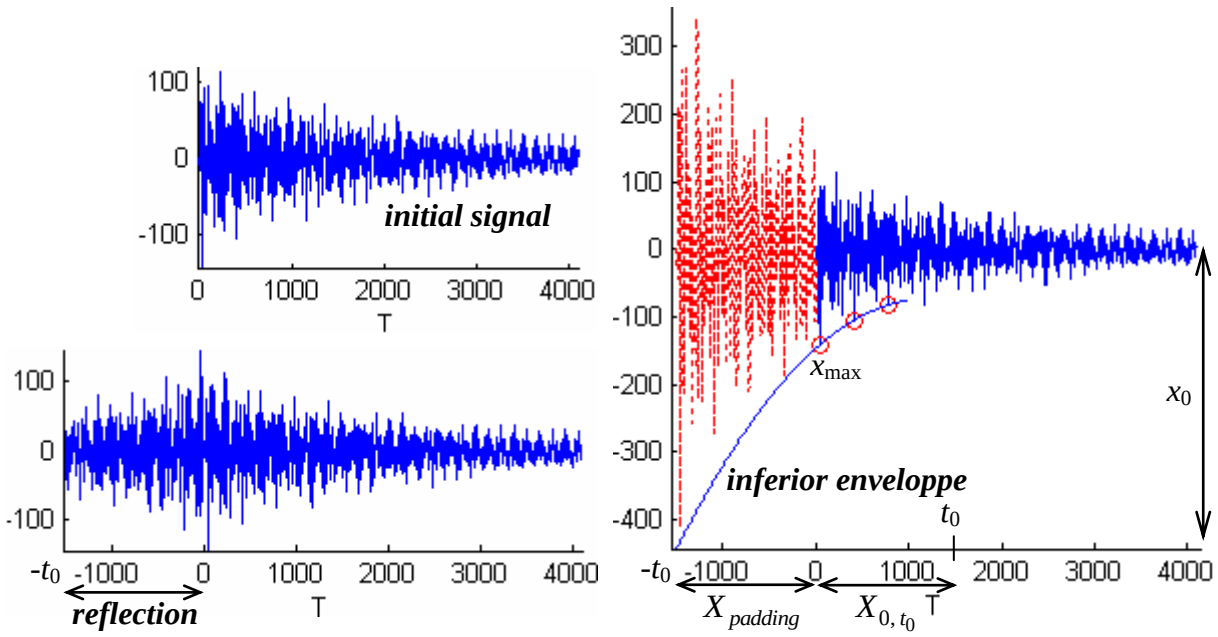

Figure 2.10: A signal and its extension

The treatment for the right end may be carried out with similar way.

Figure 2.11 shows end effects when the WT is performed respectively with the initial signal, the signal prolonged by reflection and by fitting padding, respectively.

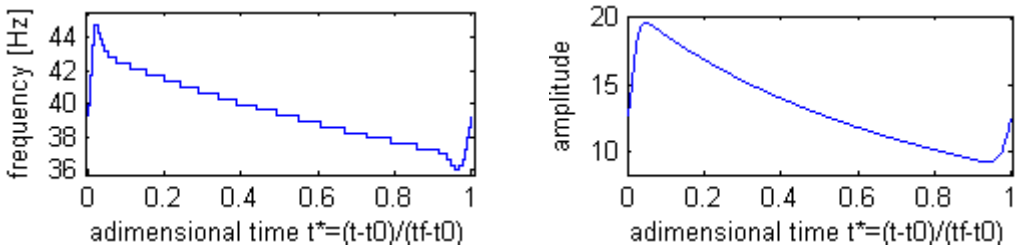

a) WT of the original signal

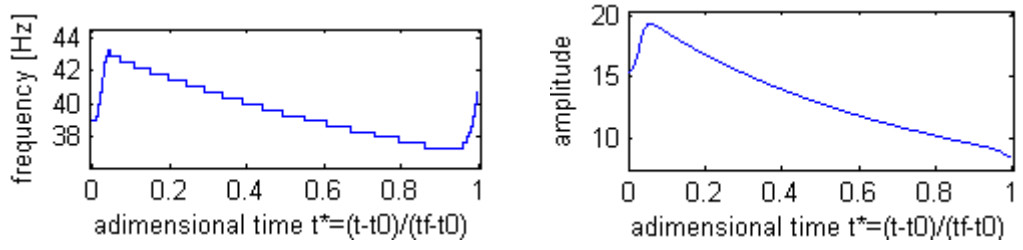

b) WT of the signal generated by reflection

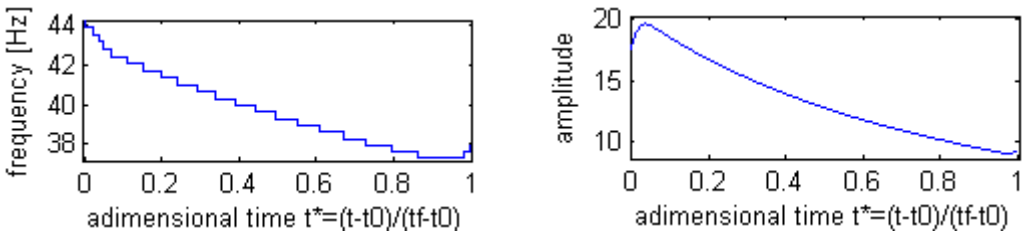

c) WT of the signal generated by fitting padding

Figure 2.11: WT of a signal and its prolongation versions

The results in Figure 2.11 show that the fitting padding improves the curves at boundaries. Instantaneous frequencies at ends accord better with the central part. Regarding instantaneous amplitudes, the end effect is effectively reduced.

2.3.3 Multiple frequencies

An important key in the multi-component signal analysis is the choice of the mother wavelet parameters in order to discriminate each component.

Let $\phi_1'(u)$ and $\phi_2'(u)$ be instantaneous frequencies of two different components, the ridges do not interfere if the dilated window gets sufficient frequency resolution at the ridge scales:

$$\hat{g}\left(s\left|\phi_1'(u)-\phi_2'(u)\right|\right) \gg 1 \tag{2.37}$$

Define $\Delta\omega$ as bandwidth of $\hat{g}(\omega)$ by:

$$\hat{g}(\omega) \ll 1 \text{ for } |\omega| \geq \Delta\omega \tag{2.38}$$

Expression (2.37) means that the wavelet needs an enough small value for $\frac{\Delta\omega}{\omega_0}$ in order to isolate those spectral components:

$$\frac{\left|\phi_1'(u)-\phi_2'(u)\right|}{\phi_1'(u)} \geq \frac{\Delta\omega}{\omega_0} \quad \text{and} \quad \frac{\left|\phi_1'(u)-\phi_2'(u)\right|}{\phi_2'(u)} \geq \frac{\Delta\omega}{\omega_0} \tag{2.39}$$

Parameter ω_0 of the mother wavelet must be chosen in an adequate manner to satisfy simultaneously the conditions (2.33) and (2.39). If two spectral lines are too close, they interfere so that the ridge pattern is destroyed.

The spectral line number is generally unknown. Ridges corresponding to a low amplitude are often carried off because they may be due to noise, or correspond to "shadows" of other instantaneous frequencies created by the side-lobes of $\hat{g}(\omega)$.

Figures 2.12 and 2.13 illustrate the interference phenomenon between the components of a signal $f(t)$ including two spectral lines:

$$f(t)=\sin\left(2\pi.5t\right)+\sin\left(2\pi.12t\right)$$

A Morlet wavelet with $\omega_0=5, \sigma=1$ yields evidently ridge interference, as shown in Figure 2.12.

It can be observed that the instantaneous amplitude associated with the frequency of 12Hz oscillates around a mean which is equal to the amplitude of the other component. If the product $\sigma\omega_0$ is chosen to be larger, this unwanted phenomenon is reduced.

Figure 2.13 shows that a larger product of $\sigma\omega_0$ improves significantly the interference between ridges but the end effect perturbs seriously the time-amplitude plan. Thus, if σ is too large, the wavelet is thus too extended, which affects the precision in time because if ω_0 is too large, the condition (2.33) is not ensured.

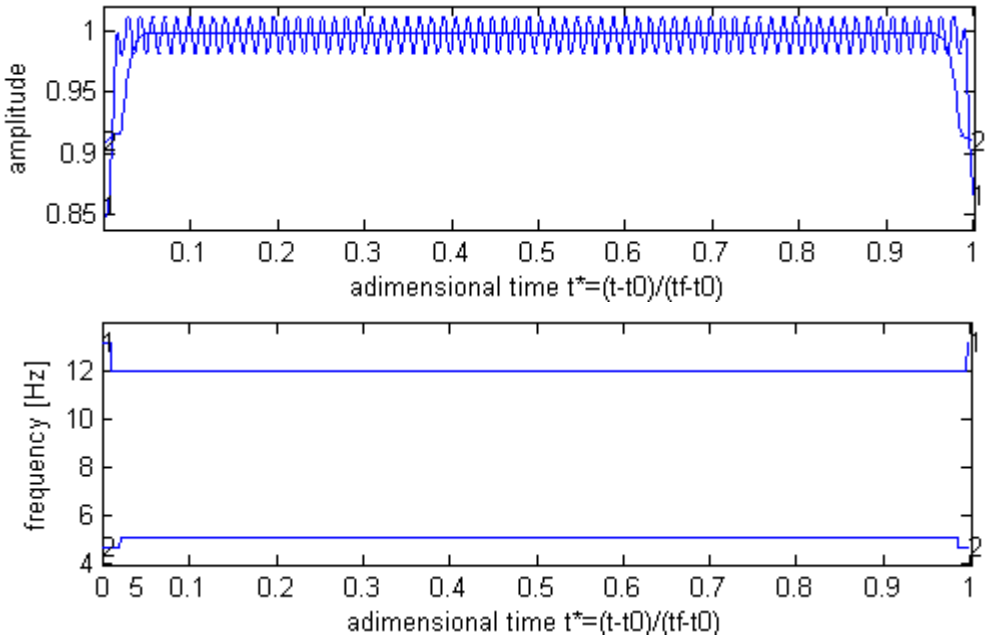

Figure 2.12: WT with $\omega_0 = 5, \sigma = 1$

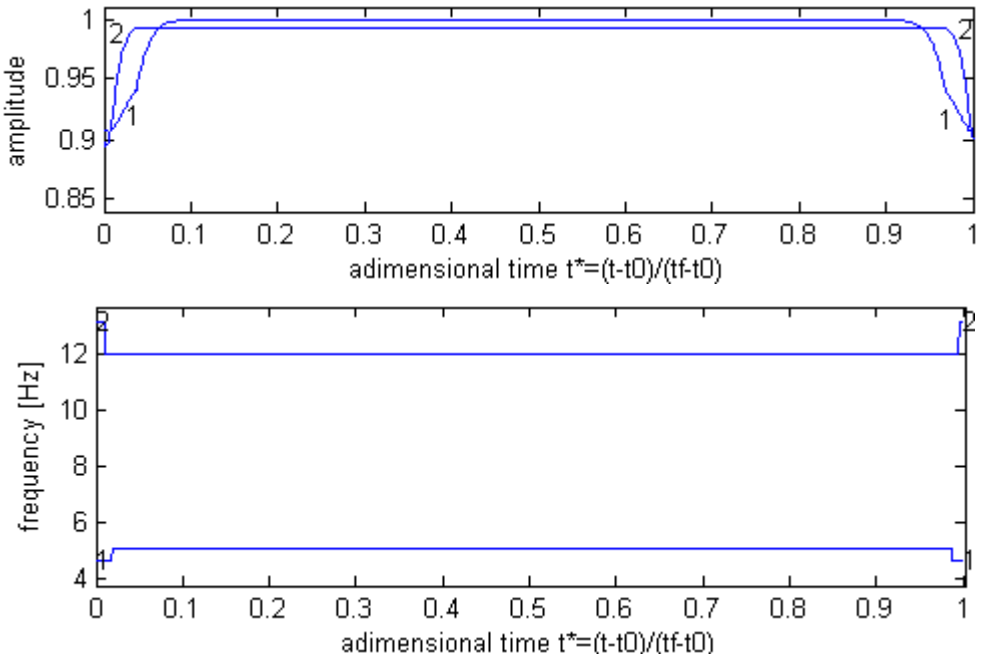

Figure 2.13: WT with $\omega_0 = 5, \sigma = 1.7$

2.3.4 The WT as a band-pass filter

In the WT of a multi-component signal, one can isolate a single frequency component of interest by choosing appropriately the scale interval as well as the characteristic factor $\sigma\omega_0$ of the mother wavelet. In this case, the WT plays the role of a band-pass filter.

2.4 Detection based on the concept of subspace angle

For a given excitation, the WT allows to identify the instantaneous frequencies (or ridges) for a set of different measurement coordinates on the structure. Accordingly, it provides the amplitude ratios between coordinates associated to an identified ridge line. Using these ratios, one can assess time-varying deformation ('mode') shapes of the system. The modes with the strongest energies may be regarded as active modes and used to construct active subspaces (which reflect states of the system) at different time instants. A change in the dynamic behaviour modifies consequently the state of the system, i.e. the instantaneous frequencies and deformation shapes. This change may be estimated using the concept of subspace angle introduced by Golub and Van Loan (1996)[35]. This concept was used in De Boe and Golinval (2003)[16] as a tool to quantify existing spatial coherence between two data sets resulting from observation of a vibration system.

Given two subspaces (each with linear independent columns) $\mathbf{S} \in \Re^{m \times p}$ and $\mathbf{D} \in \Re^{m \times q}$ ($p > q$), the procedure is as follows. Carry out the QR factorizations:

$$\mathbf{S} = \mathbf{Q}_S \mathbf{R}_S \qquad \mathbf{Q}_S \in \Re^{m \times p}$$

$$\mathbf{D} = \mathbf{Q}_D \mathbf{R}_D \qquad \mathbf{Q}_D \in \Re^{m \times q} \tag{2.40}$$

The columns of $\mathbf{Q}_S$ and $\mathbf{Q}_D$ define the orthonormal bases for **S** and **D** respectively. The angles θ_i between the subspaces **S** and **D** are computed from singular values associated with the product $\mathbf{Q}_S^T \mathbf{Q}_D$:

$$\mathbf{Q}_S^T \mathbf{Q}_D = \mathbf{U}_{SD} \boldsymbol{\Sigma}_{SD} \mathbf{V}_{SD}^T$$

$$\boldsymbol{\Sigma}_{SD} = diag\left(\cos(\theta_i)\right), \quad i = 1, ..., q \tag{2.41}$$

The largest singular value is thus related with the largest angle characterizing the geometric difference between two subspaces.

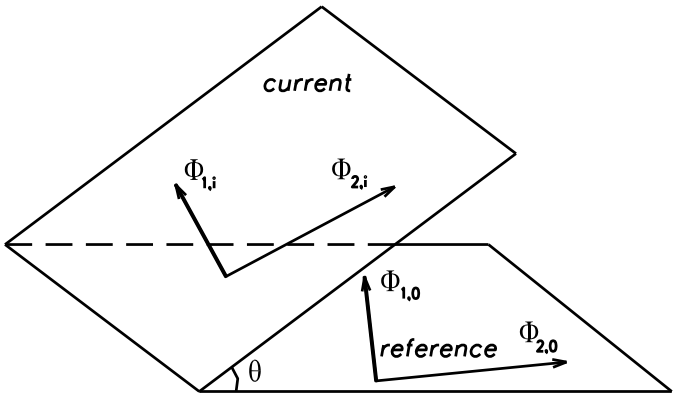

Figure 2.14: Angle θ formed by active subspaces (hyperplanes) according to the reference and current states, due to a dynamic change

The change in a structure (e.g. the onset of nonlinearity or damage) may be detected by monitoring the angular coherence between subspaces estimated from the reference observation set and from the observation set of a current state respectively. A state is considered as a reference state if the system operates in normal conditions (i.e. nonlinearity is not activated or damage does not exist). Figure 2.14 shows a 2D example in which an active subspace (or hyperplane) is built from two principal deformation shapes.

2.5 WT application to detect nonlinearity

The example consists in identifying the modal features and in detecting the level of nonlinearity in a cubic stiffness system by means of the WT. The analysis is conducted both numerically and experimentally. The studied structure is a beam clamped at one end and exhibiting a cubic stiffness at the other end (Figure 2.15). The cubic stiffness is realised by means of a very thin beam. For weak excitation, the system behaviour may be considered as linear. When the excitation level increases, the thin beam exhibits large displacements and a nonlinear geometric effect is activated resulting in a stiffening effect at the end of the main beam. The structure was used as a benchmark for nonlinear system identification during the European action COST F3 (Argoul and Le (2003)[2], Lenaerts *et al.* (2003)[65]).

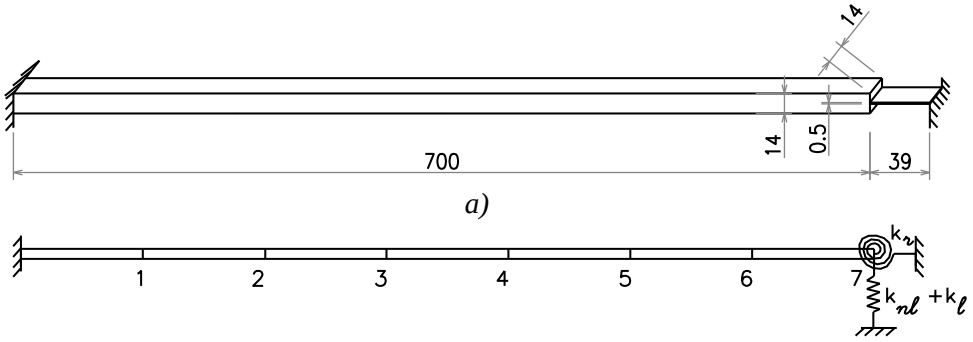

Figure 2.15: The beam with a nonlinear stiffness (*a*) and its finite element model (*b*)

2.5.1 Numerical analysis

The main beam is modelled with seven beam finite elements (Figure 2.15*b*). The thin beam is represented by two equivalent grounded springs: one in translation ($k_l + k_{nl}$) and one in rotation (k_r). The nonlinear stiffening effect of the thin beam is modelled by a nonlinear function in displacement of the form: $f_{nl}(x) = A|x|^{\alpha}\,\mathrm{sign}(x)$, where A is a nonlinear coefficient, $A = 6.1\times10^{9}\,N/m^{3}$ and α is a nonlinear exponent, $\alpha = 3$. These parameters were determined experimentally in Reference [65].

❖ ***Nonlinear normal modes***

The nonlinear normal modes (NNMs) of this structure were calculated in some companion studies (Peeters *et al.* (2009)[99], Nguyen *et al.* (2010)[87]). These modal features depend on the total energy in the system as illustrated in Figure 2.16 by the frequency-energy plot of the first and the second NNMs.

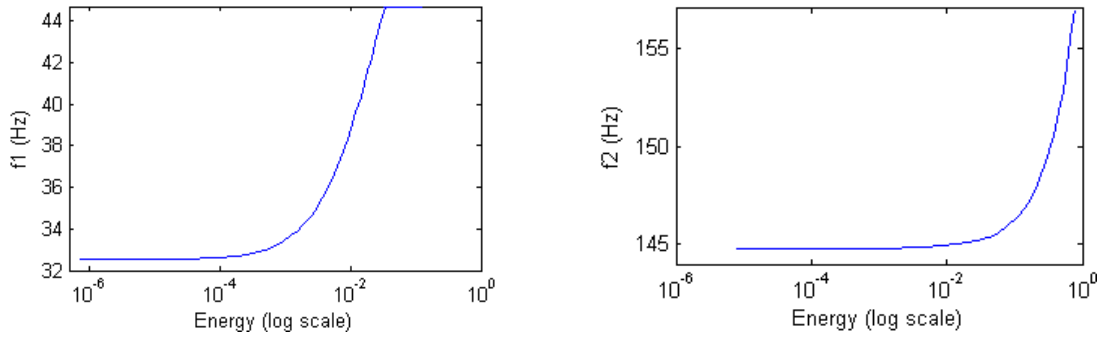

a) First NNM *b) Second NNM*

Figure 2.16: Frequency-energy plot of the first (*a*) and second (*b*) NNMs

The first and second NNM motions are plotted in Figure 2.17 at low and high energy level respectively. The low energy level (actually the linear normal modes) corresponds to $f_1 = 32.60$ Hz and $f_2 = 144.79$ Hz while the high energy level (the nonlinear case) corresponds to $f_1 = 38.46$ Hz and $f_2 = 147.67$ Hz.

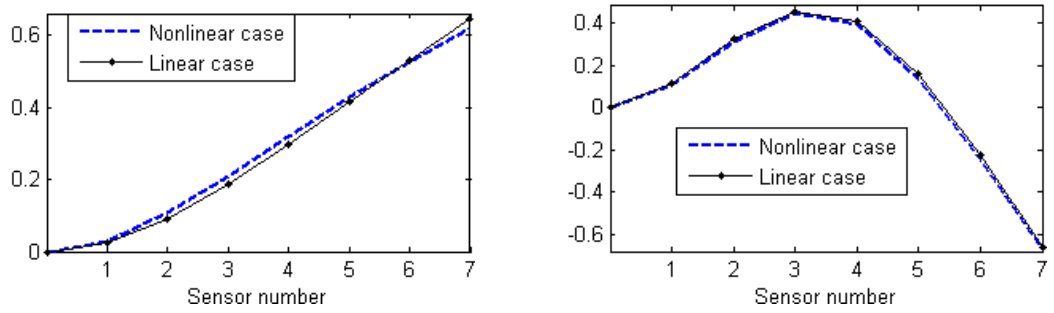

Figure 2.17: Analytical deformation shapes of the 1st, 2nd modes respectively

For the purpose of this study, the beam is supposed to be submitted to an *impact force* at its right end. The free response of the structure is measured in the vertical direction at the seven coordinates indicated in Figure 2.15*b* and the WT is applied to the measured data. Starting at a 'low' excitation level (impact of 70 N), the behaviour of the beam appears as linear (the largest displacement is lower than 0.15 mm). The WT of the displacement at coordinate n° 7 is given in Figure 2.18 in terms of instantaneous frequencies and amplitudes. Two frequency lines (called 'ridges') are observed respectively at 32.6 Hz and 144.7 Hz, which is in agreement with the frequencies occurring at low energy in the frequency-energy plot (Figure 2.16).

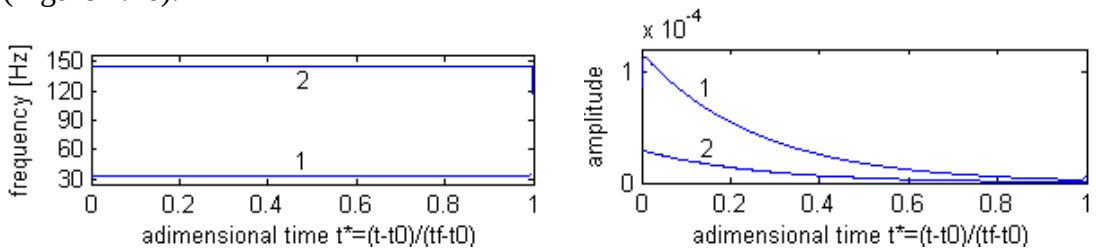

Figure 2.18: Instantaneous frequencies and amplitudes at low energy (linear case)

Let us consider next a high level of excitation (impact of 1500 N) corresponding to a maximum displacement at the right end of about 2.4 mm. Figure 2.19 presents the corresponding WT results. It clearly shows a drop-off of the frequencies down to the linear system values as the nonlinear effect vanishes progressively and the amplitude goes down. Figure 2.19 also reveals the presence of a third order super harmonic of the first frequency (curve n° 3).

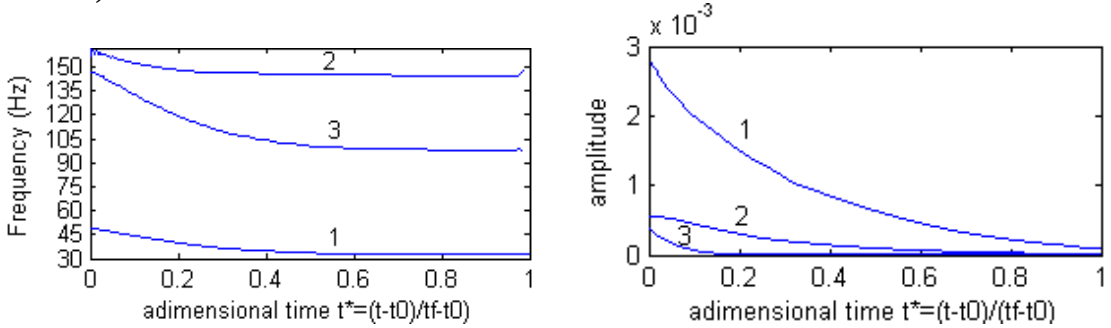

Figure 2.19: Instantaneous frequencies and amplitudes at high energy (nonlinear case)

❖ ***Identification of deformation shapes and detection of nonlinear behaviour***

Figure 2.20 presents the first two modes of the beam identified with the 'low' impact excitation when the dynamic behaviour of the structure may be considered as linear.

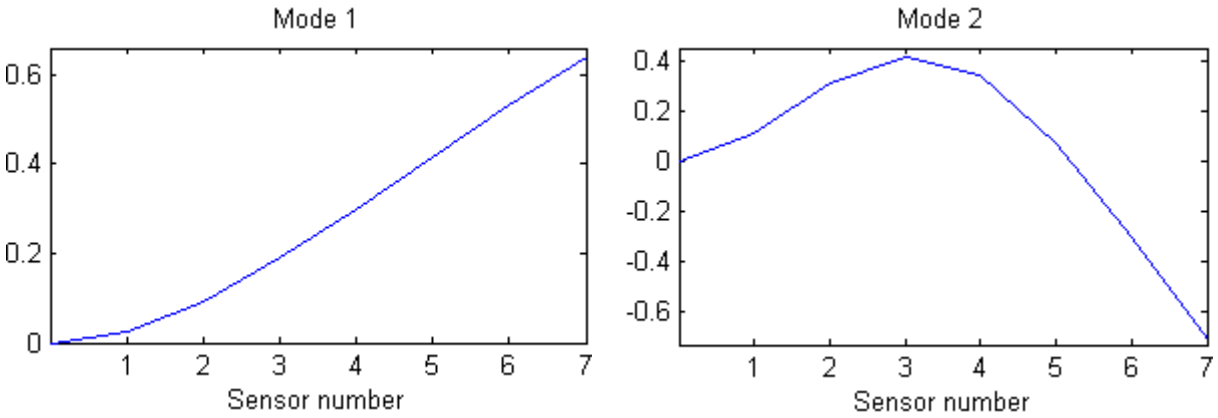

Figure 2.20: WT modes 1 and 2 in the linear case

Figure 2.21 gives the deformation shapes at higher excitation levels. When the displacement at the right end starts to be significant, both the first two deformation shapes associated to ridges n° 1 and n° 2 become influenced by the magnitude of the nonlinearity of the structure (the reference shape corresponds to the linear normal modes shown in Figure 2.20). It is interesting to note that one can find an intermediate deformation shape from ridge line n° 3; the last plot of Figure 2.21 gives the corresponding deformation shapes for different amplitudes of the displacement at the right end of the beam.

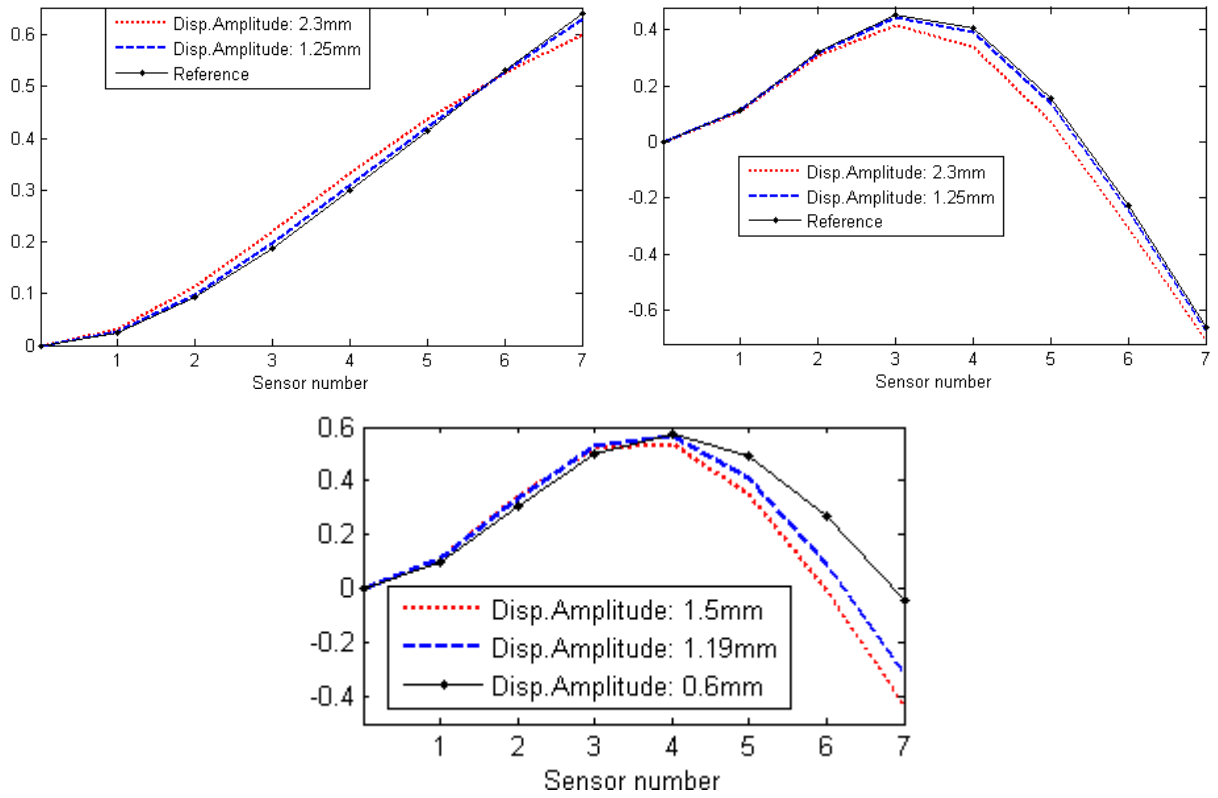

Figure 2.21: Deformation shapes associated to the 1^{st}, 2^{nd} and super harmonic modes

The instantaneous deformation shapes $\mathbf{M}_1$, $\mathbf{M}_2$ and $\mathbf{M}_3$ corresponding to the three ridges allow defining an instantaneous deformation matrix $\mathbf{A} = [\mathbf{M}_1 \ \ \mathbf{M}_2 \ \ \mathbf{M}_3]$. Performing the singular-value decomposition of matrix **A**, it can be shown that the third deformation shape ($\mathbf{M}_3$) (super harmonic) is actually a linear combination of the two other 'modes'. Figure 2.22 shows the instantaneous singular values of the decomposition in terms of energy percentage. It reveals that the third singular value is negligible compared to the two others.

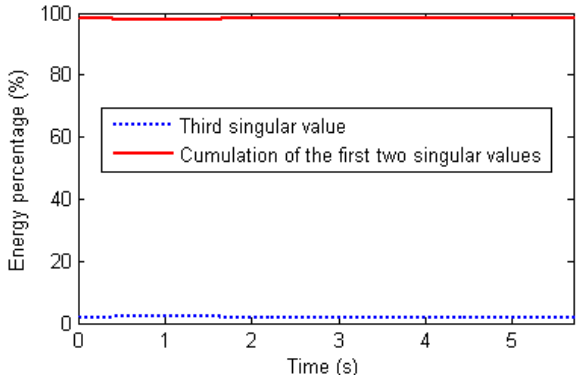

Figure 2.22: Instantaneous singular values of the deformation 'mode' matrix

The comparisons may be equally carried out by means of the MAC (Modal Assurance Criterion). In Figure 2.23, deformation shapes obtained through the WT are compared with the linear normal modes identified by the SSI (Stochastic Subspace Identification) method for different values of the displacement at the end of the beam. When the displacement is low (Figure 2.23*a*), the MAC indicates a perfect correlation. At this level of excitation, the deformation shapes are identical to the linear normal modes. On the other hand, when the displacement amplitude is high (Figure 2.23*c*), the nonlinearity is well excited which results in a frequency increase and a slight loss of correlation with the linear normal modes (identified by SSI). Figure 2.23 shows however that the MAC is not a deciding criterion for the detection of nonlinearity.

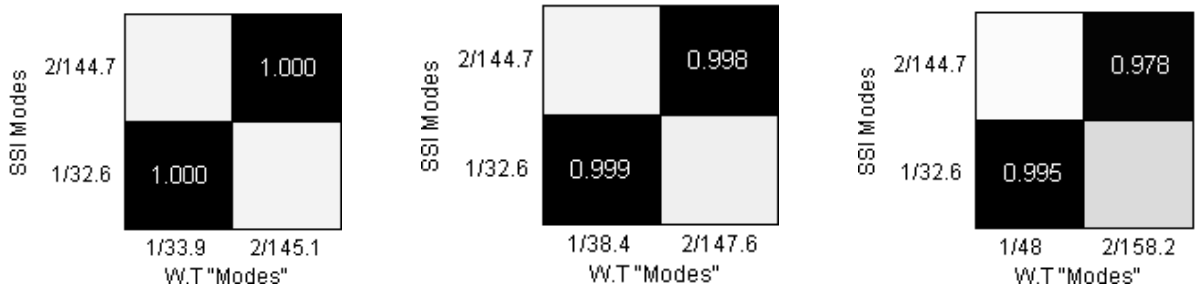

a) Displacement amplitude d ≈ 0.6 mm *b) d ≈ 1.25 mm* *c) d ≈ 2.3 mm*

Figure 2.23: MAC between WT 'modes' and SSI modes

❖ ***Detection based on the concept of subspace angle***

For the purpose of detection of nonlinearity, the structure is now supposed to be excited at increasing levels of impact force (amplitudes ranging from 100 N to 1500 N). The corresponding instantaneous frequencies obtained through the WT of the response signals at coordinate n° 7 are shown in Figure 2.24.

As explained in Section 2.4, the instantaneous deformation shapes associated to these two frequencies may be considered as instantaneous active modes to define a subspace which

characterises the dynamic state of the structure. The comparison of subspace angles between the reference state (defined by the linear normal modes) and current states at different excitation levels reveals the range of activation of the nonlinearity as illustrated in Figure 2.25. Larger is the excitation level, more significant is the angle. As responses are damped, the angles reach their largest values at the beginning and then decrease gradually to converge to zero as the dynamic behaviour of the beam becomes linear.

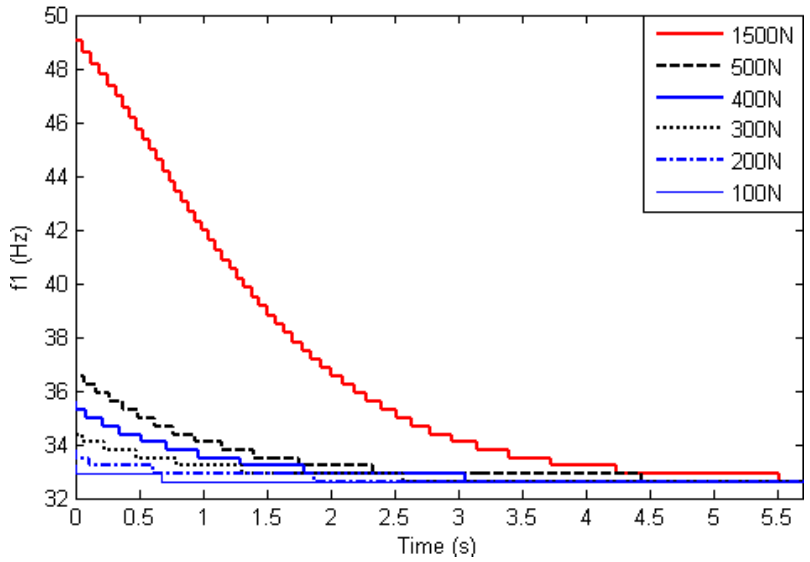

a) from the 1st ridges

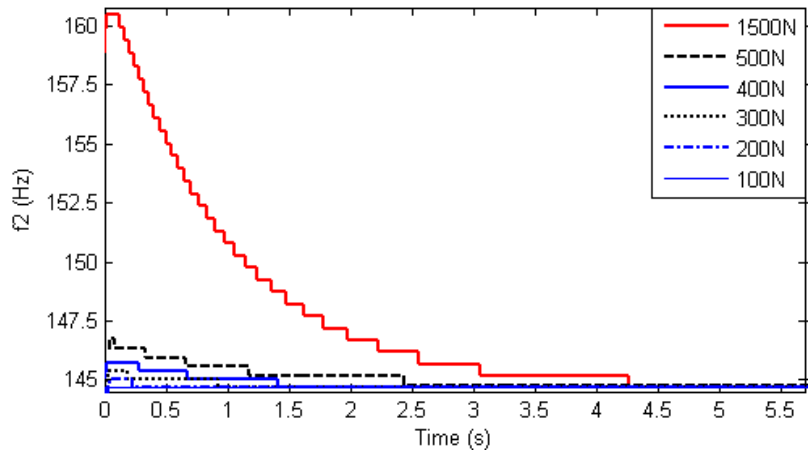

b) from the 2nd ridges

Figure 2.24: Instantaneous frequencies corresponding to different excitation levels

As the activation of the nonlinearity depends on the amplitude level of the displacement, the display of subspace angles according to the evolution of the instantaneous displacement amplitude measured at the end of the beam is informative. Figure 2.26 shows the evolution of subspace angles in function of the displacement amplitude measured at the end of the beam at time t = 0.1 s. It can be observed that the subspace angle criterion for the 2nd mode is more sensitive to the nonlinearity in comparison to the 1st mode (which is confirmed by the MAC in Figure 2.23). In terms of frequency changes however, the 1st mode appears as more affected than the 2nd mode (Figure 2.24).

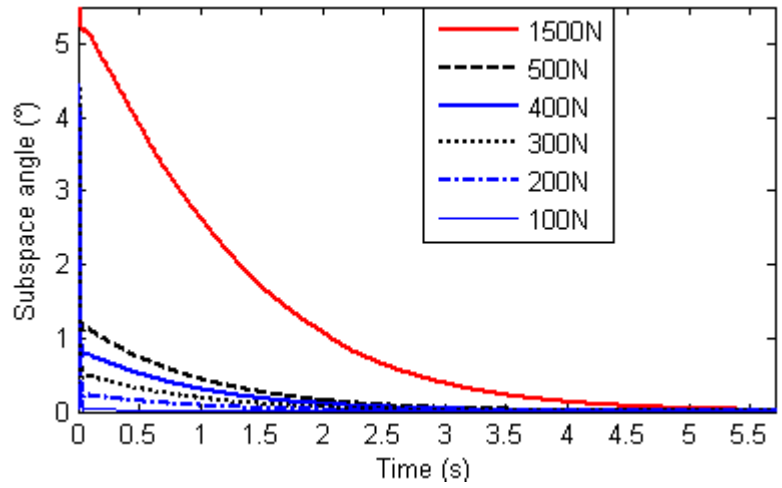

a) based on the 1st deformation mode

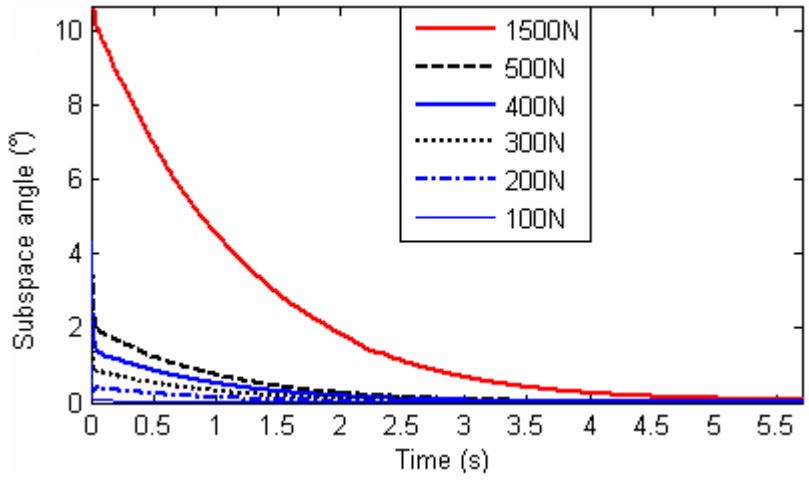

b) based on the 2nd deformation mode

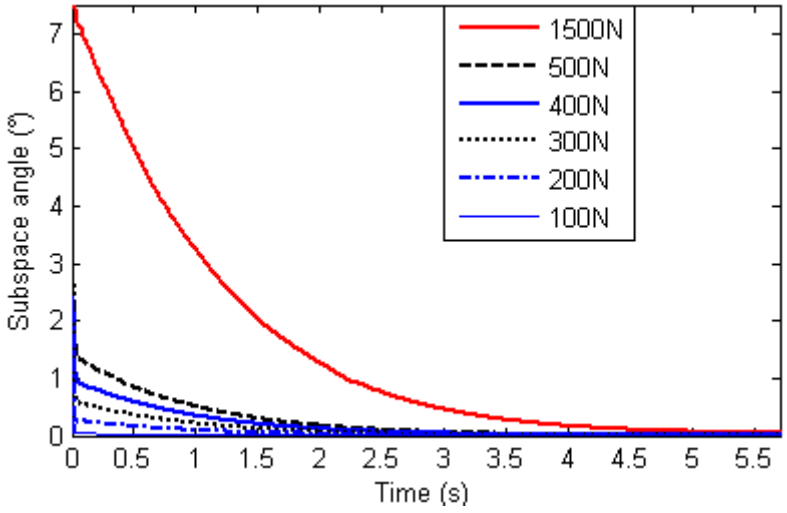

c) based on the both 2 deformation modes

Figure 2.25: Time evolution of subspace angles for different excitation levels

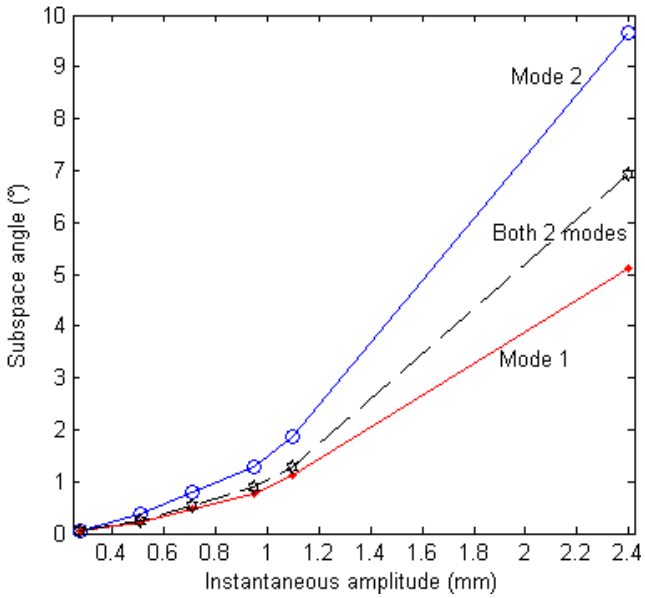

Figure 2.26: Relation angle - displacement amplitude at the end of the beam at t = 0.1 s

In summary, the onset of nonlinearity may be detected by observing the evolution of instantaneous frequencies as illustrated in Figure 2.24 but a high frequency resolution is needed to distinguish between close levels of excitation (e.g. impacts of 100 N to 500 N). In this respect, subspace angle curves look more promising as they look less affected by the frequency resolution. Another advantage is that the concept of subspace angle allows to handle several modes simultaneously in a unique detection index. Furthermore, even without processing, the end effect has less influence on the detection by subspace angle because the use of amplitude ratios in the method may weaken or even eliminate this unwanted effect.

2.5.2 Experimental results

- **Impact excitation**

Experimental results were collected using 7 accelerometers (Figure 2.27) evenly distributed along the main beam as presented in Figure 2.15. The data are recorded during 6.4 seconds with a time-step of 0.00078125 s.

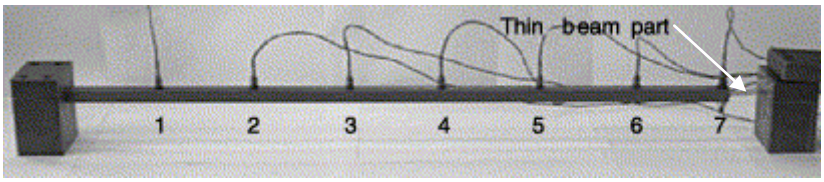

Figure 2.27: Experimental set up

An impact of very low amplitude was first applied at the end of the beam to obtain the reference state. The first two natural frequencies are observed at 31.3 Hz and 143.5 Hz respectively as shown in Figure 2.28 which gives the WT of the response measured at the end of the beam (coordinate n° 7). These values are slightly lower than the frequencies predicted by the numerical model, which is mainly due to the influence of the mass of the sensors.

An impact of higher amplitude was then applied to activate the nonlinearity. The results are shown in Figure 2.29. It is observed that three instantaneous frequencies (ridges) are detected and that they are decreasing over time.

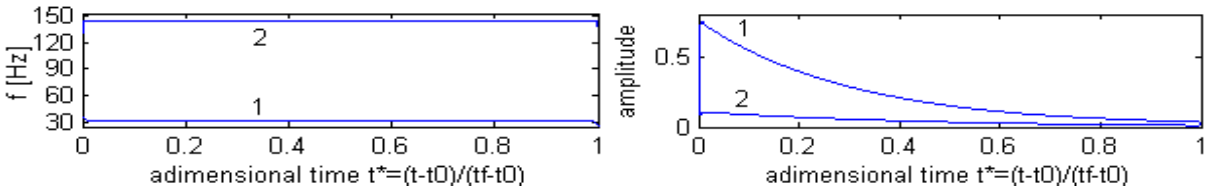

Figure 2.28: Instantaneous frequencies and amplitudes according to a low impact

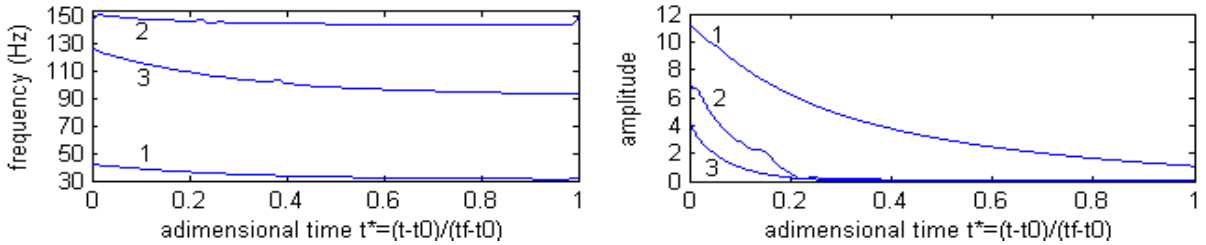

Figure 2.29: Instantaneous frequencies and amplitudes when the nonlinearity is activated

The deformation modes corresponding to those three frequencies are presented in Figure 2.30 at different instants (corresponding to different levels of displacement at the end of the beam).

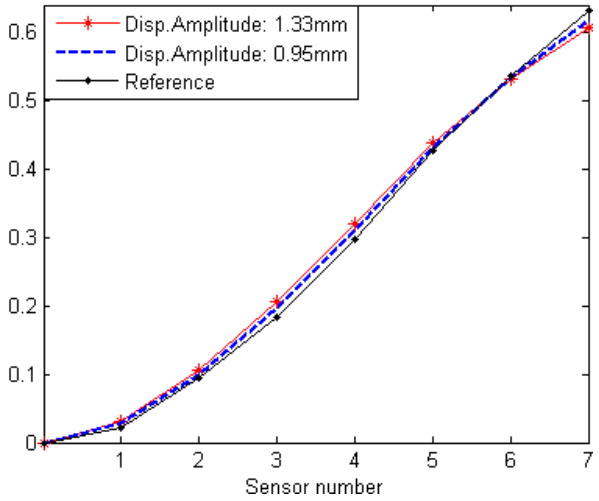

a) from the first frequency ridge

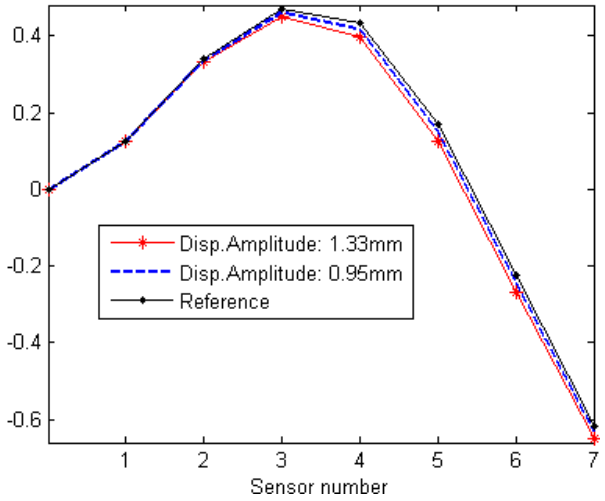

b) from the second frequency ridge

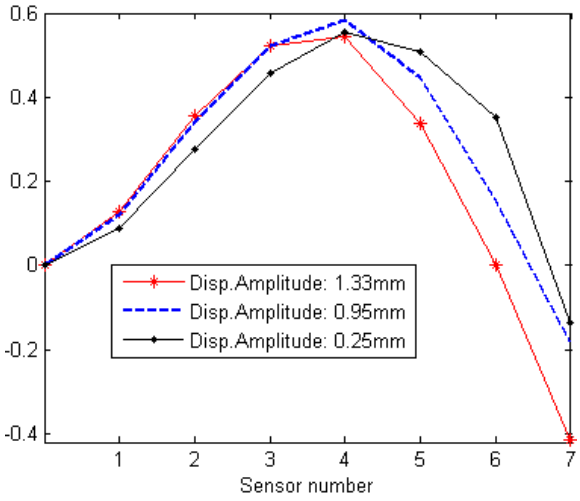

c) from the third frequency ridge

Figure 2.30: Deformation shapes corresponding to different displacement amplitudes

The singular-value decomposition (SVD) of matrix $\mathbf{A} = [\mathbf{M}_1\ \mathbf{M}_2\ \mathbf{M}_3]$ confirms that the third deformation shape ($\mathbf{M}_3$) is in fact a linear combination of the first two 'modes' (Figure 2.31).

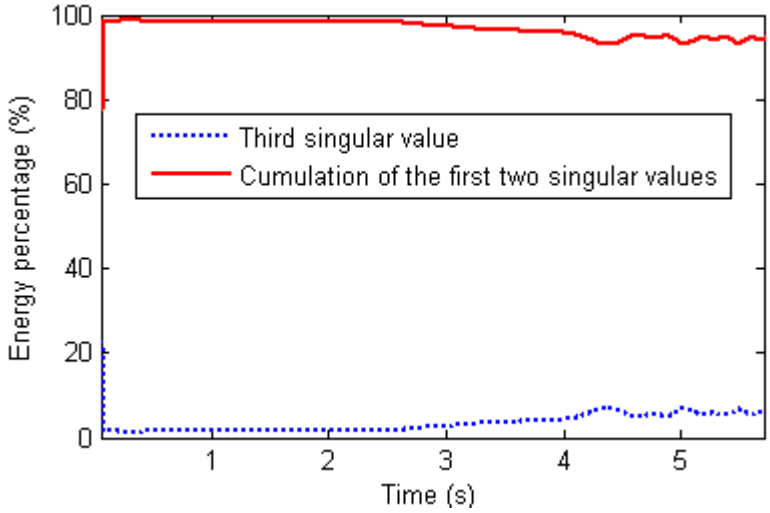

Figure 2.31: Instantaneous singular values of the deformation 'mode' matrix

The MAC between the experiment SSI and WT 'modes' is also displayed in Figure 2.32.

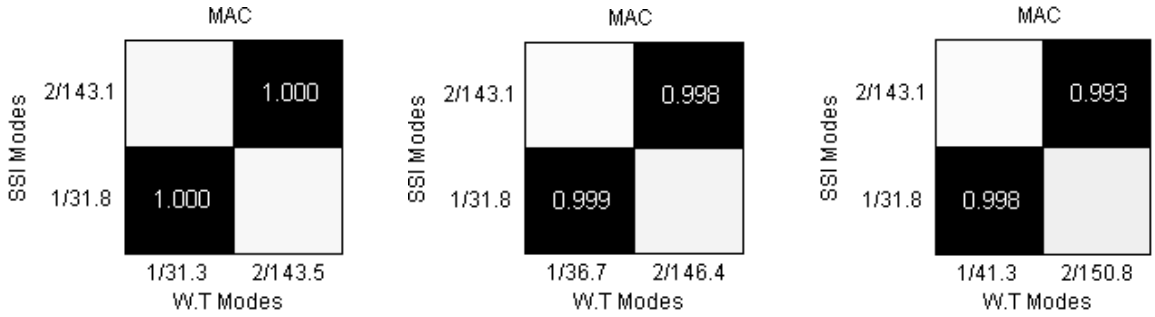

a) Displacement amplitude d ≈ 0.25 mm *b) d ≈ 0.95 mm* *c) d ≈ 1.33 mm*

Figure 2.32: MAC between WT 'modes' and SSI modes

In the following, the experiments were performed for 6 levels of excitation (L0-L5) as reported in Table 2.1.

Table 2.1: Levels of excitation and corresponding maximum displacement

Level	L5	L4	L3	L2	L1	L0
Max. displacement (mm)	1.37	1.20	0.93	0.72	0.48	0.037

The results of the WT in terms of instantaneous frequencies are given in Figure 2.33. Note that the distortions which appear in the evolution of the 2^{nd} frequency were due to set-up problems and do not influence the detection procedure.

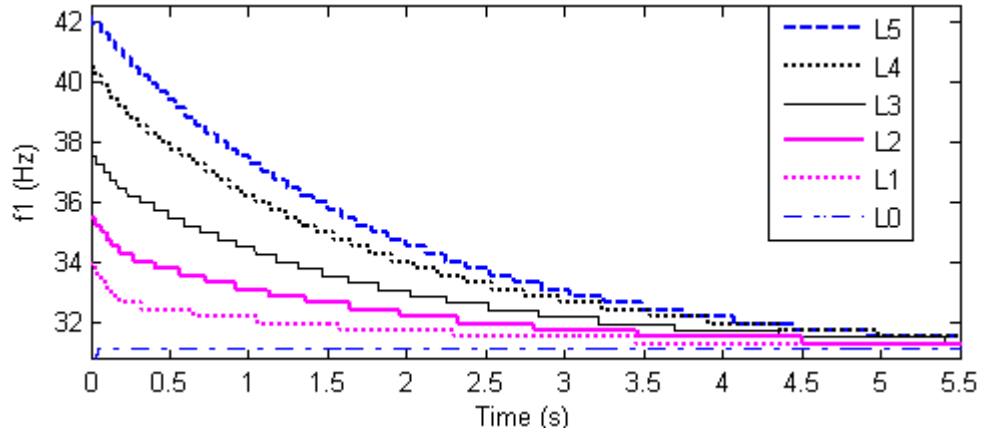

a) from the 1st ridge

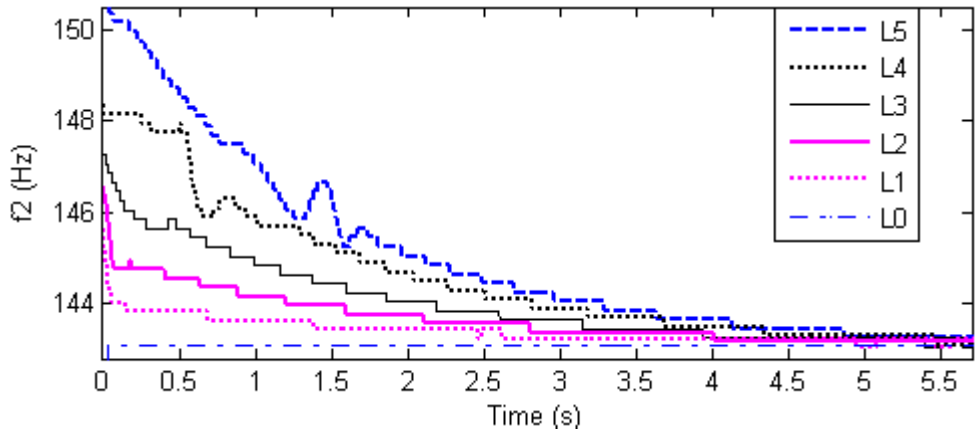

b) from the 2nd ridge

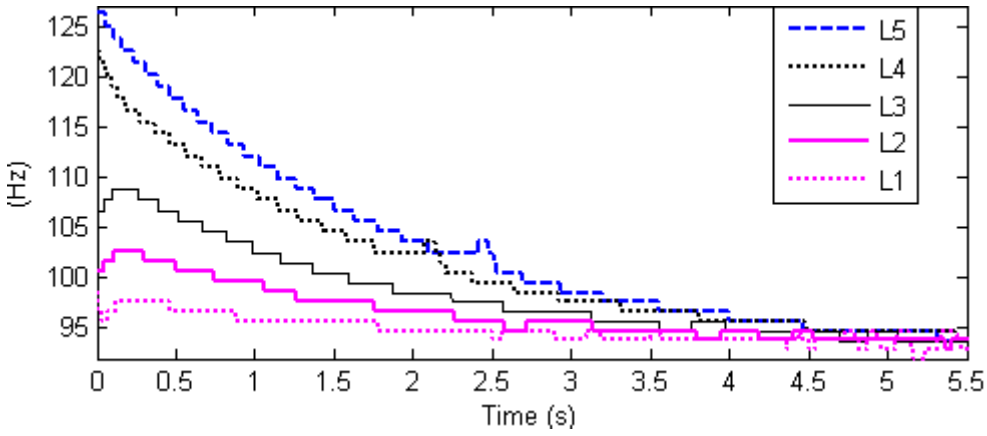

c) from the 3rd ridge

Figure 2.33: Instantaneous frequencies

Figure 2.34 gives the time evolution of subspace angles for the 6 levels of excitation. The angles are calculated respectively on the basis of one single deformation 'mode' ($\mathbf{M}_1$ or $\mathbf{M}_2$) in Figure 2.34*a*-*b* and on the basis of the two independent 'modes' obtained through the SVD of the deformation matrix in Figure 2.34*c*.

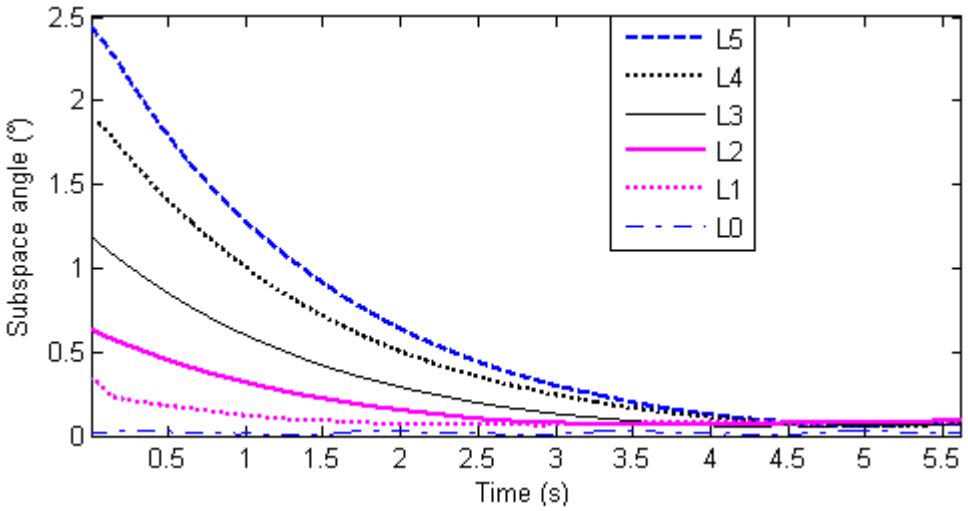

a) on the basis of 'mode' 1

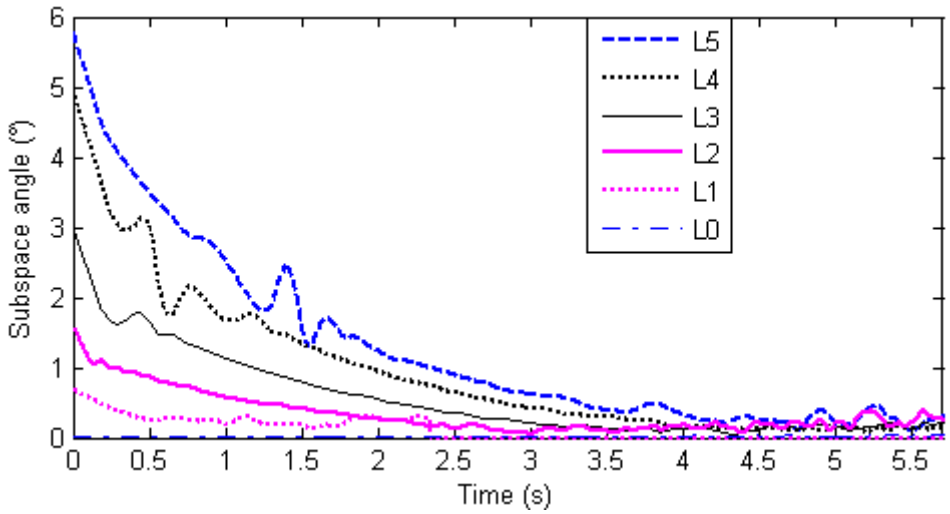

b) on the basis of 'mode' 2

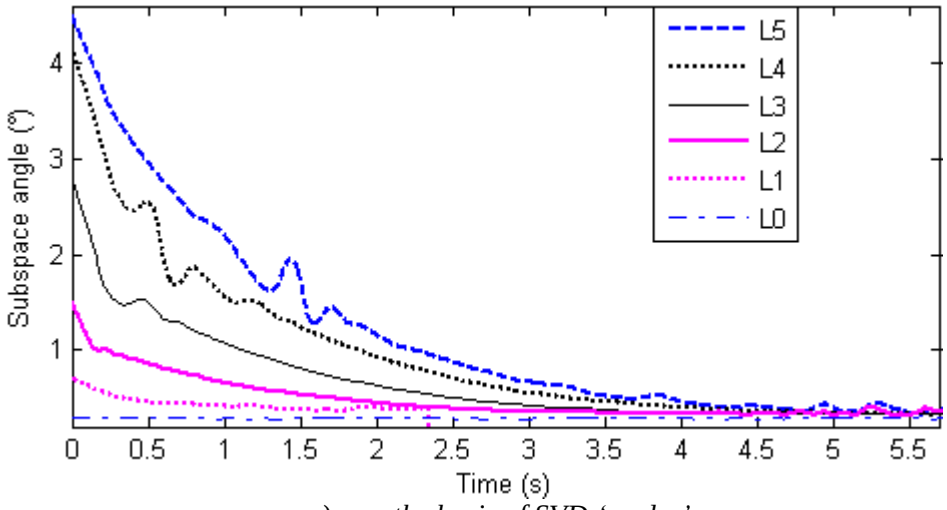

c) on the basis of SVD 'modes'

Figure 2.34: Time evolution of subspace angles for different excitation levels

Detection results are also given in Figure 2.35 in terms of displacement amplitude measured at the end of the beam at time t=0.125 s. In this figure, the first three points of the

curves correspond to weak excitations (level L0). It can be seen how the magnitude of the nonlinearity depends on the displacement level. 'Mode' 2 looks more sensible to the nonlinearity than 'mode 1'.

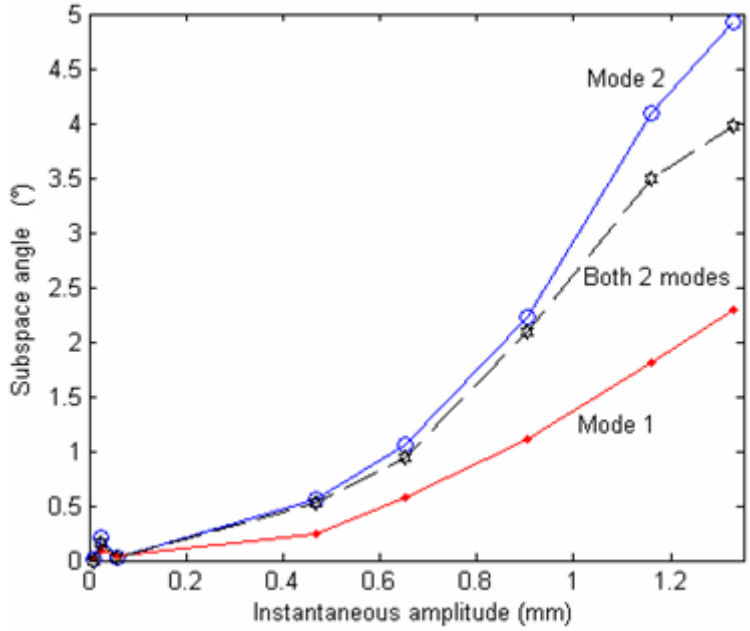

Figure 2.35: Relation angles - displacement amplitudes at the end of beam, t = 0.125 s

- **Random excitation**

Random forces of different levels were applied to the beam in order to capture random responses of the structure.

With a low excitation level resulting in a maximal displacement of 0.06 mm, the WT gives the first two frequencies represented in Figure 2.36.

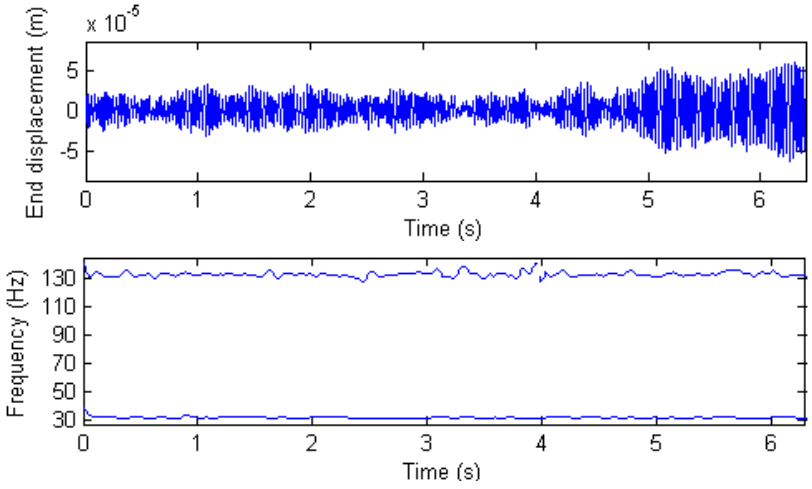

Figure 2.36: Displacement at the extremity of the main beam and WT instantaneous frequencies with a low excitation

One observes that the 1st frequency oscillates less than the 2nd one. The 2nd frequency displays large variations, for example at about 1.3 s, 2.6 s, 3.3 s, 4 s when the displacement

also shows large variation. At these instants, the corrective term $\varepsilon(u,\omega)$ in expression (2.30) may be not negligible and thus instantaneous frequencies do not completely coincide with dominant frequency components in the signal. For this reason, intervals in which the signal amplitude is stationary have to be considered as reference states.

The average frequencies in this case are 30.9 Hz and 133.3 Hz which are a little bit lower than in the free response case because of the shaker attachment to the system.

Let's now examine a higher level of excitation for which the displacement at the end of the main beam and its corresponding power spectral density (PSD) are shown in Figure 2.37. The WT responses at point 7 are shown in Figure 2.38 in terms of frequency and in Figure 2.39 in terms of amplitude. The frequencies are presented along with the reference frequencies corresponding to the low level of excitation (dashed line) to exhibit the difference between the two states.

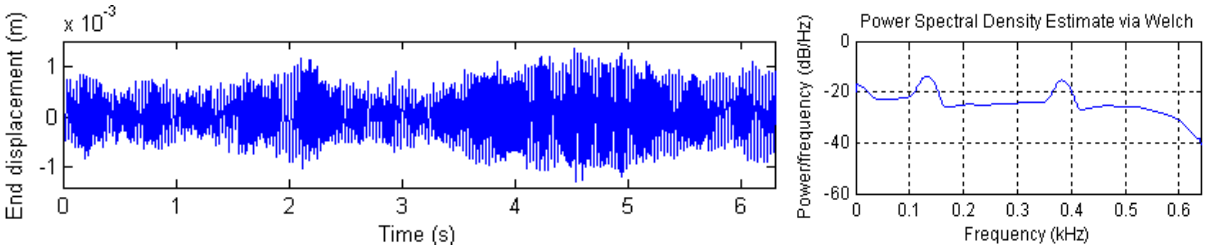

a) time response *b) PSD of the response*

Figure 2.37: Displacement measured at the end of the main beam and the corresponding PSD

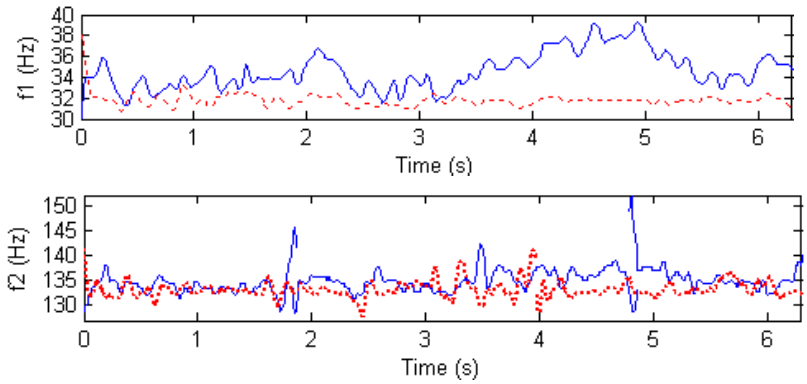

Figure 2.38: Identified instantaneous frequencies (__) compared with the reference state (…)

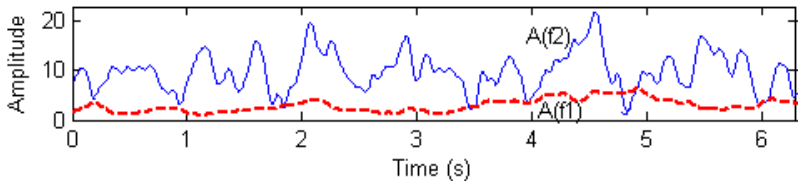

Figure 2.39: Instantaneous amplitudes of the two ridges identified from the signal in Figure 2.37 (high level of excitation)

The following remarks may be formulated from these results.

- The difference between the frequencies obtained in the two states appears clearly, especially for the first frequency.

- In intervals where the amplitude levels vary very sharply, the WT produces ridges with peaks and discontinuities; it can be clearly seen for the higher frequency ridge at about 1.8 s and 4.8 s. These intervals should not be considered in the analysis.

❖ ***Identification of deformation shapes***

Figure 2.40 shows the identified deformation shapes corresponding to different levels of displacement amplitude.

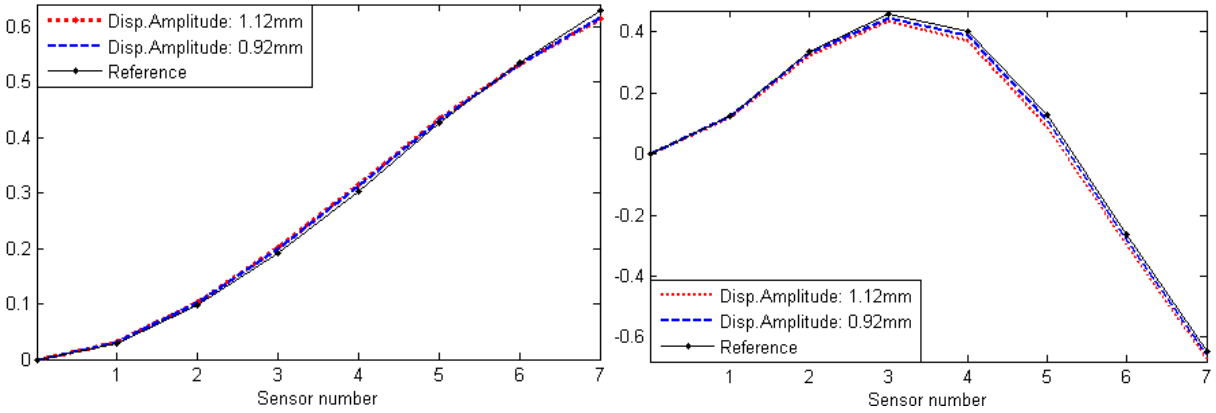

Figure 2.40: The 1st and 2nd deformation 'modes' according to displacement amplitude

❖ ***Detection based on the concept of subspace angle***

The difference between the state shown in Figure 2.37 and the reference state is given in Figure 2.41 by means of the concept of subspace angle, respectively based on 'mode' 1, 'mode' 2 and both two 'modes'.

At time intervals where the instantaneous amplitude is small, the corresponding angle is also small. Elsewhere, the subspace angle index is proportional to the amplitude level, which generally allows a good distinction between the states. As both 'modes' are sensitive to the level of nonlinearity, the subspace formed by both 'modes' gives a better detection.

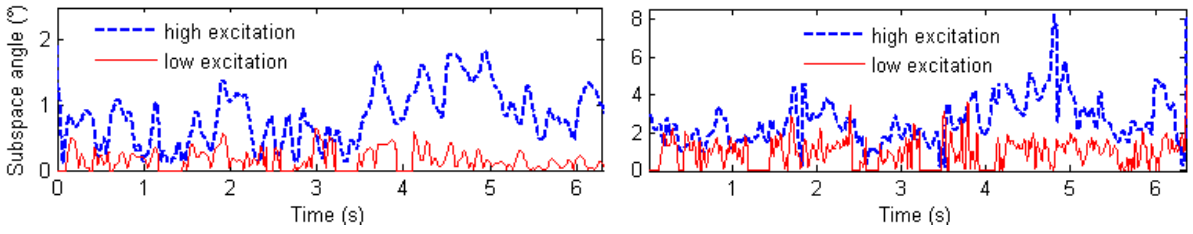

a) on the basis of 'mode' 1 *b) on the basis of 'mode' 2*

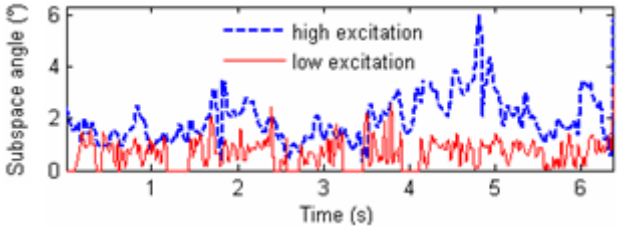

c) on the basis of both two 'modes'

Figure 2.41: Time evolution of subspace angles for two different excitation levels

It is corroborated by Figure 2.42 in which the relation between the angle and the instantaneous displacement amplitude is drawn for several levels of excitation.

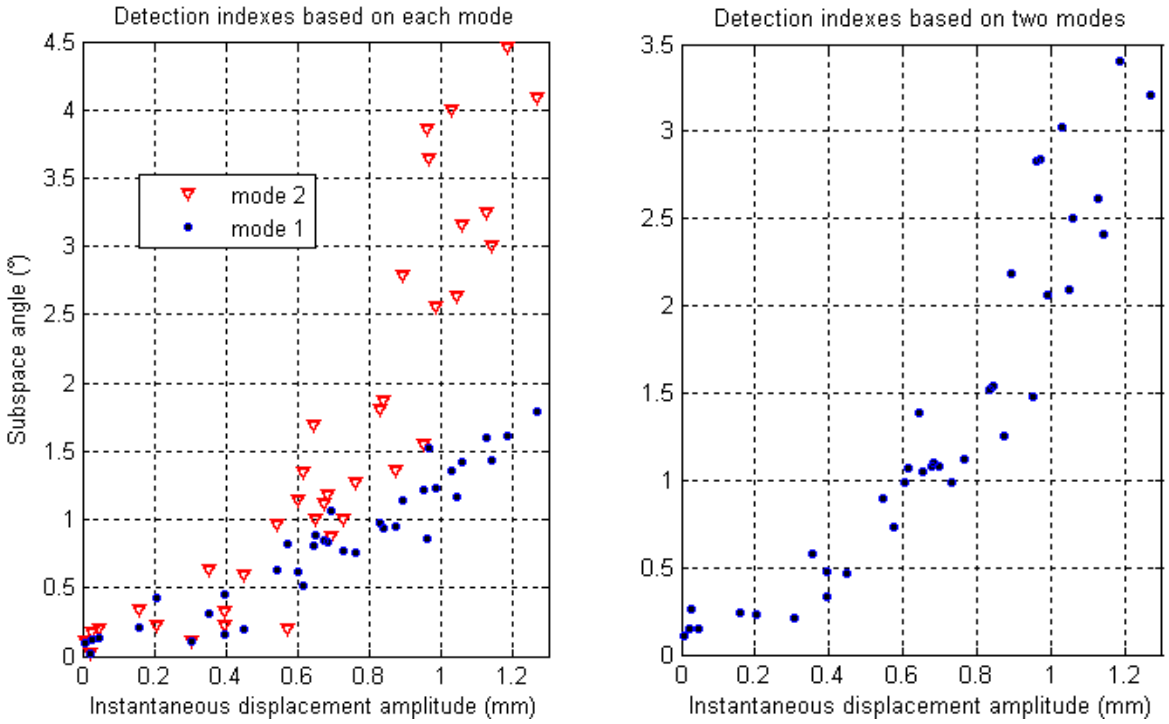

Figure 2.42: Relation between angles and displacement amplitudes at the end of beam

2.6 Discussion on the detection by WT

Detection methods based on the measurement of instantaneous frequencies are reported by many authors in the literature. It was also achieved in this work, as shown in Figures 2.24, 2.33 and 2.38. Alternatively, deformation shapes provide important information about the change in the dynamics of a structure, which is very useful for detection purposes. The concept of subspace angle is an efficient tool that allows to quantitatively monitor the onset of damage or nonlinear behaviour through deformation modes. This was illustrated in Figures 2.25, 2.34, 2.35, 2.41 and 2.42.

Through the above numerical and experimental examples, some remarks may be formulated on the detection methods based on instantaneous features. We know that the time and frequency resolutions of the WT may be chosen in order to obtain a nice frequency resolution, e.g. at a low frequency (ridge 1 in the examples), but the resolution is much rougher at a high frequency (namely, ridges 2, 3). For example, the presence of super-harmonic of the first frequency has the effect of shortening the distances between this frequency component and ridge 1, ridge 2. In order to avoid the interferences between those ridges, it becomes necessary to increase the value of the center frequency ω_0 as required by the inequalities in (2.33). On the other hand, high frequencies (ridges 2, 3) can be identified with a satisfactory resolution by choosing a fine scale vector. However, a fine scale vector and a big value of ω_0 make the computation very costly. Although Figures 2.24, 2.33 and 2.38 have been achieved paying attention to the resolution, the results are not so smooth owing to the frequency resolution. Conversely, the detection indexes represented in Figures 2.25, 2.34 and 2.41 which are determined using the concept of subspace angle demonstrate quite smooth

curves. It indicates the advantage of using instantaneous amplitudes: providing that an ω_0 high enough to well separate the ridges, the resolution is not a delicate problem for the instantaneous amplitude. It is illustrated in Appendix A by comparing the resolution in frequency and amplitude through a raw scale vector and a much finer one. In conclusion, the WT instantaneous amplitudes provide a good means of detection without the need to consider a sophisticated scale vector and the detection is advantageously performed through the use of the concept of subspace angle.

2.7 Concluding remarks

The Wavelet Transform is known for its ability to analyze non-stationary signals and to detect nonlinear behaviour in a structure. As reported in Argoul and Le (2003)[2], it can be used to identify several instantaneous indicators, namely instantaneous frequency, positive 'modal' shape.

In this study, detection of nonlinearity in a dynamic system was performed further using the concept of subspace angle between instantaneous deformation 'modes'. These deformation 'modes' are associated to instantaneous frequencies obtained from the WT of vibration signals measured at different coordinates of the system. Instantaneous bases of independent modes may be generated using the singular value decomposition of deformation 'mode' matrices, which determines the dimensionality of the system. The procedure was illustrated numerically and experimentally on the example of a nonlinear cantilever beam submitted to impact and random excitations.

The concept of subspace angle allows to define a global detection index. When used in combination with instantaneous 'modes' extracted from the WT, this index was found to be sensitive to small dynamic changes and robust with regards to frequency resolution of the transform.

Chapter 3

Second-Order Blind Identification Method Applied to Damage Detection

3.1 Introduction

Blind source separation (BSS) techniques are applied in many domains, since they allow separating a set of signals from their observed mixture, without the knowledge (or with very little knowledge) of the sources signals or the mixing process. In structural dynamics, BSS techniques showed useful for modal identification from numerical and experimental data (Kerschen *et al.* (2007)[54], Poncelet *et al.* (2007)[101], Zhou and Chelidze (2007)[142], Farooq and Feeny (2008)[23]), for separating sources from traffic-induced building vibrations (Popescu and Manolescu (2007)[103]) and for damage detection and condition monitoring (Zang *et al.* (2004)[141], Pontoppidan *et al.* (2005)[102], Jianping and Guang (2009)[49]). A particular BSS technique called second-order blind identification is considered in this chapter for the purpose of condition monitoring as well as damage detection. The beam with geometric nonlinearity presented in Chapter 2 and an airplane mock-up are used as illustrative examples.

3.2 Second-order blind identification

Second-order blind identification (SOBI) was introduced by Belouchrani *et al.* (1999)[9]. Like other BSS approaches, SOBI considers observed signals as a noisy instantaneous linear mixture of source signals. In many situations, multidimensional observations are represented as:

$$\mathbf{x}(t) = \mathbf{y}(t) + \boldsymbol{\sigma}(t) = \mathbf{A}\mathbf{s}(t) + \boldsymbol{\sigma}(t) \tag{3.1}$$

where, $\mathbf{x}(t) = \left[x_1(t), ..., x_m(t)\right]^{\mathrm{T}}$ is a linear instantaneous mixture of source signals and of noise.

$\mathbf{s}(t) = \left[s_1(t), ..., s_p(t)\right]^{\mathrm{T}}$ contains the signals issued from p narrow band sources, $p < m$.

$\mathbf{y}(t) = \left[y_1(t), ..., y_m(t)\right]^{\mathrm{T}}$ contains the sources assembly at a time t.

The transfer matrix **A** between the sources and the sensors is called the mixing matrix. $\boldsymbol{\sigma}(t)$ is the noise vector, modelled as a stationary white noise of zero mean and is assumed to be independent of the sources.

The method attempts to extract the sources **s**(*t*) and the mixing matrix **A** from the observed data **x**(*t*). The term "blind" implies that the mixing matrix **A** is not known a priori, so that only the output signals are exploited. Additionally, some assumptions on the source signals are introduced (Belouchrani *et al.* (1997)[9]). SOBI relies on the second order statistics and is based on the diagonalization of time-lagged covariance matrices.

The sources are assumed stationary, uncorrelated and of unitary variance; their covariance matrix is written:

$$\mathbf{R}_s(0) = E[\mathbf{s}(t)\mathbf{s}^*(t)] = \mathbf{I} \tag{3.2}$$

where superscript * denotes the conjugate transpose of a vector and **I** is the identity matrix.

The added noise is modeled as a stationary white, zero-mean random process independent of the source signals. For simplicity, $\boldsymbol{\sigma}(t)$ is assumed spatially white, i.e.

$$E[\boldsymbol{\sigma}(t+\tau)\boldsymbol{\sigma}^*(t)] = \sigma^2\delta(\tau)\mathbf{I} \tag{3.3}$$

The method may be extended to the case of an unknown noise variance matrix.

The matrix **A** is assumed to have full column rank but is otherwise unknown. The covariance matrix of the array output can be written under the form:

$$\mathbf{R}_x(0) = E[\mathbf{x}(t)\mathbf{x}^*(t)] = \mathbf{A}\mathbf{R}_s(0)\mathbf{A}^{\mathrm{H}} + \sigma^2\mathbf{I} \tag{3.4}$$

$$\mathbf{R}_x(\tau) = E[\mathbf{x}(t+\tau)\mathbf{x}^*(t)] = \mathbf{A}\mathbf{R}_s(\tau)\mathbf{A}^{\mathrm{H}} \qquad \tau \neq 0 \tag{3.5}$$

where superscript H denotes the complex conjugate transpose of a matrix.

As the sources are independent, one has:

$$\mathbf{R}_s(0) = \mathbf{I}, \text{ and so } \mathbf{R}_y(0) = E[\mathbf{y}(t)\mathbf{y}^*(t)] = \mathbf{A}\mathbf{A}^{\mathrm{H}} \tag{3.6}$$

The SOBI procedure comprises two steps: whitening and determination of the unitary matrix.

3.2.1 Whitening

The first step relates to the whitening of the signal **y**(*t*) such that the whitened data are uncorrelated and of unit variance. It consists in applying to **y**(*t*) a whitening matrix **W**, i.e., a $p \times m$ matrix that verifies:

$$E[\mathbf{W}\mathbf{y}(t)\mathbf{y}^*(t)\mathbf{W}^{\mathrm{H}}] = \mathbf{W}\mathbf{R}_y(0)\mathbf{W}^{\mathrm{H}} = \mathbf{W}\mathbf{A}\mathbf{A}^{\mathrm{H}}\mathbf{W}^{\mathrm{H}} = \mathbf{I} \tag{3.7}$$

Expression (3.7) shows that if **W** is a whitening matrix, then **WA** is a $p \times p$ unitary matrix. Thus, for any whitening matrix **W**, there exists a $p \times p$ unitary matrix **U** such that $\mathbf{W}\mathbf{A} = \mathbf{U}$. Consequently, matrix **A** can be deduced by the relation:

$$\mathbf{A} = \mathbf{W}^{\oplus}\mathbf{U} \tag{3.8}$$

where superscript $\oplus$ denotes the Moore-Penrose pseudo-inverse. This whitening procedure reduces the determination of the $m \times p$ mixing matrix **A** to that of a unitary $p \times p$ unitary matrix **U**. The whitened process **z**(*t*) = **W**x(*t*) still follows a linear model where the signal of the whitened process is now a "unitary mixture" of the source signals:

$$\mathbf{z}(t) = \mathbf{W}\mathbf{x}(t) = \mathbf{W}[\mathbf{A}\mathbf{s}(t) + \boldsymbol{\sigma}(t)] = \mathbf{U}\mathbf{s}(t) + \mathbf{W}\boldsymbol{\sigma}(t) \tag{3.9}$$

The effect of the whitening procedure is to "exhaust" all information contained in the covariance matrix in the sense that changing **U** in (3.8) by any other unitary matrix keeps the covariance of **z**(*t*) unchanged. Moreover, the signal of observations **z**(*t*) reduces the array output to a *p*-dimensional vector.

As $\mathbf{R}_s(0) = \mathbf{I}$ (ex. (3.6)), from (3.4), one has:

$$\mathbf{A}\mathbf{A}^{\mathrm{H}} = \mathbf{R}_x(0) - \sigma^2\mathbf{I} \tag{3.10}$$

Expressions (3.7) and (3.10) show that a whitening matrix **W** can be determined through the covariance matrix $\mathbf{R}_x(0)$ [9]. This determination is still possible even if the noise variance matrix is unknown.

3.2.2 Determination of the unitary matrix

Starting with the spatially whitened covariance matrices $\mathbf{R}^w(\tau)$:

$$\mathbf{R}^w(\tau) = \mathbf{W}\mathbf{R}_x(\tau)\mathbf{W}^{\mathrm{H}} = \mathbf{W}E[\mathbf{x}(t+\tau)\mathbf{x}^*(t)]\mathbf{W}^{\mathrm{H}} = E[\mathbf{z}(t+\tau)\mathbf{z}^*(t)] \qquad \tau \neq 0 \tag{3.11}$$

Those matrices correspond to the covariance matrices of the process **z**(*t*). From (3.5) and (3.8), the following important relation is presented:

$$\mathbf{R}^w(\tau) = \mathbf{W}\mathbf{A}\mathbf{R}_s(\tau)\mathbf{A}^{\mathrm{H}}\mathbf{W}^{\mathrm{H}} = \mathbf{U}\mathbf{R}_s(\tau)\mathbf{U}^{\mathrm{H}} \qquad \tau \neq 0 \tag{3.12}$$

where $\mathbf{R}_s(\tau) = E[\mathbf{s}(t+\tau)\mathbf{s}^*(t)]$ is the covariance matrix of the sources for some time lag τ. Since **U** is unitary and $\mathbf{R}_s(\tau)$ is diagonal, (3.12) shows that the whitened covariance matrix $\mathbf{R}^w(\tau)$ is diagonal. So, matrix **U** can be determined by an eigenvalue decomposition of the time-lagged whitened covariance matrix. This procedure can be achieved through the technique of joint diagonalization described in Belouchrani *et al.* (1997)[9]; it consists in a generalization of the Jacobi technique. Some materials for joint diagonalization presented by Cardoso can be found in [43].

The computation of the mixing matrix **A** and sources is straightforward, according to formulas (3.8) and (3.13), once **U** is determined.

$$\mathbf{s}(t) = \mathbf{U}^{\mathrm{H}}\mathbf{W}\mathbf{x}(t) = \mathbf{V}\mathbf{x}(t) \tag{3.13}$$

where $\mathbf{V} = \mathbf{U}^{\mathrm{H}}\mathbf{W}$ which is called the de-mixing matrix is the generalized inverse of the mixing matrix **A**.

The method necessitates that the diagonal elements of $\mathbf{R}_s(\tau)$ must be different, so that the eigenvalues of $\mathbf{R}^w(\tau)$ are distinct. This condition is not always checked a priori for any time lag τ. However, the choice of τ is significantly facilitated when several time lags are considered, as explained in [9]. Alternatively, the use of a few time lags makes less the probability of an unfortunate choice for τ, and matrix **U** is deduced in a more accurate way from a larger set of statistics.

3.3 Modal identification using SOBI

Consider the equations of motion of a mechanical system without damping:

$$\mathbf{M}\ddot{\mathbf{x}}(t) + \mathbf{K}\mathbf{x}(t) = \mathbf{f}(t) \tag{3.14}$$

The system responses can be expressed by modal superposition:

$$\mathbf{x}(t) = \sum_{i=1}^{p} \phi_i \eta_i(t) = \boldsymbol{\Phi}\boldsymbol{\eta}(t) \tag{3.15}$$

where the matrix $\boldsymbol{\Phi}$ is the modal matrix comprising the normal modes and $\boldsymbol{\eta}$ is the vector of normal coordinates which describes the amplitude modulations of $\boldsymbol{\Phi}$. As noted in Kerschen *et al.* (2007)[54], equation (3.15) shows that "*when expanding the system response in terms of the vibration modes, the normal coordinates may, under certain assumptions, act as virtual sources regardless of the number and type of the physical excitation forces*". On the other hand, time responses can be represented by a static mixture of those virtual sources.

If the natural frequencies are distinct, the normal coordinates are harmonic functions (Géradin and Rixen (1994)[33]) and can be considered as sources with different spectral contents, under certain assumptions [54]. Relating to SOBI, it is noticeable that the mixing matrix matches the matrix of vibration modes, and the identified sources correspond to the normal coordinates, i.e.

$$\mathbf{A} = \boldsymbol{\Phi} \quad \text{and} \quad \mathbf{s}(t) = \boldsymbol{\eta}(t) \tag{3.16}$$

In presence of damping, mode-shapes are generally complex and appear in conjugate pairs. If $\mathbf{CM}^{-1}\mathbf{K}$ is symmetric, where $\mathbf{C}$ is the damping matrix, $2p$ complex modes turn out into p real modes. For damped systems, Poncelet *et al.* (2007)[101] pointed out that BSS methods are able to identify normal coordinates as identified sources if damping ratios are low enough.

Equation (3.16) shows that the mode shapes can be found in the mixing matrix **A**. The identification of natural frequencies and damping ratios is straightforward from the identified sources, e.g. using 1 DOF fitting techniques (Maia (1997)[75]).

SOBI characterizes the dynamical features of a structure by way of the mixing matrix **A** and the sources. Thus, when the structure is perturbed or damaged, the fault may be reflected through the identified sources and the matrix **A**. In the following, damage detection is achieved by monitoring the variation of modal features (e.g. resonant frequencies, mode shapes) and the angular coherence between subspaces built from the columns of the mixing matrices.

3.4 SOBI and the Hankel matrices - ESOBI

The so-called *Block Hankel matrices* play an important role in subspace identification of linear systems (Overschee and De Moor (1997)[94]). It is also commonly used for damage detection (Yan *et al.* (2004)[132], Yan and Golinval (2006)[137]), damage localization (Yan and Golinval (2005)[133]) or even identification of nonlinear structures (Marchesiello and Garibaldi (2008)[78]). The data-driven block Hankel matrix is defined as:

$$\mathbf{H}_{1,2i} = \begin{bmatrix} \mathbf{x}_1 & \mathbf{x}_2 & \dots & \dots & \mathbf{x}_j \\ \mathbf{x}_2 & \mathbf{x}_3 & \dots & \dots & \mathbf{x}_{j+1} \\ \dots & \dots & \dots & \dots & \dots \\ \mathbf{x}_i & \mathbf{x}_{i+1} & \dots & \dots & \mathbf{x}_{i+j-1} \\ - & - & - & - & - \\ \mathbf{x}_{i+1} & \mathbf{x}_{i+2} & \dots & \dots & \mathbf{x}_{i+j} \\ \mathbf{x}_{i+2} & \mathbf{x}_{i+3} & \dots & \dots & \mathbf{x}_{i+j+1} \\ \dots & \dots & \dots & \dots & \dots \\ \mathbf{x}_{2i} & \mathbf{x}_{2i+1} & \dots & \dots & \mathbf{x}_{2i+j-1} \end{bmatrix} \equiv \begin{pmatrix} \mathbf{X}_p \\ - \\ \mathbf{X}_f \end{pmatrix} \equiv \frac{"past"}{"future"} \tag{3.17}$$

where $2i$ is a user-defined number of row blocks, each block contains m rows (number of measurement sensors), j is the number of columns (practically $j = N\text{-}2i+1$, N is the number of sampling points). The Hankel matrix $\mathbf{H}_{1,2i}$ is split into two equal parts of i block rows: past and future data. Thus, the algorithm considers vibration signals at different instants and not only instantaneous representations of responses. This allows to take into account temporal correlations between measurements when current data depends on past data. The principal idea in modal analysis is to retain all past information to predict the future. Although the past and future inputs have many elements in common, they are always distinct because the corresponding columns of $\mathbf{X}_p$ and $\mathbf{X}_f$ have no elements in common (Overschee and De Moor (1997)[94]). Therefore, the objective pursued here in using the block Hankel matrix rather than the observation matrix is to improve the sensitivity of the detection method. The combined method will be called enhanced SOBI - ESOBI in the following.

We know that in the SOBI method, the size of a column vector in the mixing matrix **A** depends on the number of sensors m; moreover, the number p of sources successfully identified cannot exceed m. It results that, if the number of sensors is very small, a perfect identification of all the resonance frequencies is impossible by means of SOBI. However, in the same situation, ESOBI, as it exploits more of the signals through the Hankel matrix, is able to provide better information about the dynamics of the system. Moreover, the detection based on the concept of subspace angle can still be achieved, even with a single sensor as illustrated later.

3.5 An extension of SOBI called Blind Modal Identification

A BSS method like SOBI for which the mixing matrix is real-valued is not always suitable for identifying generally damped systems. Recently a novel approach called Blind Modal Identification (BMID) has been proposed by McNeil and Zimmerman (2008)[79]. It uses BSS techniques to yield modal responses and complex mode shape estimates (McNeil and Zimmerman (2010)[80]). The principle of the BMID method is to apply SOBI on an augmented and pre-treated dataset.

From the measured data, denoted as $\mathbf{x}_0(t)$, the Hilbert transform pairs, $\mathbf{x}_{90}(t)$ are introduced. Note that the Hilbert transform of a sinusoid results in a 90° phase shift of the sinusoid. This results in the double sized mixing problem:

$$\mathbf{x}^{(2m\times 1)} = \mathbf{A}^{(2m\times 2p)}\mathbf{s}^{(2p\times 1)}, \qquad \mathbf{s}^{(2p\times 1)} = \mathbf{V}^{(2p\times 2m)}\mathbf{x}^{(2m\times 1)},$$

$$\begin{bmatrix}\mathbf{x}_0^{(m\times 1)}\\ \mathbf{x}_{90}^{(m\times 1)}\end{bmatrix} = \mathbf{A}^{(2m\times 2p)}\begin{bmatrix}\mathbf{s}_0^{(p\times 1)}\\ \mathbf{s}_{90}^{(p\times 1)}\end{bmatrix}, \qquad \begin{bmatrix}\mathbf{s}_0^{(p\times 1)}\\ \mathbf{s}_{90}^{(p\times 1)}\end{bmatrix} = \mathbf{V}^{(2p\times 2m)}\begin{bmatrix}\mathbf{x}_0^{(m\times 1)}\\ \mathbf{x}_{90}^{(m\times 1)}\end{bmatrix} \tag{3.18}$$

where $\mathbf{s}_{90}(t)$ are the Hilbert transform pairs of the source components $\mathbf{s}_0(t)$.

Because $\mathbf{x}_0(t)$ and $\mathbf{x}_{90}(t)$ are respectively the real and imaginary parts of the analytic signal $\mathbf{x}_a(t) = \mathbf{x}_0(t) + j\,\mathbf{x}_{90}(t)$, (with $j = \sqrt{-1}$) the partition of the augmented dataset in equation (3.18) shows similarity with the familiar concept of the analytic signal.

The matrix **A** in (3.18) can be partitioned into two block columns corresponding to $\mathbf{s}_0(t)$ and $\mathbf{s}_{90}(t)$:

$$\mathbf{A} = \begin{bmatrix}\mathbf{A}_0 & \mathbf{A}_{90}\end{bmatrix} \tag{3.19}$$

The *i*th column of $\mathbf{A}_0$ gives the contribution of $s_{0i}(t)$ to each measurement and the corresponding phase shifted measurement. Likewise, the *i*th column of $\mathbf{A}_{90}$ and $s_{90i}(t)$ presents a similar relation. Complex modes, $\mathbf{\Phi}_c$, can be formed by taking the first or last block of *m* rows in:

$$\mathbf{\Phi}'_c = \mathbf{A}_0 + j\,\mathbf{A}_{90} \tag{3.20}$$

It is important to note that the Hilbert transform presents end effects, i.e. errors are introduced at the end of $\mathbf{x}_{90}(t)$. End effects can be lessened by e.g. zero padding or reflection padding as mentioned in Chapter 2.

McNeil and Zimmerman proposed also a Modal Contribution Indicator (MCI) to measure modal strength in a simple manner. If the sources are scaled to unit variance, the mode shapes are scaled by the modal amplitude. An indicator may be put forward for a relative measure of the modal contribution of mode *k* to the overall response:

$$\mathrm{MCT}_k = \sum_{i=1}^{m} |\phi_{ik}| \tag{3.21}$$

where *m* is the number of measured DOFs. This measure can be normalized by the Modal Contribution Indicator (MCI):

$$\mathrm{MCI}_k = \frac{\mathrm{MCT}_k}{\sum_{k=1}^{p}\mathrm{MCT}_k} \tag{3.22}$$

where *p* is the number of modes. MCI_k may roughly represent the fractional contribution of the *k*th mode to the overall response. In our work, MCI is employed in order to select physical modes that have an essential impact on the system responses.

3.6 Examples of application

3.6.1 Experiments in an aircraft model in different conditions

Let us consider an aircraft model made of steel and suspended freely by means of three springs, as illustrated in Figure 3.1.

a) Aircraft model *b) removing of 1-3 connecting bolts*

Figure 3.1: An aircraft model (*a*) and the simulated damages (*b*)

A straight beam of rectangular section with a length of 1.2 m represents the fuselage. Plate-type beams connected to the fuselage form the wing (1.5 m) and tails (0.2 m). Their dimensions are detailed in Figure 3.2. The structure is randomly excited on the top of the left wing with an electro-dynamic shaker in the frequency range of 0-130 Hz. Eleven accelerometers are installed for capturing the dynamic responses of the structure in accordance with the set-up description given in Figure 3.2. Three levels of damage are simulated by removing, respectively, one, two and three connecting bolts on one side of the wing (Figure 3.1*b*). The data of this experiment was formerly used for illustrating damage detection methods based on Principal Component Analysis, on Kalman model and on Null subspace analysis (Yan *et al.* (2004)[132], Yan and Golinval (2006)[137]); it was also used for damage localization (Yan and Golinval (2005)[133]). Some results of modal identification were also described in [132].

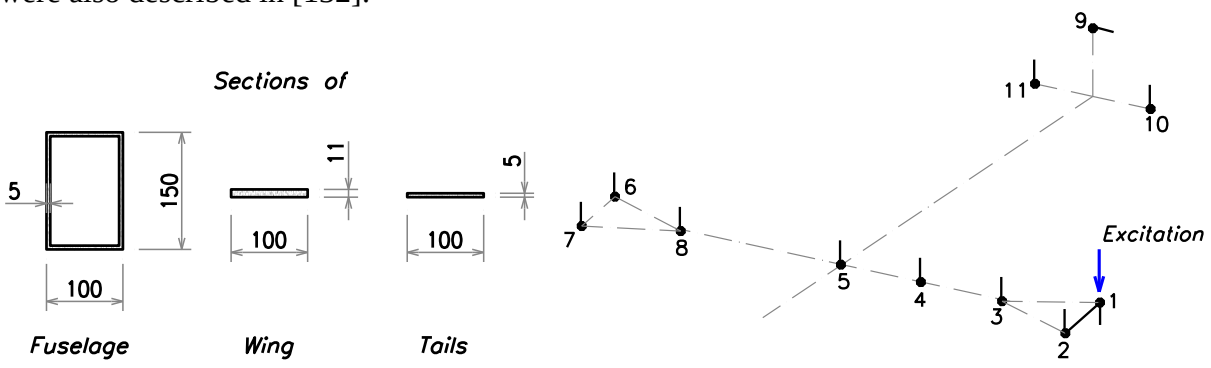

Figure 3.2: Dimensions (in millimeters) and location of the 11 sensors

❖ ***Modal identification using SOBI***

For the sake of illustrating the sensitivity of SOBI to damage occurrence, we start first to identify modal features, namely the resonance frequencies and mode shapes. Figure 3.3*a*

represents the first eight resonance frequencies obtained through the FFT of the identified sources in the healthy (undamaged) state. Some resonance frequencies are found to be relatively close, e.g. f_3 (83.29 Hz) and f_4 (85.44 Hz); f_6 (102.13 Hz) and f_7 (103.35 Hz). Those results are in perfect agreement with the identification performed in Reference [132] using the Kalman model based on SSI.

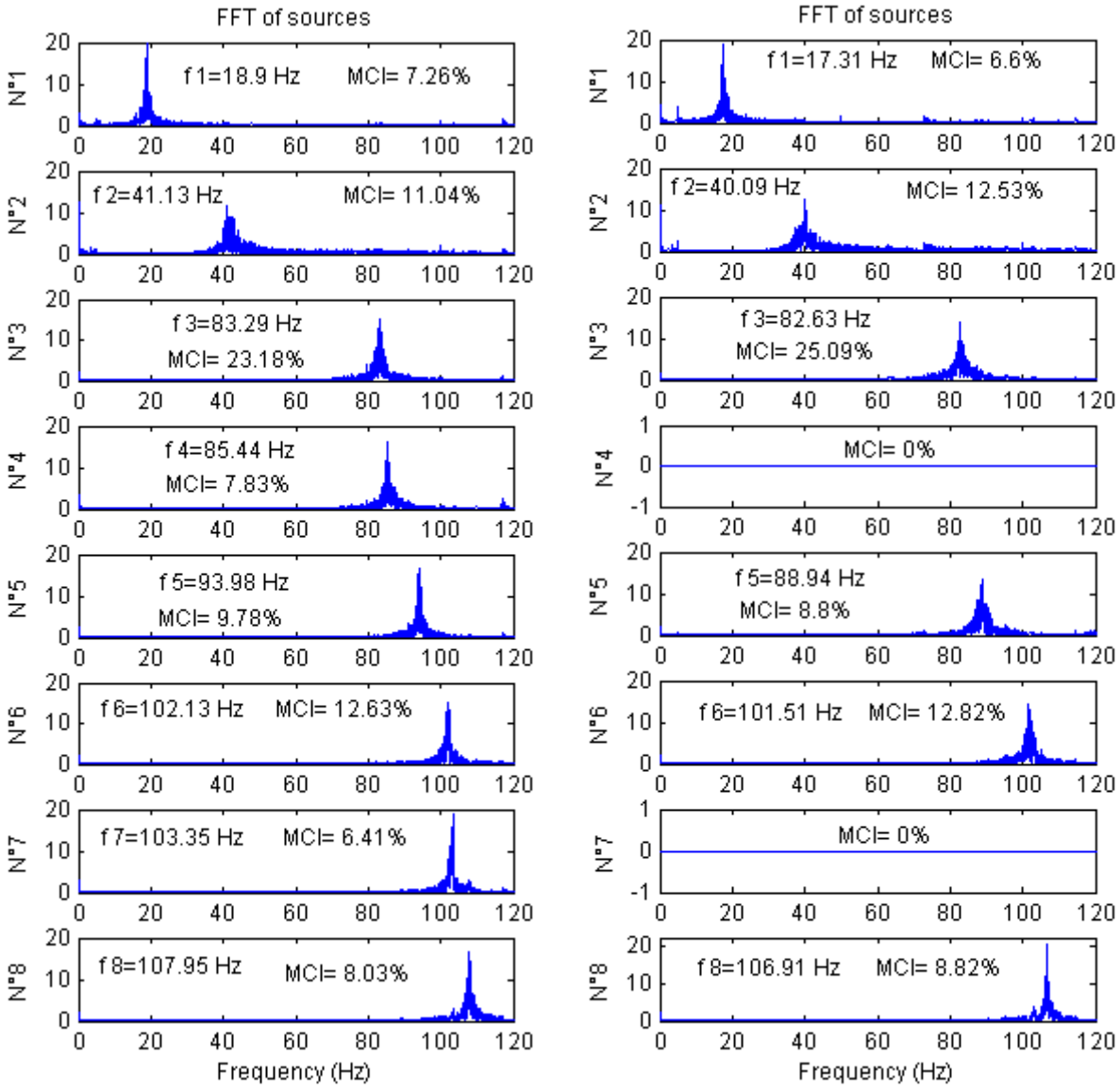

a) Healthy state *b) Damaged state*

Figure 3.3: SOBI identification of resonance frequencies by FFT of the sources

The SOBI mode-shapes, contained in the columns of the mixing matrix **A**, are represented in Figure 3.4, where sensors n° 1-8 represent the motion in the wing and sensors n° 9-11 show the responses in the tails.

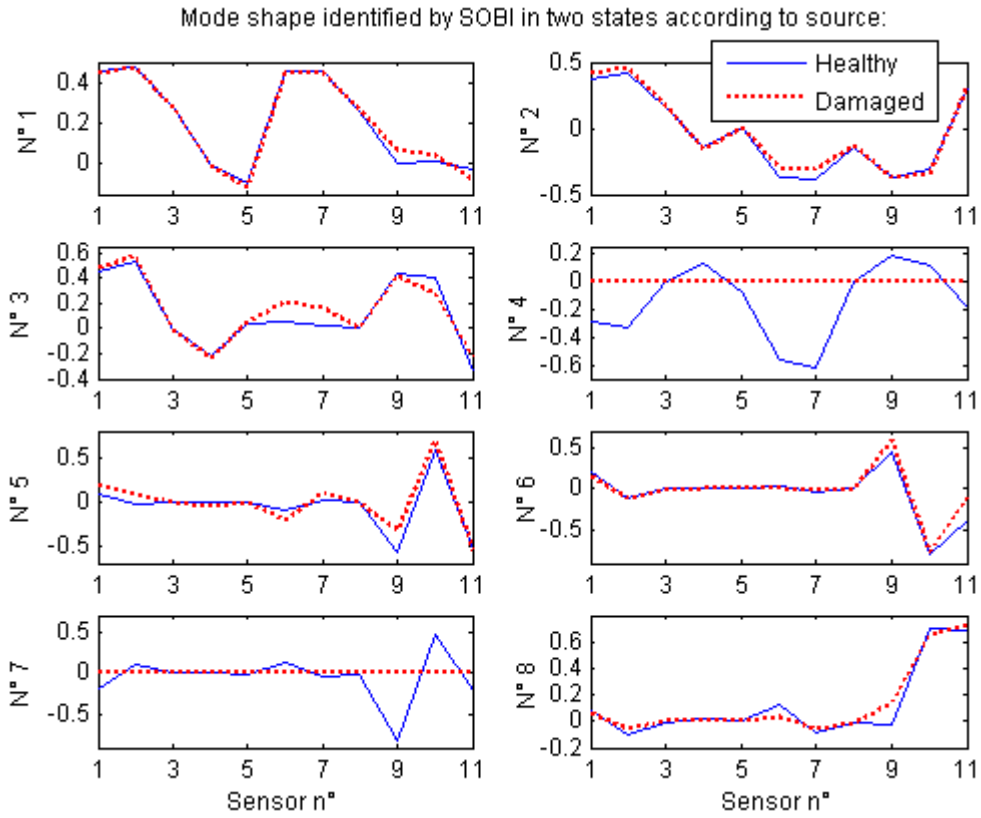

Figure 3.4: Mode shapes identified by SOBI in the healthy and damaged (dashed line) states

Let us now examine a damaged case when all the three connecting bolts are removed (Figure 3.1*b*). The FFT of the identified sources are juxtaposed to the ones corresponding to the healthy (reference) state in Figure 3.3*b*. The largest frequency variation is observed on the first frequency with 8.4% of decrease. Another very noticeable change is the disappearance of sources n° 4 and 7 when the structure is damaged. We note also that the MCI of modes n° 4 and 7 in Figure 3.3*a* is quite small in comparison to the previous components - modes n° 3 and 6. Instead of 8 sources/ modes, we can identify only 6 sources/modes in the damaged case. The obtained mode-shapes are superposed in Figure 3.4.

❖ ***Modal identification using BMID***

In the same way, FFT of sources and mode shapes identified by BMID are presented in Figures 3.5 and 3.6, respectively. It is observed in Figure 3.5 that compared to SOBI sources, BMID spectral components are slightly less noisy (e.g. sources n° 1-3). Thereto, the disparity between the healthy and damaged states is better shown by BMID mode shapes n° 2, 5 and 8.

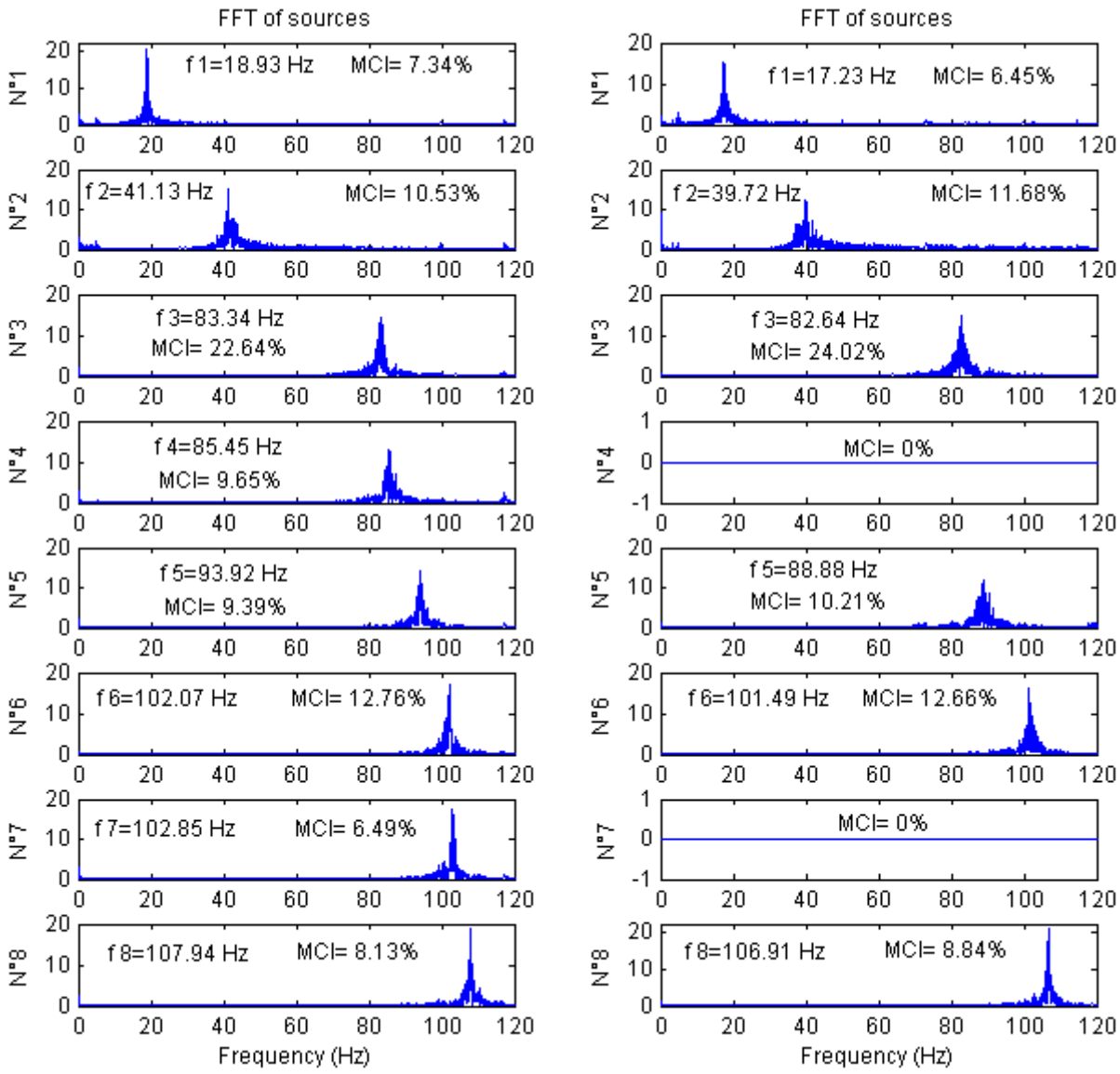

a) Healthy state *b) Damaged state*

Figure 3.5: BMID identification of resonance frequencies by FFT of the sources

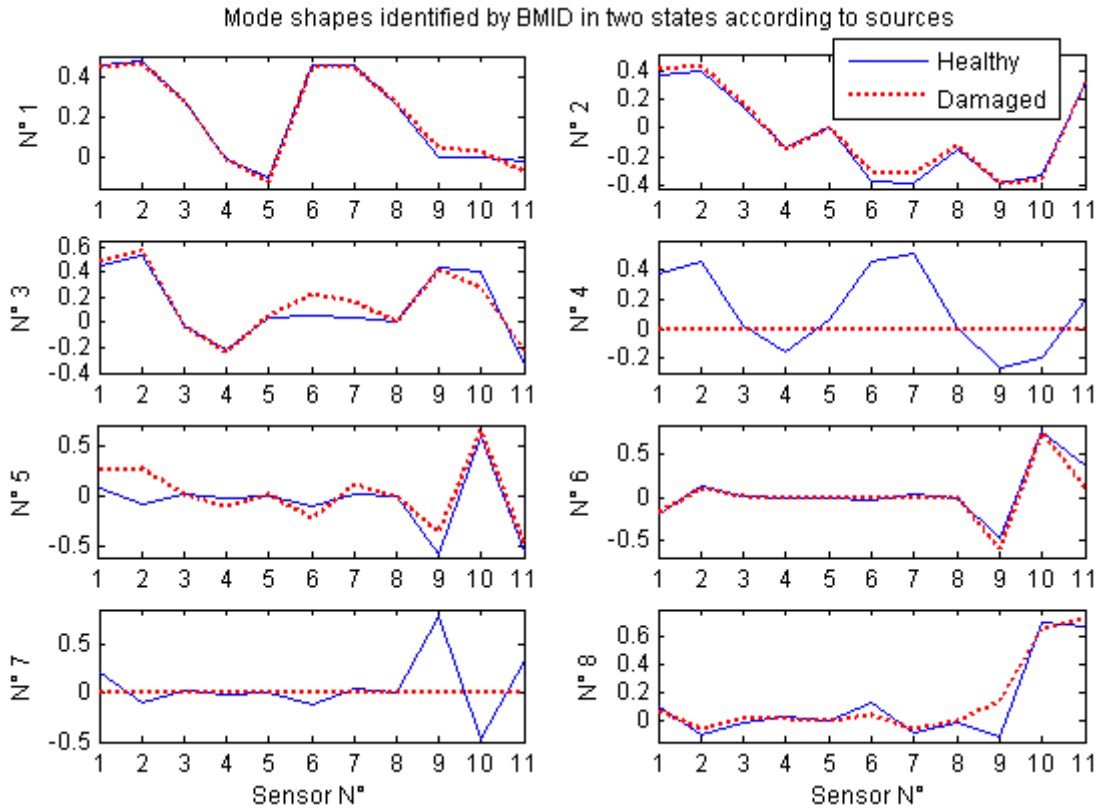

Figure 3.6: Mode shapes identified by BMID in the healthy and damaged (dashed line) states

❖ ***Modal identification using Enhanced SOBI - ESOBI***

To enrich the information in the data matrix, several block rows are assembled to build the data-driven Hankel matrix as in expression (3.17). In this application, the number of block rows has been fixed to 10. First, the enhancement provided by ESOBI can be noticed through the quality of the sources identified in Figure 3.7. The sources are now much clearer, i.e. noisy spectral components in each source are minimized with respect to Figure 3.3. It follows that the separation of the sources is considerably improved by the use of the data-driven Hankel matrix. Note also that in identification methods using the Hankel matrices (e.g. SSI (Peeters and De Roeck (2001)[98]), NSA (Yan and Golinval (2006)[137]), one mode may be represented by two components. In this case, the sum of the MCI of these two components is approximately equal to the MCI of the corresponding source in the SOBI analysis.

ESOBI mode-shapes are also presented in Figure 3.8.

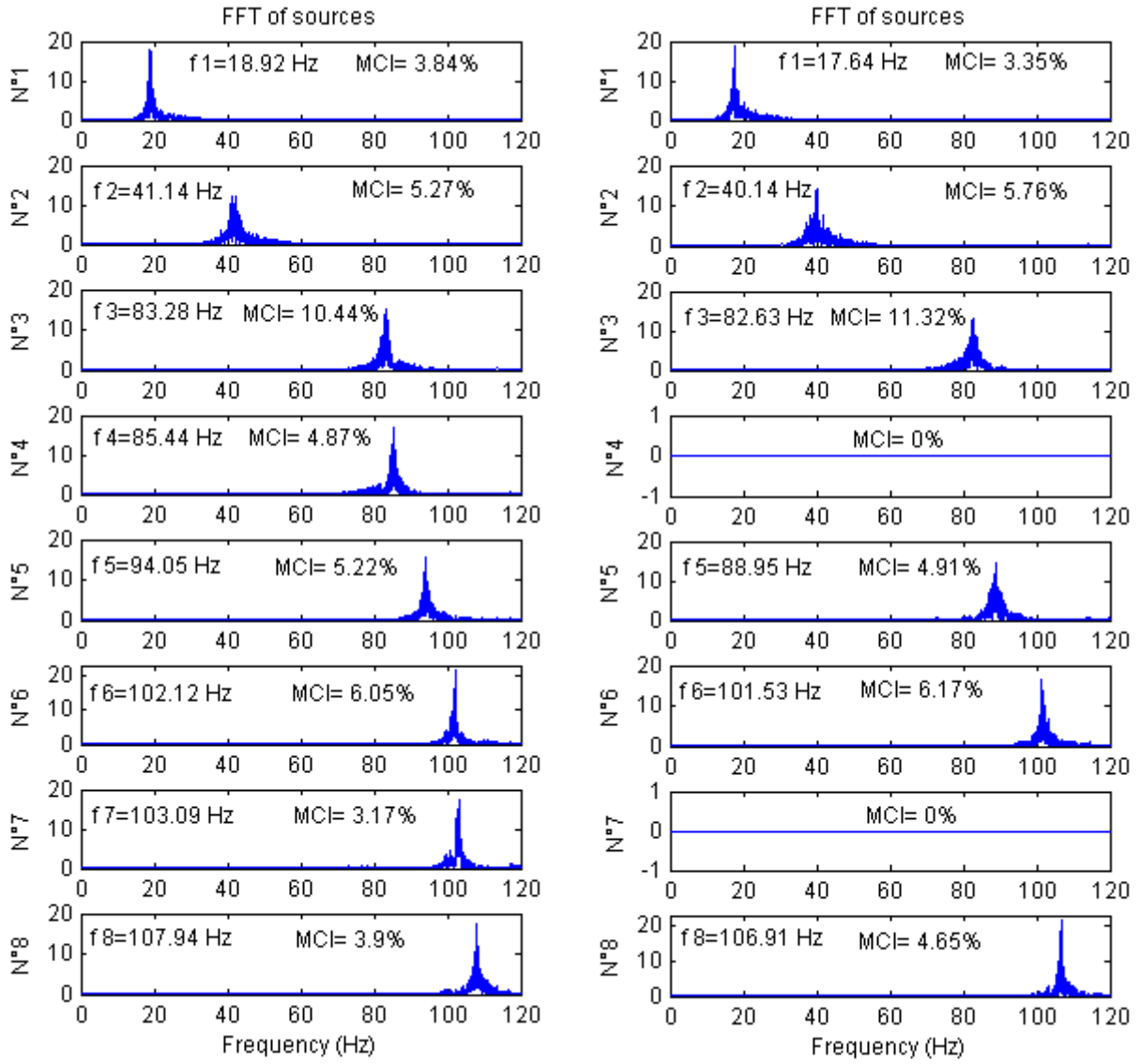

a) Healthy state *b) Damaged state*

Figure 3.7: ESOBI identification of resonance frequencies by FFT of the sources in the healthy (*a*) and damaged (*b*) states

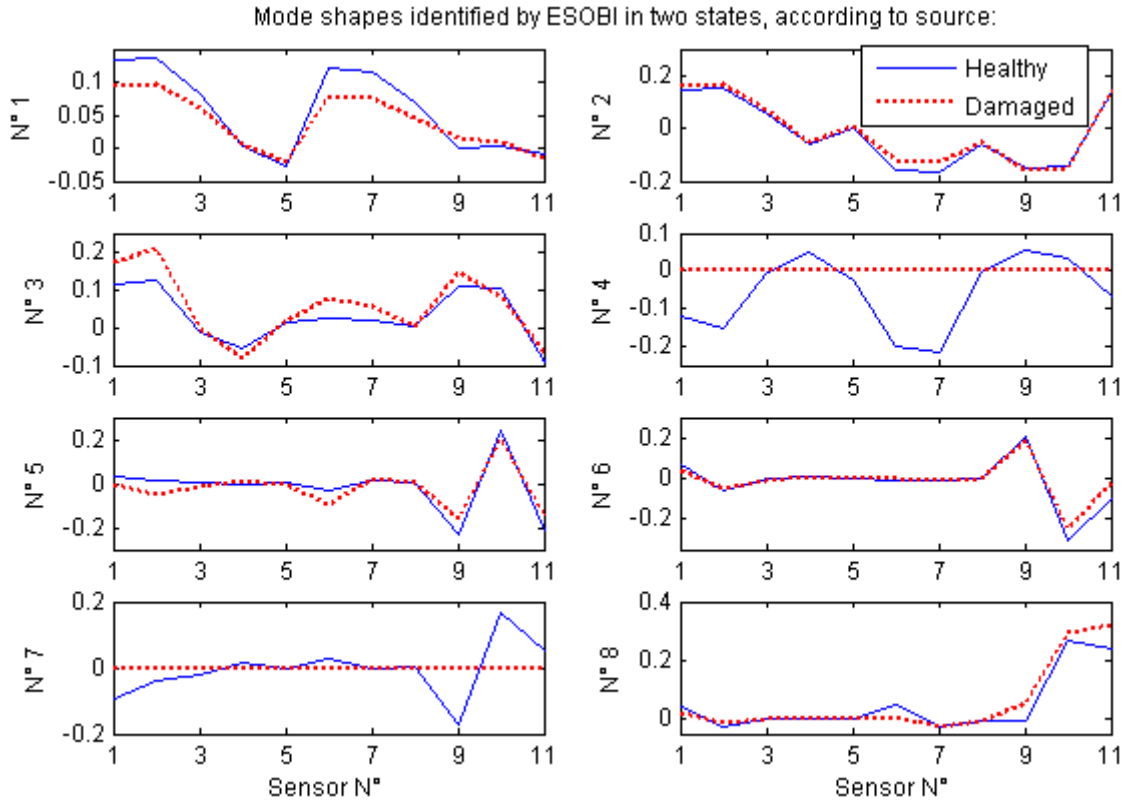

Figure 3.8: Mode shapes identified by ESOBI in two states: healthy and damaged states

❖ ***Damage detection based on subspace angles***

Several tests were achieved with the aircraft model in different conditions; they are summarized in Table 3.1. Tests n° 1-3 compare various healthy states consisting of different amplitude levels of excitation. The next tests correspond to three levels of damage with increasing degrees, according to the removing of one, two and three connecting bolts respectively.

Table 3.1: Condition of tests

Test n°	1	2	3	4	5	6
Condition	Exc. 1.5:0.5	Exc. 1:0.5	Exc. 1:1.5	Dam. 1	Dam. 2	Dam. 3

Since sources n° 4 and 7 are not identified in the damaged states, only six mode-shapes according to sources n° 1-3, 5, 6, 8 are considered in the subspace.

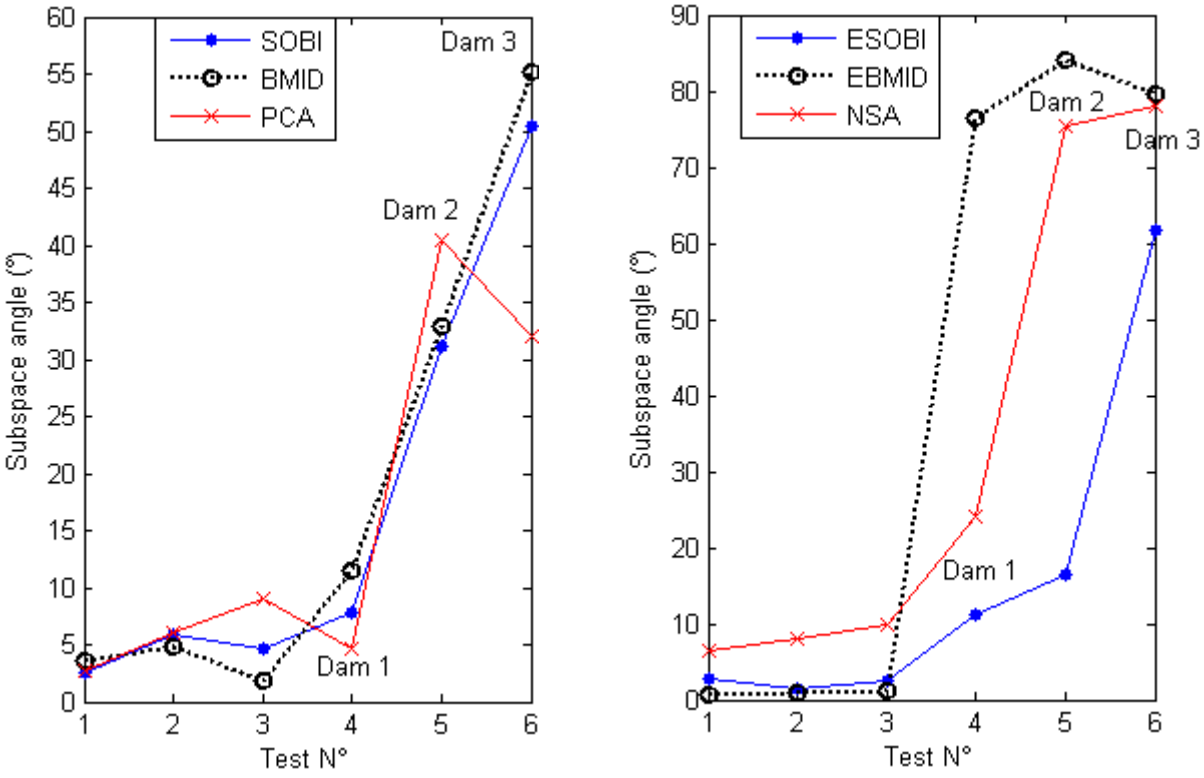

a) SOBI, BMID and PCA methods *b) ESOBI, EBMID and NSA methods*

Figure 3.9: Damage detection based on the subspace angles

Damage detection results based on the concept of subspace angle are presented in Figure 3.9. The results of the proposed methods (SOBI, BMID and ESOBI) are compared to those of Principal Component Analysis (PCA) and Null Subspace Analysis (NSA) obtained in Reference [137]. Like ESOBI and NSA, BMID may also be performed by assembling the Hankel matrix, which is denoted here by EBMID. In Figure 3.9*a*, SOBI, BMID and PCA detections are displayed together. Their indexes are quite similar; however, in the PCA-based method, the first level of damage (Dam. 1) is not detected and the index corresponding to the highest level (Dam. 3) is not the biggest. Conversely, in the SOBI and BMID-based methods, the smallest damage can be detected and the levels of damage are logically revealed. It appears in Figure 3.9*a* that the BMID-based method is the most sensitive to the presence of damage.

Detection results obtained by the use the Hankel matrix (named ESOBI, EBMID and NSA) are presented in Figure 3.9*b*.

To facilitate the comparison between the different methods, a common reference threshold is used in Figure 3.10, i.e. the indexes are normalized such that the maximal indexes according to the reference states (tests n° 1-3) are set to unity. According to Figure 3.10, the normalized indexes show that damage detection by SOBI and BMID is better than by PCA; ESOBI is more sensitive than NSA for damage levels 1 and 3 but EBMID is by far the most sensitive method.

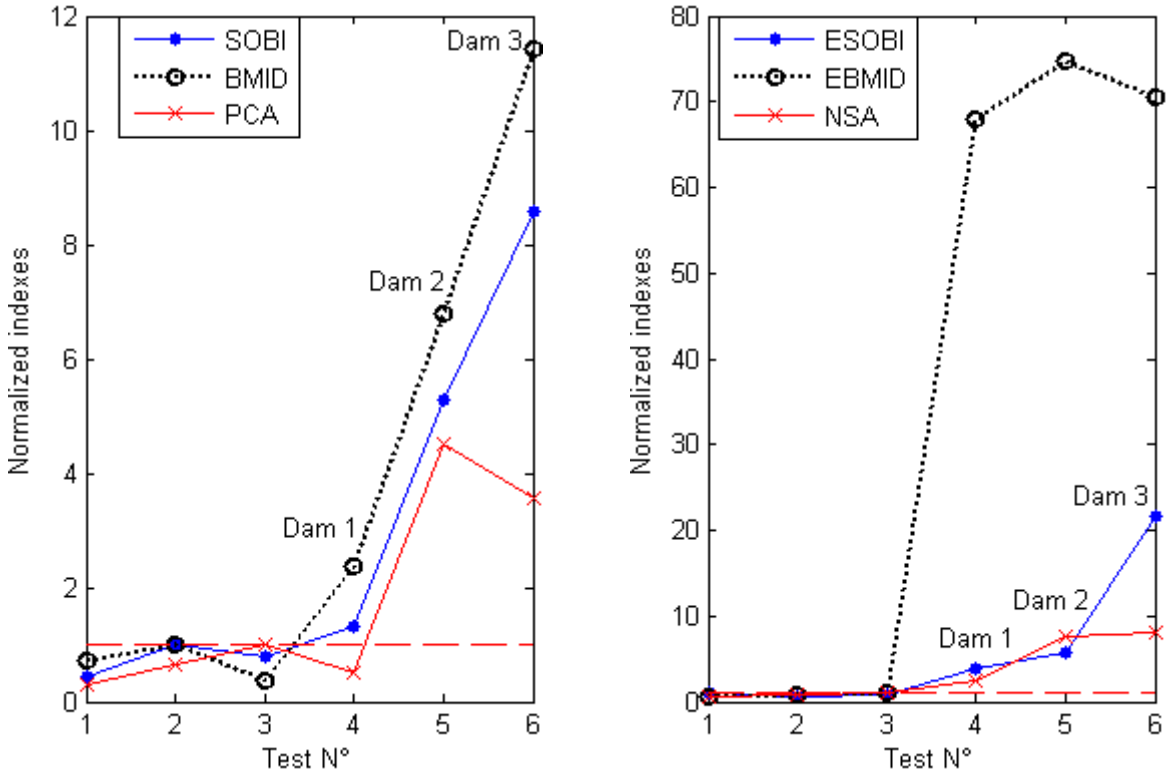

Figure 3.10: Normalized detection indexes by SOBI, PCA, BMID, ESOBI, NSA and EBMID

It is worth noting that when the Hankel matrix is combined with BMID, the number of block rows might be less than in ESOBI and NSA. Actually, as the measured data is first expanded using the Hilbert transform, BMID leads to double the size of the dataset. For an equivalent size of the generated data matrix, the Hankel matrix applied to BMID requires only half of the number of block rows which is used for ESOBI or NSA. Consequently the number of block rows of the Hankel matrix in EBMID should be kept moderate to accommodate the data generation. In Figures 3.9 and 3.10, the results were generated with a Hankel matrix containing 10 block rows in the case of ESOBI and NSA and 5 block rows in the case of EBMID.

In conclusion, damage detection based on the concept of subspace angle using SOBI or its alternatives like ESOBI, BMID and EBMID looks very useful as illustrated in the above example. The methods are sensitive to damage even if it is small. In the modal identification step, we can detect damage occurrence, not only by looking at resonance frequency shifts but also looking at disappearance of some sources. This helps to determine the dimensionality of the problem and to construct an adequate subspace containing only compatible modes in different states of the structure.

❖ ***Damage detection using one single sensor***

The construction of the Hankel matrix to apply SOBI allows to improve the identification and furthermore to detect damage even if the number of sensors is small. While SOBI cannot separate sources of narrow spectral band from only one sensor, ESOBI is able to handle this task. It is illustrated in Figure 3.11*a* when only one sensor located at point 7 and 20 block rows are used for the Hankel matrix. Similarly, the identification using EBMID is presented in Figure 3.11*b*.

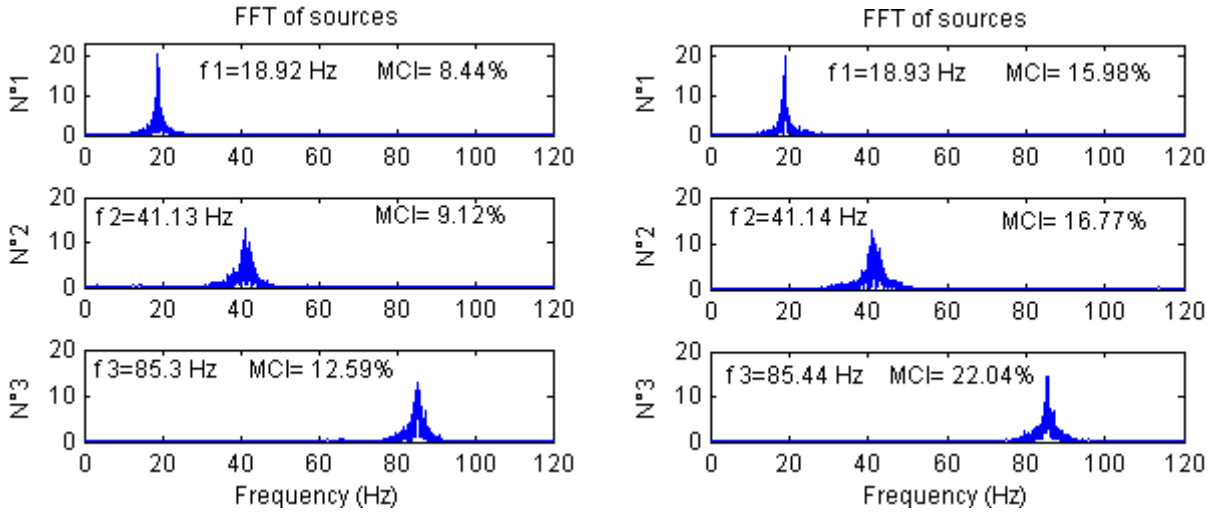

a) by ESOBI *b) by EBMID*

Figure 3.11: Identification of resonance frequencies, using only one sensor

Damage detection results based on the subspace angles are shown in Figure 3.12. In the case of ESOBI, 20 block rows are used for the Hankel matrix and the best result is obtained by considering the first two column vectors of the mixing matrix **A** in the feature subspaces. In this case, damage of level 1 can be distinguished from the false-positive tests (Figure 3.12*a*). However, this damage is ignored if more vectors are taken into account, as shown in Figure 3.12*b*. In the case of EBMID, the best detection is displayed in Figure 3.12*c* when 8 block rows are used and all the first three column vectors in matrix **A** are taken into account. If fewer vectors are considered in the subspace, damage detection is similar to ESOBI result in Figure 3.12*a*. Thus, EBMID still looks as more appealing when the number of sensor is small.

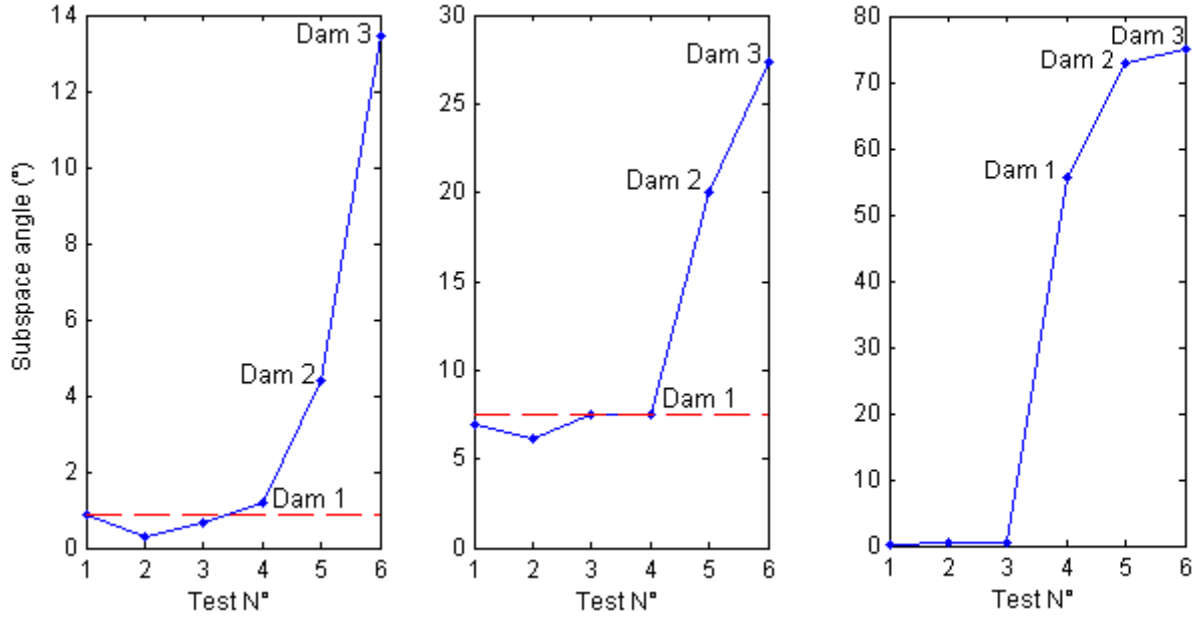

*a) ESOBI, by the first 2 vectors in **A*** *b) ESOBI, by more vectors* *c) EBMID*

Figure 3.12: Damage detection by ESOBI and EBMID, only one sensor is used

3.6.2 Experiments on a nonlinear structure (impact excitation)

Let us consider the beam with a cubic stiffness at the end presented in Section 2.5. Since the response of this structure submitted to impact excitation is non-stationary, the behavior of SOBI depends on the excitation amplitude.

As shown in Poncelet *et al.*, (2007)[101], SOBI identification is accurate for linear systems with weak damping and distinct frequencies. So, at low impact level, the beam behaves as a linear structure and the identification using SOBI gives good results. Figure 3.13 presents all the sources identified and their FFT respectively. Thanks to the MCI indicator, it is easy to select three actual sources s_1, s_4 and s_7. Each of these sources shows a monochrome appearance with a pure dominant frequency.

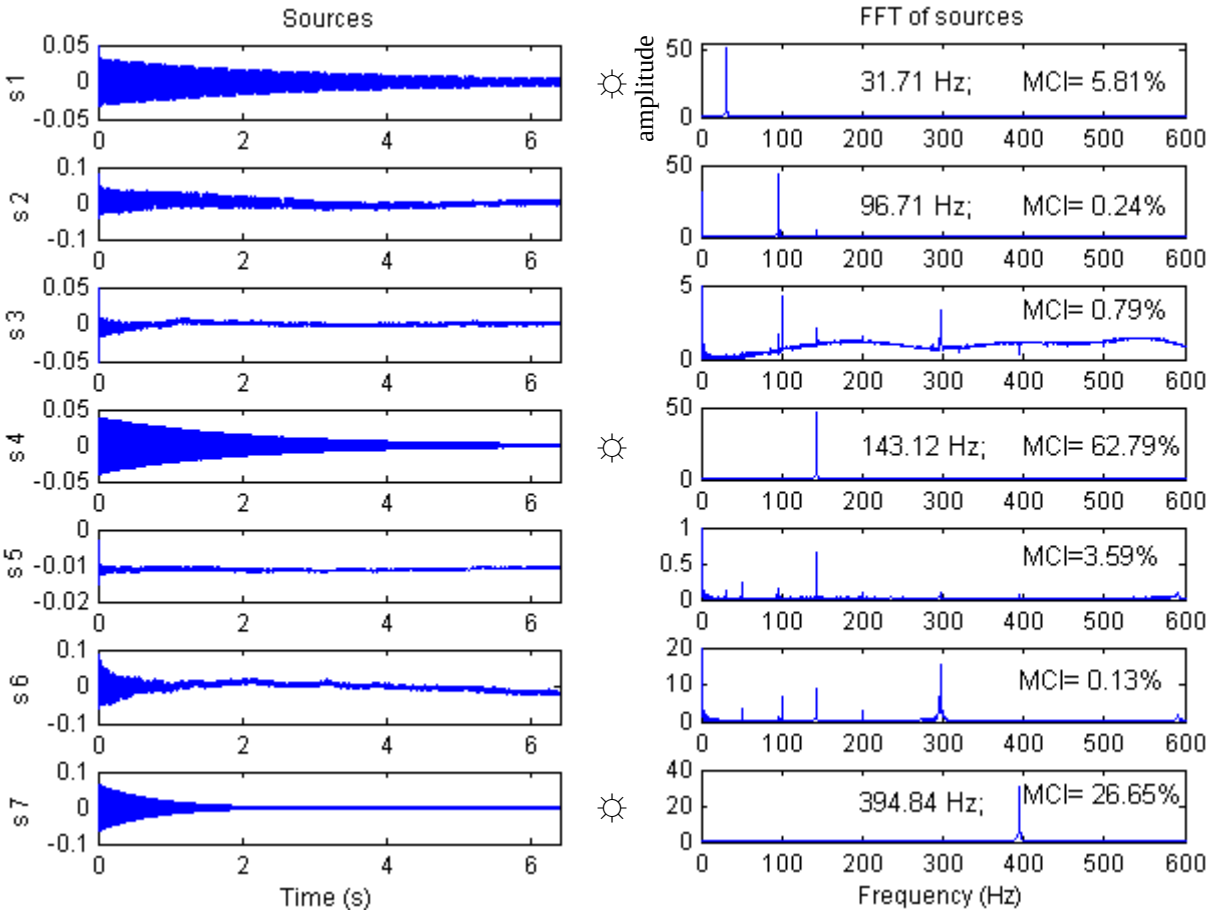

a) *b)*

Figure 3.13: Sources (*a*) and their FFT (*b*) identified by SOBI for the linear state

Let us now examine an impact level at which nonlinearity is excited – (level L5 in §2.5.2). As illustrated in Figure 3.14, the modal contribution indicator (MCI) allows the selection of three sources s_1, s_3 and s_6 for which the dominant frequencies correspond to the three actual sources in the linear case. However, the perfect separation of the sources fails. Only the source corresponding to the highest frequency (s_6) appears to be not affected by the nonlinearity. Sources s_1 and s_3, according to modes 1 and 2, show peaks respectively at 39.84 and 149.37 Hz which are clearly higher than in the linear case, but multiple frequency components are also observed. A new frequency at 122.1 Hz appearing in those sources corresponds to the third harmonic of the first frequency. As noted in the WT analysis, the

'mode' associated to this harmonic is a combination of the first two 'modes'. This is the reason why it prevents separating the first and the second 'modes': the assumption of SOBI that the sources are uncorrelated is no longer guaranteed in the nonlinear case.

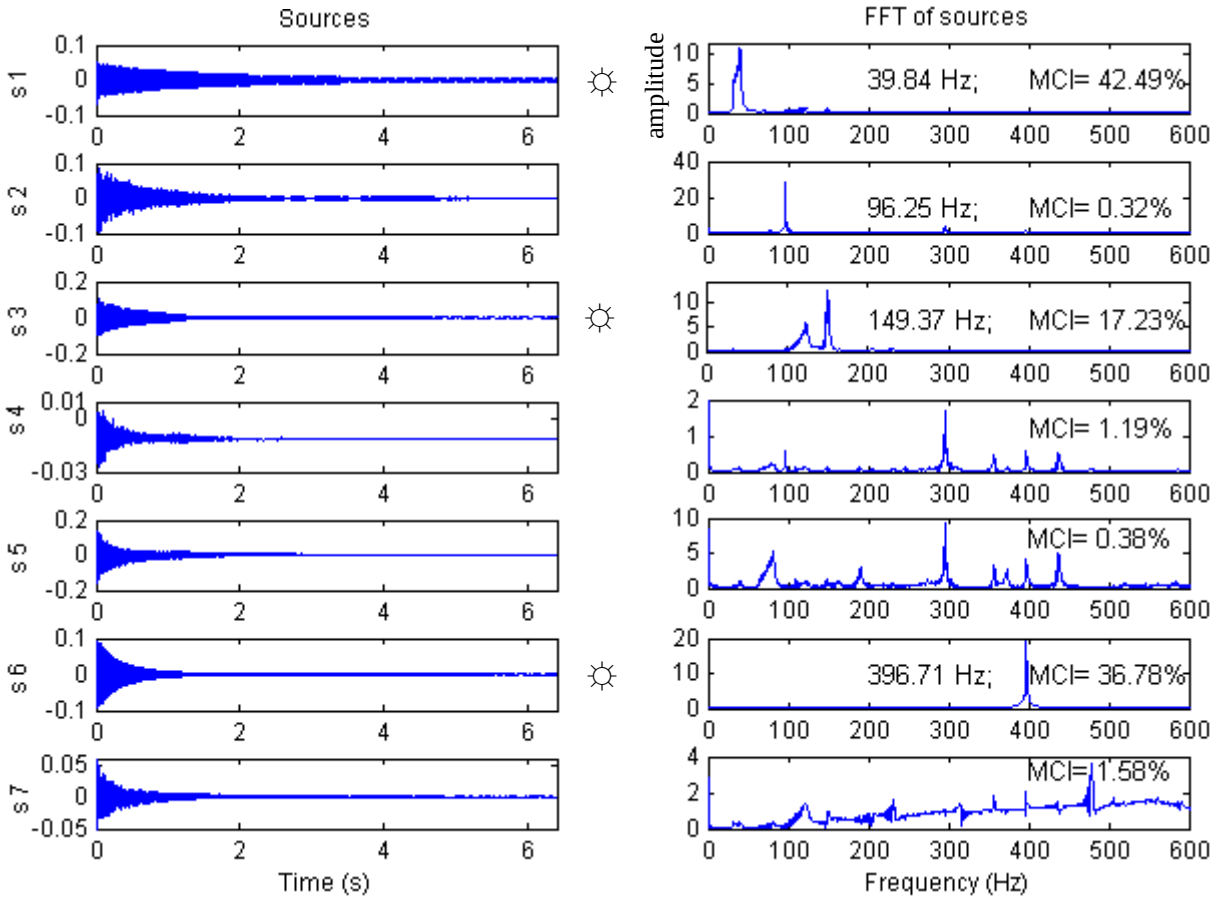

a) *b)*

Figure 3.14: Sources (*a*) and their FFT (*b*) identified by SOBI for a nonlinear state

❖ ***ESOBI***

Figure 3.15 shows that ESOBI is successful in providing 'monochrome' sources in the interested frequency range. In this example, 35 block rows were used to construct the Hankel matrix. The sources are sorted in ascending order of frequencies so that the harmonic of f_1 corresponds to source s_2; the remaining components correspond to f_1, f_2 and f_3 respectively.

The corresponding columns in the mixing matrix **A** give deformation shapes of the structure. Modes 1 and 2 are shown in Figure 3.16 for the linear state (maximum displacement of 0.1 mm) and for the nonlinear state (maximum displacement of 1.4 mm) respectively. The distinction between those two states is less clear in Figure 2.30 based on the Wavelet Transform. The third mode at about 400 Hz is not influenced by the nonlinearity and thus is not presented. The deformation shape corresponding to the 3^{rd} harmonic of the 1^{st} frequency is plotted in Figure 3.17. It is worth noting that this shape looks like the 2^{nd} mode, which explains why this harmonic merges considerably with the second frequency in the SOBI source s_3 (Figure 3.14).

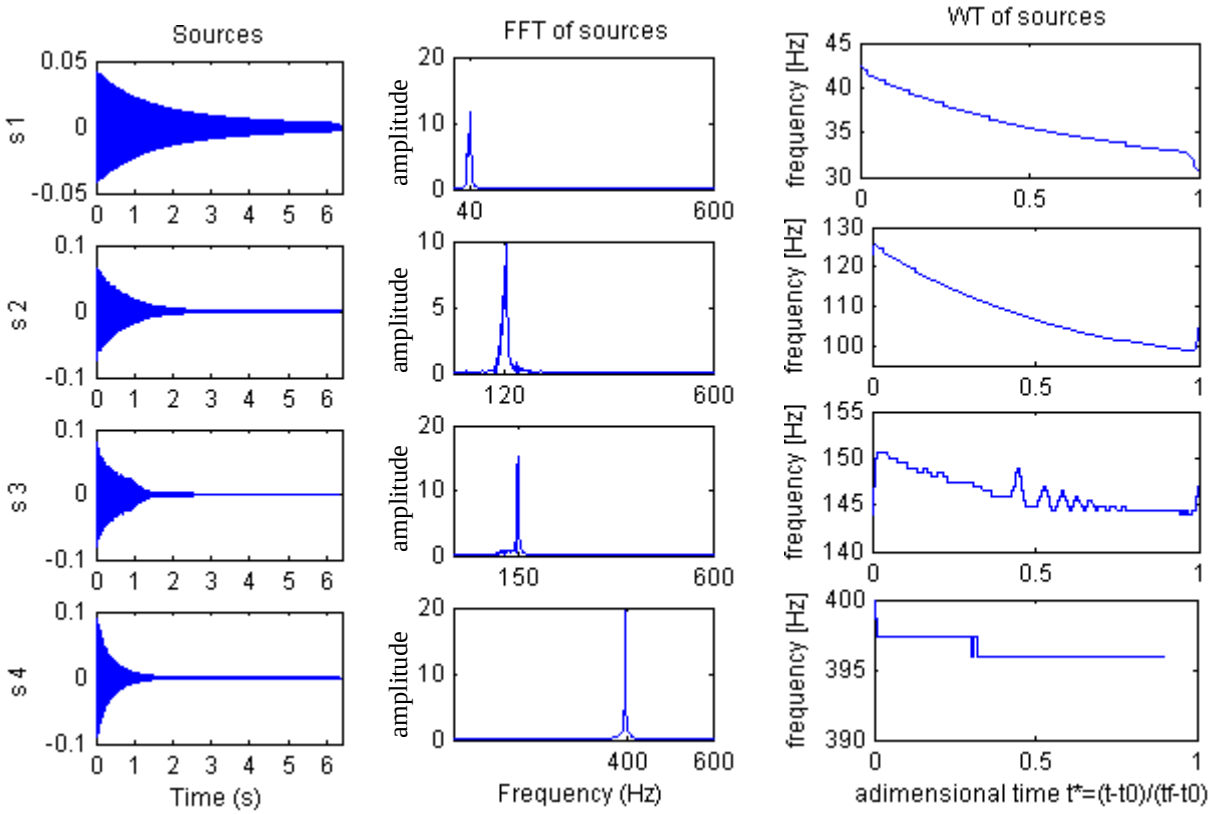

Figure 3.15: Sources and their characteristics identified by ESOBI for the nonlinear state

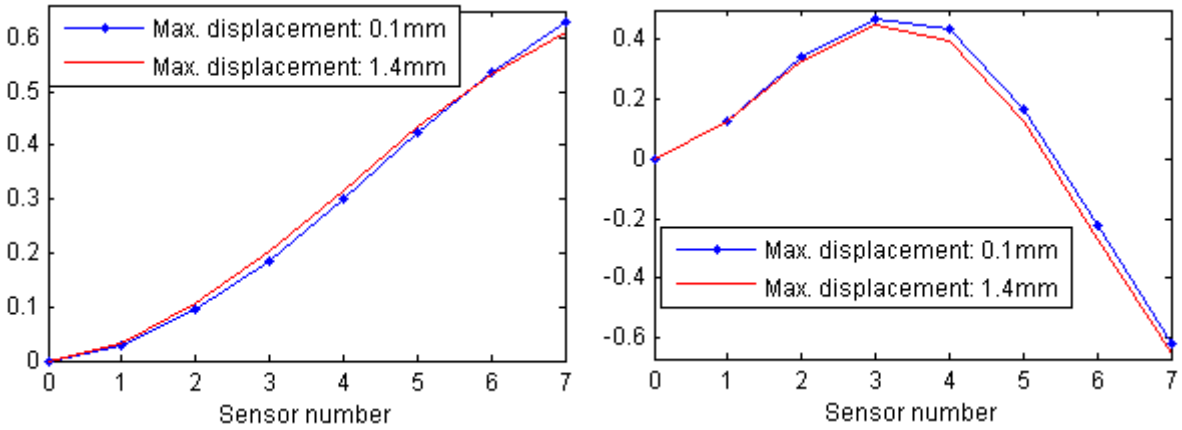

Figure 3.16: Deformation shapes corresponding to the first two frequencies, according to 2 levels of nonlinearity

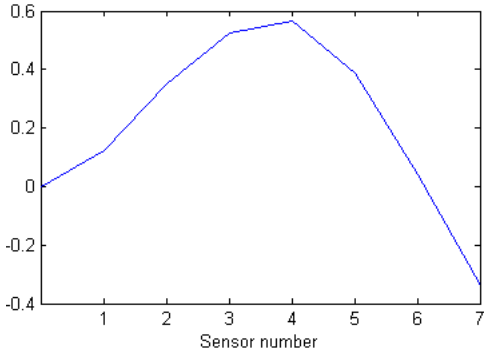

Figure 3.17: Deformation shape corresponding to the 3rd harmonic of the first frequency

❖ ***Nonlinearity detection based on the concept of subspace angle***

As the identification by SOBI fails when the behavior of the structure becomes nonlinear, only ESOBI is considered in this section. As determined previously, the reference subspace for the linear state contains three basic modes corresponding to the frequencies 31.8; 143.1 and 394.8 Hz. In Figure 3.18, the angles are represented in terms of the maximal displacement measured at the end of the beam. The first tests correspond to the linear state of the structure for which the maximal displacements is less than 0.1 mm. The last five tests correspond to levels L1-L5 reported in § 2.5.2.

In Figure 3.18*a*, all the sensors are considered to determine the subspace angle index. In Figure 3.18*b*, only one sensor (sensor n° 7) is used. These results show that ESOBI is able to detect the onset of nonlinearity.

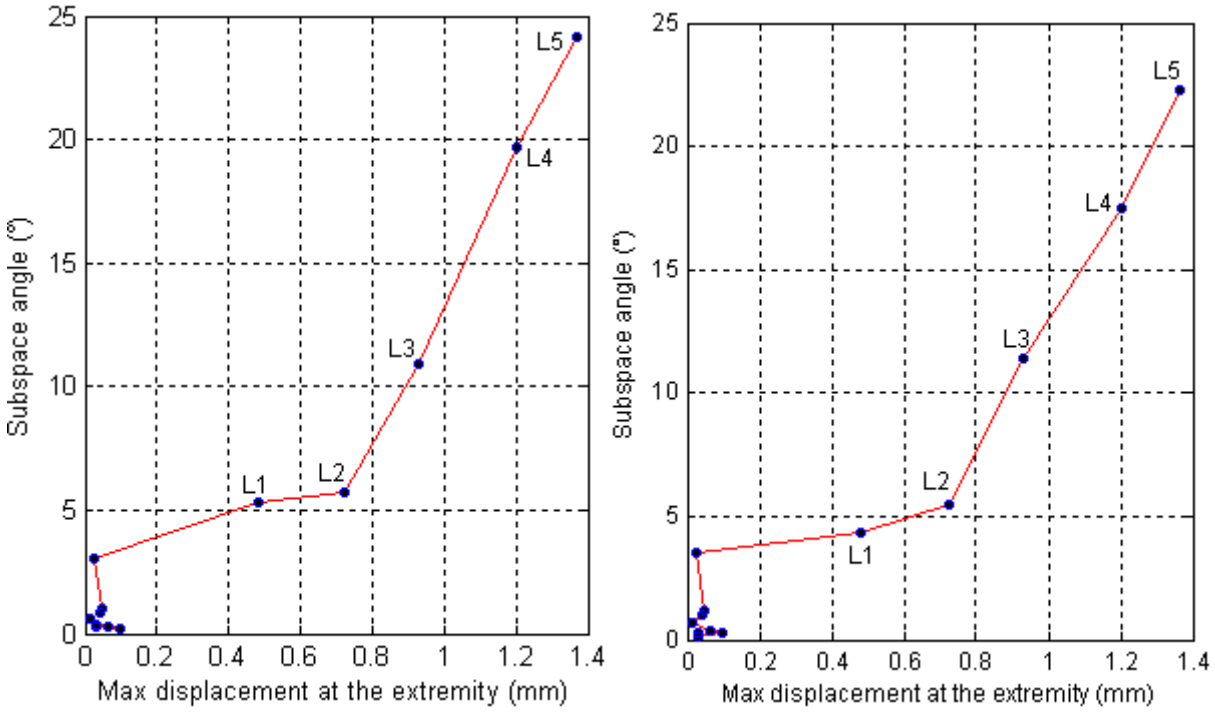

a) with full range of sensors *b) with only one sensor*

Figure 3.18: Detection by ESOBI

❖ ***ESOBI with time-lag calibration***

When SOBI and ESOBI are applied on the whole history of the data, they provide a single set of modal characteristics. It is then necessary to resort to the Wavelet transform to determine the instantaneous frequencies of the identified sources. However, it is also possible to observe the non-stationary behavior of the structure thanks to the following technique proposed for the ESOBI process. It consists in adjusting the time-lag between successive block rows to construct the data-driven Hankel matrix. In equation (3.17), block rows are shifted by one time sample. The time-shift can be extended to several intervals, i.e. the data matrix is assembled in the following way:

$$\mathbf{H}_{1,2i}^{\Delta} = \begin{bmatrix} \mathbf{x}_1 & \mathbf{x}_2 & \cdots & \cdots & \mathbf{x}_j \\ \mathbf{x}_{1+\Delta} & \mathbf{x}_{2+\Delta} & \cdots & \cdots & \mathbf{x}_{j+\Delta} \\ \cdots & \cdots & \cdots & \cdots & \cdots \\ \mathbf{x}_{1+(i-1)\Delta} & \mathbf{x}_{2+(i-1)\Delta} & \cdots & \cdots & \mathbf{x}_{j+(i-1)\Delta} \\ \mathbf{x}_{1+i\Delta} & \mathbf{x}_{2+i\Delta} & \cdots & \cdots & \mathbf{x}_{j+i\Delta} \\ \mathbf{x}_{1+(i+1)\Delta} & \mathbf{x}_{2+(i+1)\Delta} & \cdots & \cdots & \mathbf{x}_{j+(i+1)\Delta} \\ \cdots & \cdots & \cdots & \cdots & \cdots \\ \mathbf{x}_{1+(2i-1)\Delta} & \mathbf{x}_{2+(2i-1)\Delta} & \cdots & \cdots & \mathbf{x}_{j+(2i-1)\Delta} \end{bmatrix} \tag{3.23}$$

where $\Delta > 1$ and $j = N - (2i-1)\Delta$.

By choosing an adequate number of time-lags to represent the time distinction between the block rows (so that the modulation of the dynamic responses is better exhibited), the data matrix in (3.23) facilitates the analysis of signals involving time-varied dynamic states. In this way, ESOBI becomes able to treat non-stationary data.

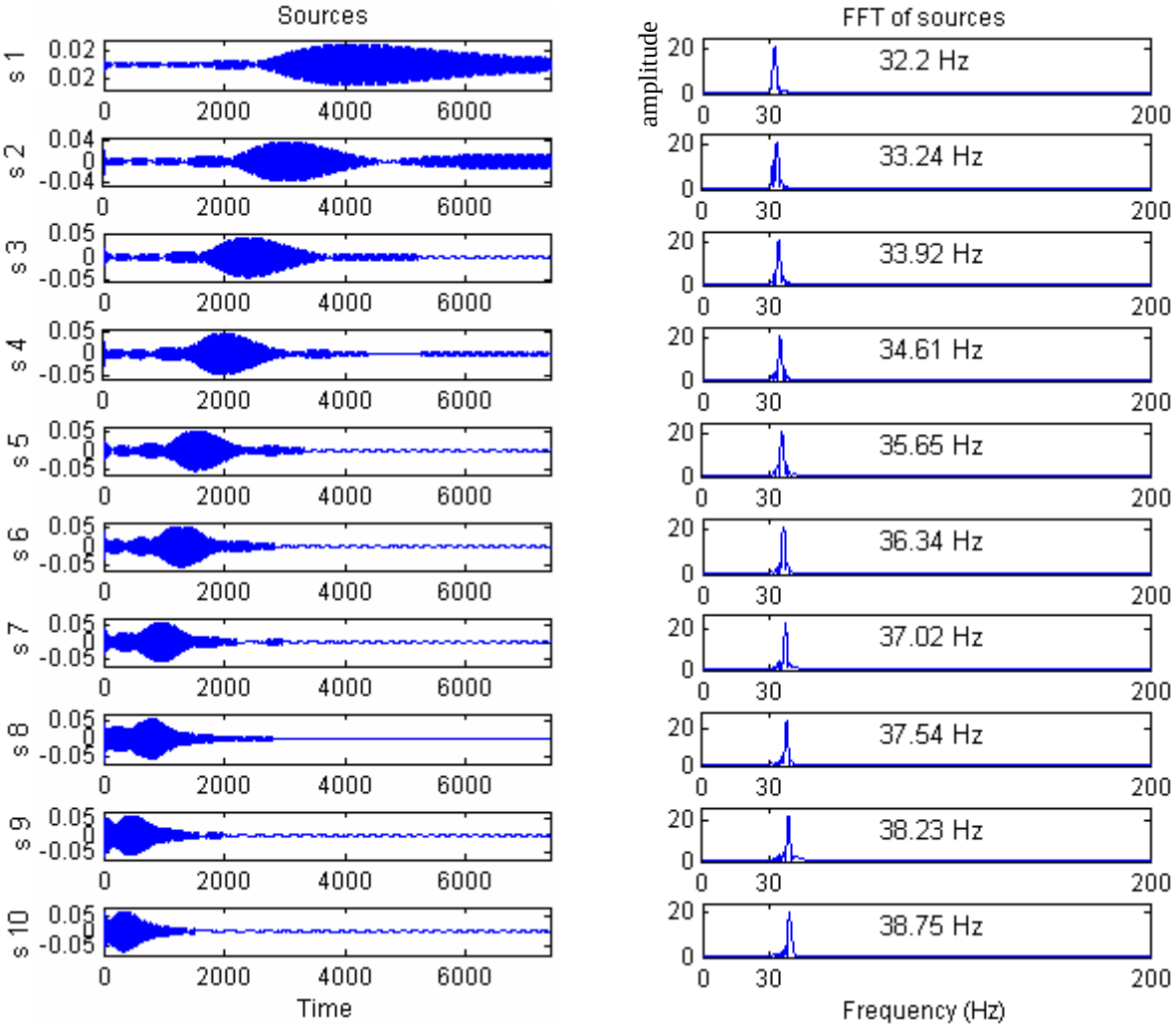

Figure 3.19: Sources of nonlinear behavior and their FFT according to the 1st linear mode, by ESOBI with $\Delta = 40$

Figure 3.19 presents identified sources and their FFTs corresponding to the first mode. In this case, the blocks rows are shifted by 40 time samples, i.e. 0.0313 second. It can be observed that each source appears at different instants: sources of higher frequency are active at earlier times and vice-versa. The deformation shapes corresponding to some identified sources are presented in Figure 3.20, which can also indicate varied levels of nonlinearity during the measured period. Similar results are presented for the second mode in Figures 3.21 and 3.22.

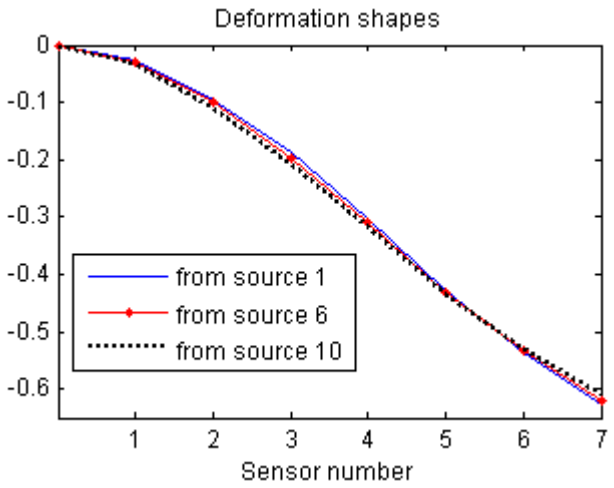

Figure 3.20: Deformation shapes according to some sources in Figure 3.19

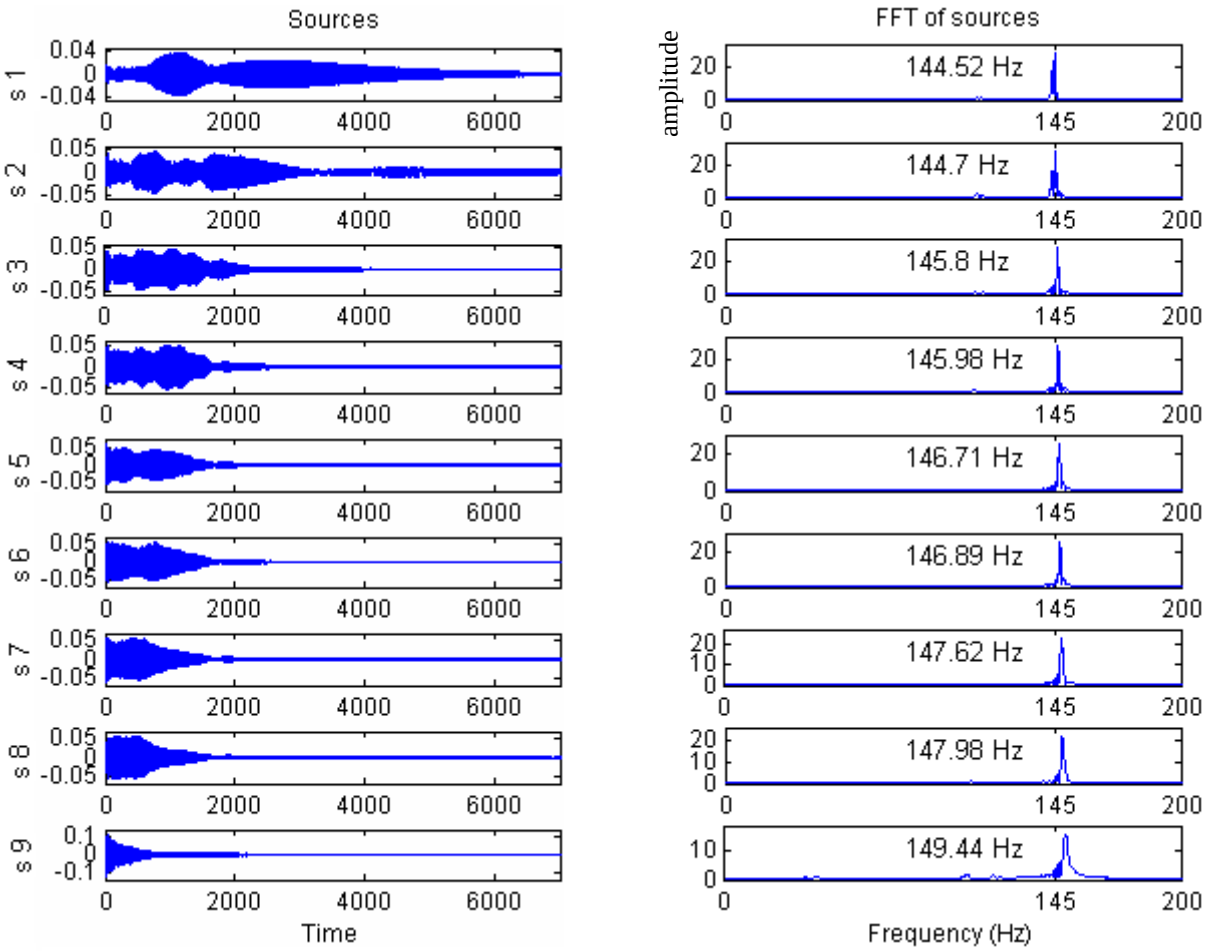

Figure 3.21: Sources according to the 2^{nd} linear mode and their FFT, by ESOBI with $\Delta = 40$

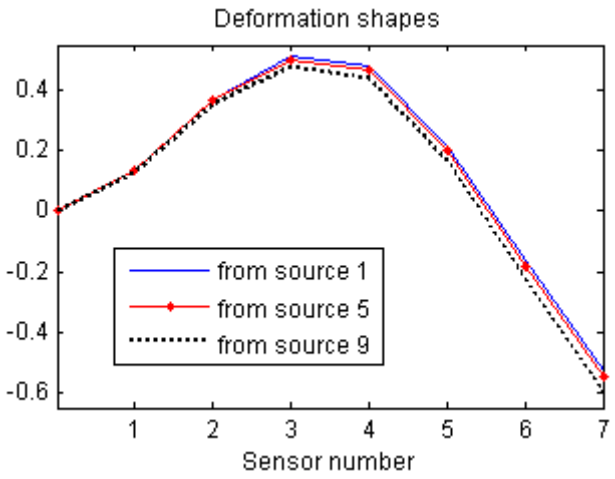

Figure 3.22: Deformation shapes according to some sources in Figure 3.21

3.6.3 Experiments on a nonlinear structure (random excitation)

We first consider the nonlinear beam submitted to a low excitation level (as reported in Figure 2.36). The application of SOBI gives the results shown in Figure 3.23. Even if the sources are quite separated, some other components of very weak energy are present. The application of ESOBI allows to improve the results as shown in Figure 3.24.

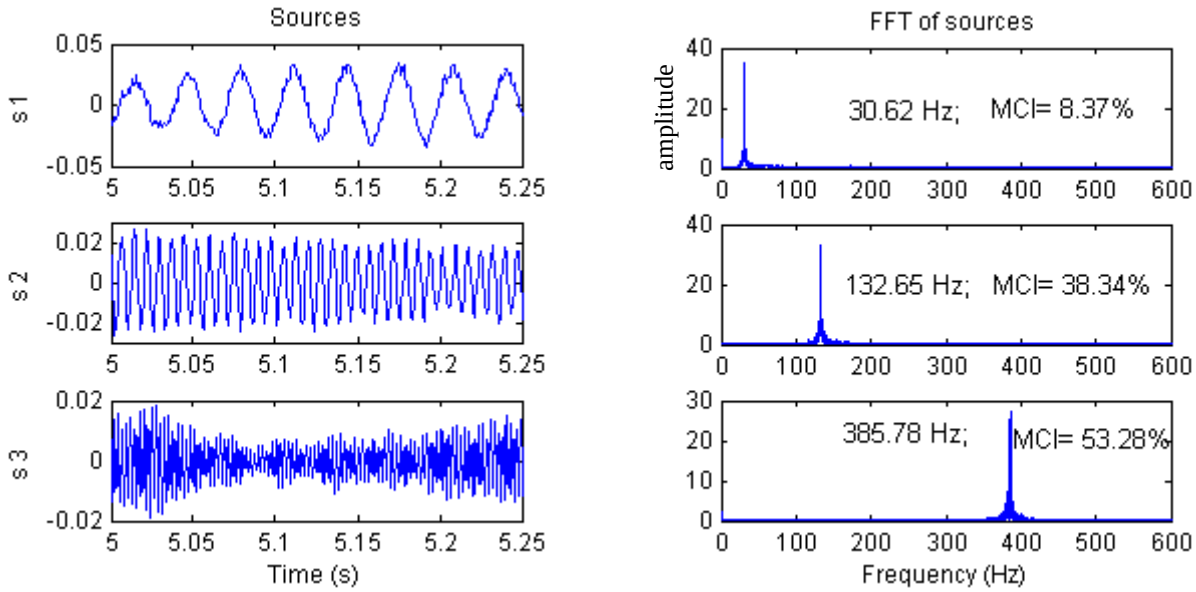

Figure 3.23: Sources and their FFTs identified by SOBI for low excitation

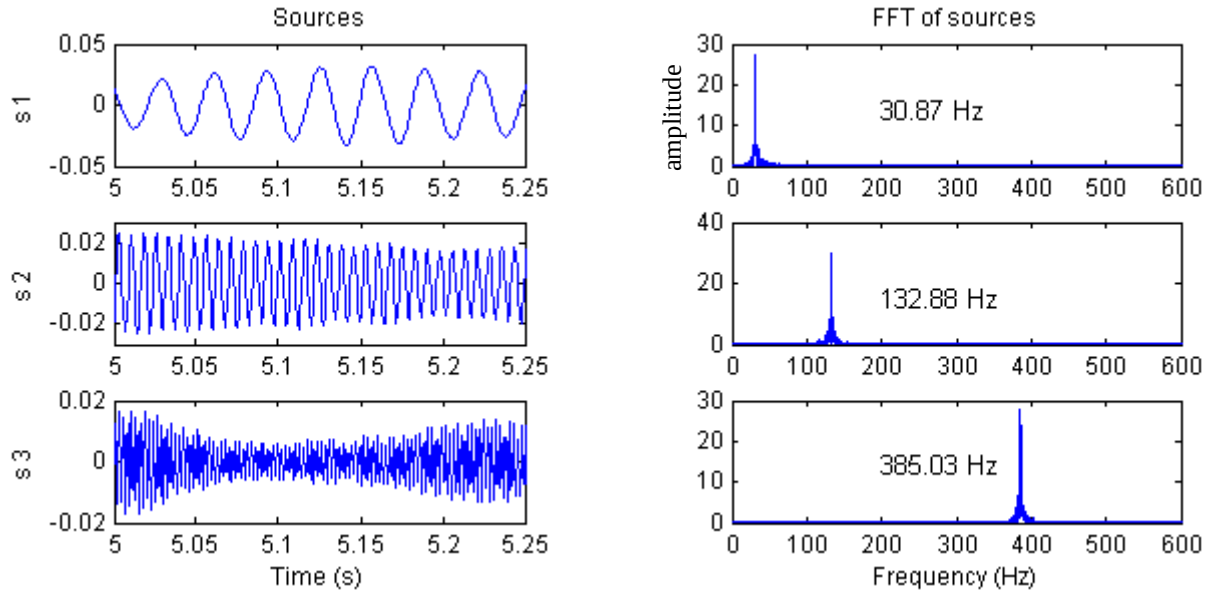

Figure 3.24: Sources and their FFTs identified by ESOBI for low excitation

Results obtained with a higher level of excitation (as reported in Figure 2.37) are shown in Figures 3.25 and 3.26 for SOBI and ESOBI respectively. It can be observed that the problem of mixing is more serious for SOBI. Fortunately, ESOBI appears to be still robust in this case because it cleans up noisy components around the main frequency. As the vibration amplitude of the beam varies in a quite large band, the first and second sources obtained do not show a single spectral component. For example, f_1 presents some peaks in the frequency range from 32.5 to 38 Hz; f_2 from 133.5 to 136 Hz and f_3 appears as unchanged. For the sake of completeness, the WT of sources s_1 and s_2 is given in Figure 3.27.

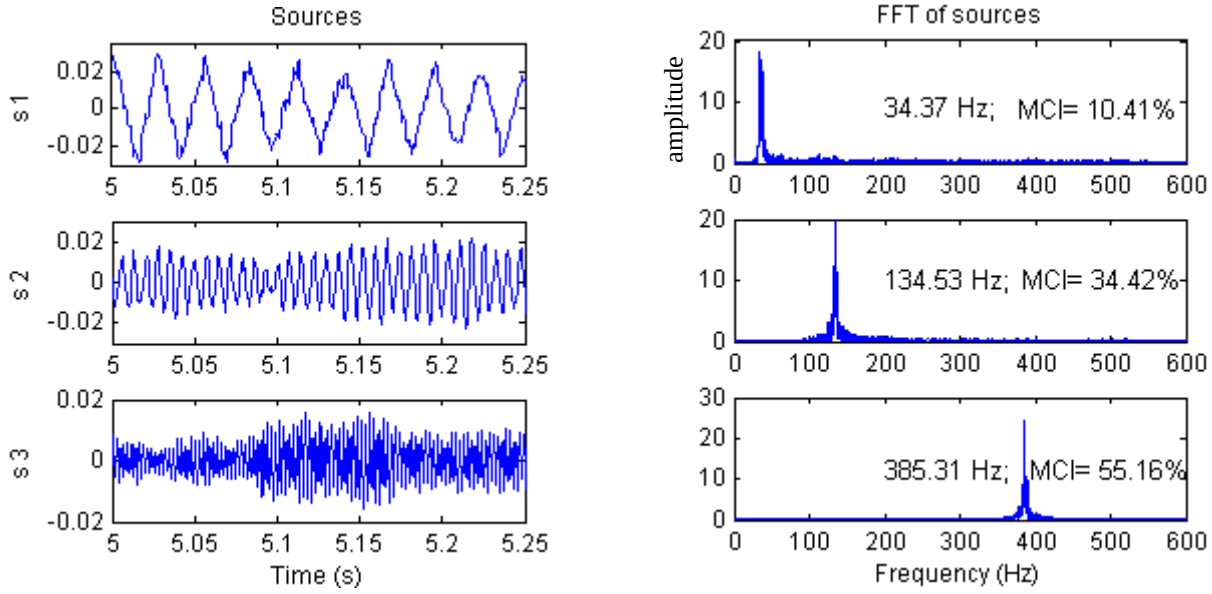

Figure 3.25: Sources and their FFTs identified by SOBI for high excitation

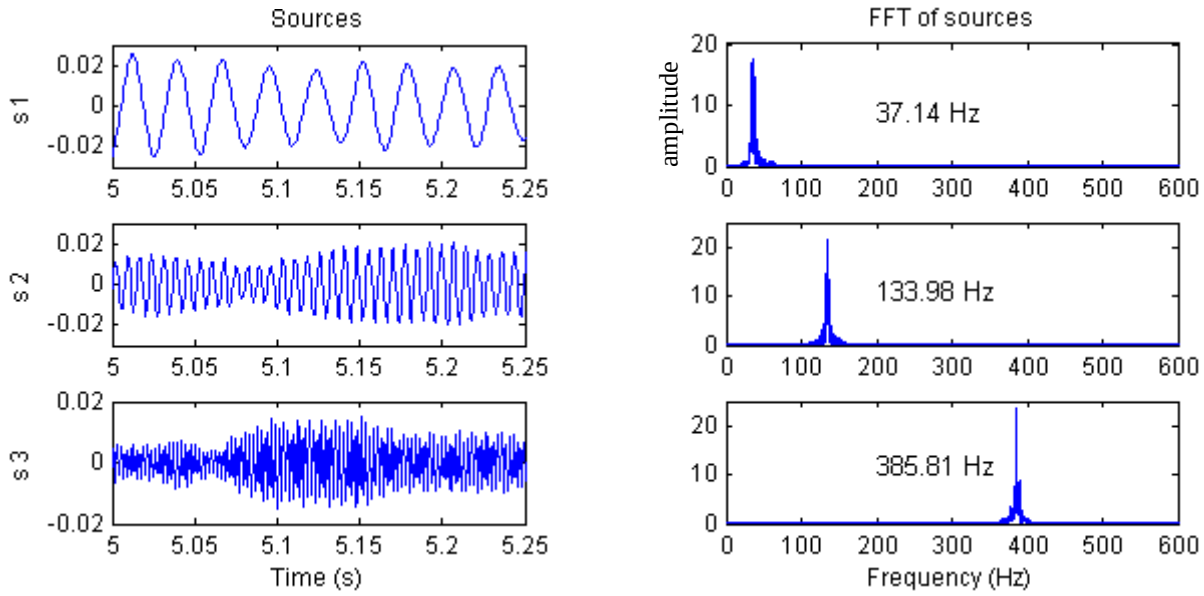

Figure 3.26: Sources and their FFTs identified by ESOBI for high excitation

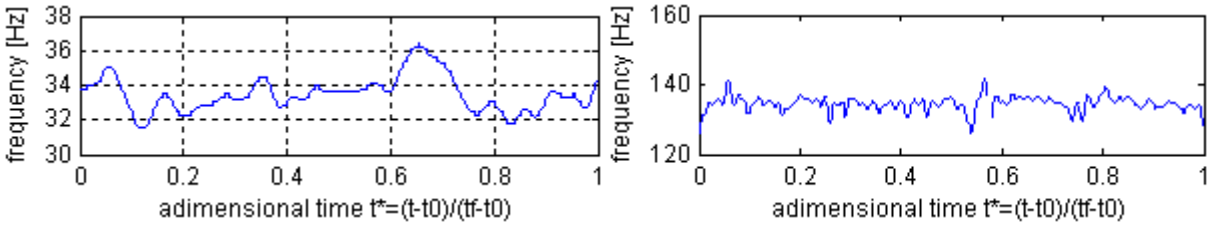

Figure 3.27: WT of sources s_1 and s_2 respectively

Figure 3.28 gives ESOBI deformation shapes according to the first two frequencies for two levels of excitation.

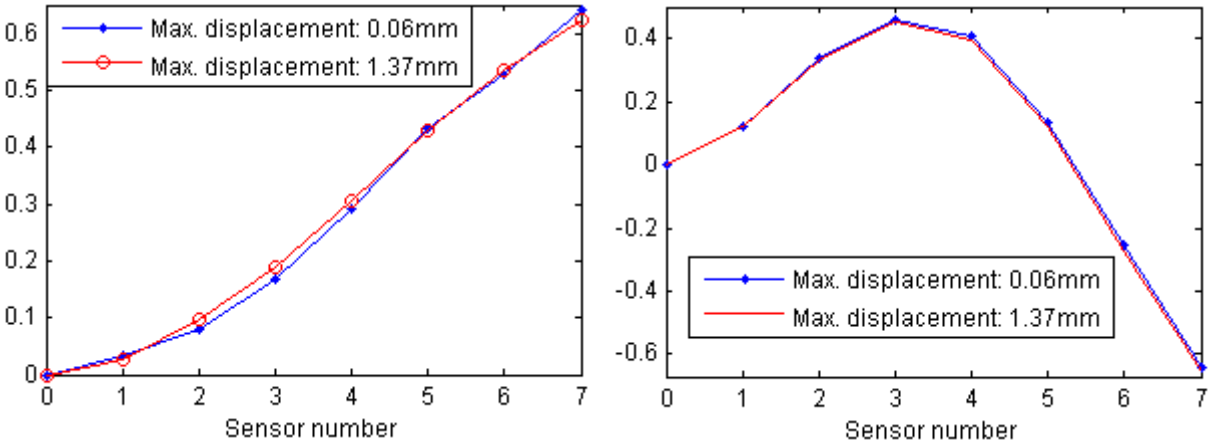

a) the 1st deformation shape *b) the 2nd deformation shape*

Figure 3.28: ESOBI deformation shapes corresponding to the first two sources, according to 2 levels of nonlinearity

❖ ***Nonlinearity detection based on the concept of subspace angle***

Using ESOBI, we examine some different levels of random excitation which active various degrees of nonlinearity in the beam. Figure 3.29*a* gives the subspace angles in function of the root-mean-square (RMS) displacement measured at the end of the beam. This figure shows that the degree of the nonlinearity is well revealed by ESOBI in the case of random responses.

If only one sensor is used as illustrated in Figure 3.29*b*, the method is also able to achieve the detection.

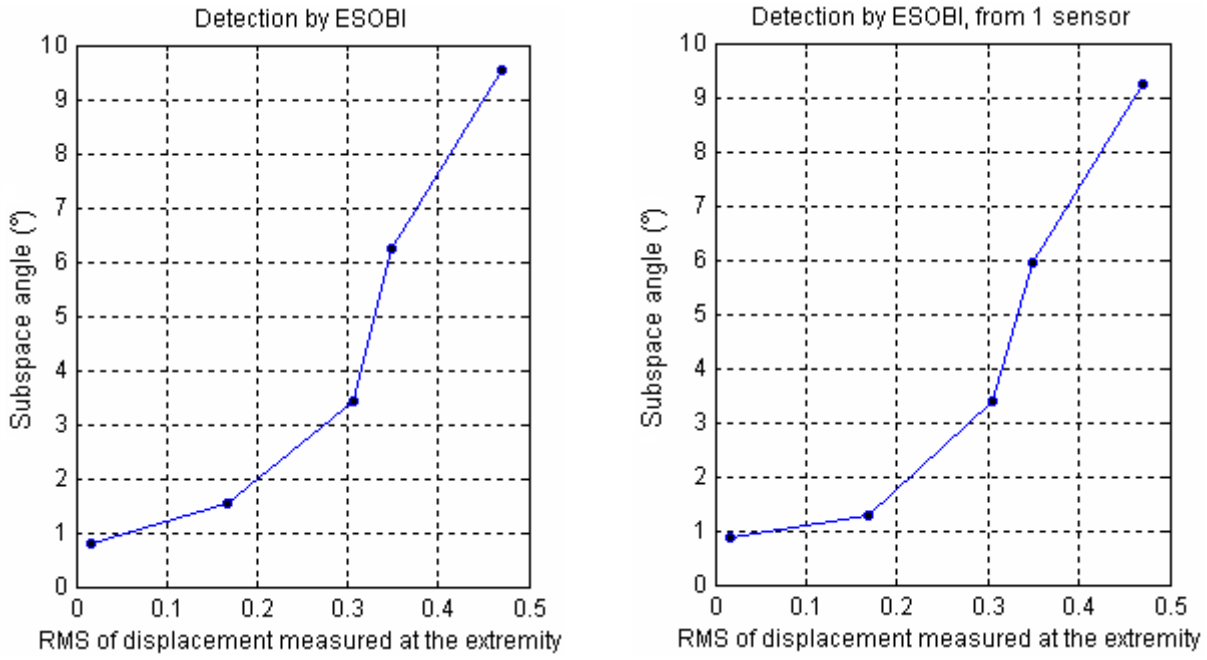

a) with full range of sensors *b) with only one sensor*

Figure 3.29: Detection by ESOBI with all measurements (*a*) and with one sensor (*b*)

3.7 Concluding remarks

SOBI is well known as a modal identification method in the literature. It is appreciated because of its accuracy combined with its low computational cost and also because the selection of the model order is quite automatic. The accuracy of the method can be visually assessed by inspecting the modal responses (sources) in both the time and the frequency domains. However, many works have shown that the main drawback of SOBI is the need of a number of sensors greater or equal to the number of active modes (Poncelet *et al.* (2007)[101], McNeil and Zimmerman (2008)[79], Rainieri and Fabbrocino (2010)[105]).

In this chapter, SOBI was applied to study the change in the dynamic behavior of structures under different conditions. Two types of problems were considered: the detection of damage and the onset of nonlinear behavior. The examined examples show that the identification and detection problem by SOBI may be improved efficiently with the help of the Hankel matrices. Using ESOBI, the detection remains still possible even if the number of available sensors is small. The BMID technique which is an extension of SOBI has been proven to be very robust and suitable for structures with general damping.

When time signals are non-stationary, the Wavelet Transform provides a better mathematical framework for the analysis. However, ESOBI can also give helpful information at a low computational cost as the time transformation of the dynamic responses can be observed by enlarging the time-lag between block rows of the data matrix or by the application of WT on the sources.

Chapter 4

Fault Detection Based on Kernel Principal Component Analysis

4.1 Introduction

Principal Component Analysis (PCA) is a linear multivariable statistical method that can be used for damage detection of structures or fault diagnosis in mechanical systems. In Section 1.3, the advantages and limitations of PCA have been discussed along with its derivations for nonlinear contexts. This chapter focuses on a nonlinear extension of PCA named Kernel Principal Component Analysis (KPCA) which authorizes features such that the relation between variables is nonlinear.

The KPCA method is "flexible" in the sense that different kernel functions may be used to better fit the testing data. KPCA shows a remarkable advantage with respect to other nonlinear PCA approaches because the method does not require nonlinear optimization. In the beginning, KPCA has interested many scientists in the domain of image processing (Schölkopf *et al.* (1998)[115], (1999)[116] and Kim *et al.* (2005)[58]). These researchers showed that KPCA may reveal more advantageous than other techniques such as PCA or Wavelet transform etc. in encoding image structure. In the last five years, KPCA has been introduced in other fields of research as reported in Chapter 1 (chemical domain, industrial machine or mechanical system) and has shown its ability in the monitoring of nonlinear process.

We deal here with the detection problem in mechanical structures where nonlinearity appears implicitly in the responses. The content of the chapter is as follows. First the PCA method is described briefly as it constitutes the background of the proposed method. Next, the kernel PCA method is introduced to deal with nonlinear systems and the definition of the covariance-driven block Hankel matrix is recalled. The method is illustrated on experimental examples and applications. The first example is the detection of the nonlinearity onset in the beam with geometric nonlinearity. The next examples consist in detecting damage in a rotating device and in controlling quality of welded joints. Two types of index are used for the detection: (1)-the subspace angle and (2)-the Hotelling's T^2 statistics and the Q-statistics.

4.2 Principal Component Analysis

Let us suppose that a dynamical system characterized by a set of vibration features identified at time t_k is represented by the m-dimensional vector $\mathbf{x}_k$ $(k = 1,..., N)$, where N is

the number of samplings. All the samples are collected in the observation matrix $\mathbf{X} \in \Re^{m \times N}$. In general, PCA involves a data normalization procedure, which leads to a set of variables with zero-mean and unitary standard deviation (Yan *et al.* (2005)[134]), i.e.

$$\mathbf{x}_k^{\text{norm}} = \frac{\left(\mathbf{x}_k - \bar{\mathbf{x}}\right)}{\sigma_x} \tag{4.1}$$

where $\bar{\mathbf{x}}$ and σ_x are the mean and standard deviation of each dataset, respectively:

$$\bar{\mathbf{x}} = \frac{1}{N}\sum_{k=1}^{N}\mathbf{x}_k \; ; \qquad \sigma_x = \sqrt{\frac{1}{N}\sum_{k=1}^{N}\left(\mathbf{x}_k - \bar{\mathbf{x}}\right)^2}$$

PCA, known as Karhunen-Loève transform or Proper Orthogonal Decomposition (POD) (Krzanowski (2000)[63]), provides a linear mapping of data from the original dimension *m* to a lower dimension *p* using the transformation:

$$\mathbf{Y} = \mathbf{T}\mathbf{X} \tag{4.2}$$

where $\mathbf{Y} \in \Re^{p \times N}$ is called the score matrix and $\mathbf{T} \in \Re^{p \times m}$ the loading matrix. The dimension *p* represents the physical order of the system or the number of principal components which affect the vibration features. The loading matrix may be found from the main *p* eigenvectors of the covariance matrix of **X**. In practice, PCA is often computed by Singular Value Decomposition of the covariance matrix, i.e.

$$\mathbf{X}\mathbf{X}^{\mathrm{T}} = \mathbf{U}\boldsymbol{\Sigma}\mathbf{U}^{\mathrm{T}} \tag{4.3}$$

where **U** is an orthonormal matrix whose columns define the principal components (PCs) and form a subspace spanning the data. The energy of those PCs is represented by the corresponding singular values on the diagonal of matrix $\boldsymbol{\Sigma}$. The singular values are written in decreasing order:

$$\text{diag}(\boldsymbol{\Sigma}) = \left(\sigma_1, \sigma_2, ..., \sigma_p, \sigma_{p+1}, ..., \sigma_m\right) \text{ with } \sigma_1 \geq \sigma_2 \geq ... \geq \sigma_p \; \sigma_{p+1} \geq ... \geq \sigma_m \to 0 \tag{4.4}$$

The order *p* of the system is determined by selecting the first *p* singular values in $\boldsymbol{\Sigma}$ which have a significant magnitude ('energy') as described in De Boe (2003)[17]. However, the remaining singular values do not entirely equal zero due to noise or to nonlinear effects.

It is worth noting that, under some assumptions, PCs in matrix **U** may represent the vibration modes of the system (Feeny and Kappagantu (1998)[26], Feeny and Liang (2002)[27]).

- **Selection of active principal components**

The quality of the representation of the observation space through PCs can by quantified by inspection of the values σ_j. The percentage of energy associated to a PC is defined by De Boe (2003)[17]:

$$\text{Energy}_j = \frac{\sigma_j}{\sum_{i=1}^{m}\sigma_i} \tag{4.5}$$

One can fix a threshold in terms of cumulated energies: $\sum_{i=1}^{j}\text{Energy}_i$ (j = 1,…, m) which allows to select the effective number of PCs that is required for a good representation of the

observation matrix **X**. In practice, a cumulated energy of 75% to 95% is generally adequate for the selection of the active PCs.

4.3 Kernel Principal Component Analysis

The definitions and formulation presented here follow closely the ones described in Schölkopf *et al.* (1999)[116] and He *et al.* (2007)[40].

The key idea of KPCA is first to define a nonlinear map $\mathbf{x}_k \mapsto \Phi(\mathbf{x}_k)$ with $\mathbf{x}_k \in \Re^m, (k = 1,..., N)$ which represents a high dimensional feature space *F*, and then to apply PCA to the data in space *F*.

Suppose that the mapped data are centered, i.e. $\sum_{i=1}^{N} \Phi(\mathbf{x}_i) = 0$, then the covariance matrix in the space *F* is:

$$\mathbf{C} = \frac{1}{N} \sum_{i=1}^{N} \Phi(\mathbf{x}_i) \Phi(\mathbf{x}_i)^{\mathrm{T}} \tag{4.6}$$

Principal components may be next extracted by solving the eigenvalue equation:

$$\lambda \mathbf{V} = \mathbf{C}\mathbf{V} \tag{4.7}$$

All the eigensolutions **V** with $\lambda \neq 0$ must lie in the subspace spanned by $\Phi(\mathbf{x}_1),..., \Phi(\mathbf{x}_N)$, which means that coefficients α_i, $(i = 1,..., N)$ exist such that:

$$\mathbf{V} = \sum_{i=1}^{N} \alpha_i \Phi(\mathbf{x}_i) \tag{4.8}$$

Pre-multiplication of equation (4.7) by $\Phi(\mathbf{x}_k)^{\mathrm{T}}$ gives:

$$\lambda \, \Phi(\mathbf{x}_k)^{\mathrm{T}} \, \mathbf{V} = \Phi(\mathbf{x}_k)^{\mathrm{T}} \, \mathbf{C}\mathbf{V} \qquad (k = 1,..., N) \tag{4.9}$$

Let us define the kernel matrix **K** of dimension $N \times N$ such that:

$$K(\mathbf{x}_i, \mathbf{x}_j) = K_{ij} = \Phi(\mathbf{x}_i)^{\mathrm{T}} \, \Phi(\mathbf{x}_j) \tag{4.10}$$

Mercer's theorem of functional analysis implies that the kernel function is a continuous kernel of a positive integral operator. For instance, the following kernel functions proposed by Vapnik (1995)[127], may be used:

- *polynomial kernel,*

  $K(\mathbf{x}_i, \mathbf{x}_j) = (\mathbf{x}_i^{\mathrm{T}} \, \mathbf{x}_j + 1)^d$, where *d* is a positive integer (4.11)

- *radial basis function (RBF),*

$$K(\mathbf{x}_i, \mathbf{x}_j) = \exp\left(-\frac{\left\| \mathbf{x}_i - \mathbf{x}_j \right\|^2}{2\sigma^2} \right) \tag{4.12}$$

  where $2\sigma^2 = w$ is the width of the Gaussian kernel

- *sigmoid kernel,*

$$K(\mathbf{x}_i, \mathbf{x}_j) = \tanh\left((\mathbf{x}_i^{\mathrm{T}}\ \mathbf{x}_j) + b\right) \tag{4.13}$$

It is worth noting that in general, the above kernel functions give similar results if appropriate parameters are chosen. The sigmoid kernel does not always satisfy Mercer's theorem. The RBF can present advantages owing to its flexibility in choosing the associated parameter. For example, the width of the Gaussian kernel can be very small (<1) or quite large. Contrarily the polynomial kernel requires a positive integer for the exponent. In the present work, we use the polynomial and RBF kernels.

The combination of equations (4.6) to (4.10) yields:

$$N\lambda\boldsymbol{\alpha} = \mathbf{K}\boldsymbol{\alpha} \tag{4.14}$$

where $\boldsymbol{\alpha}$ is the column vector collecting the coefficients $\alpha_1,...,\alpha_N$. Similarly to PCA, KPCA requires the data points $\Phi(\mathbf{x}_i)$, $(i = 1,..., N)$ to be centered in the feature space *F*, so that the centered kernel matrix is defined:

$$\tilde{K}_{ij} = \left(K - 1_N K - K 1_N + 1_N K 1_N\right)_{ij} \tag{4.15}$$

where 1_N is a matrix of dimension $N \times N$ of which $\left(1_N\right)_{ij} = 1/N$. Further details may be found in Reference Schölkopf *et al.* (1998)[115].

Replacing **K** in equation (4.14) by $\tilde{\mathbf{K}}$, the eigenvalue equation may be rewritten by:

$$N\lambda\boldsymbol{\alpha} = \tilde{\mathbf{K}}\boldsymbol{\alpha} \tag{4.16}$$

The eigenvalues associated to the eigenvectors of $\tilde{\mathbf{K}}$: $\boldsymbol{\alpha}_1, \boldsymbol{\alpha}_2, ..., \boldsymbol{\alpha}_N$, are ordered in descending order $\lambda_1 \geq \lambda_2 \geq ... \geq \lambda_p \square\ \lambda_{p+1} \geq ... \geq \lambda_N \to 0$ where $\lambda_{p+1}, ..., \lambda_N$ are negligible with respect to the first *p* eigenvalues (suppose that $\Phi \neq 0$). Normalization of $\boldsymbol{\alpha}_1, ..., \boldsymbol{\alpha}_p$ results from the normalization of the corresponding vectors in *F*, i.e.

$$\mathbf{V}_k^{\mathrm{T}}\ \mathbf{V}_k = 1 \qquad (k = 1, ..., p) \tag{4.17}$$

According to equations (4.8), (4.10) and (4.16), it follows that:

$$\lambda_k \left(\boldsymbol{\alpha}_k^{\mathrm{T}}\ \boldsymbol{\alpha}_k\right) = 1 \tag{4.18}$$

The eigenvectors identified in the feature space *F* can be considered as kernel principal components (KPCs), which characterize the dynamical system in each working state.

Note that, since the number of eigenvectors (i.e. nonlinear PCs) is the same as the number of samples, it is higher than the number of (linear) PCs given by PCA. The KPCA method is termed "nonlinear" since the feature mapping in the space *F* is achieved by a nonlinear function (Eqs. 4.11-4.13). Thanks to that property, extracted KPCs should be able to reflect nonlinear or high order features which allow the representation and classification of varied states. For example, Figure 4.1 represents the PCA and KPCA features and the corresponding principal eigenvector **V** in the bi-dimensional input space. According to Schölkopf *et al.* (1999)[116], KPCA has the capability to use more nonlinear PCs than PCA, which allows to collect more structural features rather than noise.

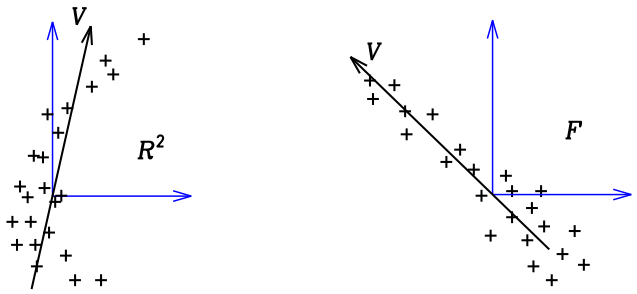

a) Linear PCA $K(\mathbf{x},\mathbf{y})=(\mathbf{x}^{\mathrm{T}}\mathbf{y})$ *b) Kernel PCA, e.g.* $K(\mathbf{x},\mathbf{y})=\exp\left(-\|\mathbf{x}-\mathbf{y}\|^2/w\right)$

Figure 4.1: a) PCA in the input space, b) KPCA as a linear PCA in the high dimensional feature space *F*, that joins nonlinearly with the input space by Φ.

It is also of interest to note that the method enables to characterize a dynamic behavior even if the number of measurements is small (for example, if only one sensor is available, as illustrated later).

The kernel principal component representation $\mathbf{u}_k$ may be obtained by projecting all the observations onto the direction of the *k* th eigenvector:

$$\mathbf{u}_k=\mathbf{V}_k^{\mathrm{T}}\tilde{\Phi}(\mathbf{x}_i)=\sum_{v=1}^{N}\alpha_{k,v}\tilde{K}\left(\mathbf{x}_v,\mathbf{x}_i\right)\qquad(i=1,...,N)\tag{4.19}$$

where $\mathbf{V}_k$ is the *k* th eigenvector of equation (4.7), $\mathbf{x}_i$ indicates a sample feature vector in the data matrix and *N* is number of all samples.

Let us consider now a set of current test data $\mathbf{t}_1,\ldots,\mathbf{t}_L$, the kernel matrix $L\times N$ and its centering are defined by $K^{test}(\mathbf{t}_i,\mathbf{x}_j)=\Phi(\mathbf{t}_i)^{\mathrm{T}}\Phi(\mathbf{x}_j)$ and:

$$\tilde{\mathbf{K}}^{test}=\mathbf{K}^{test}-1'_N\mathbf{K}-\mathbf{K}^{test}1_N+1'_N\mathbf{K}1_N,$$

where $1'_N$ is a $L\times N$ matrix of which all entries are $1/N$. With a set of data $\mathbf{t}_r$, one can extract a nonlinear component by:

$$\mathbf{u}_k=\mathbf{V}_k^{\mathrm{T}}\tilde{\Phi}(\mathbf{t}_r)=\sum_{v=1}^{N}\alpha_{k,v}\tilde{K}^{test}\left(\mathbf{x}_v,\mathbf{t}_r\right)\qquad(r=1,...,L)\tag{4.20}$$

Difficulties are encountered with KPCA when solving the eigenvalue problem if the dimension of matrix **K** is high. Two problems arise: the difficulty to find out good eigensolutions and the computation time. A quite efficient algorithm, called Kernel Hebbian Algorithm has been proposed in Kim *et al.* (2005)[58] to get an approximate solution. To avoid high-dimensional eigenvalue problem, He *et al.* (2007)[40] extracted nonlinear features from raw time series data and then performed KPCA on those nonlinear features. Cui *et al.* (2008)[14] carried out a feature vector selection scheme. In this study, the covariance-driven Hankel matrix is proposed to assemble the data matrix for the purpose of resolving the above drawback.

4.4 KPCA and the covariance-driven block Hankel matrix

The covariance-driven block Hankel matrix is defined as:

$$\mathbf{X} = \begin{bmatrix} \mathbf{\Delta}_1 & \mathbf{\Delta}_2 & \dots & \dots & \mathbf{\Delta}_c \\ \mathbf{\Delta}_2 & \mathbf{\Delta}_3 & \dots & \dots & \mathbf{\Delta}_{c+1} \\ \dots & \dots & \dots & \dots & \dots \\ \mathbf{\Delta}_r & \mathbf{\Delta}_{r+1} & \dots & \dots & \mathbf{\Delta}_{r+c-1} \end{bmatrix} \qquad (c \geq r) \tag{4.21}$$

where r, c are user-defined parameters ($r = c$ in this study) and $\mathbf{\Delta}_i$ represents the output covariance matrix defined by:

$$\mathbf{\Delta}_i = \frac{1}{N-i} \sum_{k=1}^{N-i} \mathbf{x}_{k+i} \, \mathbf{x}_k^{\mathrm{T}} \qquad (0 \leq i < N-1) \tag{4.22}$$

where $\mathbf{x}_k$ is the measurement vector at time step k and N is the number of sampling points.

The covariance-driven Hankel matrix characterizes the dynamics of the analyzed signals and has been used for modal identification and damage detection. If the covariance-driven Hankel matrix is considered as the input data matrix for the KPCA procedure and the number of block rows r is equal to the number of block columns c, so $\mathbf{X}$ is a square matrix. Its size is determined by the product of the number of blocks and the dimension m of vector $\mathbf{x}_k$.

4.5 KPCA monitoring using the concept of subspace angle and statistics

In the previous chapters, the detection problem has been achieved using the concept of subspace angle between subspaces constructed by mode-shape vectors (in WT, SOBI) or by principal component vectors (in PCA). In KPCA, the same procedure may be applied by constructing the subspace with the kernel principal components (KPCs) which characterize the feature space F. This section presents other detection indexes based on statistics.

A popular method for dynamical monitoring is the chart of Hotelling's T^2 statistics and the Q-statistics, also known as the squared prediction error (SPE) which are depicted in Figure 4.2. T^2 measures the distance in the principal subspace (spanned by the first p PCs), whereas SPE characterizes the distance in the residual subspace (spanned by the remaining PCs, which is orthogonal to the principal subspace). In general, the use of T^2 and SPE distances in detection methods based on linear PCs (PCA method) is expressed in terms of *Mahalanobis* and *Euclidian distances*, respectively. The only difference here is that those indexes are built in the feature subspace in order to exploit the results of KPCA. The following formulation proposed by Lee *et al*. (2004)[69] shows interesting because of its simplicity.

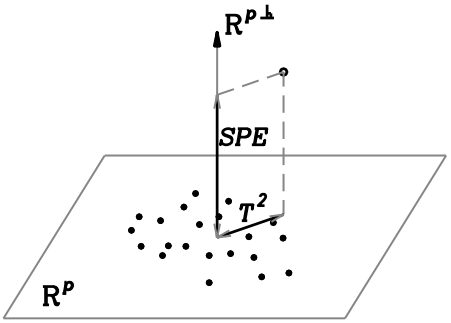

Figure 4.2: Graphical description of the two monitoring statistics T^2 and SPE

T^2 measures the variation within the model subspace, which is the sum of the normalized squared scores defined as:

$$T^2 = \left[\mathbf{u}_1, ..., \mathbf{u}_p\right] \mathbf{\Lambda}^{-1} \left[\mathbf{u}_1, ..., \mathbf{u}_p\right]^{\mathrm{T}} \tag{4.23}$$

where $\mathbf{u}_k$ is obtained by (4.19) or (4.20) and $\mathbf{\Lambda}^{-1}$ is the diagonal matrix of the inverse of the eigenvalues associated with p retained PCs. Assuming that the scores have a multivariate normal distribution, the confidence limit for T^2 is calculated using the Snedecor's F distribution (F-distribution) as:

$$T^2_{p,N,\alpha} \approx \frac{p(N-1)}{N-p} F_{p,N-p,\alpha} \tag{4.24}$$

where N is the number of samples in the model or the size of the covariance-driven block Hankel matrix if this matrix is used. $F_{p,N-p,\alpha}$ is a F-distribution with degrees of freedom p and N-p with level of significance α [69].

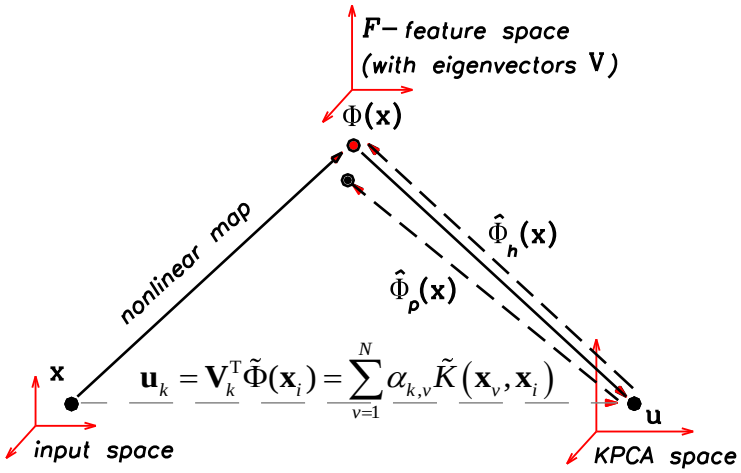

Figure 4.3: Conceptual diagram of KPCA

In the KPCA method, the observations are not analyzed in the input space, but in the feature space F. The measure of goodness of fit of a sample to the PCA model was suggested through a simple calculation of SPE in the feature space F. The conceptual framework of the KPCA method is shown schematically in Figure 4.3 (Romdhani *et al.* (1999)[110]). First, an input vector $\mathbf{x}$ is projected using a nonlinear mapping Φ in a high-dimensional feature space F. Then linear PCA is performed in this feature space and gives score values $\mathbf{u}_k$ in a lower p-dimensional KPCA space (eq. (4.19) or (4.20)). A feature vector $\Phi(\mathbf{x})$ may be reconstructed from $\mathbf{u}_k$ by projecting $\mathbf{u}_k$ into the feature space via $\mathbf{V}_k$ and it results in a reconstruction with p PCs in the feature space: $\hat{\Phi}_p(\mathbf{x}) = \sum_{k=1}^{p} \mathbf{u}_k \mathbf{V}_k$. The SPE statistics in the feature space is defined by: $\mathrm{SPE} = \left\|\Phi(\mathbf{x}) - \hat{\Phi}_p(\mathbf{x})\right\|^2$. $\Phi(\mathbf{x})$ is just identical to $\hat{\Phi}_h(\mathbf{x}) = \sum_{k=1}^{h} \mathbf{u}_k \mathbf{V}_k$ where h is the number of nonzero eigenvalues generated from (4.14) among all the N eigenvalues. The SPE can be deduced from the expression:

$$\begin{aligned}
\mathrm{SPE} &= \left\|\Phi(\mathbf{x}) - \hat{\Phi}_p(\mathbf{x})\right\|^2 = \left\|\hat{\Phi}_h(\mathbf{x}) - \hat{\Phi}_p(\mathbf{x})\right\|^2 = \hat{\Phi}_h(\mathbf{x})^{\mathrm{T}} \hat{\Phi}_h(\mathbf{x}) - 2\hat{\Phi}_h(\mathbf{x})^{\mathrm{T}} \hat{\Phi}_p(\mathbf{x}) + \hat{\Phi}_p(\mathbf{x})^{\mathrm{T}} \hat{\Phi}_p(\mathbf{x}) \\
&= \sum_{k=1}^{h} \mathbf{u}_k \mathbf{V}_k^{\mathrm{T}} \sum_{i=1}^{h} \mathbf{u}_i \mathbf{V}_i - 2\sum_{k=1}^{h} \mathbf{u}_k \mathbf{V}_k^{\mathrm{T}} \sum_{i=1}^{p} \mathbf{u}_i \mathbf{V}_i + \sum_{k=1}^{p} \mathbf{u}_k \mathbf{V}_k^{\mathrm{T}} \sum_{i=1}^{p} \mathbf{u}_i \mathbf{V}_i \\
&= \sum_{k=1}^{h} \mathbf{u}_k^2 - 2\sum_{k=1}^{p} \mathbf{u}_k^2 + \sum_{k=1}^{p} \mathbf{u}_k^2 = \sum_{k=1}^{h} \mathbf{u}_k^2 - \sum_{k=1}^{p} \mathbf{u}_k^2
\end{aligned} \tag{4.25}$$

as $\mathbf{V}_k^{\mathrm{T}}\mathbf{V}_i = 1$ when $k=i$, otherwise $\mathbf{V}_k^{\mathrm{T}}\mathbf{V}_i = 0$.

Assuming that the prediction errors are normally distributed, the confidence limit for the SPE is calculated by fitting a weighted χ^2-distribution and is given by:

$$\mathrm{SPE}_\alpha \approx \frac{v}{2e}\chi^2_{2e^2/v,\alpha} \tag{4.26}$$

where e and v are the estimated mean and variance of the SPE, respectively (Nomikos and MacGregor (1995)[93]). This approximating distribution works well even in cases for which the errors do not follow a Gaussian distribution.

Given the T^2 and SPE statistics as well as their control limits, we can compute outlier statistics to count how many prediction errors (represented in percentage) overpass the control limits for each state. In normal condition, i.e. without damage, the outlier statistics of the current data should be similar to the statistics of the reference state. Conversely, the feature subspace associated with a damage state should present significant changes from the reference state. Thus, the outlier statistics in this case should increase clearly. In order to compare the statistics related to two different sets of data, the ratio S_d/S_r is also computed, where d and r denote the damage and the reference states respectively, S describes the average SPE or T^2 in according statistic measurements. While $S_d/S_r \rightarrow 1$ indicates a normal state, a higher value of this ratio can indicates the occurrence of a possible damage.

In the following, the KPCA-based detection method is illustrated on some examples in which the different indexes (based on the concept of subspace angle and on the T^2 and SPE statistics) are considered.

4.6 Detection of nonlinearity onset

Let us consider again the beam with the geometric nonlinearity presented in Chapters 2 and 3. Now KPCA is used on the experimental data corresponding to the two types of excitation (impact and random).

In this example, KPCA is used with the aim of detecting the onset of nonlinear behavior when the load level is increasing. The detection is first based on the concept of subspace angle and KPCA is compared to the classical PCA. A zero-mean normalization of the measured responses is first performed in order to obtain centered data sets. A mean-variance normalization procedure can be also realized to take into account different working conditions of the system and the variety of sensors. Results based on the T^2 and SPE statistics are presented later.

4.6.1 Impact excitation

Twelve impact tests were performed as reported in Table 4.1. Tests n° 1-7 correspond to the linear behavior of the structure and play the role of false-positive. In tests n° 8-12, the nonlinear behavior of the structure is activated with increasing levels.

For this type of excitation, the nonlinear behavior is the strongest at early stages and vanishes progressively due to the presence of damping. For this reason, we consider responses in the first time interval of [0; 0.5 *s*]. Accelerations measured at the seven locations in Figure 2.27 are used for constructing the observation matrix **X**.

❖ ***PCA-based detection method***

For the sake of comparison, nonlinearity detection is first conducted using PCA and the results are shown in Figure 4.4. As the observation matrix includes seven response vectors, seven principal components (PCs) may be calculated as shown in Figure 4.4*a*. It is observed that PC n°1 concentrates about 70% of the system 'energy' and that, with the first threes PCs, we attaint nearly 100%.

Detection of nonlinearity based on the concept of subspace angle using 1, 2 and 3 PCs respectively is reported in Figure 4.4*b*. The vertical dashed line separates the linear states of the structure (tests 1-7) from the nonlinear states (tests 8-12). Based on the first PC, the detection index gives large angle values for all the tests 8-12 but tests n° 5 and 6 also present high angle values that are just false alarms. By considering 2 PCs in the subspace (which collect nearly 90% of the 'energy'), the detection is considerably improved. In this case, tests in the linear and nonlinear states can be well distinguished. However, if more PCs are included in the subspace, detection fails as noise enters into the PCs extraction process, which deteriorates the quality of the reference subspaces. This is illustrated in Figure 4.4*b* by the result obtained using 3 PCs.

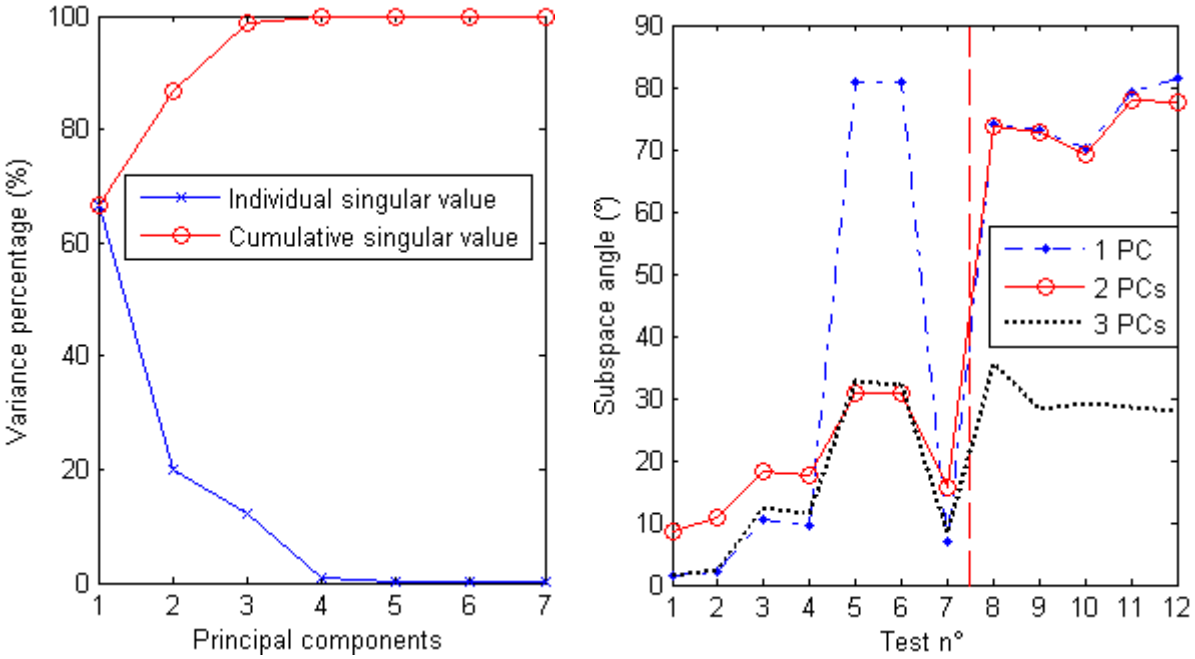

a) Singular-value diagram *b) PCA detection based on the subspace angle*

Figure 4.4: Analysis by PCA

Table 4.1: List of tests according to level of nonlinearity

Test n°	1-7	8	9	10	11	12
Largest displacement (*mm*)	< 0.04	0.48	0.72	0.93	1.20	1.37

According to this example, we may conclude that the PCA-based method is very delicate to use for detecting the onset of nonlinearity in the system.

❖ ***KPCA-based detection method***

KPCA differs from PCA, notably in the number of kernel principal components (KPCs) which is equal to the number N (e.g. of time samples) whereas the number of PCs in the PCA method is equal to the number m of measurement responses. In the KPCA method, the energy distribution of KPCs depends on the parameter chosen in the kernel function. The results shown in Figure 4.5 were achieved with KPCA using the polynomial kernel function with the exponent $d = 2$. The eigenvalue diagram shows that the first seven KPCs capture most of the system energy.

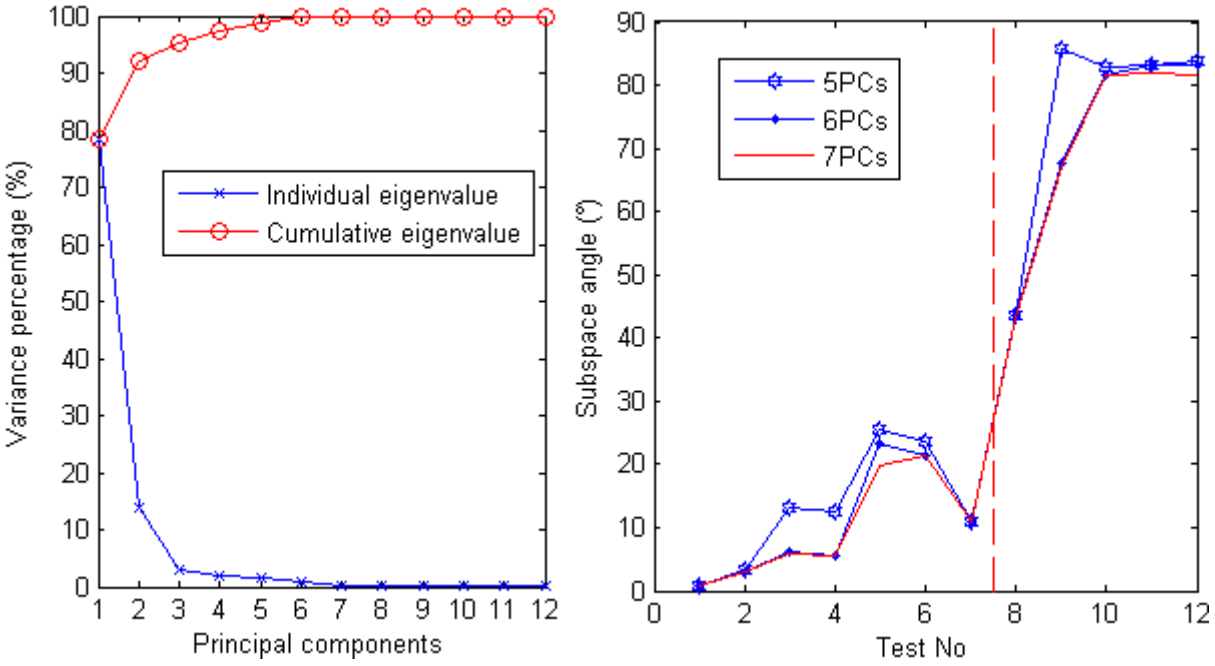

a) Eigenvalue diagram *b) KPCA detection based on the subspace angle*

Figure 4.5: Analysis by KPCA

Note that KPCs do not have any specific physical meanings, as reported in He *et al.* (2007)[40], contrary to PCs in PCA which may represent modal features (e.g. mode-shapes) under certain circumstances [26]. However, KPCs are useful for classifying different dynamic behaviors of the system. To assemble enough effective information, the KPCA method needs to add up a sufficiently large number of KPCs in the subspace. Regarding PCA, as discussed earlier, the quality of the detection may be deteriorated by the use of more and more PCs in the analysis as noise energy is then taken into account and perturbs the procedure. On the other hand, KPCA offers a possibility to redistribute the energy of KPCs, i.e. to regulate the main energy on the first but also on secondary KPCs (as discussed in the next paragraph). In other words, KPCA helps to extract several first representative KPCs and to decline noise which is related mainly to last components. As shown in Figure 4.5*b*, the use of 5 KPCs allows a good detection as the index given by false-positives tests remains low. It is interesting to note that by taking into account more KPCs, the detection is actually performed in a stable manner. In this example, it is optimal with 6 or 7 KPCs. In conclusion, the KPCA-based method looks more effective than the PCA-based method for the detection of the onset of the nonlinear behavior of a system.

❖ ***Discussion on the choice of the kernel parameter***

Kernel parameters (e.g the exponent in the polynomial kernel or the width of the Gaussian kernel) are user-defined quantities and different values of these parameters may produce unequal effects. For illustration, let us consider further two examples by varying the kernel parameters, as shown in Figures 4.6 and 4.7. The comparison between pictures (*a*) of these figures and Figure 4.5*a* reveals clear differences.

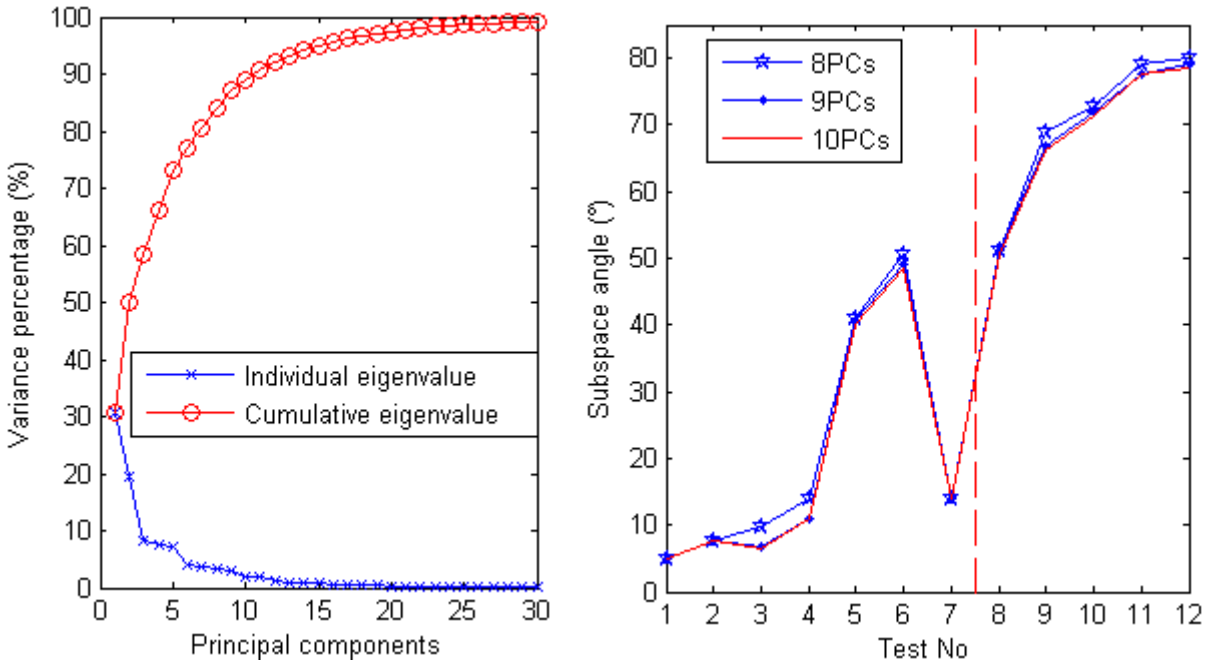

a) Eigenvalue diagram *b) KPCA detection based on the subspace angle*

Figure 4.6: KPCA detection with the width of the Gaussian kernel $w = 4$

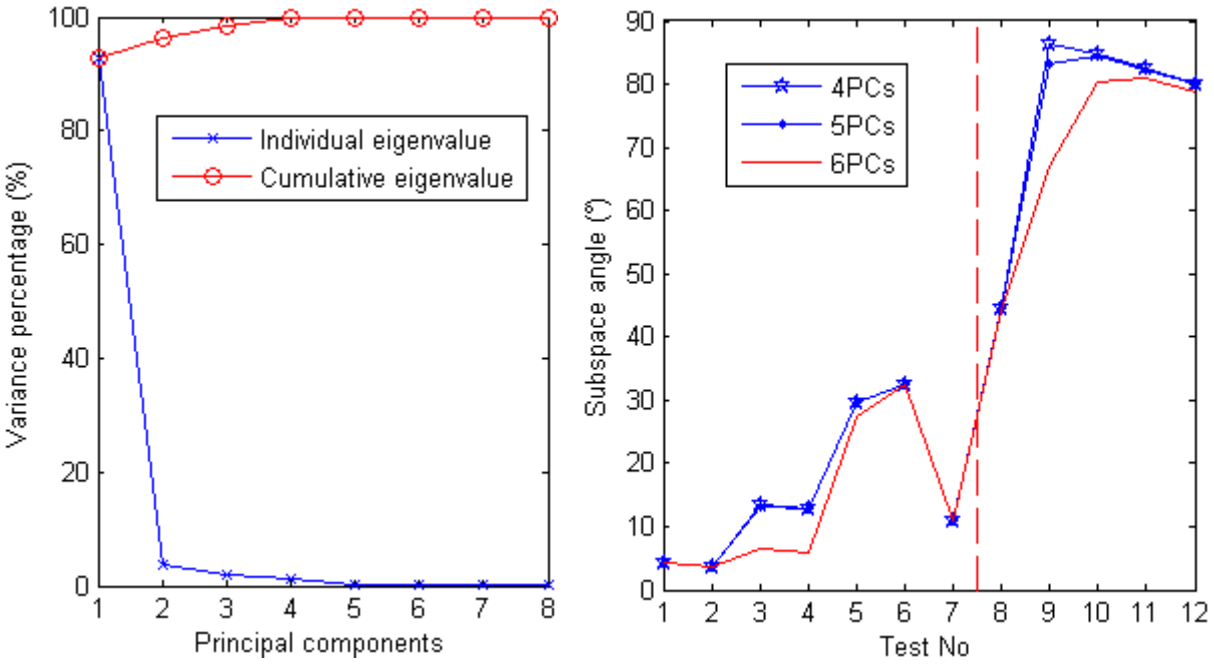

a) Eigenvalue diagram *b) KPCA detection based on the subspace angle*

Figure 4.7: KPCA detection with the width of the Gaussian kernel $w = 35$

It is observed that the variance percentage of the first eigenvalue in Figure 4.5*a* is relatively higher than in Figure 4.6*a*, but on the contrary, it is smaller than in Figure 4.7*a*. When the variance percentage of the first eigenvalue is small as in Figure 4.6, tests n° 9-12 remain well detected but the index of test n° 8 is of the same order of magnitude as is tests n° 5 and 6. On the other hand, when the first eigenvalue concentrates much of the variance percentage (up to more than 90%) as in the case presented in Figure 4.7, detection is still effective even if it is a little less sensitive than in Figure 4.5. For this reason, it is recommended to choose the kernel parameter based on the eigenvalue diagram so that the variance percentage of the first eigenvalues is high enough.

❖ ***Enhanced PCA and KPCA-based detection methods using the Hankel matrix***

The key idea developed here is to build data matrices using the definition of the block Hankel matrices. Thus, PCA and KPCA are applied to this enhanced observation matrix and the concept of subspace angle is again used to detect a change in the dynamic behavior. In the following, letter *E* is used when PCA and KPCA are performed on the block Hankel matrices to refer to the "enhanced" methods, i.e. EPCA and EKPCA respectively.

Results are shown in Figures 4.8 and 4.9 for a number of block rows in the Hankel matrix equal to 10.

Figure 4.8 presents the best result given by the EPCA-based detection method. This result was obtained using 5 PCs extracted from the block Hankel matrix which accumulate about 90% the system energy. It is observed that the onset of nonlinearity is well detected even if angle indexes for tests n° 5 and 6 (false-positive tests) are not so small.

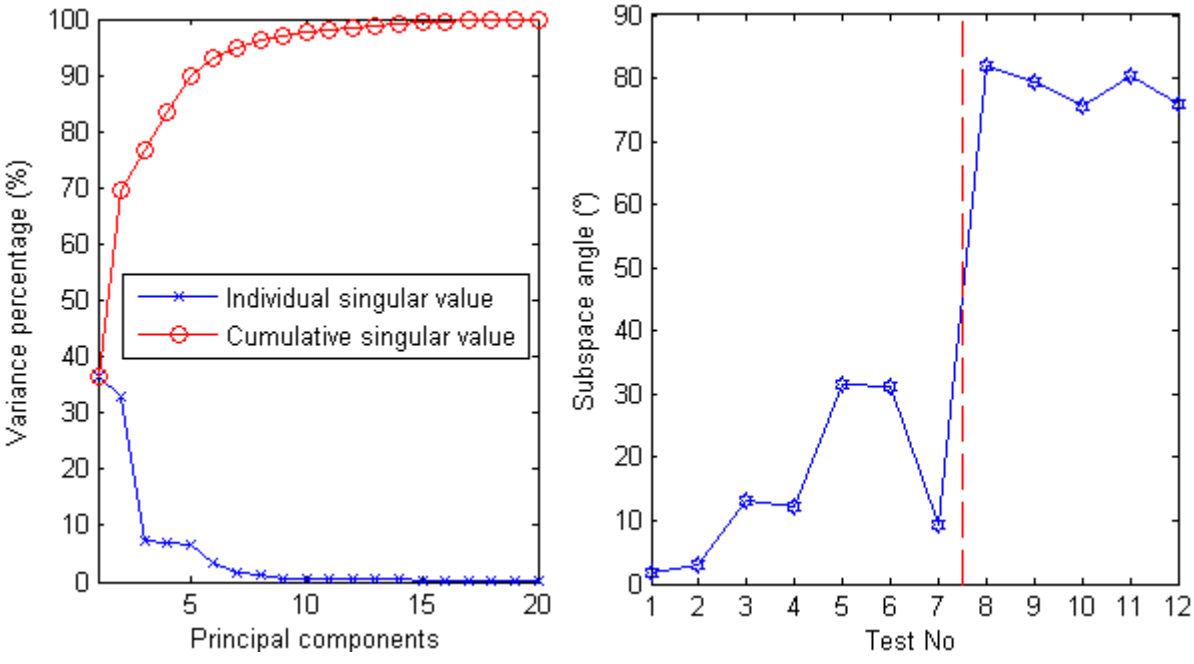

a) Singular-value diagram *b) EPCA detection based on the subspace angle*

Figure 4.8: Analysis by EPCA

EKPCA was performed using the radial basis function as kernel with a width $w = 1100$. As shown in Figure 4.9, detection has improved significantly. The best results are obtained

with 7 or 8 KPCs (up to 95% of the system energy). According to this example, EKPCA enables a clear classification between linear and nonlinear behaviors.

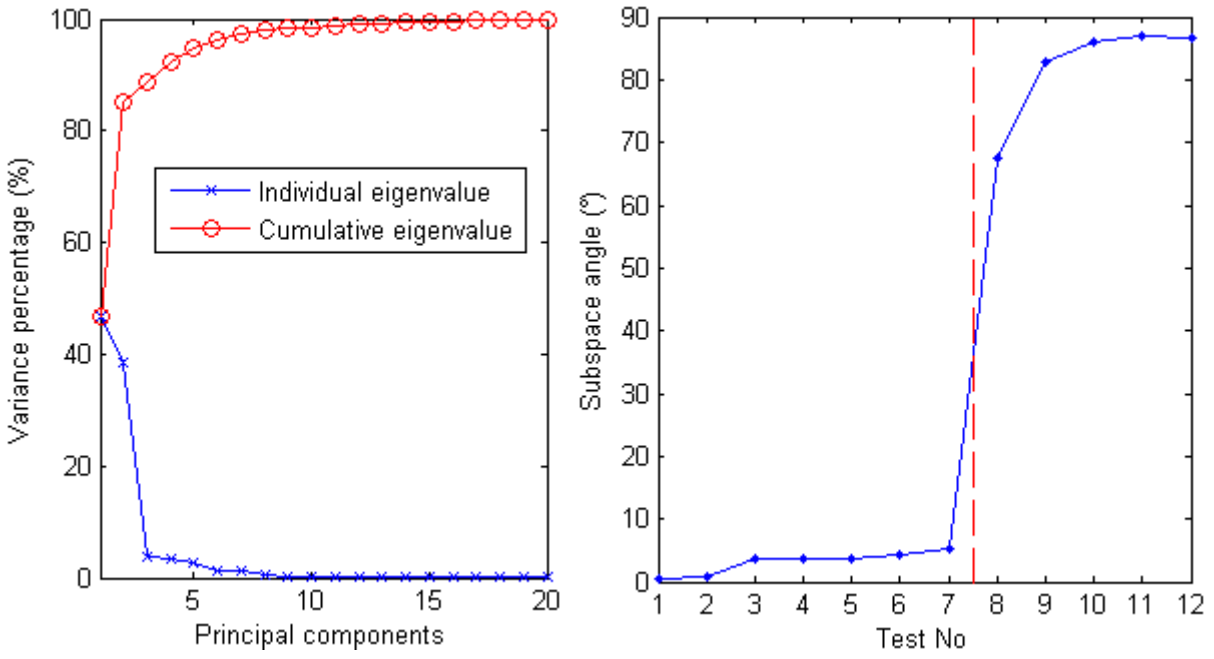

a) Eigenvalue diagram *b) EKPCA detection based on the subspace angle*

Figure 4.9: Analysis by EKPCA

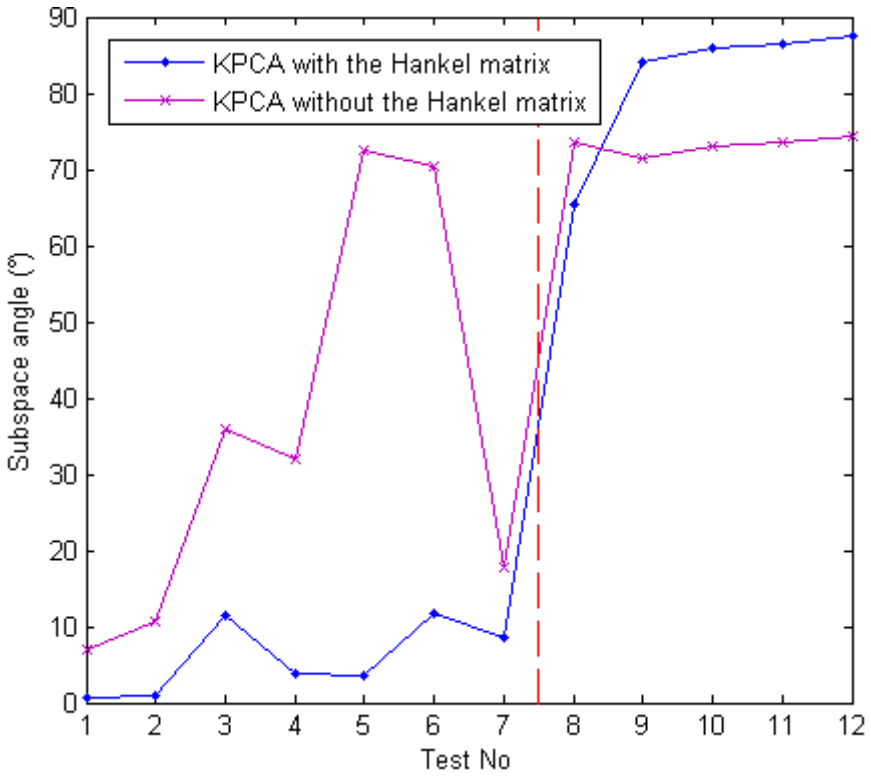

Figure 4.10: KPCA and EKPCA detections by only one sensor

As mentioned earlier, the number of KPCs in KPCA is directly related to the number *N* of time samples and thus, is not conditioned by the number of measured responses. For this

reason, it is always possible to construct a subspace even if only one response signal is available. (Note that it is also the case with PCA if the block Hankel matrix is exploited). For example, the detection results using KPCA and EKPCA based on the single response of sensor 7 are given in Figure 4.10. It can be seen that, using one sensor only, KPCA suffers the same problem as PCA: tests n° 5 and 6 (which differs from the other linear states by the testing conditions) are falsely detected positive. On the other hand, EKPCA shows its capability to make a clear distinction between the linear and the nonlinear states of the structure.

Let us now examine the problem through the T^2 and SPE statistics. Since the detection indexes are statistics measured according to various excitation levels, the data is normalized to have zero mean and a unitary standard deviation. For example, two tests representing two different states (test n° 1 and 8) are examined and the results are shown in Figures 4.11 and 4.12 respectively when all sensors are used. The monitoring diagram is split into two parts: the left part trains the reference data and the right part analyzes the current data. The difference between the two tests can be revealed by the SPE statistics, especially by the ratios S_d/S_r. For test n° 1, S_d/S_r is equal to about 6 but it rises up to more than 2000 for test n° 8. Nevertheless, the T^2 charts do not reveal any change. The SPE result is summarily reported in Figure 4.13 for all tests. The SPE monitoring, presenting outlier statistics, is 100% for all nonlinear states but also for tests n° 5 and 6. Fortunately, linear and nonlinear behaviours can be perfectly distinguished through the ratio S_d/S_r. All tests n° 8-12 show predominant SPE ratios with respect to the previous tests. Those results reveal also that the nonlinearity onset is clearly detected by the SPE ratios even if the level of nonlinearity is not well identified. For instance, tests n° 11 and 12 which correspond to the highest levels of nonlinearity present smaller indexes than tests n° 8-10. Consequently, in this problem, the detection of nonlinear behaviour based on the concept of subspace angle seems more attractive because the angles reflect well the level of nonlinearity.

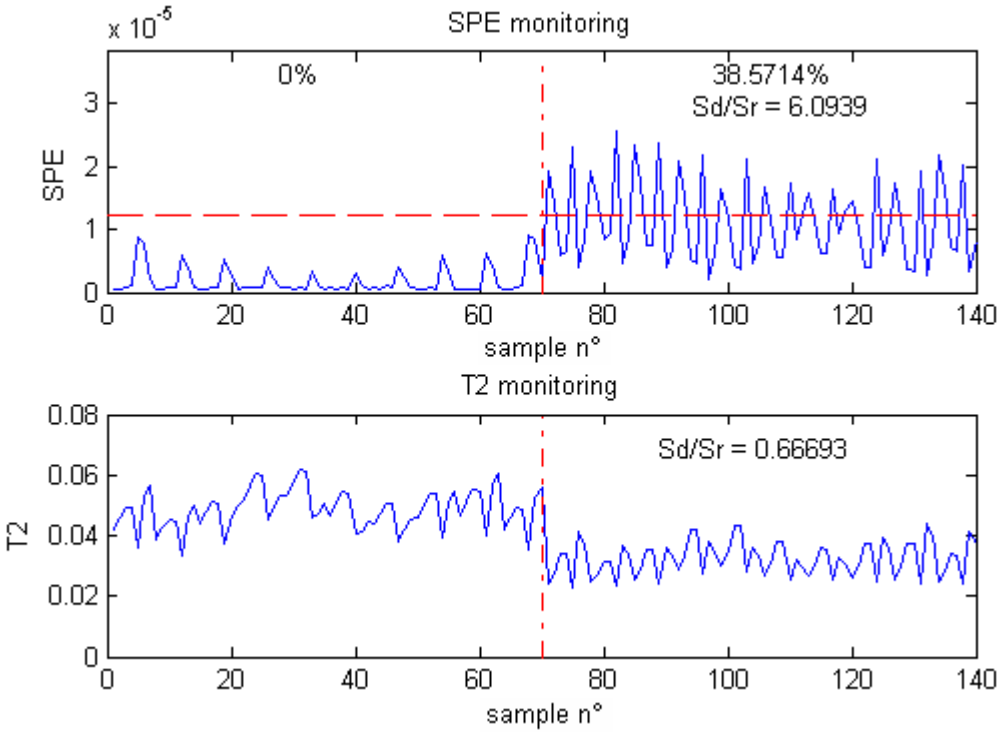

Figure 4.11: SPE and T^2 statistics - test n° 1 (linear behavior)

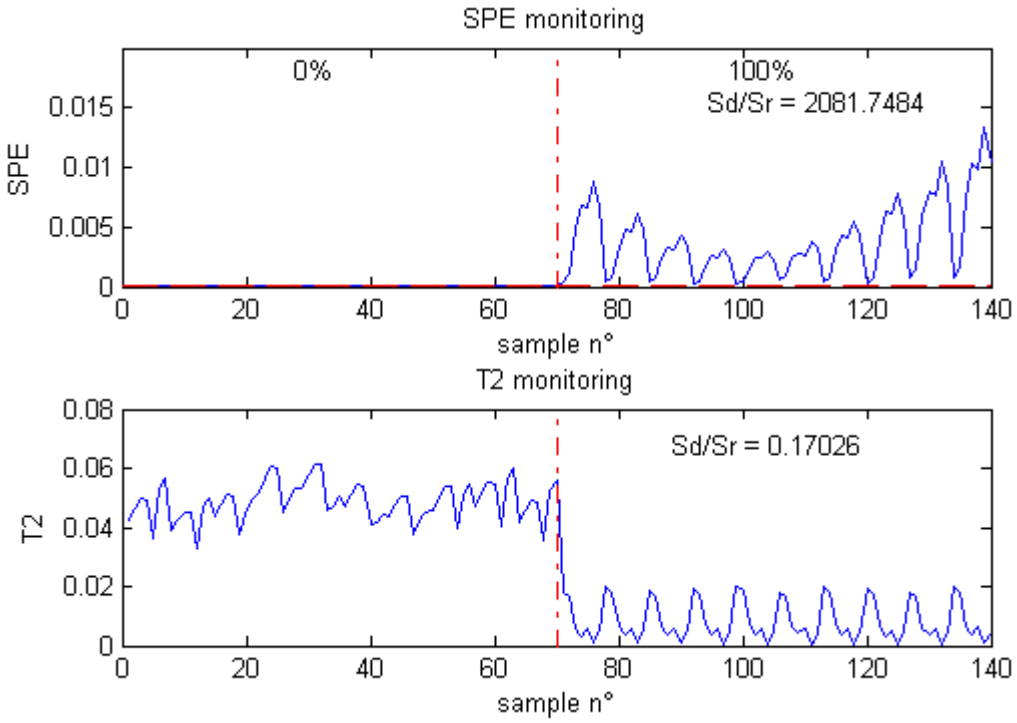

Figure 4.12: SPE and T^2 statistics - test n° 8 (nonlinear behavior)

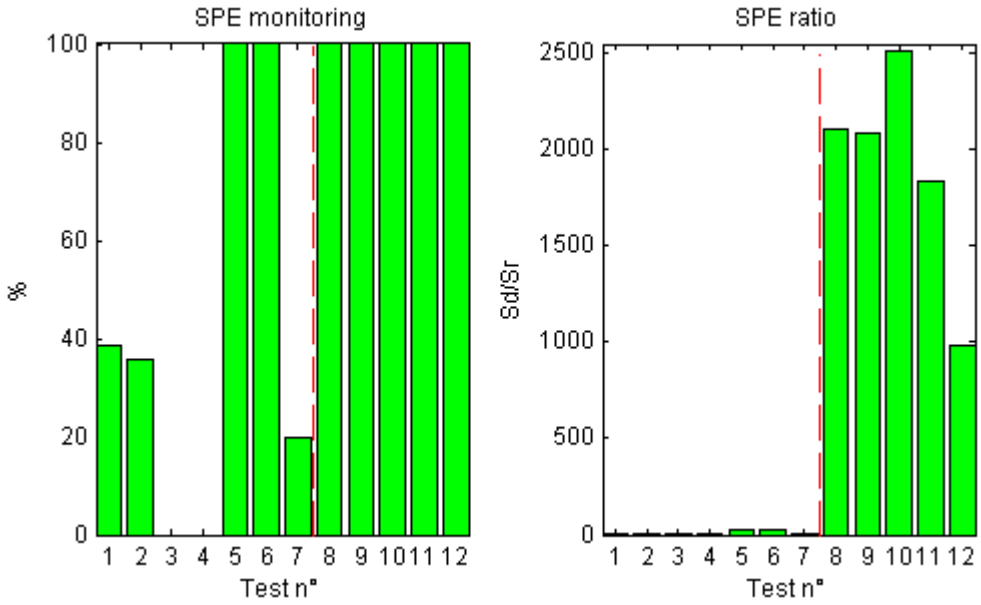

Figure 4.13: EKPCA detection based on the SPE statistics

4.6.2 Random excitation

Time samples of 0.5*s* were analyzed and classified according to the root-mean-square (RMS) value of the measured displacement amplitude at the end of the beam.

Twenty tests were studied as shown in Figure 4.14: seven training samples corresponding to tests n° 1-7 play the role of false-positive and thirteen testing samples corresponding to tests n° 8-20 present nonlinear behaviors.

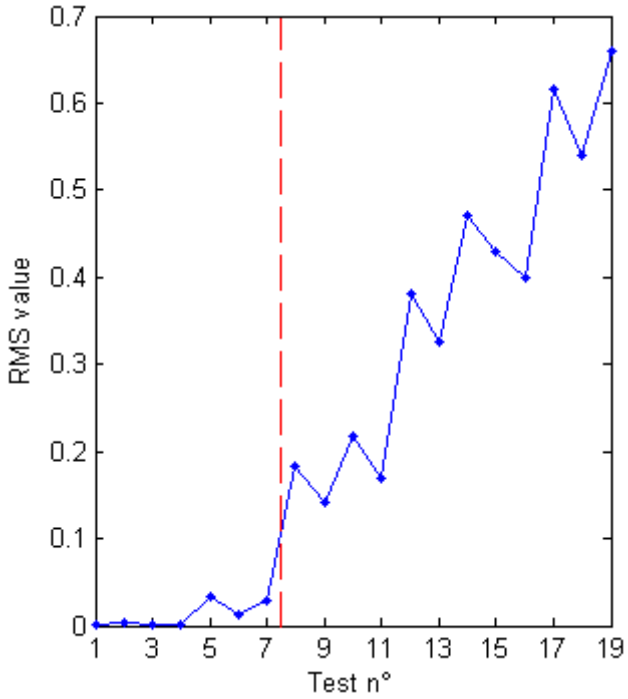

Figure 4.14: Classification of tests according to the RMS value of the displacement measured at the end of the main beam

Detection results based on the concept of subspace angle using KPCA are presented in Figure 4.15. It can be observed that the onset of nonlinearity is clearly revealed. Even if the subspace angles corresponding to low random excitation levels are not small, a strong alarm is produced from the first level of the nonlinear states (test n° 8). The use of the Hankel matrix (EKPCA) in this case does not improve the results but it remains of great interest when the number of sensors is limited. For example, Figure 4.16 shows the EKPCA detection results when only one sensor (sensor 7) is used.

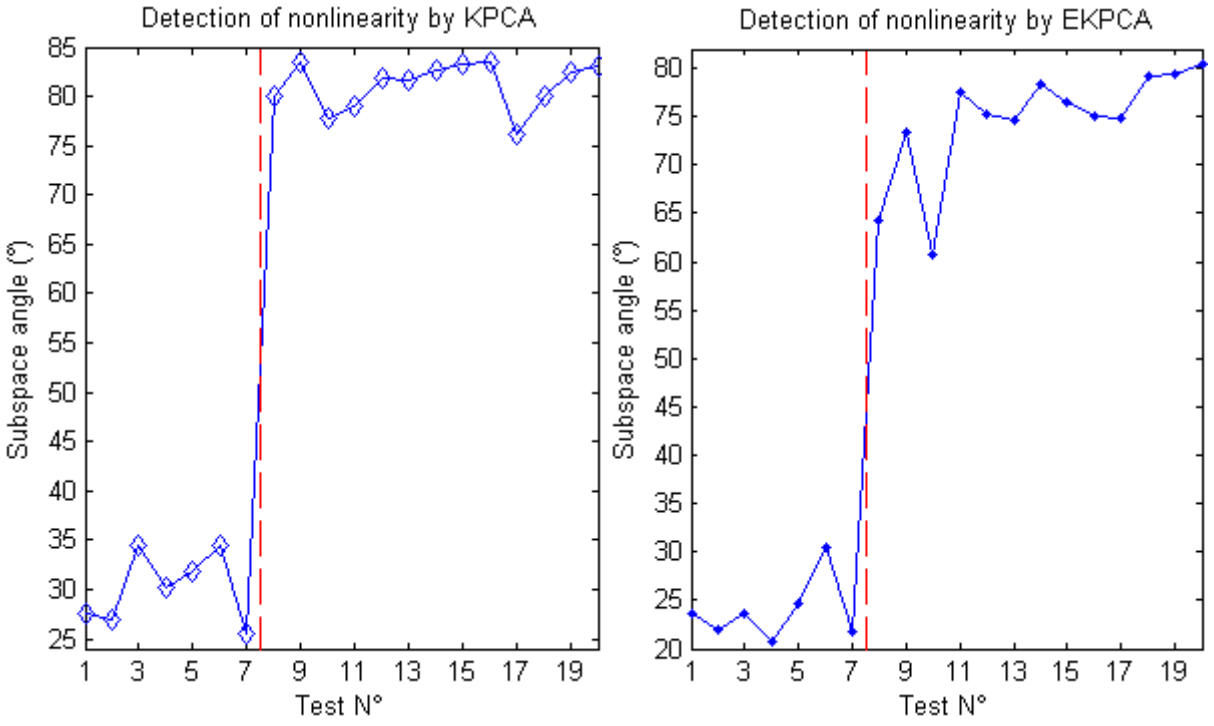

Figure 4.15: Detection index by KPCA and EKPCA

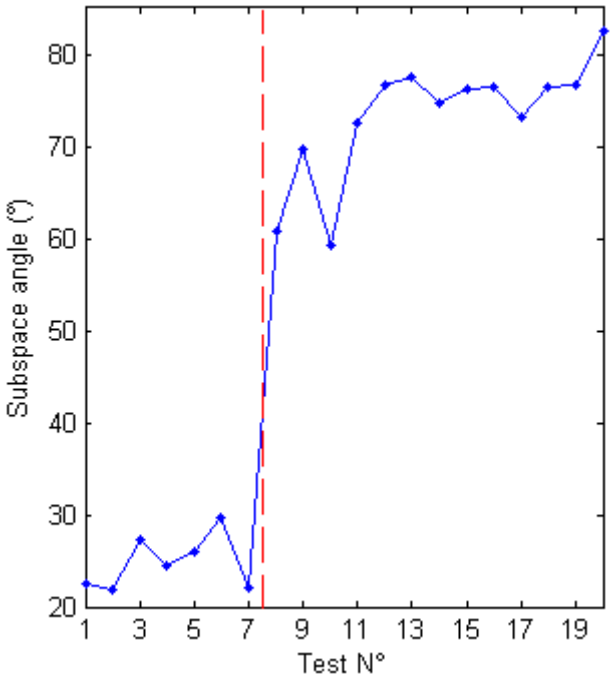

Figure 4.16: Detection using only one sensor

4.7 Fault detection in industrial applications

4.7.1 Damage detection in electro-mechanical devices

This industrial application concerns the case of electro-mechanical devices for which the overall quality at the end of the assembly line has to be assessed.

A set of five good (healthy) devices and four damaged devices was considered. Dynamic responses were collected by one mono-axial accelerometer on the top and one tri-axial accelerometer on the flank of the device as illustrated in Figure 4.17. Only data measured in one direction on the flank (X, Y, Z in Figure 4.17) or on the top of the device is used for the detection.

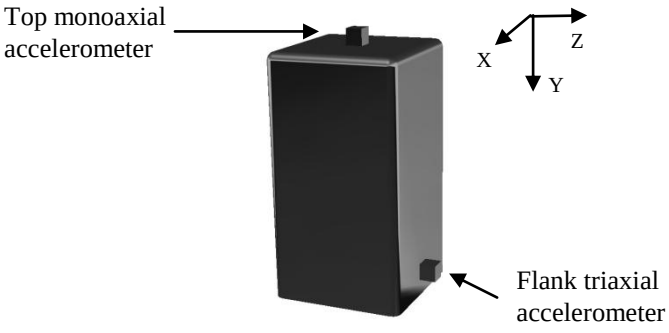

Figure 4.17: Location of the accelerometers on the electro-mechanical device: one mono-axial accelerometer on the top and one tri-axial accelerometer on the flank of the device

It is worth recalling that with only one sensor response, detection cannot be performed by a subspace method like PCA. For this reason, fault detection was realized by Rutten *et al.* (2009)[112] through Null subspace analysis (NSA), using the Novelty Index (*NI*) based on the Mahalanobis norm. In this work, the authors based their detection on outlier statistics

(Novelty Index) by computing a confidence limit: $NI_{\lim} = \overline{NI} + 6\sigma$, where $\overline{NI}$ and σ are the mean value and standard deviation of *NI* for the reference test. As it was found in [112] that detection is better when using the data in the Y direction, the data in this direction is exploited here to test the KPCA-based detection method. In order to increase the sensitivity to damage, the covariance-driven Hankel matrix is constructed by using 35 blocks. The radial basis function (RBF) is used with the width of Gaussian kernel $w = 3$. The eigenvalue diagram for the kernel matrix **K** in Figure 4.18 helps to choose an appropriate number of PCs which defines the optimal dimension of the KPCA space. This dimension was finally chosen equal to 3 as the first three eigenvalues present about 90% of variance percentage and the next value shows a clear decrease.

Figure 4.19 reports the results based on the subspace angle of the set of eight rotating devices which are compared to the healthy device considered as reference. Among the eight devices, four of them may be considered as good (Ok 1-Ok 4) and four of them as damaged (NOk 1-NOk 4). The dashed horizontal line corresponds to the largest angle given by the healthy devices. It can be seen that the good and damaged devices can be well classified.

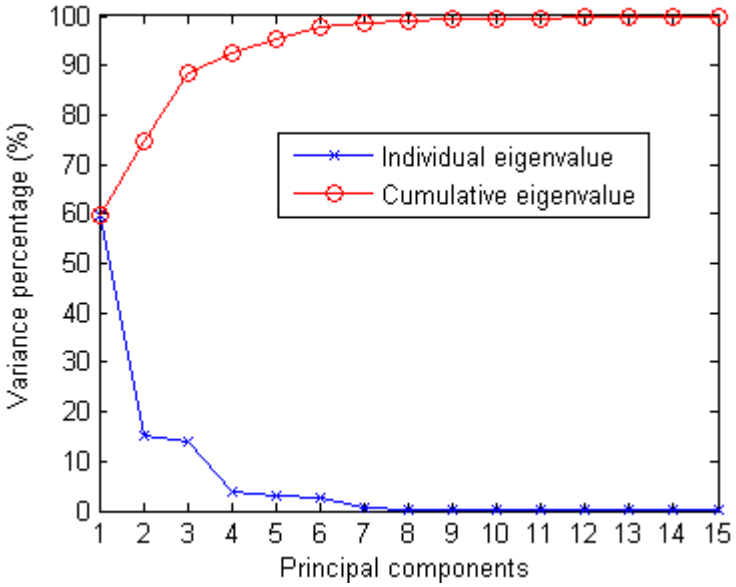

Figure 4.18: Eigenvalues of the kernel matrix vs. the number of PCs

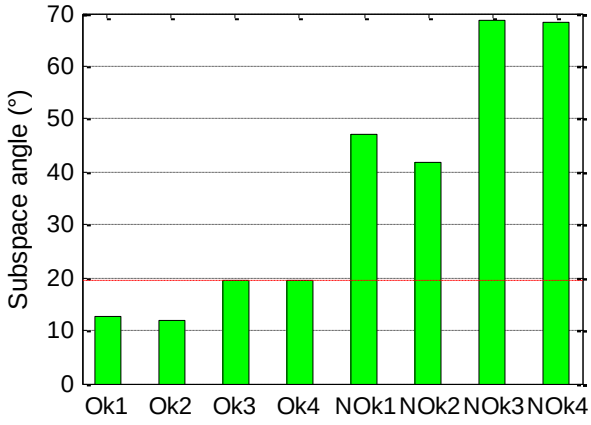

Figure 4.19: EKPCA detection based on the subspace angle

On the other hand, the devices are also controlled by means of the statistics. First, a healthy device is examined and the results are shown in Figure 4.20. As expected, Figure 4.20 does not reveal any fault because the outlier statistics of the current data is not relevant and the ratios S_d/S_r remain close to unity for both SPE and T^2. The confidence limit for T^2 is much bigger than all T^2 values and is not shown in the figure.

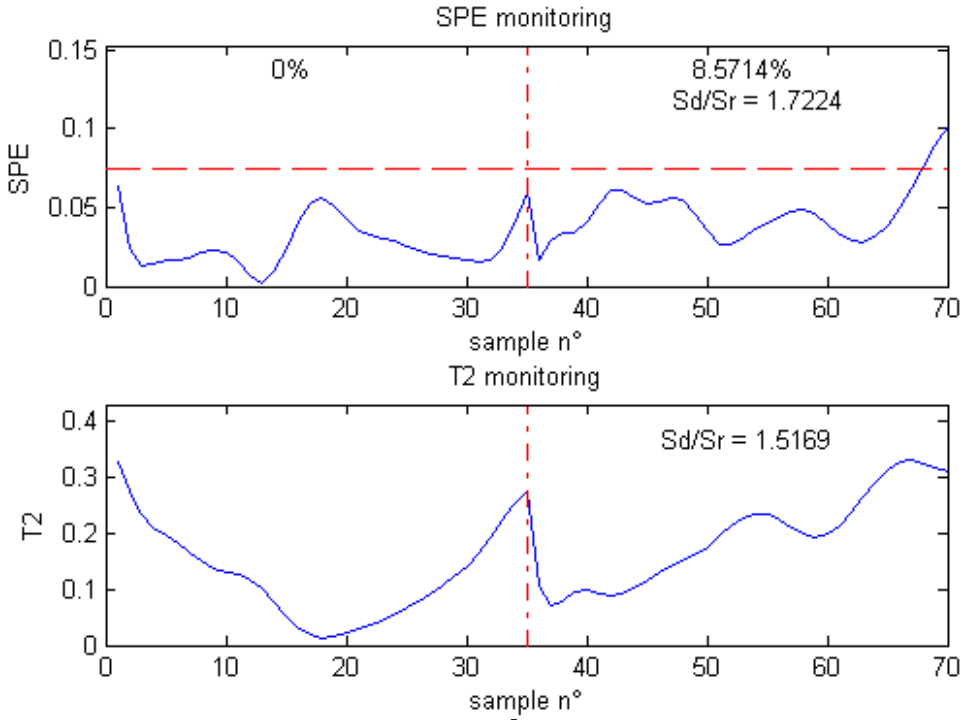

Figure 4.20: SPE and T^2 statistics - no damage

In Figure 4.21, one damaged device is considered. In this case, the SPE outlier statistics goes to 100%; the ratios S_d/S_r reach 13.75 for the SPE and 2.49 for the T^2 index.

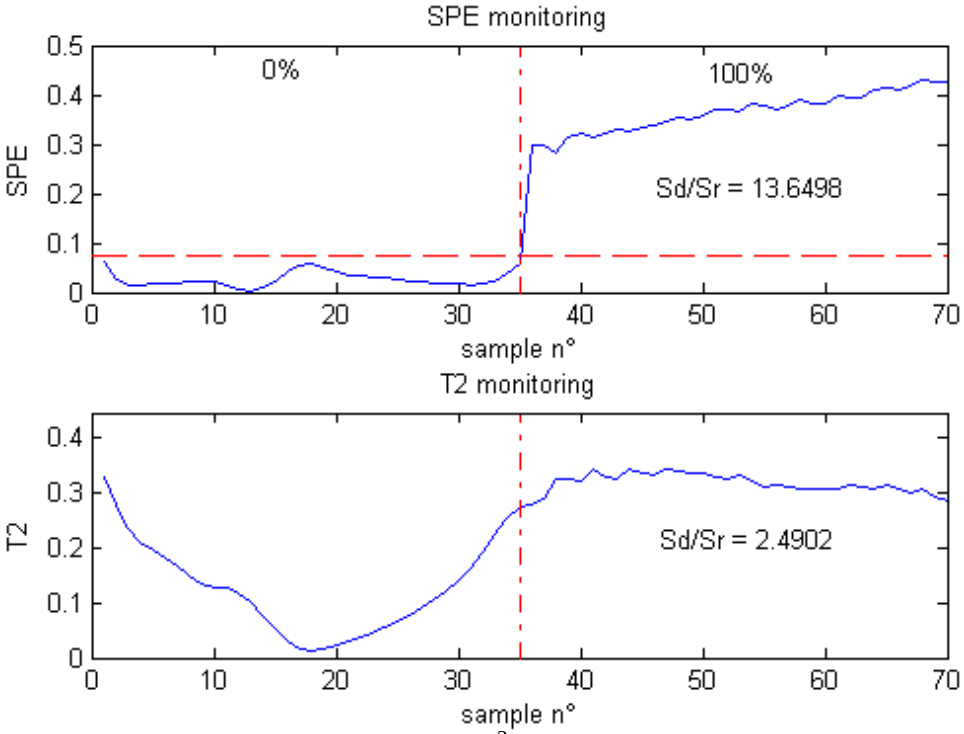

Figure 4.21: SPE and T^2 statistics - with damage

Figure 4.22 presents the monitoring of the whole set of rotating devices. NSA results (Rutten *et al.* (2009)[112]) are also served as reference for the comparison. Figures 4.22*a* and *b* show that both NSA and EKPCA are able to detect accurately the four damaged devices (NOk). Among the four NOk-cases, three of them are diagnosed with 100% of SPE monitoring. The SPE ratios S_d /S_r in Figure 4.22*c* gives also a clear distinction between healthy and damaged devices. However, the T^2 norm does not provide useful information in this problem (Figure 4.22*d*).

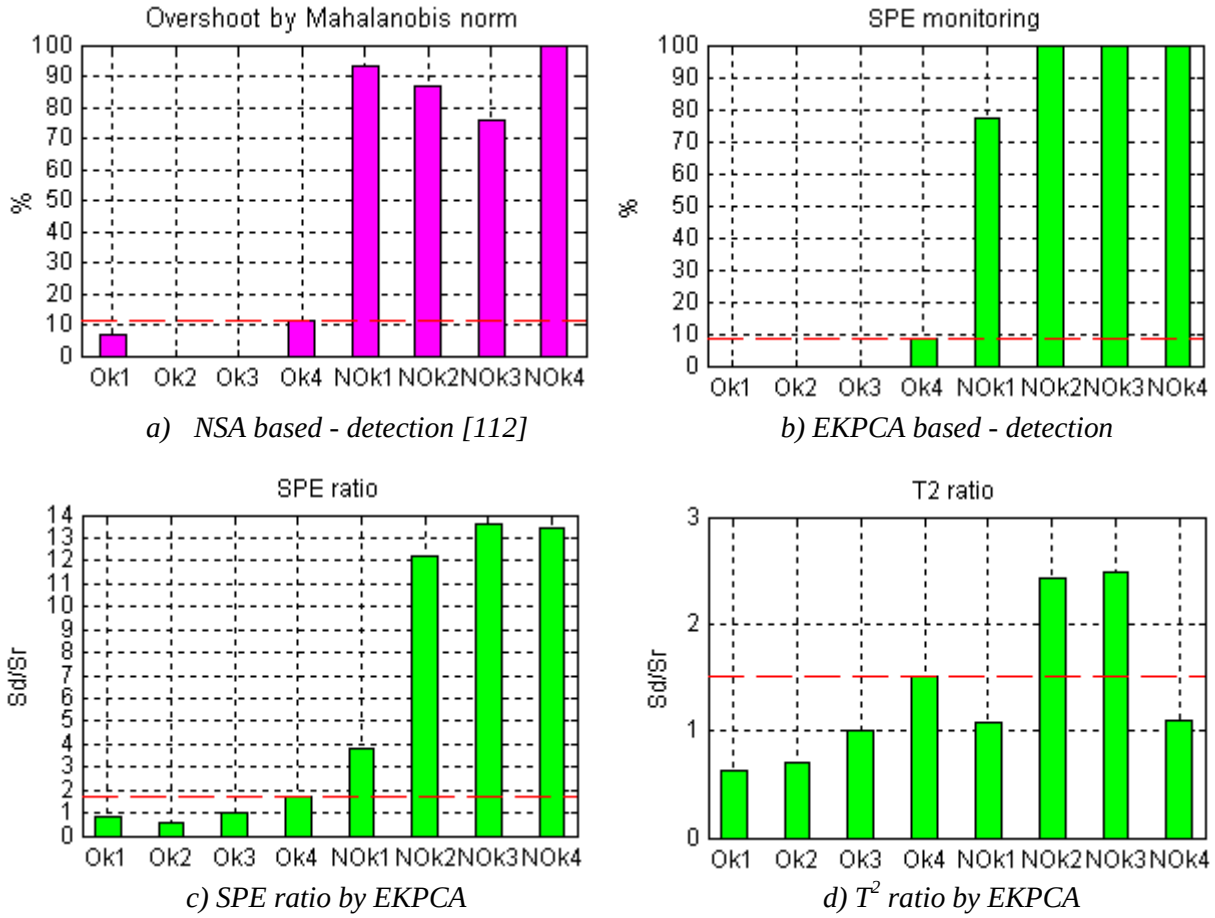

a) NSA based - detection [112]

b) EKPCA based - detection

c) SPE ratio by EKPCA

d) T^2 ratio by EKPCA

Figure 4.22: Damage detection by NSA and EKPCA methods based on statistics (dashed horizontal lines correspond to the maximal values for good devices)

4.7.2 Quality control of welded joints

The third example involves an industrial welding machine from a steel processing plan. The machine was instrumented with a mono-axial accelerometer on the forging wheel, as illustrated in Figure 4.23. The purpose of this wheel is to flatten the welded joint.

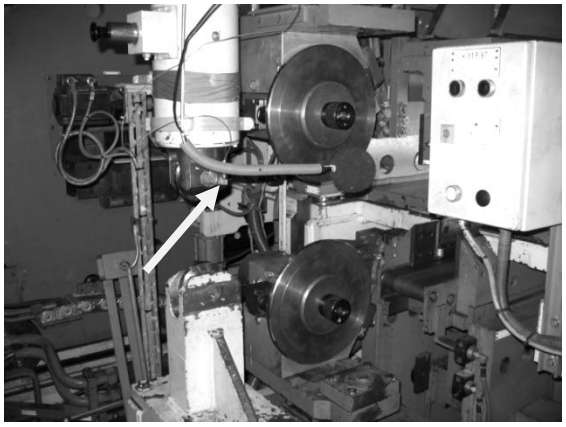

Figure 4.23: Location of the accelerometer on the forging wheel of the welding machine

The quality of the weld depends on several parameters. In Rutten *et al.* (2009)[112], six welded joints with nominal welding parameters (OK 1-OK 6) and 27 joints with out-of-range parameters were studied. Some welding parameters were altered, namely covering, compensation, current and forging pressure, as reported in Table 4.2. From a microscope quality control, welded joints C and G were diagnosed good, welded joints A, D, E, H were diagnosed acceptable and welded joints named B, F, I were diagnosed bad.

Table 4.2: Welds realized with altered parameters (with respect to the nominal parameters)

Name	Modified parameter	Weld quality
Welding A	-33% covering	Acceptable
Welding B	-66% covering	Bad
Welding C	-33% compensation	Good
Welding D	-66% compensation	Acceptable
Welding E	-10% current	Acceptable
Welding F	-20% current	Bad
Welding G	-10% forging pressure	Good
Welding H	+5% forging pressure	Acceptable
Welding I	-66% covering and compensation	Bad

The parameter modifications were clearly identified using the NSA-based detection method as presented in Figure 4.24. It is observed that all OK welded joints do not present non-zero outlier statistic, and so do welded joints C and G.

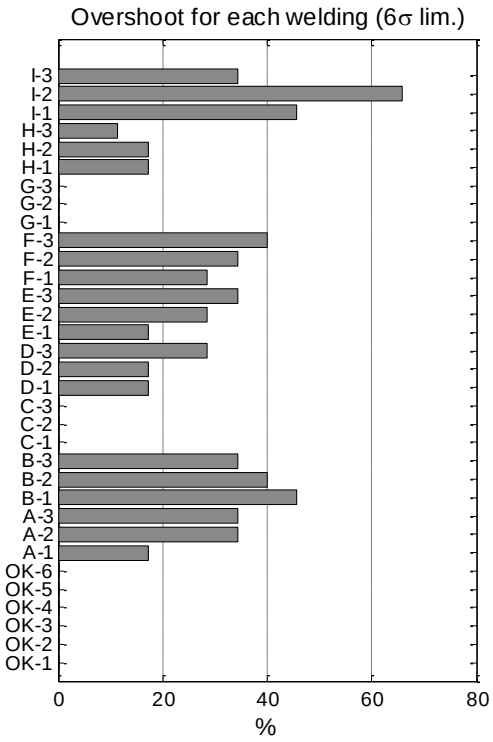

Figure 4.24: NSA-based detection (from [112], $NI_{\lim} = \overline{NI} + 6\sigma$)

The welded joints are now examined by means of the EKPCA method. From only one response vector, the covariance-driven Hankel matrix is built using 30 blocks. The width of Gaussian kernel w = 150 was chosen for the RBF kernel. The eigenvalue diagram is presented in Figure 4.25. It reveals that the first three PCs concentrate 70% of the accumulated variance percentage. It is interesting to note that, as long as the number of principal components is higher than 3, detection results lead to the same conclusion. The best results are obtained within the range of 5-7 PCs which accumulate 80-90% of the variance percentage. They are presented in Figures 4.26 and 4.27 on the basis of the concept of subspace angle and on statistics, respectively.

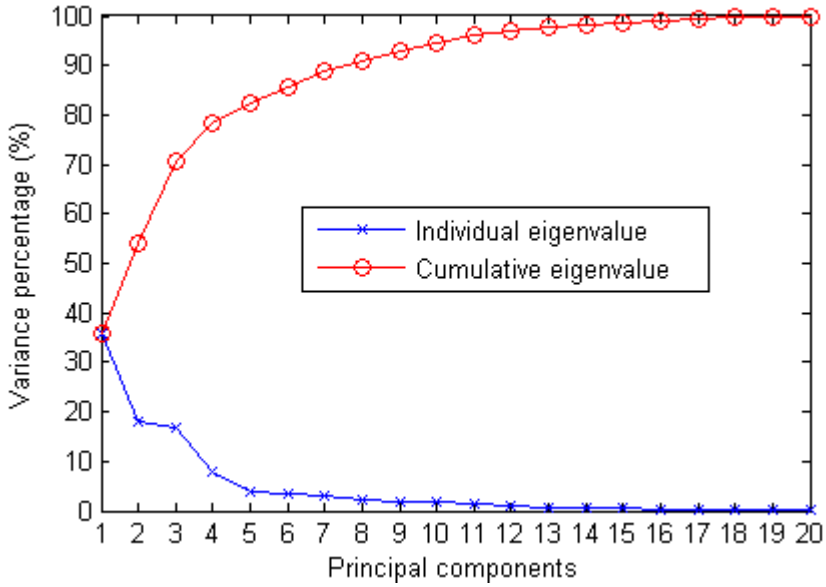

Figure 4.25: Eigenvalues of the kernel matrix vs. the number of PCs

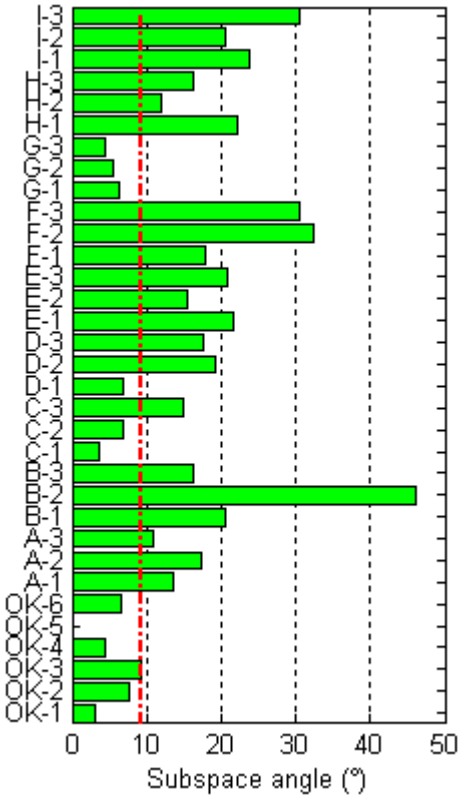

Figure 4.26: EKPCA detection based on the subspace angle (the dash-dot line corresponds to the maximal value for healthy welded joints)

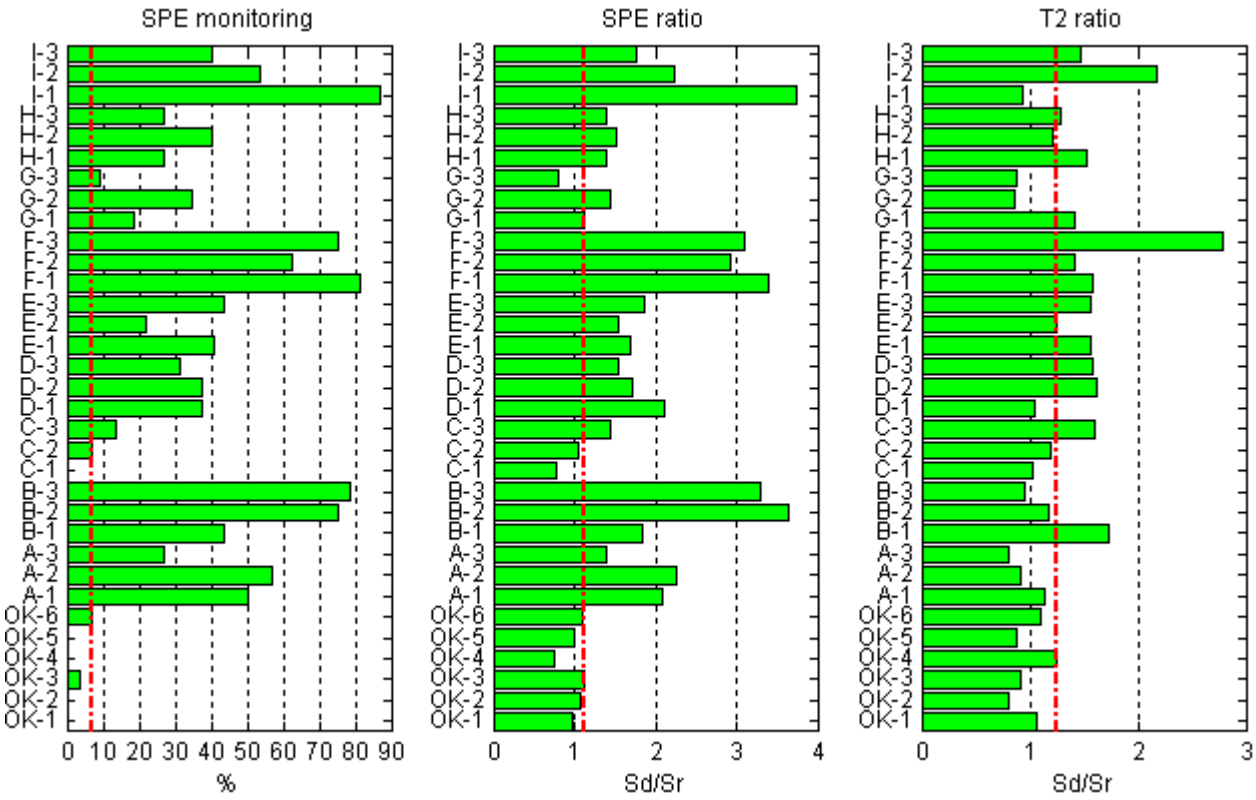

Figure 4.27: EKPCA detection based on statistics

In general, the subspace angles given in Figure 4.26 and the SPE-based indexes in Figure 4.27 allow to identify the alterations reported in Table 4.2. The SPE statistics appears fairly better in this example. For instance, the indexes of welded joints C1-C3, G1, G3 are in the same range as for healthy welded joints OK1-OK6 (i.e. with nominal parameters). This is in good agreement with microscopic quality control inspections. Weld G2 gives an index close to the one of welds A, D, E, H which are diagnosed as acceptable. Finally, welds B, F and I are characterized by significant overshoots and high ratios S_d / S_r. Their diagnosis as bad joints is corroborated by the quality control inspection. It should be noted also that index T^2 does not lead to significant detection results in this problem. Furthermore, the detection indicators used in the EKPCA method as well as in the NSA method are not proportional to the severity of the defects.

4.8 Concluding remarks

KPCA is useful for the processing of nonlinear systems. The robustness of the method for the detection of dynamic changes (due to nonlinear behavior or damage) has been illustrated on several experimental examples and applications in comparison with other methods. Two types of indicators (subspace angle and statistics) were used for detection and were compared regarding to their performance.

Combined with the Hankel matrix, the EKPCA method provides a very appropriate tool for monitoring a structure. Especially, the covariance-data Hankel matrix allows to lessen considerably the computation load by reducing the size of the eigenvalue problem to solve. The method works well even if only one sensor is available.

Chapter 5

Damage Localization using Sensitivities of Principal Component Analysis Results

5.1 Introduction

Let us now deal with another aspect of the detection problem which is the localization. As presented in Section 1.4, damage localization can be performed using output-only measurements or be based on a mathematical model. To solve the problem of localization in beam-like structure, this chapter focuses on the use of sensitivity analysis of measurements.

Natural frequency sensitivity has been also used *extensively* for the purpose of damage localization. However, most of the methods based on frequency sensitivity with respect to damage variables require an accurate analytical model. Jiang and Wang (2009)[48] extended the frequency sensitivity approach by eliminating that requirement. However, an optimization scheme is still needed to estimate the unknown system matrices through an identified model using input-output measurement data.

Natural frequencies are known to be successful in characterizing dynamical systems. Mode shapes are used in model updating because they give information regarding the spatial distribution of damage whereas it is difficult to locate the damage by using the frequencies only in the objective function constructed for minimization. Hence, we use not only sensitivity of frequencies, but also of mode shapes in this work. Modal identification and construction of an analytical model are not necessary for the localization procedure. Damage localization may be carried out by monitoring the distortion of a sensitivity vector. Illustrations are performed through several examples as mass-spring systems, a cantilever beam and a real bridge structure.

5.2 Methodology: Some approaches for Sensitivity Analysis

The behavior of a dynamical system depends on many parameters related to material, geometry and dimensions. The sensitivity of a quantity to a parameter is described by the first and higher orders of its partial derivatives with respect to the parameter. Sensitivity analysis of modal parameters may be a useful tool for uncovering and locating damaged or changed components of a structure. On one hand, we know that the dynamic behavior of a system is fully characterized by its modal parameters which result from the resolution of an eigenvalue problem based on the system matrices (when a model is available). On the other hand, Principal Component Analysis (PCA) of the response matrix of the system is also a way to extract modal features (i.e. principal directions) which span the same subspace as the

eigenmodes of the system (Todd (2009)[126]). In the following, these two approaches are used to examine modal parameter sensitivities.

5.2.1 Approach 1: Sensitivity analysis based on Eigenvalue Analysis

Let us examine a structure that may be modeled by real, symmetric stiffness and mass matrices **K** and **M**. If λ_i and Φ_i are respectively the *i* th eigenvalue (natural frequency squared) and eigenvector (mode-shape), they are solutions of:

$$\left[\mathbf{K}-\lambda_i\mathbf{M}\right]\Phi_i=0 \tag{5.1}$$

Suppose that the eigenvalues of interest are distinct and the eigenvectors are mass normalized so that:

$$\Phi_i^{\mathrm{T}}\mathbf{M}\Phi_i=\mathbf{I} \tag{5.2}$$

If the stiffness and mass matrices are functions of some system parameters, differentiating equation (5.1) with respect to a system parameter p_k gives:

$$\left[\mathbf{K}-\lambda_i\mathbf{M}\right]\frac{\partial\Phi_i}{\partial p_k}+\left[\frac{\partial\mathbf{K}}{\partial p_k}-\lambda_i\frac{\partial\mathbf{M}}{\partial p_k}\right]\Phi_i-\frac{\partial\lambda_i}{\partial p_k}\mathbf{M}\Phi_i=0 \tag{5.3}$$

The first-order eigenvalue derivative is given by Friswell (1994)[29]:

$$\frac{\partial\lambda_i}{\partial p_k}=\Phi_i^{\mathrm{T}}\left[\frac{\partial\mathbf{K}}{\partial p_k}-\lambda_i\frac{\partial\mathbf{M}}{\partial p_k}\right]\Phi_i \tag{5.4}$$

Setting $\mathbf{D}_i=\left[\mathbf{K}-\lambda_i\mathbf{M}\right]$, $b_{ik}=\frac{\partial\lambda_i}{\partial p_k}\mathbf{M}\Phi_i-\left[\frac{\partial\mathbf{K}}{\partial p_k}-\lambda_i\frac{\partial\mathbf{M}}{\partial p_k}\right]\Phi_i$, equation (5.3) becomes:

$$\mathbf{D}_i\frac{\partial\Phi_i}{\partial p_k}=b_{ik} \tag{5.5}$$

$\mathbf{D}_i$ is rank deficient and singular. To overcome this drawback in eigenvector sensitivity computation, Nelson (1976)[86] wrote it under the form:

$$\frac{\partial\Phi_i}{\partial p_k}=v_{ik}+c_{ik}\Phi_i \tag{5.6}$$

for some vectors v_{ik} and scalar c_{ik}. Thus (5.5) can be rewritten in terms of v_{ik}:

$$\mathbf{D}_i v_{ik}=b_{ik} \tag{5.7}$$

Starting to find the element of highest magnitude in the eigenvector Φ_i, then its corresponding element in v_{ik} and b_{ik} is set to zero. The next step is to zero out the corresponding row and the corresponding column of $\mathbf{D}_i$, except the corresponding diagonal element which is set to unity. Once v_{ik} is calculated from (5.7), the scalar c_{ik} is determined as follows:

$$c_{ik}=-\Phi_i^{\mathrm{T}}\mathbf{M}v_{ik}-\frac{1}{2}\Phi_i^{\mathrm{T}}\frac{\partial\mathbf{M}}{\partial p_k}\Phi_i \tag{5.8}$$

Furthermore, Eigen Analysis may be realized by Singular Value Decomposition from output-only as proposed in Reference Todd (2009)[126].

5.2.2 Approach 2: Sensitivity analysis for Principal Component Analysis in the time domain

Principal Component Analysis (PCA) may be computed by a general method - Singular Value Decomposition (SVD). Let us consider the observation matrix $\mathbf{x}(t) = \mathbf{X}^{m \times N}$ which contains the dynamic responses (snapshots) of the system such that:

$$\mathbf{x}(t) = \mathbf{X} = \begin{bmatrix} x_1(t_1) & x_1(t_2) & ... & x_1(t_N) \\ x_2(t_1) & x_2(t_2) & ... & x_2(t_N) \\ ... & ... & ... & ... \\ x_m(t_1) & x_m(t_2) & ... & x_m(t_N) \end{bmatrix} \tag{5.9}$$

where *m* is the number of measured co-ordinates and *N* is the number of time instants. We will assume that it depends on a vector of parameters **p**. This vector of parameters may consist of system parameters or state variables. The observation matrix **X** can be decomposed using Singular Value Decomposition:

$$\mathbf{X} = \mathbf{X}(\mathbf{p}) = \mathbf{U}\boldsymbol{\Sigma}\mathbf{V}^{\mathrm{T}} \tag{5.10}$$

where **U** and **V** are two orthogonal matrices, whose columns represent respectively left and right singular vectors; $\boldsymbol{\Sigma}$ contains singular values of descending importance: $\sigma_1 > \sigma_2 > ... > \sigma_m$.

A sensitivity analysis is performed here by taking the derivative of the observation matrix with respect to **p**:

$$\frac{\partial \mathbf{X}}{\partial \mathbf{p}} = \frac{\partial \mathbf{U}}{\partial \mathbf{p}} \boldsymbol{\Sigma}\mathbf{V}^{\mathrm{T}} + \mathbf{U}\frac{\partial \boldsymbol{\Sigma}}{\partial \mathbf{p}}\mathbf{V}^{\mathrm{T}} + \mathbf{U}\boldsymbol{\Sigma}\frac{\partial \mathbf{V}^{\mathrm{T}}}{\partial \mathbf{p}} \tag{5.11}$$

Through this equation, the sensitivity of the system dynamic response shows its dependence on the sensitivity of each SVD term. So, the determination of $\frac{\partial \mathbf{U}}{\partial \mathbf{p}}$, $\frac{\partial \boldsymbol{\Sigma}}{\partial \mathbf{p}}$ and $\frac{\partial \mathbf{V}}{\partial \mathbf{p}}$ is necessary. Junkins and Kim (1993)[50] developed a method to compute the partial derivatives of SVD factors. The singular value sensitivity and the left and right singular vector sensitivities are simply given by the following equations:

$$\frac{\partial \sigma_i}{\partial p_k} = \mathbf{U}_i^{\mathrm{T}} \frac{\partial \mathbf{X}}{\partial p_k} \mathbf{V}_i \tag{5.12}$$

$$\frac{\partial \mathbf{U}_i}{\partial p_k} = \sum_{j=1}^{m} \alpha_{ji}^k \mathbf{U}_j \tag{5.13}$$

$$\frac{\partial \mathbf{V}_i}{\partial p_k} = \sum_{j=1}^{m} \beta_{ji}^k \mathbf{V}_j \tag{5.14}$$

The partial derivatives of the singular vectors are computed through multiplying them by projection coefficients. These coefficients are given by equation (5.15) for the off-diagonal cases and by equation (5.16) for the diagonal elements.

$$\alpha_{ji}^{k} = \frac{1}{\sigma_i^2 - \sigma_j^2}\left[\sigma_i\left(\mathbf{U}_j^{\mathrm{T}}\frac{\partial \mathbf{X}}{\partial p_k}\mathbf{V}_i\right) + \sigma_j\left(\mathbf{U}_i^{\mathrm{T}}\frac{\partial \mathbf{X}}{\partial p_k}\mathbf{V}_j\right)^{\mathrm{T}}\right]$$
$$\beta_{ji}^{k} = \frac{1}{\sigma_i^2 - \sigma_j^2}\left[\sigma_j\left(\mathbf{U}_j^{\mathrm{T}}\frac{\partial \mathbf{X}}{\partial p_k}\mathbf{V}_i\right) + \sigma_i\left(\mathbf{U}_i^{\mathrm{T}}\frac{\partial \mathbf{X}}{\partial p_k}\mathbf{V}_j\right)^{\mathrm{T}}\right] \quad , \; j \neq i \tag{5.15}$$

$$\alpha_{ii}^{k} - \beta_{ii}^{k} = \frac{1}{\sigma_i}\left(\mathbf{U}_i^{\mathrm{T}}\frac{\partial \mathbf{X}}{\partial p_k}\mathbf{V}_i - \frac{\partial \sigma_i}{\partial p_k}\right)$$
$$\alpha_{ii}^{k} - \beta_{ii}^{k} = \frac{1}{\sigma_i}\left(-\mathbf{V}_i^{\mathrm{T}}\frac{\partial \mathbf{X}^{\mathrm{T}}}{\partial p_k}\mathbf{U}_i + \frac{\partial \sigma_i}{\partial p_k}\right) \quad , \; j = i \tag{5.16}$$

Junkins and Kim (1993)[50] showed also that the diagonal coefficients keep only their imaginary part (their real parts are empty).

5.2.3 PCA-based methodology developed in the frequency domain

Sensitivity analysis for PCA may be developed in the frequency domain, e.g. by considering frequency response functions (FRFs) (Todd (2009)[126]).

As the dynamical system matrices depend on a vector of parameters **p**, the FRF matrix takes the form:

$$\mathbf{H}(\omega,\mathbf{p}) = \left[-\omega^2\mathbf{M}(\mathbf{p}) + i\omega\mathbf{C}(\mathbf{p}) + \mathbf{K}(\mathbf{p})\right]^{-1} \tag{5.17}$$

where ω represents the circular frequency. With regard to sensitivity analysis, the partial derivative of equation (5.17) with respect to one parameter p_k may be written [126]:

$$\begin{aligned}\frac{\partial \mathbf{H}}{\partial p_k} &= -\mathbf{H}(\omega,\mathbf{p})\frac{\partial\left(-\omega^2\mathbf{M} + i\omega\mathbf{C} + \mathbf{K}\right)}{\partial p_k}\mathbf{H}(\omega,\mathbf{p}) \\ &= \mathbf{H}(\omega,\mathbf{p})\left(\omega^2\frac{\partial \mathbf{M}}{\partial p_k} - i\omega\frac{\partial \mathbf{C}}{\partial p_k} - \frac{\partial \mathbf{K}}{\partial p_k}\right)\mathbf{H}(\omega,\mathbf{p})\end{aligned} \tag{5.18}$$

Equation (5.18) provides a way of determining the derivative of the FRF matrix needed for the sensitivity analysis by means of the partial derivative of the system matrices.

Let us consider the FRFs for a single input at location *s*, and build a subset of the FRF matrix (5.17):

$$\mathbf{H}^{s}(\omega) = \begin{bmatrix} h_1(\omega_1) & h_1(\omega_2) & \ldots & h_1(\omega_N) \\ h_2(\omega_1) & h_2(\omega_2) & \ldots & h_2(\omega_N) \\ \ldots & \ldots & \ldots & \ldots \\ h_m(\omega_1) & h_m(\omega_2) & \ldots & h_m(\omega_N) \end{bmatrix} \tag{5.19}$$

where *m* is the number of measured co-ordinates and *N* is the number of frequency lines.

This matrix is the frequency domain analog of the observation matrix (5.9). The rows in (5.19) represent the response at the measured degrees of freedom (DOFs), while the columns

are “snapshots” of the FRFs at different frequencies. We consider that this matrix depends on a given set of parameters. We can assess its principal components through SVD by (5.10):

$$\mathbf{H}^s(\omega,\mathbf{p}) = \mathbf{U}_f \boldsymbol{\Sigma}_f \mathbf{V}_f^{\mathrm{T}} \tag{5.20}$$

where the left singular vectors $\mathbf{U}_f$ give spatial information, the diagonal matrix of singular values $\boldsymbol{\Sigma}_f$ shows scaling parameters and the right singular vectors $\mathbf{V}_f$ represents modulation functions depending on frequency. In other words, this SVD separates information depending on space and on frequency.

The sensitivity of the *i*th principal component in (5.20) can be computed by (5.12-5.16). First, we compute the SVD of the FRF matrix in (5.19) for the set of responses and the chosen input location. Then, the partial derivatives of (5.19) are determined using equation (5.18). For a particular input, only a subset of the derivatives in (5.18) is needed.

5.3 Damage localization based on sensitivity analysis of FRF matrix

In the following, sensitivity analysis is used to resolve the problem of damage localization. According to Eigen Analysis, sensitivity of eigensolution is straightforward if the system matrices are available. Regarding FRF analysis, we present now some simplifications that may be carried out in experimental practice.

Giving the FRF matrix $\mathbf{H}^s$ for a single input at location *s* of the system and its SVD, the sensitivity computation of the principal components (PCs) requires the partial derivatives $\partial\mathbf{H}^s/\partial p_k$ which are a subset of $\partial\mathbf{H}/\partial p_k$. This quantity may be assessed by (5.18) requiring the partial derivative of the system matrices with respect to system parameters. If the parameter concerned is a coefficient k_e of the stiffness matrix **K**, the partial derivatives of the system matrices are selected such that $\partial\mathbf{M}/\partial p_k$ and $\partial\mathbf{C}/\partial p_k$ equal zero and $\partial\mathbf{K}/\partial p_k = \partial\mathbf{K}/\partial k_e$.

Although only a subset of $\partial\mathbf{H}/\partial p_k$ is needed for a particular input *s*, i.e. $\partial\mathbf{H}^s/\partial p_k$ which corresponds to the *s* th column of $\partial\mathbf{H}/\partial p_k$, the calculation of (5.18) demands the whole matrix $\mathbf{H}$, which turns out to be costly. However, we can compute $\partial\mathbf{H}^s/\partial p_k$ by measuring only some columns of $\mathbf{H}$, as explained below.

We recall that our parameter of interest is some coefficient k_e of the stiffness matrix **K**. Equation (5.17) shows that FRF matrices are symmetric if system matrices are symmetric. In experiment, the number of degrees of freedom (DOF) equals the number of response sensors. So, the FRF matrix has the same size as the number of sensors. Let us consider for instance a structure instrumented with four sensors. The FRF matrix takes the symmetrical form:

$$\mathbf{H}(\omega) = \begin{bmatrix} a & b & c & d \\ b & e & f & g \\ c & f & h & i \\ d & g & i & k \end{bmatrix} \tag{5.21}$$

Assuming that k_e accords to the element between DOFs 2 and 3, we have: $\partial\mathbf{M}/\partial p_k = 0$; $\partial\mathbf{C}/\partial p_k = 0$ and:

$$\partial \mathbf{K} / \partial p_k = \partial \mathbf{K} / \partial k_e = \begin{bmatrix} 0 & 0 & 0 & 0 \\ 0 & 1 & -1 & 0 \\ 0 & -1 & 1 & 0 \\ 0 & 0 & 0 & 0 \end{bmatrix} \tag{5.22}$$

Equation (5.18) allows us to deduce the partial derivative of the FRF matrix:

$$\frac{\partial \mathbf{H}}{\partial p_k} = -\mathbf{H}(\omega, \mathbf{p}) \frac{\partial \mathbf{K}}{\partial p_k} \mathbf{H}(\omega, \mathbf{p}) = -\begin{bmatrix} [(b-c) & (e-f) & (f-h) & (g-i)](b-c) \\ [(b-c) & (e-f) & (f-h) & (g-i)](e-f) \\ [(b-c) & (e-f) & (f-h) & (g-i)](f-h) \\ [(b-c) & (e-f) & (f-h) & (g-i)](g-i) \end{bmatrix} \tag{5.23}$$

To compute the sensitivity of $\mathbf{H}^s$, only the s th column of $\partial \mathbf{H} / \partial p_k$ is needed, which is written in (5.25) in setting:

$$\mathbf{H}_{k_e} = [(b-c) \quad (e-f) \quad (f-h) \quad (g-i)]^{\mathrm{T}} \tag{5.24}$$

This relies entirely upon the columns corresponding to k_e in the FRF matrix in equation (5.21).

$$\frac{\partial \mathbf{H}^s}{\partial p_k} = -\mathbf{H}_{k_e} . \mathbf{H}_{k_e, s} \tag{5.25}$$

where $\mathbf{H}_{k_e, s}$ is the s th element of the vector $\mathbf{H}_{k_e}$. Thus, the sensitivity of $\mathbf{H}^s$ with respect to k_e does not involve the entire matrix $\mathbf{H}$; only the columns relating to k_e is needed.

It is worth noting that the choice of system parameter in the derivative process is not unique. The parameter can consist in a DOF only, i.e. it relates to a coefficient k_e of the stiffness matrix. For example, assuming that k_e accords to the second DOF only, we have:

$$\partial \mathbf{K} / \partial p_k = \partial \mathbf{K} / \partial k_e = \begin{bmatrix} 0 & 0 & 0 & 0 \\ 0 & 1 & 0 & 0 \\ 0 & 0 & 0 & 0 \\ 0 & 0 & 0 & 0 \end{bmatrix}, \qquad \frac{\partial \mathbf{H}}{\partial p_k} = -\begin{bmatrix} [b & e & f & g]b \\ [b & e & f & g]e \\ [b & e & f & g]f \\ [b & e & f & g]g \end{bmatrix} \tag{5.26}$$

Setting $\mathbf{H}_{k_e} = [b \quad e \quad f \quad g]^{\mathrm{T}}$ (5.27)

this is just the column corresponding to k_e in the FRF matrix in equation (5.21). Finally, the same equation in (5.25) may be found for $\partial \mathbf{H}^s / \partial p_k$. This time again, only the column related to k_e is needed for the sensitivity of $\mathbf{H}^s$ with respect to k_e.

5.4 Localization indicators

Once $\partial \mathbf{H}^s / \partial p_k$ has been computed, the sensitivity of principal components can be determined using equations (5.12-5.16). The sensitivities of the left singular vectors or eigenvectors are good candidates for resolving localization problems of linear-form structures, e.g. chain-like or beam-like structures. In each working condition of the system, we can

compute the sensitivity $\partial \mathbf{U}_i / \partial p_k$. The reference state is denoted by $\dfrac{\partial \mathbf{U}_i^{\,R}}{\partial p_k}$, and the deviation of the current condition may be assessed as follows:

$$\Delta = \Delta \frac{\partial \mathbf{U}_i}{\partial p_k} = \frac{\partial \mathbf{U}_i}{\partial p_k} - \frac{\partial \mathbf{U}_i^{\,R}}{\partial p_k} \tag{5.28}$$

For structure that has several spans, a normalized deviation Δ_{norm} can be used to count on the influence of different magnitudes of the sensitivity vector in the spans. It is computed in accordance with the span:

$$\Delta_{\text{norm}}^{t} = \frac{\Delta^t}{\text{norm}\left(\partial \mathbf{U}_i^{\,R} / \partial p_k\right)^t} \tag{5.29}$$

where Δ^t contains the elements according to span t of vector Δ, $\left(\partial \mathbf{U}_i^{\,R} / \partial p_k\right)^t$ describes the sensitivity elements in span t in the reference state and $\text{norm}(\cdot)$ is an operator giving the maximal singular value of a vector.

Other indicators may be utilized to better locate dynamic change, such as:

$$d_j^{\text{I}} = \frac{1}{r}\left(\Delta_{j+1} - \Delta_j\right) \tag{5.30}$$

$$d_j^{\text{II}} = \frac{1}{r^2}\left(\Delta_{j+1} - 2\Delta_j + \Delta_{j-1}\right) \tag{5.31}$$

where r is average distance between measurement points and Δ_j denotes the j^{th} element of Δ.

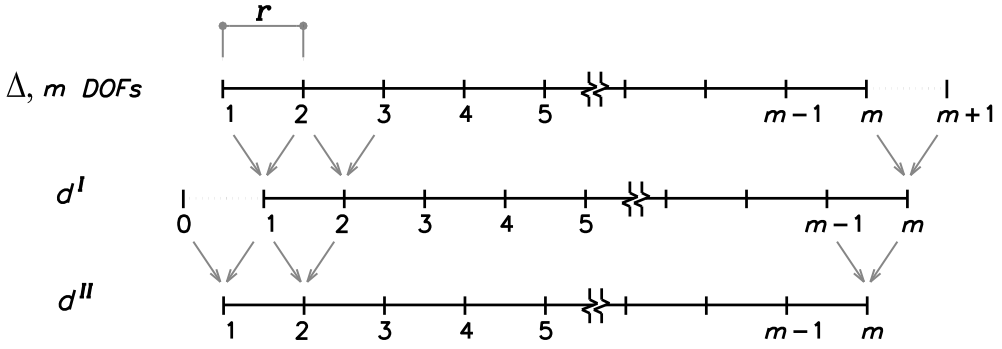

Figure 5.1: Geometrical illustration for position of elements in the indicators

d^{I} in eq. (5.30) represents the relative difference between adjacent elements of Δ and has one element less than Δ. For a d^{I} vector containing all the m elements (as the number of DOFs), one more element in Δ may be generated, e.g. element m+1, as illustrated in Figure 5.1. Of course, this generated element must not affect the remaining elements; a technique that may be applied is the cubic spline extrapolation. We can proceed similarly for the d^{II} vector. The indicators d^{I} and d^{II} are effectively comparable with the first and second derivatives of vector $\Delta \dfrac{\partial \mathbf{U}_i}{\partial p_k}$ and allow the maximization of useful information for damage localization.

The indicator d^{II} is widely used in the literature of damage localization, e.g. in Pandey *et al.* (1991)[96], Sampaio *et al.* (1999)[113]. However, the methods proposed in the literature compare mode shape vectors or FRF data. In this study, the sensitivity of singular vectors is the subject under examination.

It should be noted that a zero-mean normalization is generally applied to the data in the classical PCA technique. However, such normalization can be avoided in the present case because the localization indicators are characterized by the principal components vectors and their derivatives. This is illustrated in Figure 5.2 in a two-dimensional case where two features y_1 and y_2 are considered. The features in data set S_1 are distributed around their geometric centre - point O_1 and if a zero-mean normalization is achieved, they are represented by data set S_0. The application of PCA to S_1 gives two principal components PC 1 and PC 2, which are just the principal components of set S_0. In our application, a health state of the dynamic structure is shown by the vectors of principal components and their sensitivities; and the localization is achieved by comparing the last vectors of two different health states. To this purpose, a zero-mean normalization is not necessary for the data preprocessing. However, in order to facilitate the comparison between two states, the unit-norm normalization is implemented to the sensitivity vectors, i.e.

$$\partial \mathbf{U}_i / \partial p_k = \frac{\partial \mathbf{U}_i / \partial p_k}{\text{norm}(\partial \mathbf{U}_i / \partial p_k)} \tag{5.32}$$

This normalization step provides more meaningful and accurate comparison between different conditions.

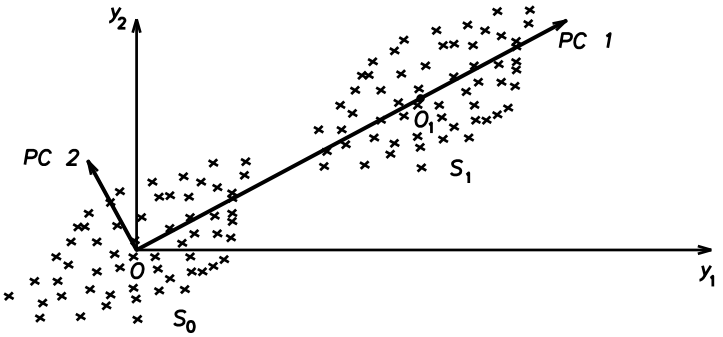

Figure 5.2: Geometric interpretation of PCA

5.5 Applications to damage localization

5.5.1 Numerical example of a spring-mass-damper system

Let us examine the system studied in Todd (2009)[126] which consists in a linear system of 20 degrees of freedom as presented in Figure 5.3.

The damping matrix is set to $\mathbf{C} = 0.01\mathbf{M}$. Input is introduced at point 18. The frequency range is selected from 0 to 2 rad/sec at intervals of 0.005 rad/sec. Some results of principal component sensitivities with respect to a spring constant are presented in [126].

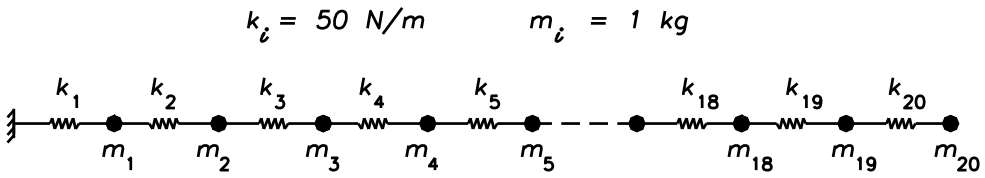

Figure 5.3: Spring-mass-damper system

In this study, sensitivity analysis is applied with the aim of damage localization. For this purpose, damage is simulated in the system by a stiffness reduction of spring n° 8. Both approaches based on Eigen analysis and PCA are considered. Figure 5.4 compares the sensitivities of the first eigenvector and of the first left singular vector with respect to the stiffness of the second spring (k_2). As can be observed, both techniques lead to similar results; in the following, we present the development of damage localization based on PCA analysis.

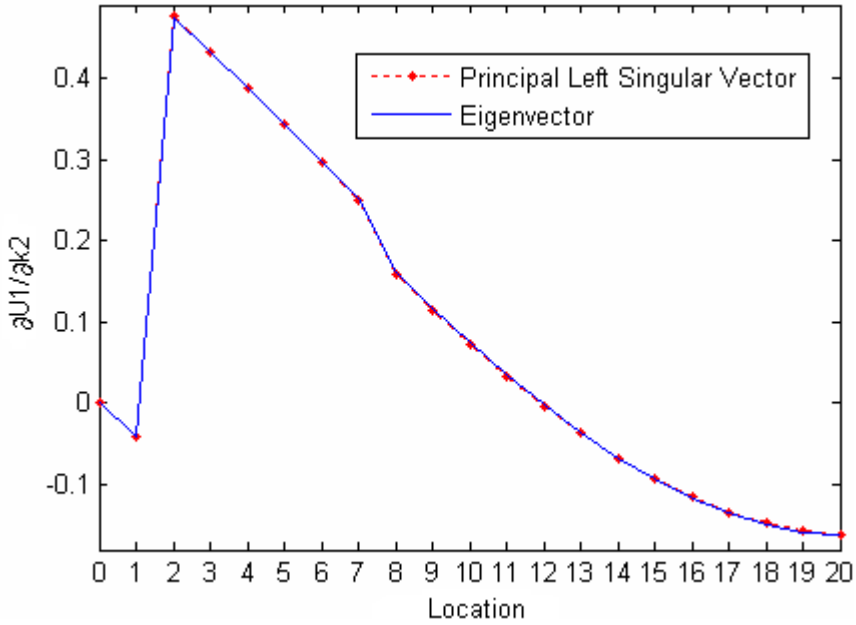

Figure 5.4: Analytical sensitivities of the first eigenvector and of the first left singular vector

Let us consider now the structure in three states: the reference state (no damage), level 1 and level 2 induced by a stiffness reduction of 20% and 50% of the 8th spring. Figure 5.5 shows the sensitivity of the first left singular vector with respect to several system parameters for all the states.

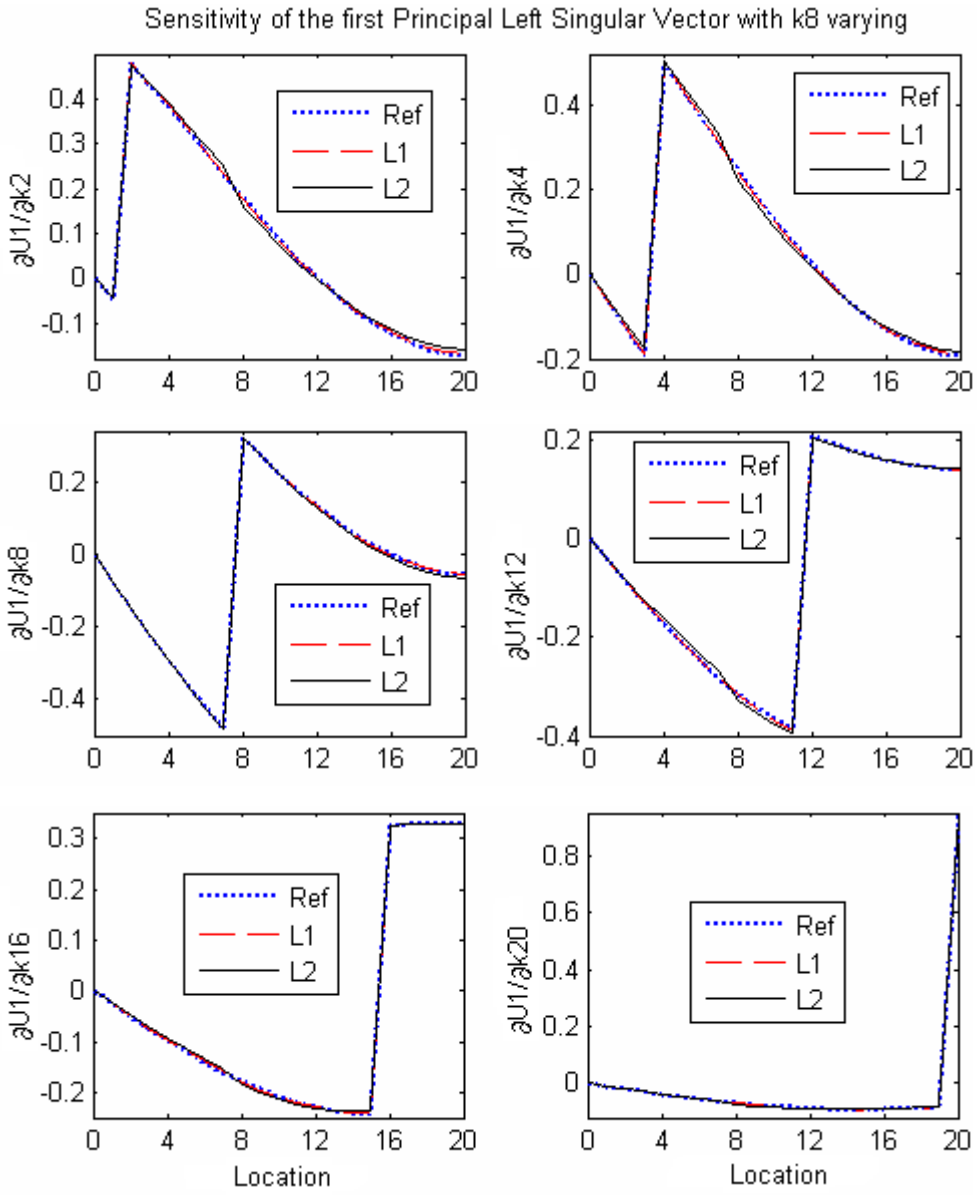

Figure 5.5: $\partial \mathbf{U}_1 / \partial p_k$, with $p_k = k_2, k_4, k_8, k_{12}, k_{16}, k_{20}$ respectively

The difference between the two levels of damage at element k_8 and the reference state is shown in terms of $\Delta \frac{\partial \mathbf{U}_1}{\partial p_k}$ in Figure 5.6. This quantity presents large variations at two locations according to the chosen parameter p_k and the damaged element k_8. The use of indicator d^{I} gives a better detection as shown in Figure 5.7.

In each subplot of Figure 5.7, a dominant peak appears clearly at the damaged element (location n° 8) but a secondary peak at the element corresponding to the parameter p_k can be observed. Thus, by taking the partial derivative with respect to several parameters, a common preeminent peak between all subplots allows to assert the location of damage.

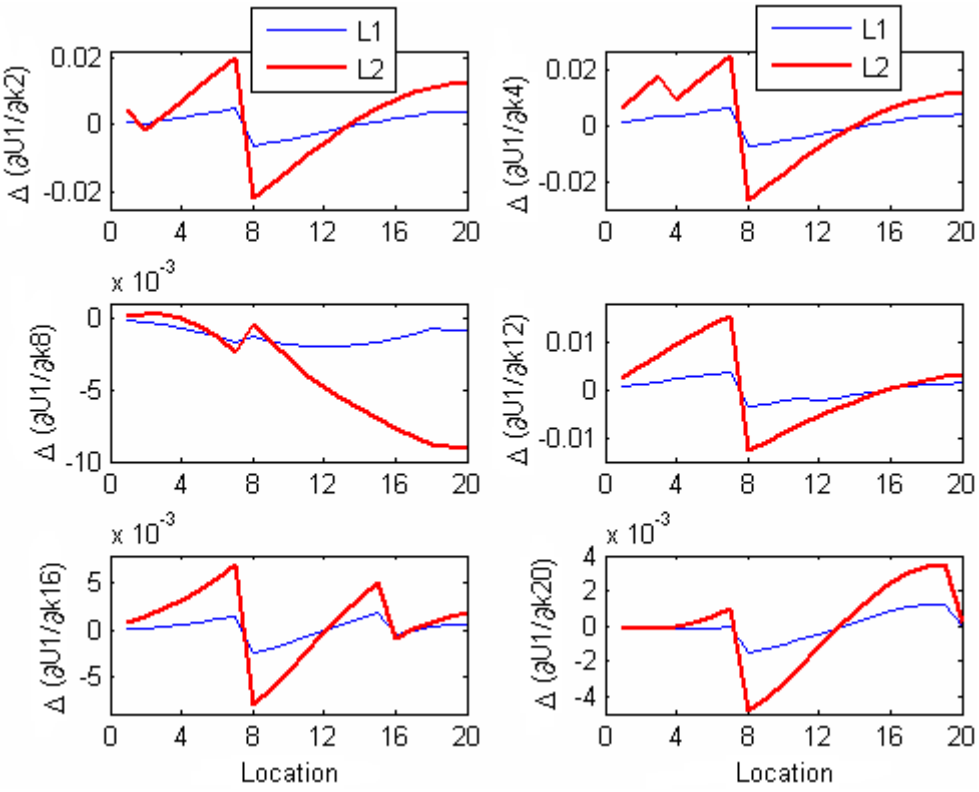

Figure 5.6: $\Delta\dfrac{\partial \mathbf{U}_1}{\partial p_k}$ for levels 1 and 2 with $p_k = k_2, k_4, k_8, k_{12}, k_{16}, k_{20}$ respectively

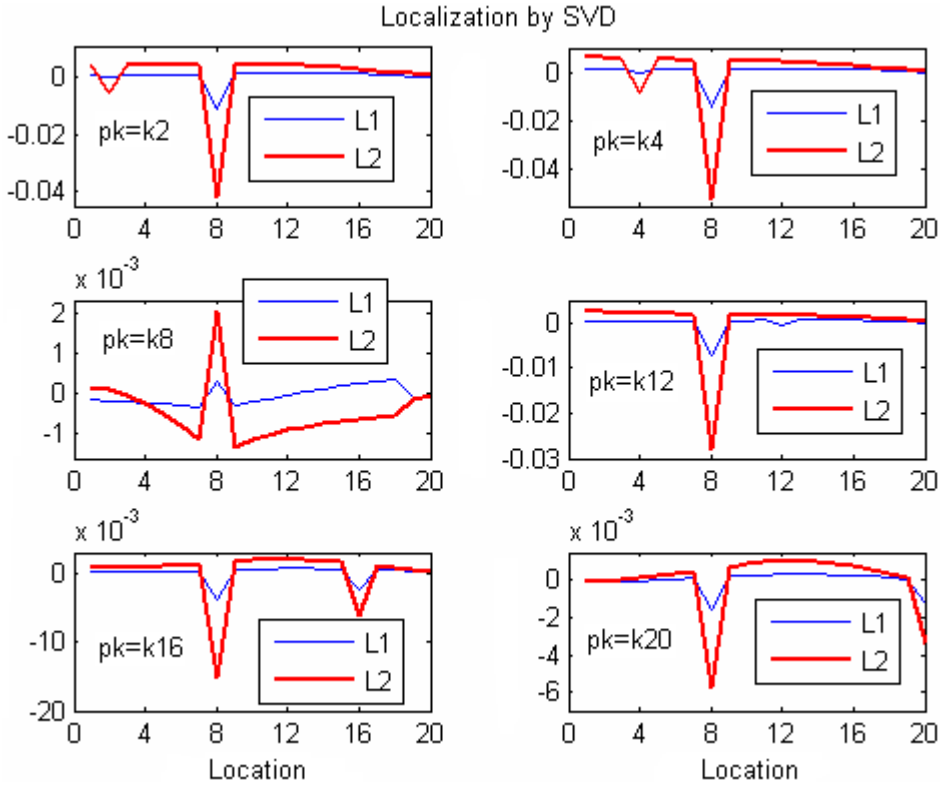

Figure 5.7: d^1 for levels 1 and 2 with $p_k = k_2, k_4, k_8, k_{12}, k_{16}, k_{20}$ respectively

The damage is also exactly located even if it occurs far from the clamping. In Figure 5.8, the damaged element (stiffness reduction of the 20th spring) is well detected.

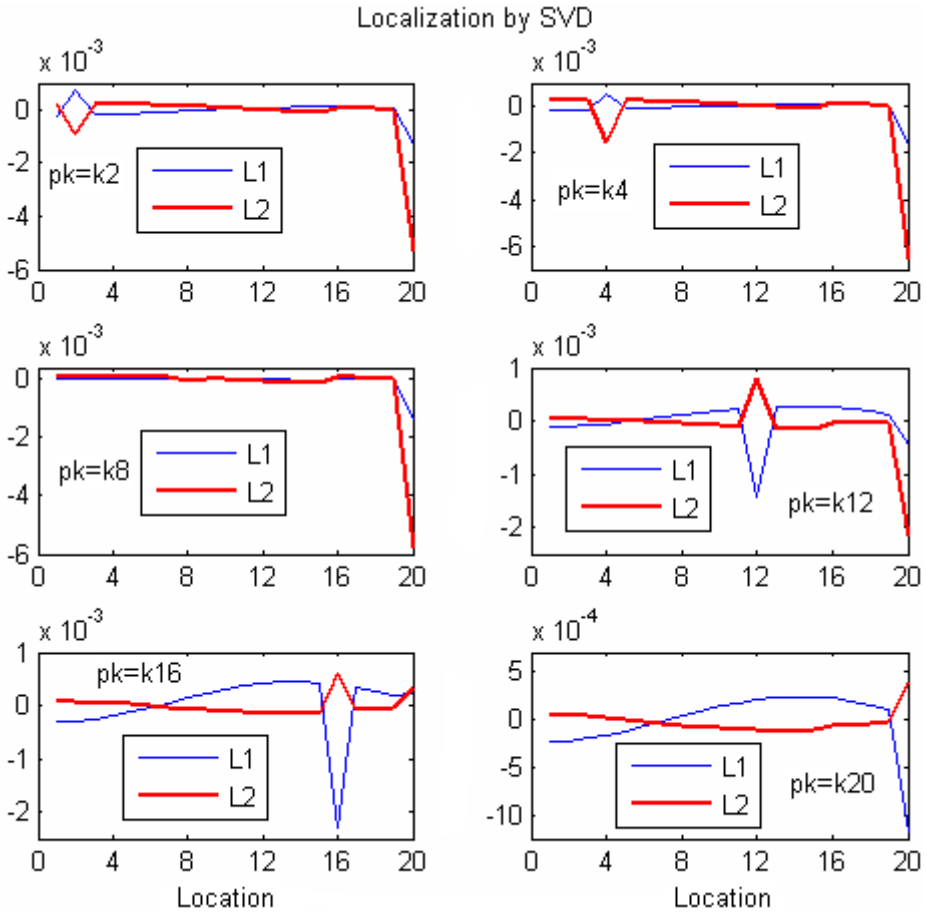

Figure 5.8: d^1 with damage in k_{20}

5.5.2 Numerical example of a cantilever beam

Let us examine a steel cantilever beam with a length of 700 mm and a square section of dimension $14\times14(\text{mm}^2)$. The beam is modeled by twenty finite elements as illustrated in Figure 5.9. The input location is chosen at node 7 and the snapshot matrix is assembled from FRFs corresponding to the vertical displacements at nodes 1 to 20.

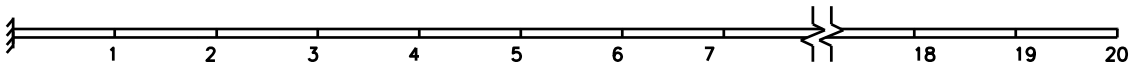

Figure 5.9: Discretization of cantilever beam

We model the damage by a stiffness reduction of a beam element. Four states are examined: the reference (healthy) state, and three levels of damage (L_1, L_2, L_3) induced by a reduction of stiffness of respectively 10%, 20% and 40%. The damage is assumed to occur in element 12. Note that the maximum deviations on the first three frequencies from the reference state are 0.70%, 1.41% and 2.81% for the three levels respectively.

For illustration, sensitivity analysis results are shown in Figures 5.10 and 5.11 according to the parameter $p_k=k_{15}$. Note that similar results were obtained for other stiffness parameter in various positions. The FRFs were considered in the frequency range from 0 Hz to 165 Hz at intervals of 1 Hz.

Figure 5.10 shows the sensitivity difference $\Delta = \Delta \frac{\partial \mathbf{U}_1}{\partial k_{15}}$ of the first left singular vector with respect to the coefficient associated to the 15th DOF in the stiffness matrix and its derivatives d^{I}, d^{II} are presented in Figure 5.11. It is observed that the Δ curves are discontinuous at DOFs 11 and 12, index d^{I} shows a discontinuity with large variations around element 12 and finally, index d^{II} allows us to discover explicitly the position of the damaged element.

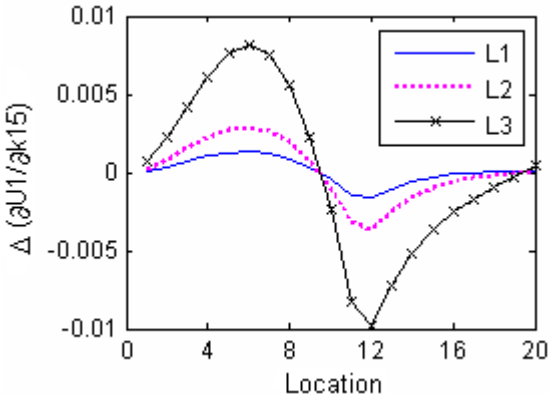

Figure 5.10: $\Delta \frac{\partial \mathbf{U}_1}{\partial k_{15}}$ for 3 levels with p_k=k_{15}

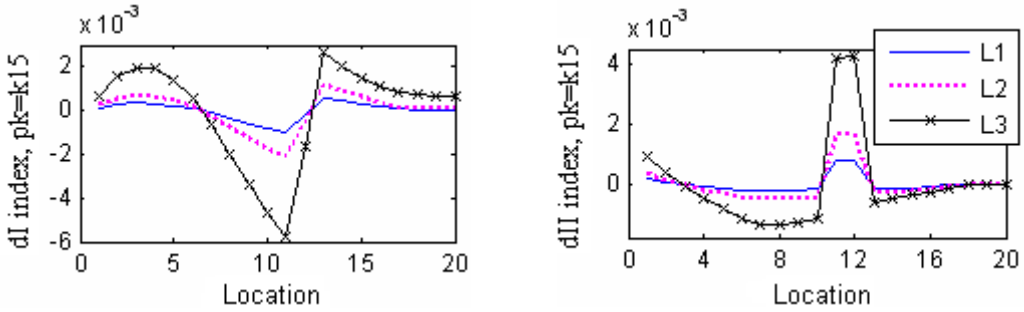

Figure 5.11: d^{I} and d^{II} indexes for 3 levels with p_k=k_{15}

Even though damage occurs at a delicate location, it can be indicated. For example, Figure 5.12 detects damage taking place at the first or at the last element respectively.

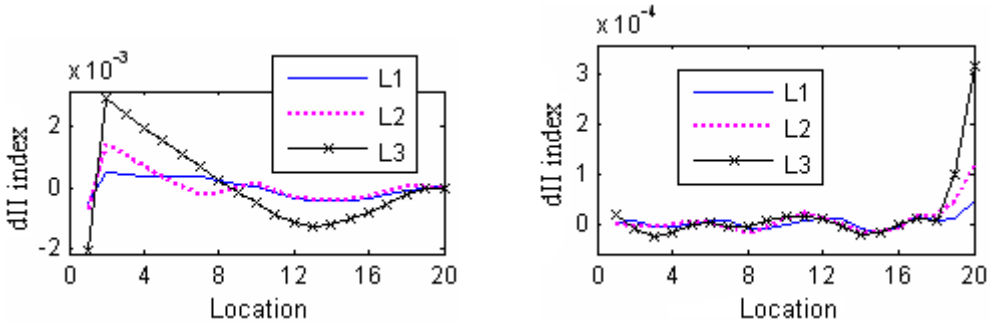

Figure 5.12: d^{II} for 3 levels with damage at element 1 and 20 respectively

The method reveals itself robust when damage develops simultaneously in several elements. Localization results are shown in Figure 5.13 for two different cases of damage. We note that index d^{II} does not indicate the same level of damage in the damaged elements. However, the damage locations are accurately indicated. The difference in magnitude is due

to unequal sensitivities for various damage locations, as discussed in Ray and Tian (1999) [106].

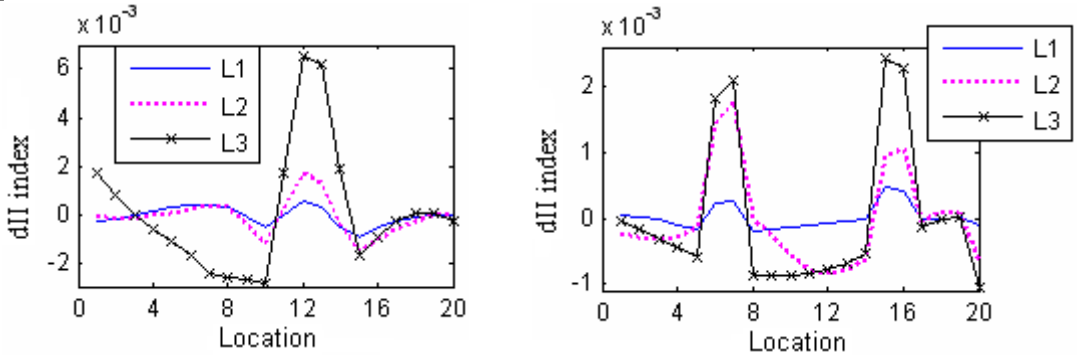

a) damage at elements 12, 13, 14 *b) damage at elements 7 and 16*

Figure 5.13: d^{II} for three levels of damages

Furthermore, the following remarks may be formulated regarding to the sensitivity of the damage localization method to different factors.

- ***Influence of noise***

In order to examine the robustness of the proposed method to noise, the time responses (vertical displacements) are perturbed by adding 5% of noise. Indicators d^{I} and d^{II}, which are the most sensitive to damage in this cantilever beam, are considered. Figure 5.14 corresponds to a damage localized in element 12 and Figure 5.15 to a damage localized in element 15. It appears from these examples that levels L2 and L3 are well detected, however, due to noise, the lowest damage-level L1 is not identified.

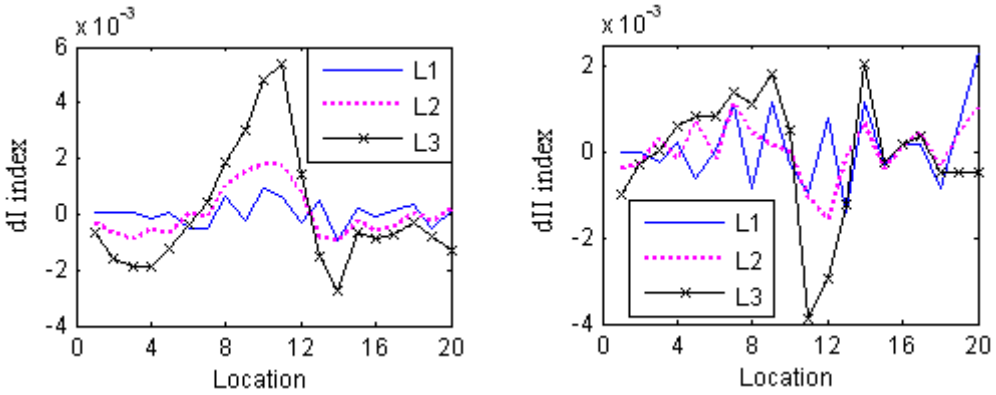

Figure 5.14: Three damage levels in element 12: reduction of stiffness of 10%, 20% and 40%; 5% of noise

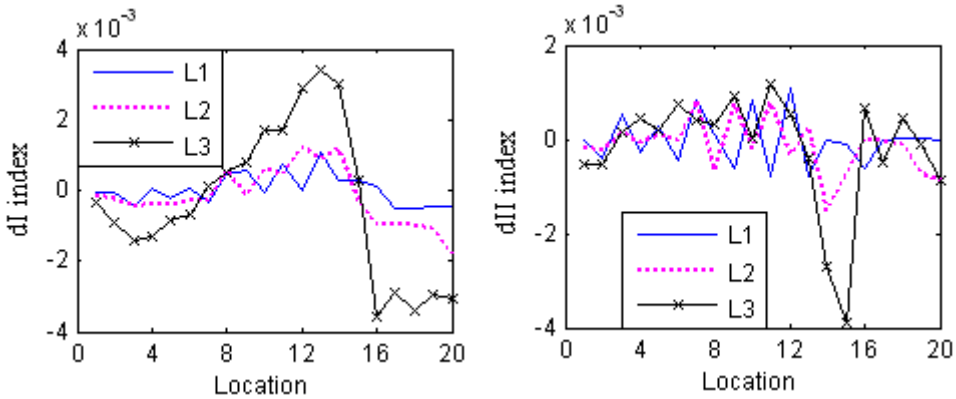

Figure 5.15: Three damage levels in element 15: reduction of stiffness of 10%, 20% and 40%; 5% of noise

- ***Influence of the number of sensors***

Let us assume that the full range of sensors is not available and that the measurements are implemented at fewer locations, which is very common in practical applications. As an example, we consider again the case in which damage is located at element 12 (element between DOFs 11 and 12 of the initial model in Figure 5.9); however, we suppose that only seven sensors are available and distributed as shown in Figure 5.16*a*. In this new situation, the damaged element lays between sensors n° 4 and 5, which is perfectly indicated in Figure 5.16*b, c*.

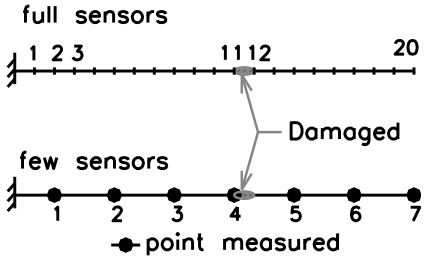

a) Damaged element and sensor instrumentation

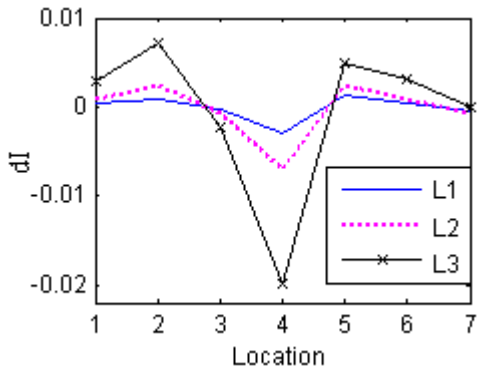

b) d^{I} index

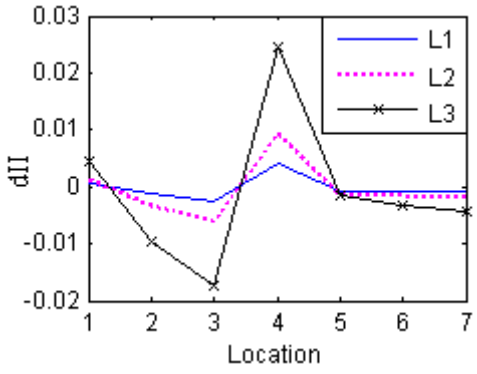

c) d^{II} index

Figure 5.16: Localization of damage in element 12 using 7 sensors only

For a more detailed localization, a deductive technique may be proposed as follows. Based on the real measurements, indexes at other positions between the available sensors can be deducted. For example, the vector of sensitivity computed from the real measurements can be generated by interpolation; the results of this interpolation are illustrated in Figure 5.17*a* in which 19 points (including the 7 points instrumented by sensors) are examined. According to those 19 points, the damaged element is correctly located at points 10 and 11 as illustrated in Figure 5.17*b* and *c*.

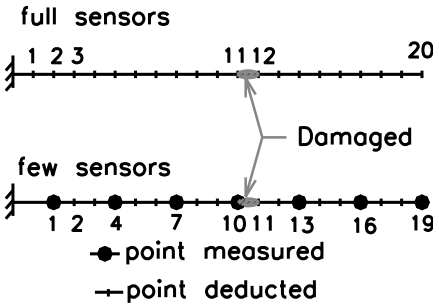

a) Position of points measured (n° 1, 4, 7, 10, 13, 16, 19 - few sensors) and points deducted

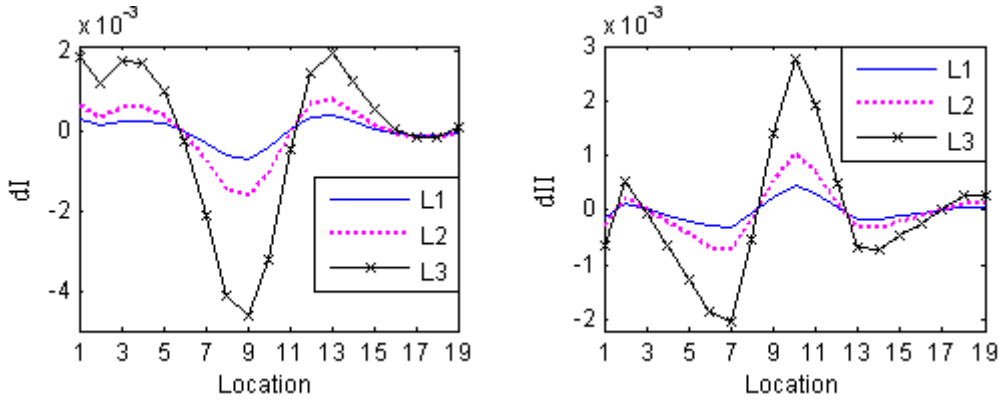

b) d^{I} index *c) d^{II} index*

Figure 5.17: Localization of damage in element 12, represented according to 19 points in the generated sensitivity vector

Other results are also presented in Figures 5.18 and 5.19, when damage occurs in element 14. Figure 5.18 shows localization results based on 7 sensors only and Figure 5.19 gives localization results with a better resolution based on interpolation.

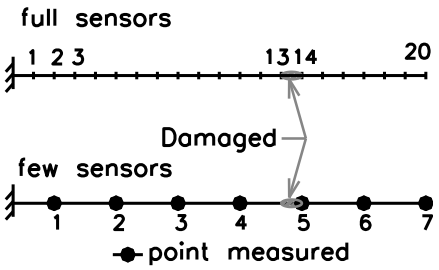

a) Damaged element and sensor instrumentation

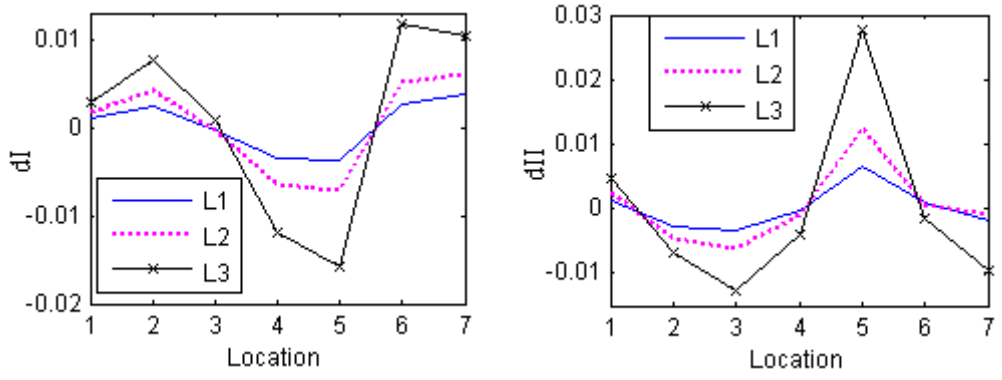

b) d^{I} index *c) d^{II} index*

Figure 5.18: Localization of damage in element 14 using 7 sensors only

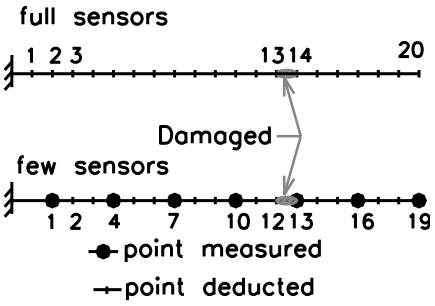

a) Position of points measured (n° 1, 4, 7, 10, 13, 16, 19 - few sensors) and points deducted

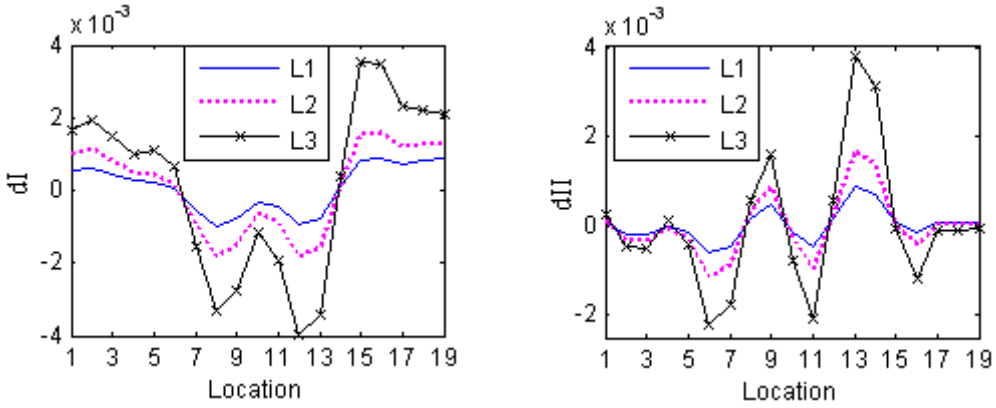

b) d^{I} index *c) d^{II} index*

Figure 5.19: Localization of damage in element 14, represented according to 19 points in the generated sensitivity vector

The results above show that, when only a few sensors are available, damage localization is satisfactory by both d^{I} and d^{II}, if there is a sensor located close to the damaged element. In the next example (Figure 5.20*a*), the case when sensors are not close to the damaged element is examined.

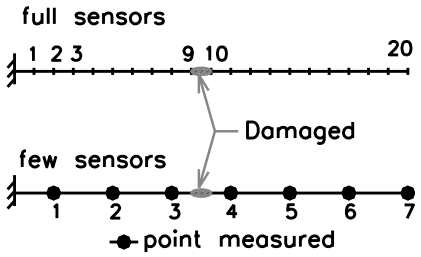

a) Damaged element and sensor instrumentation

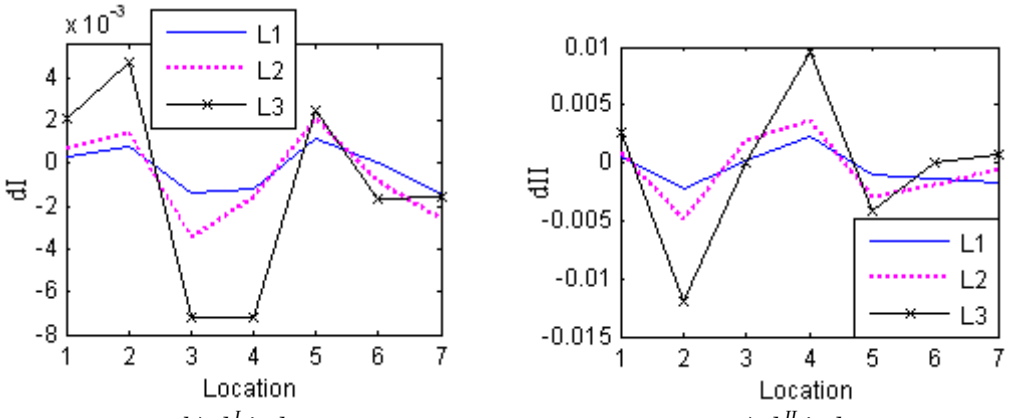

b) d^{I} index *c) d^{II} index*

Figure 5.20: Localization of damage in element 10 using 7 sensors

In Figure 5.20*b*, *c*, the highest index values are found at locations 3 and 4 for index d^{I} and at locations 2 and 4 for index d^{II}. This is a reasonable result because these locations are close to the damage which is located actually between sensors 3 and 4. Regarding the deductive technique, the results are given in Figure 5.21. As shown in Figure 5.21*a*, the damaged element corresponds to points 8 and 9 in the generated vector. Indicators d^{I} and d^{II} are able to find these locations but they also point out other locations, e.g. points 2-4.

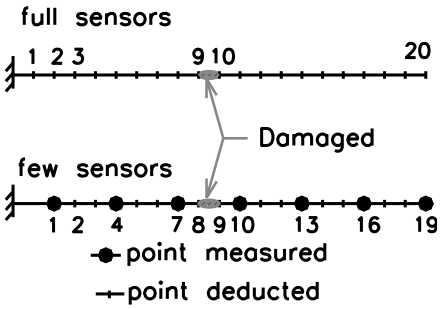

a) Position of points measured (n° 1, 4, 7, 10, 13, 16, 19 - few sensors) and points deducted

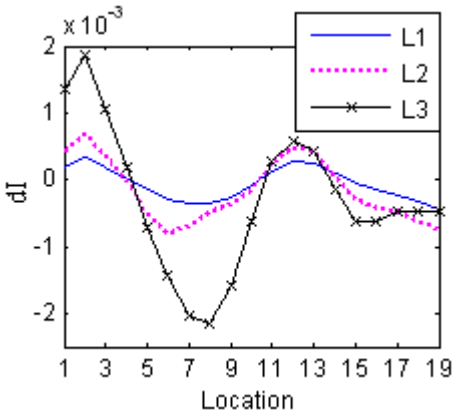

b) d^{I} index

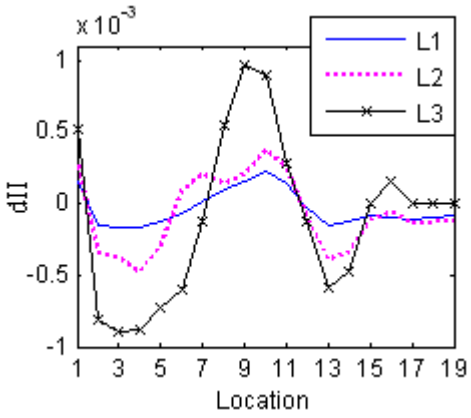

c) d^{II} index

Figure 5.21: Localization of damage in element 10, represented according to 19 points in the generated sensitivity vector

The examples above show that damage can still be localized when the number of sensors is limited. The deductive technique allows to refine localization if sensors are instrumented close to the damage.

5.5.3 Experiments involving a mass-spring system

The next example involves the system of eight DOFs (Figure 5.22) constructed by Los Alamos National Laboratory - LANL and for which data are available in [42]. The system comprises eight translating masses connected by springs. In the undamaged configuration, all the springs have the same constant: 56.7 kN/m. Each mass weighs 419.5 grams; the weight is 559.3 grams for the mass located at the end which is attached to the shaker.

The acceleration response and also the FRFs of all the masses are measured with the excitation force applied to mass 1 - the first mass at the right-hand end (Figure 5.22). The FRFs are assembled so as to localize the damage by the proposed method. Frequency lines are selected from 0 to 55 Hz at intervals of 0.1562 Hz.

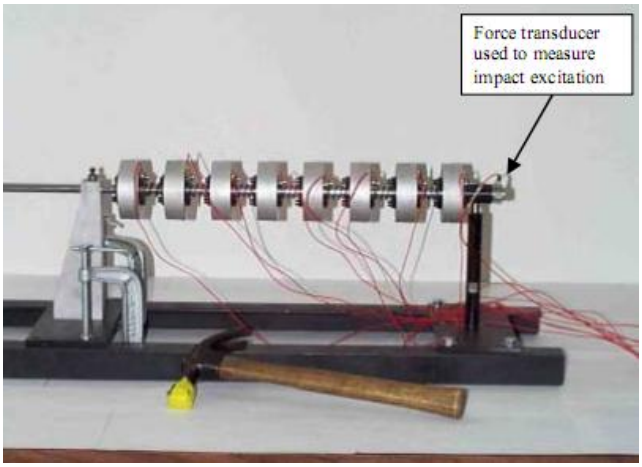

Figure 5.22: Eight degrees of freedom system

First, several experiments were implemented with the system in the healthy state (denoted "H"). Then, the damage (denoted "D") was simulated by a 14% stiffness reduction in spring 5 (between masses 5 and 6). As the excitation was applied only on mass 1, the partial derivative was taken with respect to the first DOF.

The vectors $\Delta\left(\partial \mathbf{U}_1 / \partial k_1\right)$ and d^{I} are shown in Figure 5.23, where the healthy states are denoted "H" and the damaged states "D". Both vectors mark a clear distinction between the two groups - healthy and damaged and can be candidate for damage localization (the d^{I} indicator looks better).

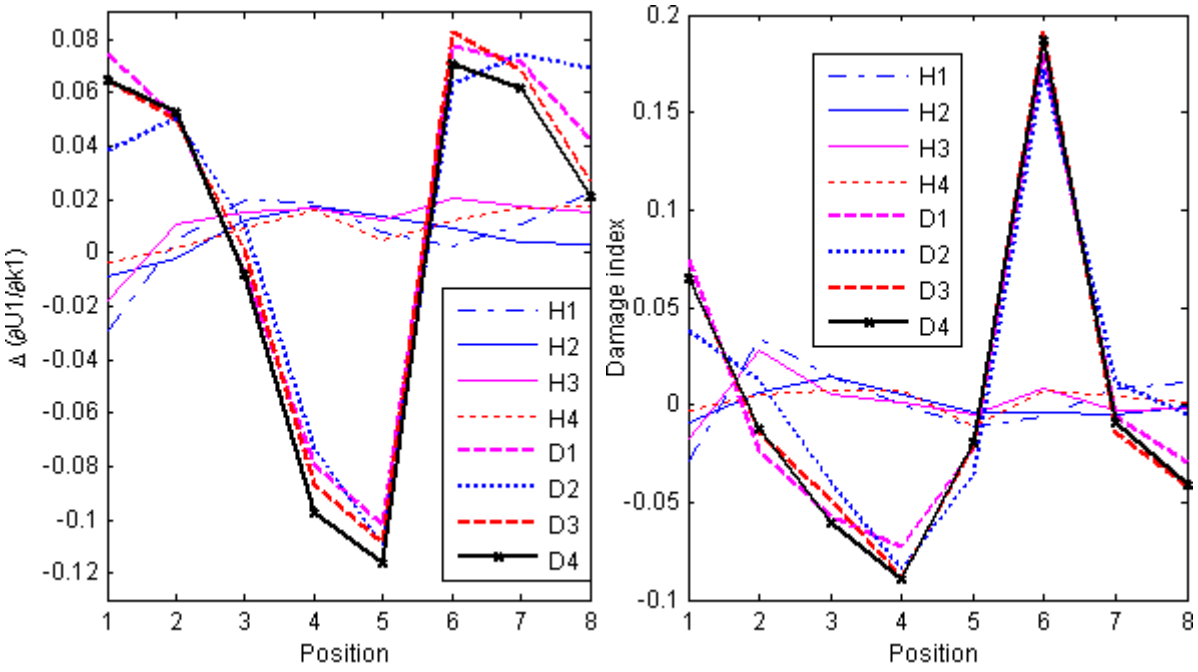

Figure 5.23: $\Delta \dfrac{\partial \mathbf{U}_1}{\partial k_1}$ and d^{I} by impact excitation

Damage is also localized for the random case in Figure 5.24 using d^{I}. Healthy states show regular indexes in all positions, so they do not display any abnormality. By contrast, all the "damaged" curves reveal a high peak in point 6 or 5 where the slope is the most noticeable.

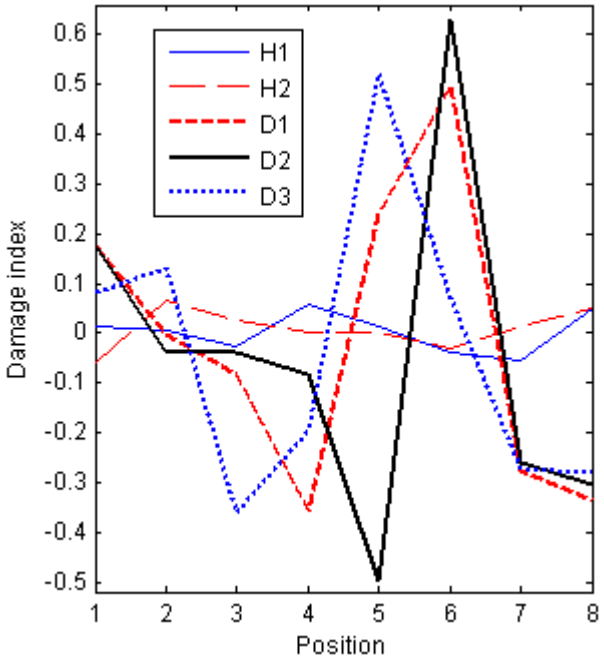

Figure 5.24: d^{I} by random excitation

5.5.4 Experiments in a real bridge case

In this subsection, the case of a real bridge is studied. It has been examined by many authors in the literature (Farrar and Jauregui (1996)[24]; Sampaio *et al.* (1999)[113] and Bayissa *et al.* (2008)[6]) and consists in the I-40 Bridge in New Mexico, which was razed in 1993. Vibration response data of the bridge were recorded for healthy and damaged states. The data used in this example are provided by LANL [42].

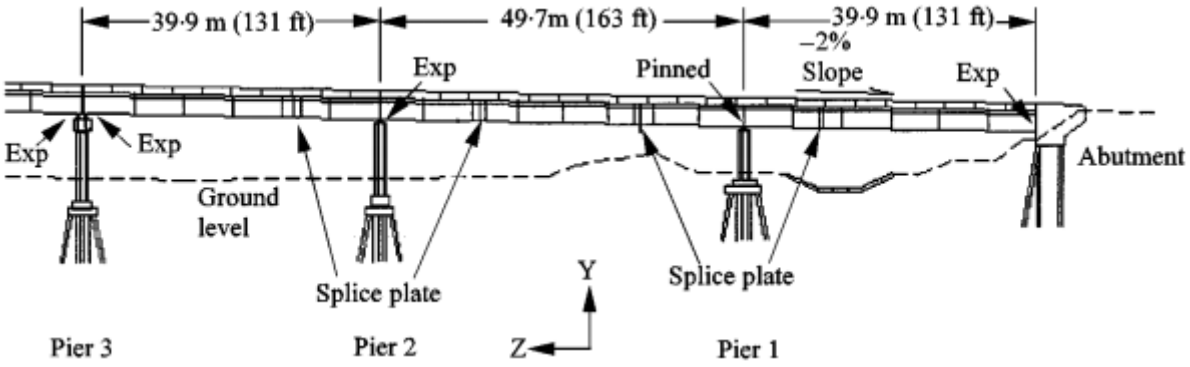

Figure 5.25: Elevation view of the I-40 Bridge [113]

The I-40 Bridge was composed of three continuous spans being supported by concrete piers and abutment (Figure 5.25). The damages were introduced into the middle span of the North plate girder with intention to simulate fatigue cracking that has been observed in plate-girder bridges. Two rows of 13 accelerometers were used for the vibration measurements in

the North and South girders and equally spaced within a span (Figure 5.26). Four levels of damage, denoted from E1 to E4 with increasing degrees were performed (Table 5.1). As noticed in Farrar and Jauregui (1996)[24], based on natural frequencies and mode shapes, the dynamic properties have no change until the final level of damage is introduced. Based on FRF curvature method, Sampaio *et al.* (1999)[113] localized the damage according to all of levels with unequal effects. Bayissa *et al.* (2008)[6] used the Continuous Wavelet Transform and the Zeroth-order moment in localizing the damage of levels E3 and E4.

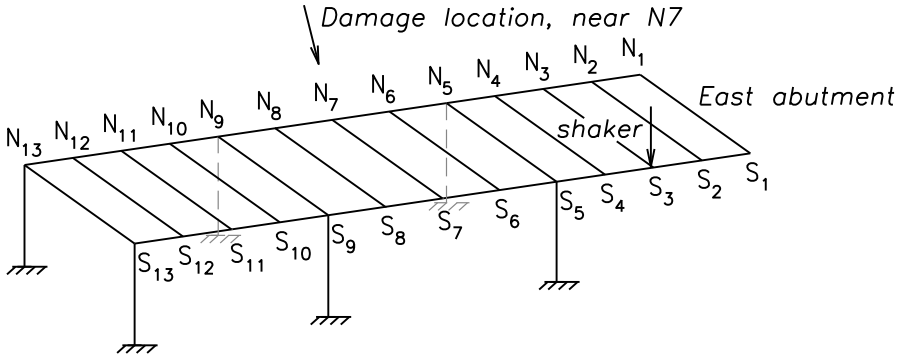

Figure 5.26: Disposition of the accelerometers and damage location

Table 5.1: The first two resonant frequencies from undamaged and damaged forced vibration tests (Farrar and Jauregui (1996)[24])

	Undamaged	E1	E2	E3	E4
f_1 (Hz)	**2.48**	2.52	2.52	2.46	2.30
$\Delta(f_1)$ (%)		1.6	1.6	-0.8	-7.3
f_2 (Hz)	**2.96**	3.00	2.99	2.95	2.84
$\Delta(f_2)$ (%)		1.4	1.0	-0.3	-4.1

Since the FRF matrix is available for the input according to S3 in Figure 5.26, the parameter chosen for the purpose of damage localization in our sensitivity analysis is the coefficient k_3 corresponding to the input. The FRFs measured on the South girder are used. The frequency range [1.8-3 Hz] is selected to eliminate the low-frequency noise and the higher frequency modes.

Figure 5.27*a* presents the sensitivity vectors $\partial \mathbf{U}_1 / \partial k_3$ in two conditions: no damage and damage at the final level - E4. In this picture, the end points delimiting the spans correspond to locations 1, 5, 9 and 13 where the sensitivity is close to zero. It can be observed that the highest sensitivity appears exactly at the position associated to the parameter - k_3, which correspond also to the middle point of the first span. The difference Δ between the two states (undamaged and damaged) is also represented in Figure 5.27*b*. It shows that the largest deviation occurs in the middle span at locations 6, 7 and 8. The normalized deviation Δ_{norm} defined by equation (5.29) is also given in Figure 5.28 in terms of normalized absolute values so that they can be compared to results reported previously (e.g. Sampaio *et al.* (1999)[113]). It shows that localization appears more clearly than in Figure 5.28.

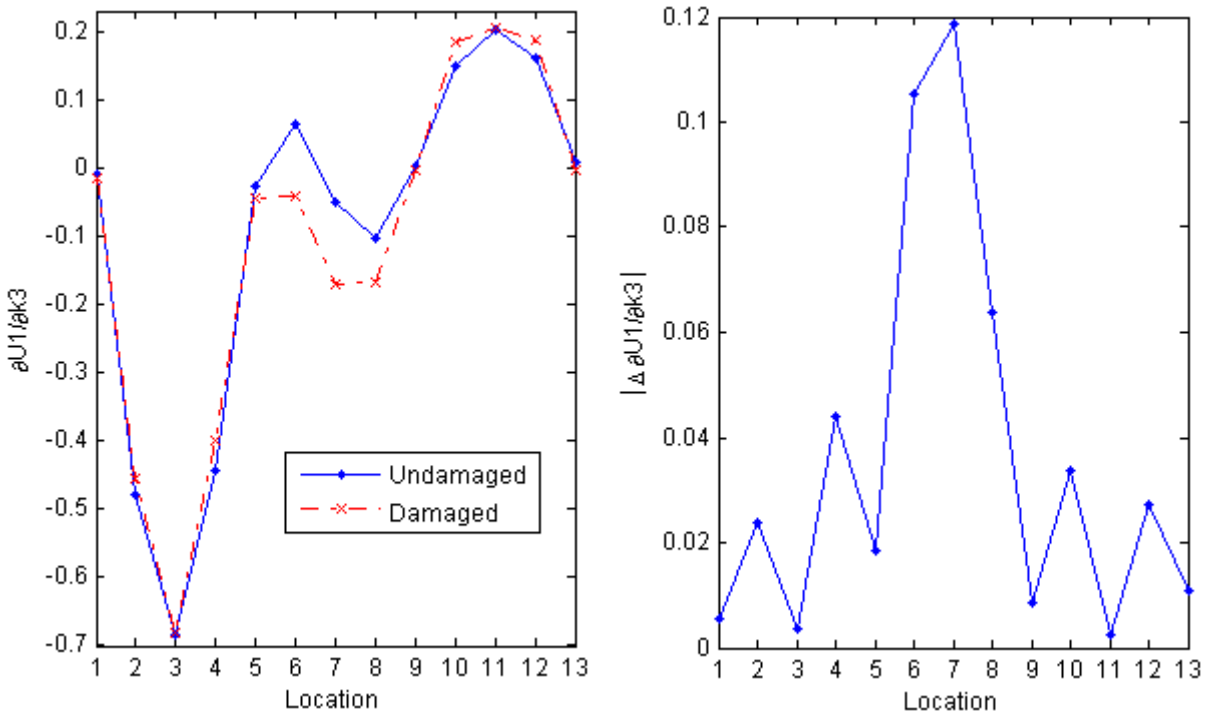

a) sensitivity vectors $\partial \mathbf{U}_1 / \partial k_3$ *b) difference* $|\Delta|$

Figure 5.27: $\partial \mathbf{U}_1 / \partial k_3$ in the healthy and damage (E4) states and their difference $|\Delta|$

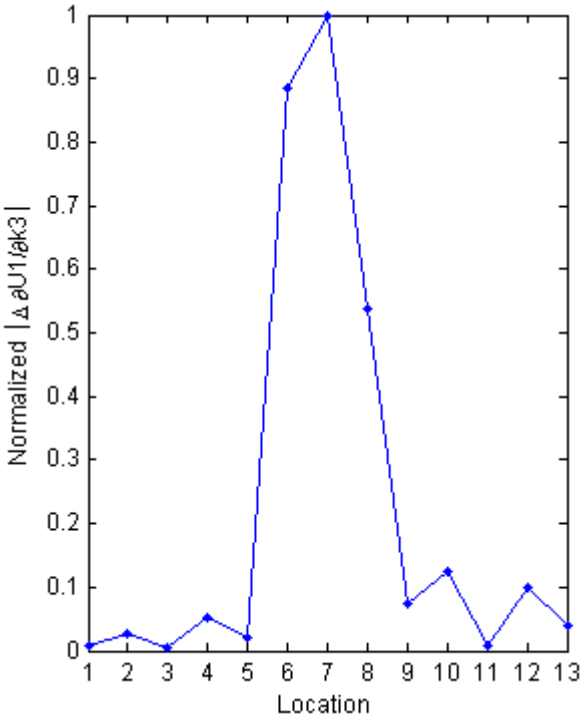

Figure 5.28: Normalized $|\Delta_{\text{norm}}|$, damage E4

Next, the lower levels of damage E3, E2 and E1 are examined successively and the results are presented in Figure 5.29*a*, *b* and *c* respectively. The better localization result is attained for damage state E2. Regarding to damage state E3, the index is higher at locations 8 and 7 as

expected but it also points out a lesser degree at locations 11, 12. This problem can be also noticed in previous works based on the FRF curvature method [113]. According to the results of Reference Farrar and Jauregui (1996)[24] given in Table 5.1, it can be seen that the first two resonant frequencies of state E3 are the closest to the frequencies identified in the undamaged state. Finally, the lowest level of damage E1 is treated in Figure 5.29*c* which also shows a principal peak at location 7 but again another peak at location 12.

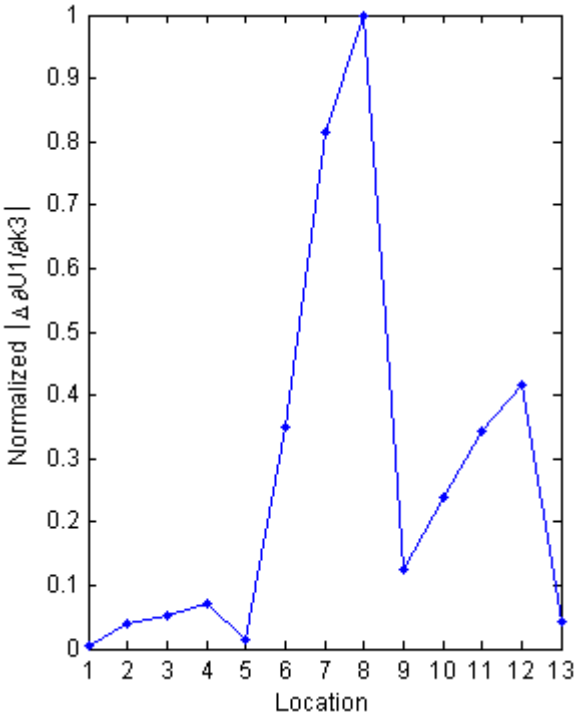

a) Damage localization for damage E3

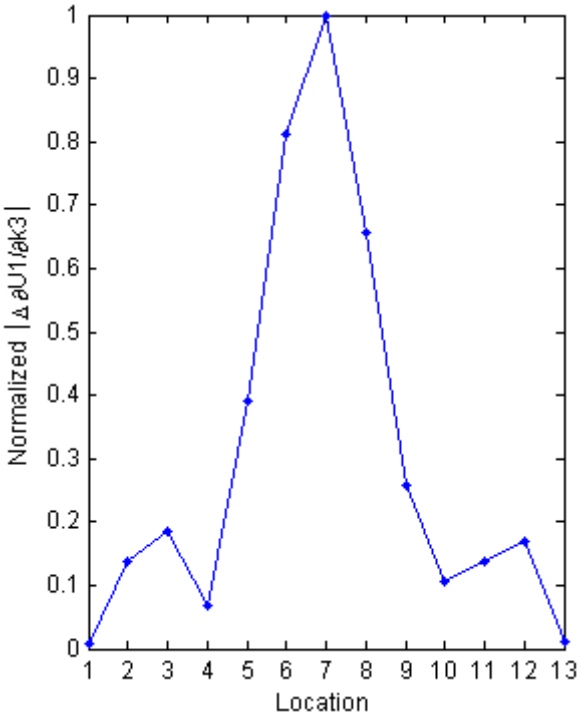

b) Damage localization for damage E2

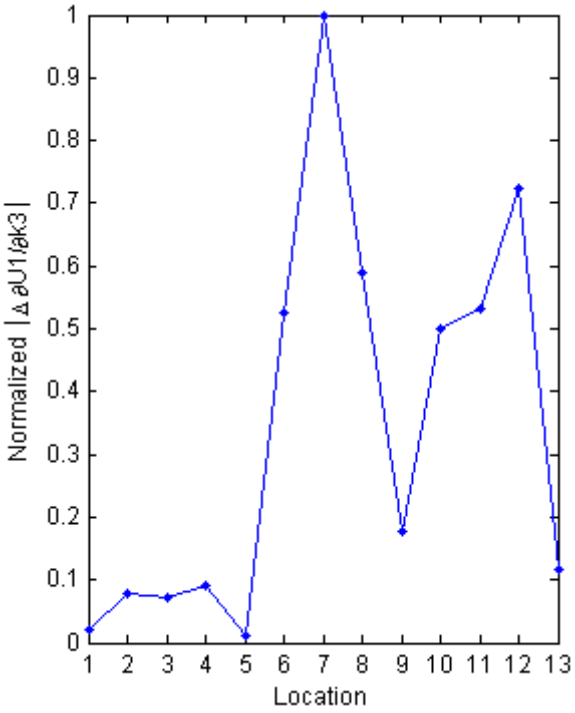

c) Damage localization for damage E1

Figure 5.29: Damage localization for three levels E3, E2, E1

So, through this example, the proposed method shows also robust in localization of damage, particularly the damages are not well remarked by resonant frequency monitoring. The damage location is determined in all conditions; however the effectiveness of the detection is affected by the damage degree.

5.6 Concluding remarks

The sensitivity computation of principal components by analytical methods has been presented in Todd (2009)[126] in both the time domain and the frequency domain. The contribution of the present study is the application of sensitivity analysis in the frequency domain to the problem of damage localization. Damage localization is achieved here as a result of the difference in principal component /eigenvector sensitivity between the reference and the damaged states.

The method relies on the measurement of frequency response functions. However, as demonstrated, it is not necessary to measure the complete FRF matrix in (5.17). If the system matrices are symmetrical, only responses according to parameter p_k are necessary to compute sensitivity with respect to this parameter.

As sensitivity computation from FRFs is easy and does not need an analytical model, the technique should be suitable for online monitoring.

Chapter 6

Parameter Assessment using Sensitivities of Principal Component Analysis

6.1 Introduction

For the sake of efficiency and safety, it is important to well understand the dynamics of structures in operation. To this purpose, it is necessary to have a good knowledge on the structural parameters (namely the geometric and material properties), the applied loads, the nonlinear characteristics, etc. If damage occurs in operation, its knowledge in terms of localization and magnitude is of primary importance for the evaluation of the remaining lifetime of the system. The objective of this chapter is to focus on parameter evaluation with the aim of qualifying the severity of damage.

During the last years, the assessment of parameters has increasingly attracted the interest of researchers (see Ray and Tian (1999)[106], Kim and Stubbs (2002)[57], Koh and Ray (2003)[59], Jiang (2007)[47], Gomes and Silva (2008)[36], Jiang and Wang (2009)[48] for the purpose of damage estimation). Parameter identification has also been used to characterize the nonlinearity of structures (Adams and Allemang (2000)[1], Kerschen *et al.* (2006)[53], Marchesiello and Garibaldi (2008)[78] and Da Silva *et al.* (2010)[15], etc.).

A popular way for evaluating parameters is to resort to model updating, which reduces the discrepancy between the actual responses of the real-life structure and the corresponding analytical responses (often predicted using a finite element model). In this chapter, model updating based on analytical sensitivities of Principal Component Analysis results is utilized for the assessment of parameters, e.g. the severity of damage.

6.2 Model parameter estimation technique

We first assemble the modal features of a system coming from the singular value decomposition (SVD) of the FRF matrix (5.19) into a vector **v** called the model vector. Principal components (PCs) in **U** or their energies in $\mathbf{\Sigma}$ (5.20) may be considered to construct the model vector. In the literature, PC vectors have been often considered as more convenient for damage detection so they will be used here.

The model vector **v** of a system is usually a nonlinear function of the parameters $\mathbf{p} = [p_1 \ldots p_{n_p}]^{\mathrm{T}}$ where n_p is the number of parameters. The Taylor series expansion (limited to the first two terms) of this vector in terms of the parameter is given by:

$$\mathbf{v}(\mathbf{p}) = \mathbf{v}_a + \sum_{k=1}^{n_p} \frac{\partial \mathbf{v}}{\partial p_k} p_k = \mathbf{v}_a + \mathbf{S}\,\Delta\mathbf{p} \tag{6.1}$$

where $\mathbf{v}_a = \mathbf{v}\big|_{\mathbf{p}=\mathbf{p}_a}$ represents the model vector evaluated at the linearization point $\mathbf{p} = \mathbf{p}_a$. **S** is the sensitivity matrix of which the columns are the sensitivity vectors. The changes in parameters are represented by $\Delta\mathbf{p} = \mathbf{p} - \mathbf{p}_a$.

The residual vector measures the difference between analytical and measured structural behaviors (Link (1999)[71]):

$$\mathbf{r}_w = \mathbf{W}_\mathbf{v}\mathbf{r} = \mathbf{W}_\mathbf{v}\left(\mathbf{v}_m - \mathbf{v}(\mathbf{p})\right) \tag{6.2}$$

where $\mathbf{v}_m$ represents measured quantities. The weighting matrix $\mathbf{W}_\mathbf{v}$ (according to a weighted least squares approach) takes care of the relative importance of each term in the residual vector **r**. Substituting (6.1) into (6.2) and setting $\mathbf{r}_a = \mathbf{v}_m - \mathbf{v}_a$ leads to the linearized residual vector:

$$\mathbf{r}_w = \mathbf{W}_\mathbf{v}\mathbf{r} = \mathbf{W}_\mathbf{v}(\mathbf{v}_m - \mathbf{v}_a - \mathbf{S}\Delta\mathbf{p}) = \mathbf{W}_\mathbf{v}(\mathbf{r}_a - \mathbf{S}\Delta\mathbf{p}) \tag{6.3}$$

Let us define the penalty (objective) function to be minimized as the weighted squared sum of the residual vector:

$$\mathbf{J} = \min\left(\mathbf{r}_w^{\mathrm{T}}\mathbf{r}_w\right) = \min\left(\mathbf{r}^{\mathrm{T}}\mathbf{W}\mathbf{r}\right), \quad \mathbf{W} = \mathbf{W}_\mathbf{v}^{\mathrm{T}}\mathbf{W}_\mathbf{v} \tag{6.4}$$

Equation (6.3) may be solved from the objective function derivative $\partial\mathbf{J}/\partial\Delta\mathbf{p} = 0$, which produces the linear equation:

$$\mathbf{W}_\mathbf{v}\mathbf{S}\Delta\mathbf{p} = \mathbf{W}_\mathbf{v}\mathbf{r}_a \tag{6.5}$$

for which the solution is:

$$\Delta\mathbf{p} = (\mathbf{S}^{\mathrm{T}}\,\mathbf{W}\mathbf{S})^{-1}\mathbf{S}^{\mathrm{T}}\,\mathbf{W}\mathbf{r}_a \tag{6.6}$$

In our approach, we will assume that the number of measurements is larger than the number of updating parameters, which yields an overdetermined system of equations. Note that the conditioning of the sensitivity matrix **S** plays an important role in the accuracy and the uniqueness of the solution. The solution may be implemented using QR decomposition or SVD, which allows to check the conditioning of **S** [71].

The updating process is shown in Figure 6.1 where the *i* th PC is considered as the model vector. The two separated branches correspond to: 1) the analytical model which will be updated; 2) experimental responses of the damaged structure, input position and correction parameters. The choice of correction parameters may be based on the damage localization results. A minimum number of correction parameters facilitates an accurate and efficient estimation.

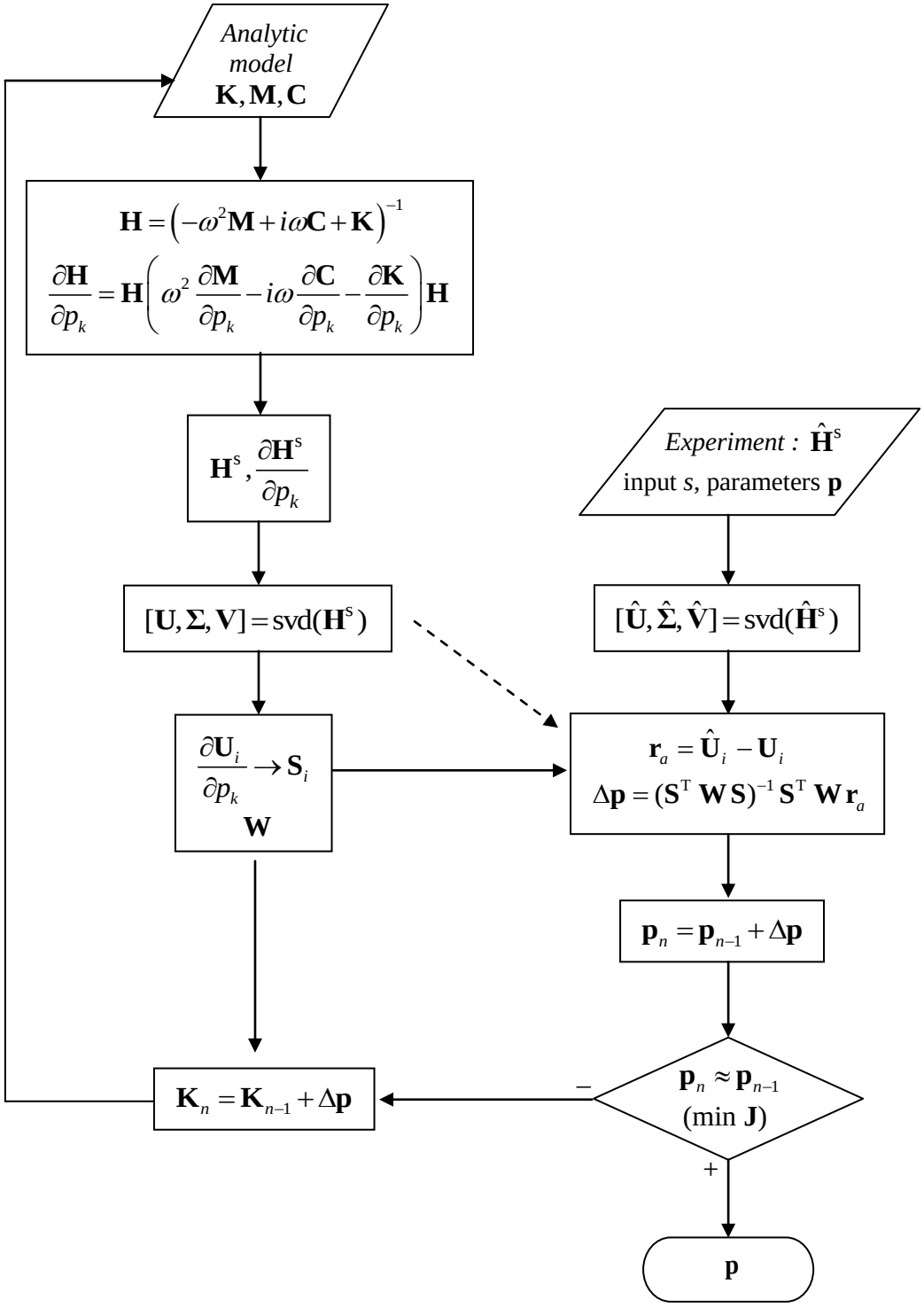

Figure 6.1: Updating diagram

- **Choice of weighting matrix**

The positive definite weighting matrix is usually a diagonal matrix whose elements are given by the reciprocals of the variance of the corresponding measurements (Friswell and Mottershead (1995)[30]):

$$\mathbf{W} = \mathrm{diag}(w_1, w_2, ..., w_i, ..., w_m) \tag{6.7}$$

where m is the number of measurements. This matrix may be based on estimated standard deviations to take into account the relative uncertainty in the parameters and measurements:

$$\mathbf{W} = \mathbf{Var}^{-1} \text{ with } \mathbf{Var} = \text{diag}(\sigma_1^2, \sigma_2^2, ..., \sigma_i^2, ..., \sigma_m^2) \tag{6.8}$$

and σ_i is the standard deviation of the i th measurement. The relationship between **W** and the variance matrix **Var** is assumed to be reciprocal because a correct data has a small variance but presents a significant weight in the estimate. Similarly, in the problem of damage evaluation, the weight may be intensified according to damaged locations in order to improve the efficiency of the technique, i.e. to accelerate the convergence and raise the accuracy.

In the following, the parameter estimation technique described above is used for the quantitative assessment of damage.

6.3 Applications to the quantitative assessment of damage

6.3.1 Spring-mass-damper system

Let us consider again the spring-mass-damper system of 20 DOFs presented in §5.5.1. Damage is simulated by a stiffness reduction of some elements and the input is introduced at DOF n° 8. The corresponding frequency response functions (FRFs) are measured in the frequency range from 0 to 2 rad/sec with a sampling frequency of 0.005 rad/sec. The first principal component and its sensitivity are used for damage evaluation.

If all spring constants are taken into account in the parameter vector **p**, we can find out the damaged element looking at the evolution of **p** through the iteration process. Figure 6.2 shows the results when damage corresponding to a stiffness reduction of 10% occurs in a single element (element n° 5 or 9 respectively). No weighting matrix was introduced in the procedure.

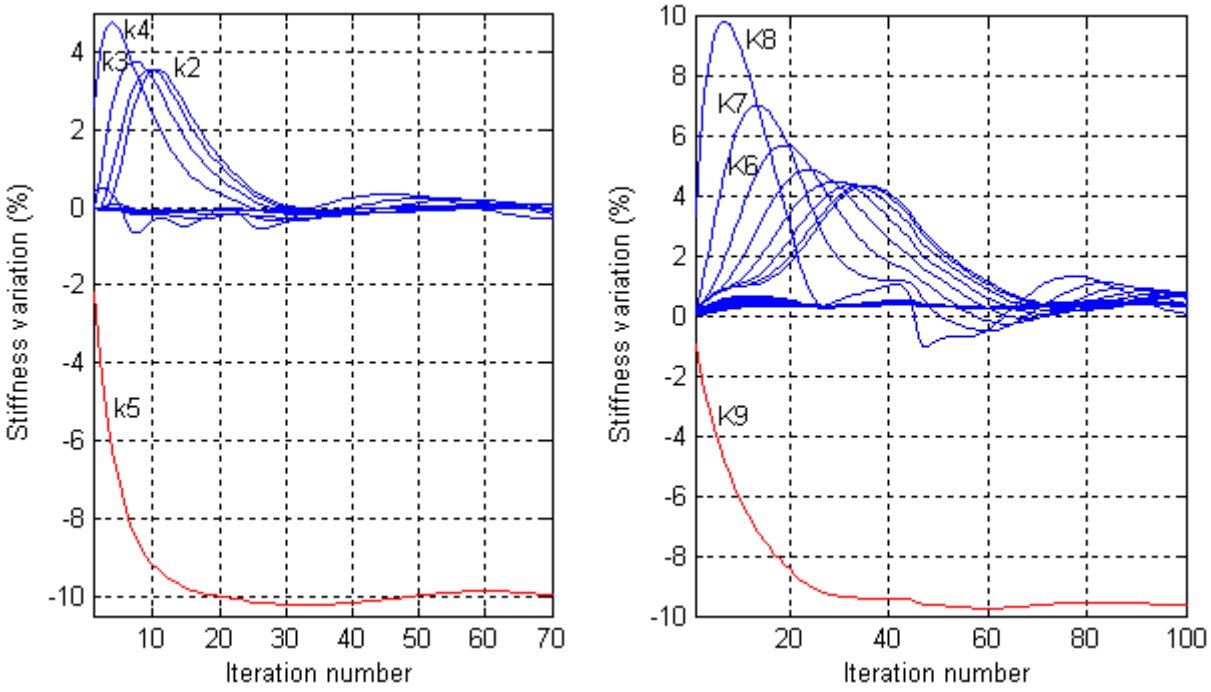

a) damage in element 5 *b) damage in element 9*

Figure 6.2: Evaluation of the stiffness change in all elements

The number of iterations to converge to the solution is very high in this case. However, if only the damaged element is considered in the parameter vector (based on the damage localization results previously performed in Chapter 5), the convergence rate and the accuracy are largely improved.

For illustration, only spring n° 9 (corresponding to the damaged element) is considered now in the parameter vector. Different levels of damage (stiffness reduction of 5%, 10%, 20%, 25% and 30%) are considered and the results are shown in Figure 6.3*a*.

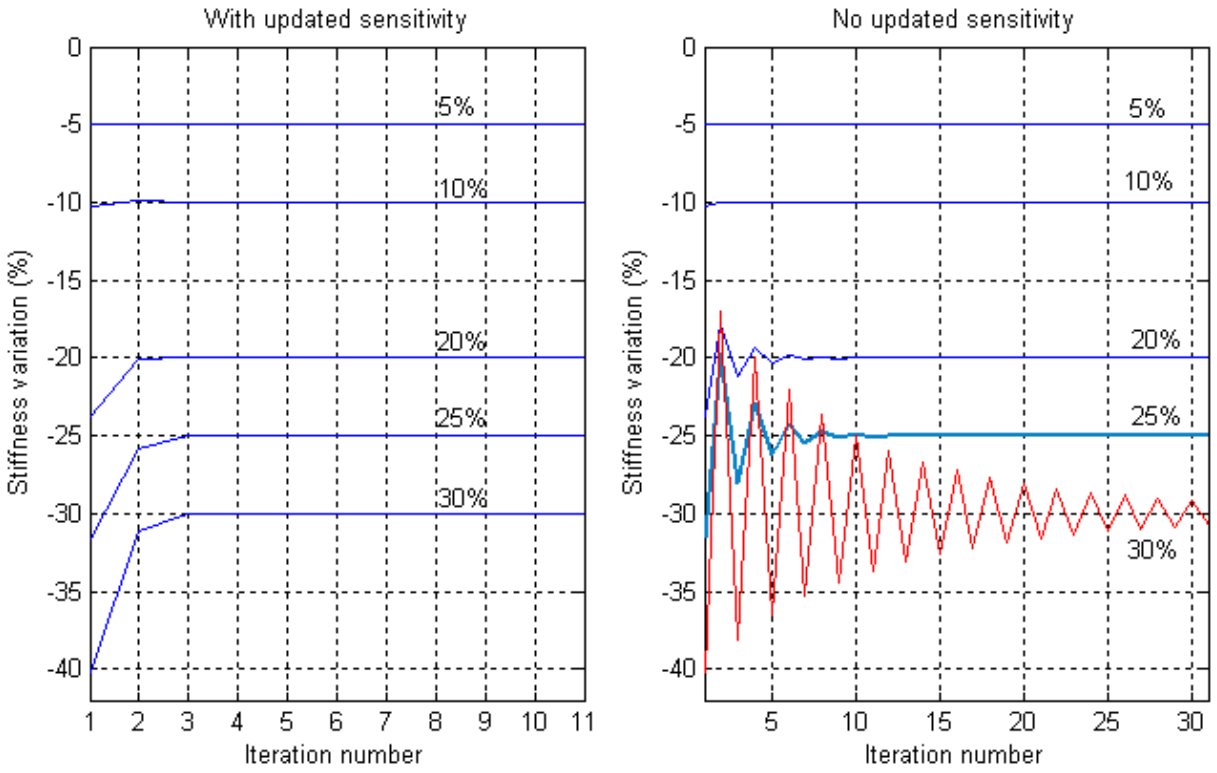

a) with updated $\partial \mathbf{U}_i^a / \partial p_k$ *b) without updated* $\partial \mathbf{U}_i^a / \partial p_k$

Figure 6.3: Damage evaluation

Let us discuss the use of the sensitivity vector at each iteration step. The question is if we can use the initial sensitivity during the whole iteration process, i.e. is it necessary to update $\partial \mathbf{U}_i / \partial p_k$ at each iteration step? This short cut which is illustrated in Figure 6.1 by the arrow in dashed line, is proposed to save the computation of sensitivities at each iteration step, which may be sometimes costly.

The results of damage evaluation without updating of the sensitivity vector $\partial \mathbf{U}_i / \partial p_k$ are presented in Figure 6.3*b*. Compared to Figure 6.3*a*, it can be observed that results are quite similar in the case of small damages for both ways of calculation. However, for higher damages, the difference between $\partial \mathbf{U}_i / \partial p_k$ before and after an iteration step may be high and more iterations are necessary to converge.

If several elements are damaged, the procedure also works. Two examples are presented in Figure 6.4 for which the parameter vector contains many damaged elements (as well as undamaged elements).

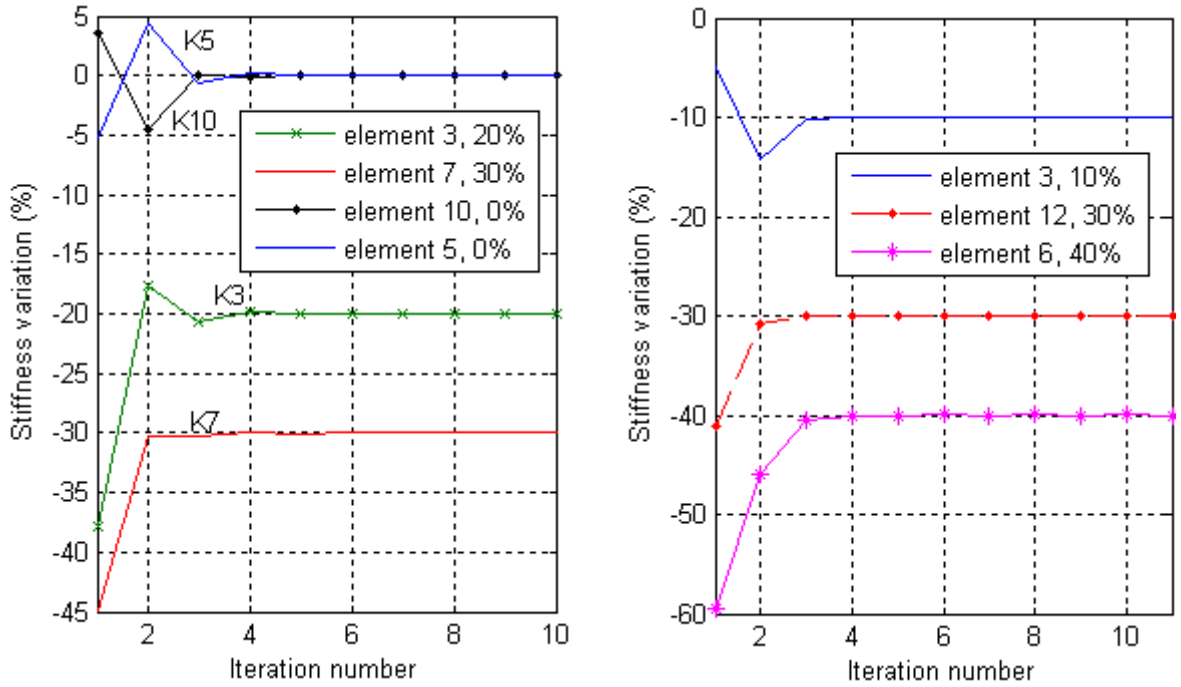

Figure 6.4: Evaluation for damages in several elements

6.3.2 Cantilever beam

The cantilever beam examined in §5.5.2 is now considered with the model of 10 elements. We consider firstly the damage occurring in a single element. For example, the stiffness of element 5 is subjected to reduction. FRF matrices are considered for an excitation in node 9. Frequency lines are selected from 0 to 200 rad/sec. Because the damage localization is readily identified, the first PC and its derivative with respect to the damaged element are considered. For the sake of efficiency and accuracy, only the coefficients of the stiffness matrix corresponding to the damaged element are taken into account in the parameter vector **p**.

The diagonal weighting matrix defined by (6.8), as discussed above, is intensified in entries according to damaged elements in order to increase the calculation efficiency. For this purpose, the standard deviation of the principal component (PC) vector elements is preliminarily assumed to be 10% of the corresponding element in the considered PC. And in particular, to take advantage of sensitivity vector, the entries matched to the damaged elements are assigned a lower variance so as to give a larger weighting in the algorithm. A fitting variance for measurement in damaged elements can improve significantly the convergence speed. In the tests below, the standard deviation values according to the damaged elements were multiplied by a factor between 1% and 3%. The evaluation of some of the damages is shown in Figure 6.5. Several levels are considered so that the stiffness of element 5 is reduced by 5%, 10%, 20%, 30% and 50%. The data has also been perturbed with 5% of noise, but it still shows satisfactory results.

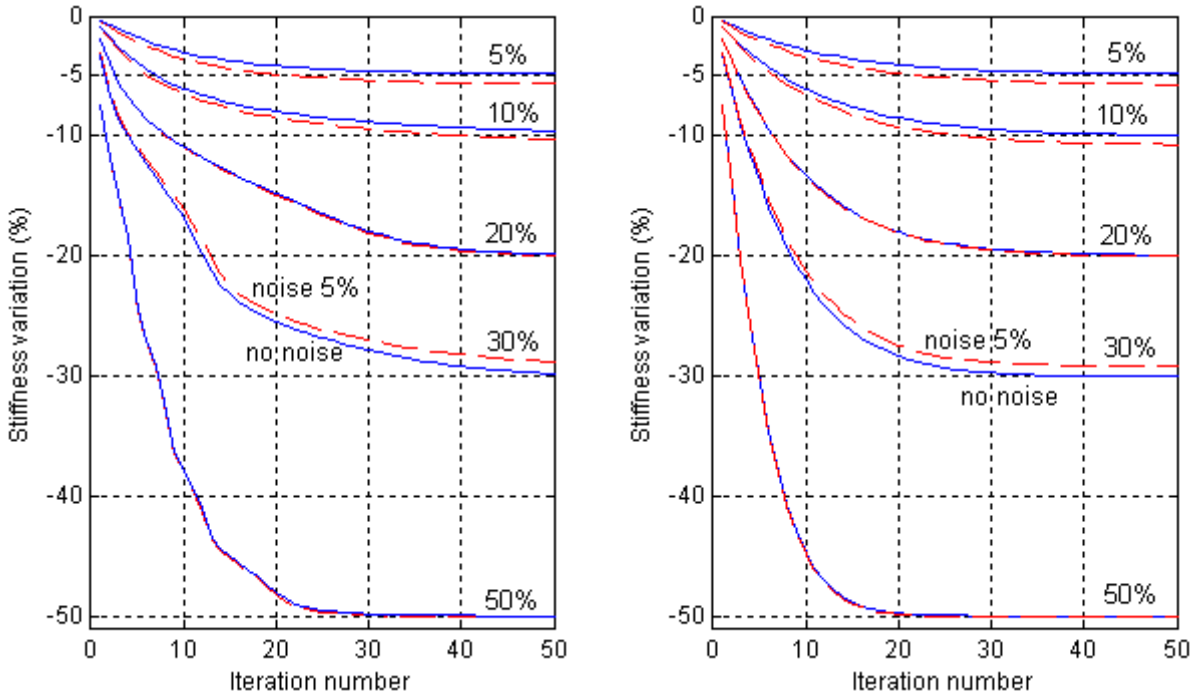

a) with updated $\partial \mathbf{U}_i / \partial p_k$ *b) without updated* $\partial \mathbf{U}_i / \partial p_k$

Figure 6.5: Evaluation damage, noise free (____) and noise 5% (__ __ __)

In this particular problem, we note that the convergence rate to the correct answer is not accelerated when the sensitivity is updated. Moreover, without sensitivity updating, the parameter evolution looks more stable and smoother. It can be explains as follows. Since we have only one term in the parameter vector (p_k is the coefficient corresponding to DOF n° 5 in the stiffness matrix), the matrix **S** contains one column and equation (6.6) can be expressed as:

$$\Delta \mathbf{p} = \frac{\mathbf{S}^{\mathrm{T}} \mathbf{W} \mathbf{r}_a}{\mathbf{S}^{\mathrm{T}} \mathbf{W} \mathbf{S}} \tag{6.9}$$

If the sensitivity is updated at each step, the variation of the denominator in (6.9) affects clearly the evolution rate of the parameter. On the contrary, when the initial sensitivity is used at each iteration step, only the numerator of (6.9) is updated, which assures a smooth convergence to the good solution, as illustrated in Figure 6.5*b*.

So in this example, the use of the initial sensitivity appears advantageous since it ensures a more stable evolution of the computation when estimating the damage. Moreover, the CPU time is efficiently reduced for two reasons: the convergence to the good solution is faster and the calculation of sensitivities is avoided at each step.

Let us now examine the problem of many elements being simultaneously damaged; these elements may be close or distant from each other. The results of various occurrences of damage are given in Figures 6.6 and 6.7 for the same or for different levels, respectively. In this example, about 5% of noise was taken into account.

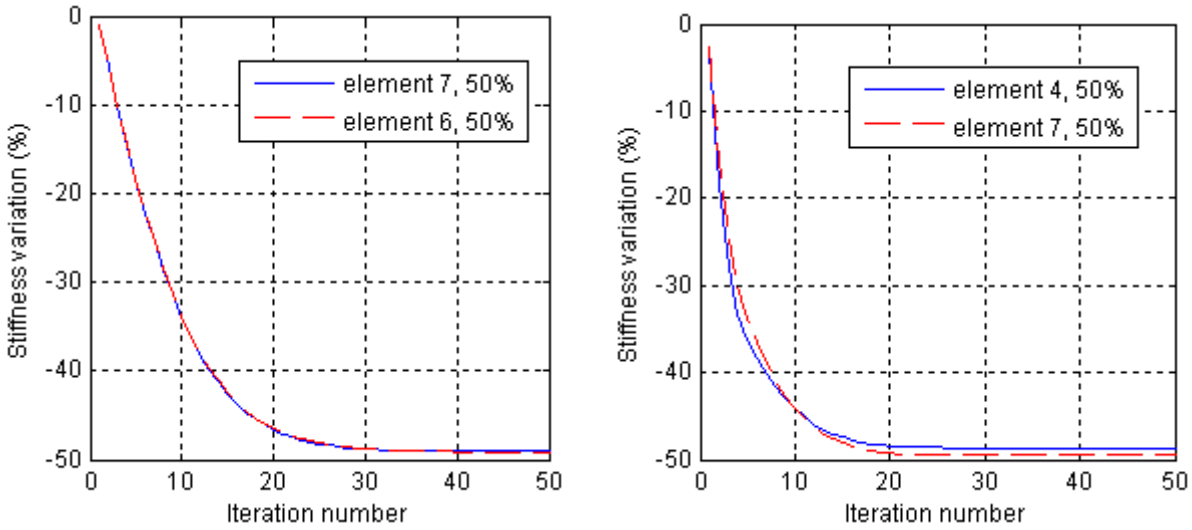

Figure 6.6: Damage of the same level in several elements

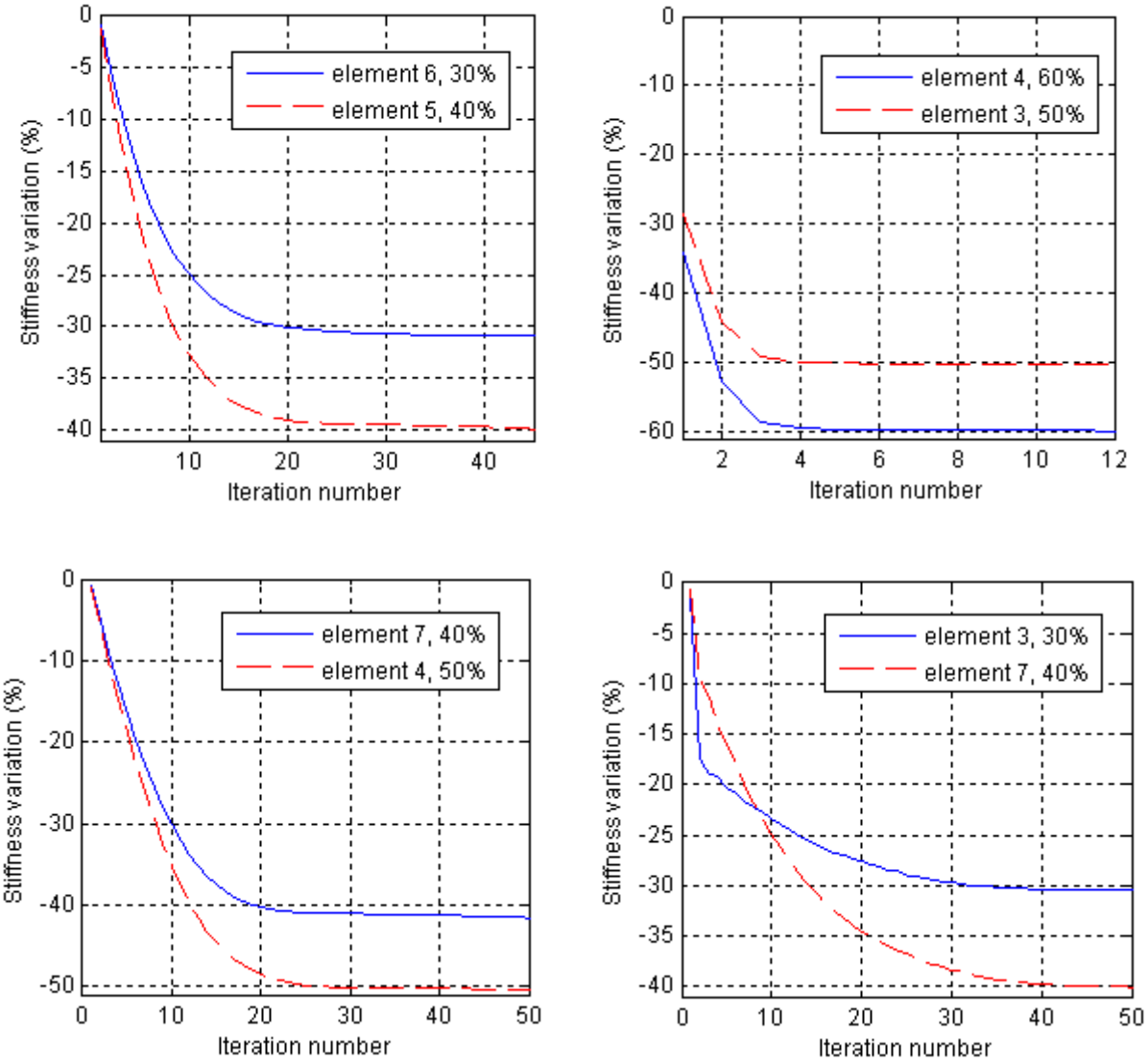

Figure 6.7: Damage of different levels in several elements

It is worth noting that the accuracy of the result depends on several factors when many elements are damaged, namely, the relative position of the damaged elements and the difference between their levels of damage. Input position also plays an important role on the number of iterations of the updating process. Generally, the estimate is more effective if the degrees of damage of different elements are not too different. Data recorded from an excitation close to the damaged location often accelerates the convergence speed.

6.3.3 Experiments on the Eight Degree of Freedom system

We examine again the 8 DOF system considered in §5.5.3. In order to evaluate the amplitude of damage, it is necessary to build an analytical model of the system (Figure 6.8). The assembly of the stiffness and mass matrices is straightforward since the masses and the spring constants are known. Damping in the system is caused primarily by Coulomb friction and was minimized in the experiments. Proportional damping is assumed here with the damping matrix equal to 1% of the mass matrix. According to §5.5.3, we also recall that damage was simulated by a reduction of 14% of the stiffness in spring n° 5.

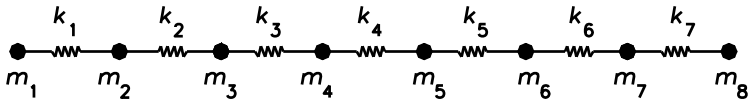

Figure 6.8: Mass-spring model

For the sake of consistent data, a frequency line is selected from 6 to 29 Hz, which covers only the first physical mode and removes noisy low frequencies. The variations in stiffness of spring n° 5 are shown in Figure 6.9 for impact and random excitations respectively. The healthy states are denoted “H” and the damaged states “D”.

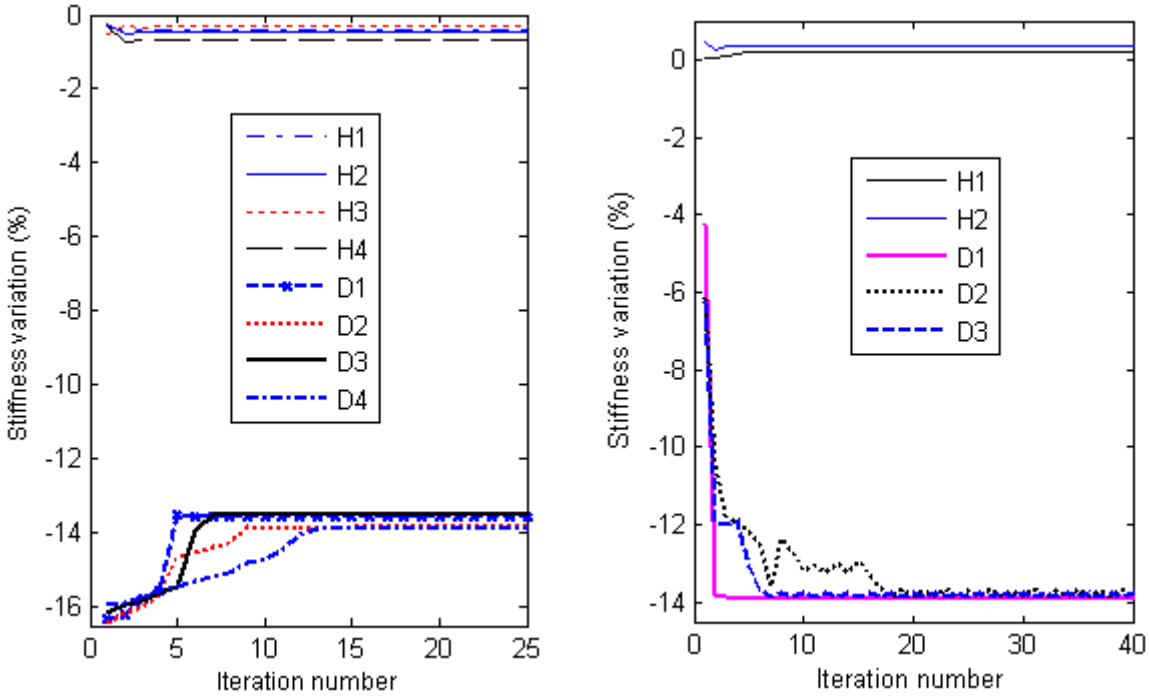

a) case of impact excitation *b) case of random excitation*

Figure 6.9: Evaluation of damage

For both two types of excitation, the results are very satisfactory. All false-positives indicate small stiffness variations in the element concerned, and they show any detection of damage. Conversely, all damaged states give an evaluation very close to the exact damage – a stiffness reduction of 14%.

6.4 Concluding remarks

The results obtained in this chapter on numerical and experimental examples show that the method presented here is efficient for assessing the severity of damages even if data is perturbed by noise. The use of the weighting matrix in the computation of residuals may not only enhance the convergence speed, but also enable and facilitate the evaluation of damage when it occurs at several locations. Furthermore, an appropriate input position is important for the convergence to the solution.

Damage evaluation is based on the correlation of a principal component between experimental (current) and analytical data. So it is necessary to verify that the considered PC describes the same “mode” in both the experimental and the analytical model. Otherwise, the problem may lead to divergence.

Conclusions

Several monitoring methods of dynamical systems were studied in this work. The objective of these methods (WT, SOBI and KPCA) is to diagnose the presence of structural damage or the onset of a nonlinear behaviour from output-only measurements. Along with these detection methods, sensitivity analysis of PCA was developed to localize and quantify the detected damage. The robustness of the methods was studied using numerical and experimental examples (e.g. beam with nonlinearity, aeroplane model, mass-spring and beam systems) and illustrated on data obtained from industrial and civil engineering applications (electro-mechanical devices, quality control of welded joints and I-40 bridge).

The WT is very convenient when analysing non-stationary signals and is well adapted to observe nonlinear behaviours of dynamical systems. For example, the WT is able to put in evidence phenomena such as the occurrence of sub- or super-harmonics, the combination of fundamental 'modes', etc. By combining the results of the WT on an ensemble of signals (at different DOFs) in terms of amplitude, it is possible to inspect the time evolution of deformation modes associated to the ridges of the transform. Calculation of the angles between the subspaces spanned by those deformation modes provides a detection index that allows indicating the onset of nonlinearity in the system. This index is able to associate several modes simultaneously and appears fine with regard to the frequency resolution of the transform. However, the WT shows some drawbacks when the natural frequencies of the system are close or when noise contaminating the signals causes intermittences in the WT responses.

SOBI, as other BSS techniques based on the assumption of system linearity is attractive because of its rapidity and easiness of implementation. Some of the WT drawbacks cited above are relieved with SOBI which reveals quite adequate for identification and damage detection. However, the use of SOBI is more restrictive when processing nonlinear/non-stationary signals and systems with high damping. In this case, the combination of SOBI with the Hankel matrix (ESOBI) enhances considerably the identification and detection processes. ESOBI can also provide more useful information for non-stationary signals by adjusting the time-lag in the Hankel matrix. Moreover, ESOBI may be applied even using one sensor only.

The BMID technique which is an extension of SOBI looks really promising because it is able to examine structures of general damping. BMID was found to be more efficient than SOBI for modal identification as well as for damage detection.

The KPCA method reveals quite appealing in processing nonlinear data. Contrary to the WT and SOBI, KPCA achieves the detection problem without modal identification. In KPCA, the vibration data is first projected into a high dimensional feature space using a nonlinear mapping, and PCA is then performed in this space for the purpose of detection. As in SOBI, the use of the Hankel matrix improves the robustness of KPCA in all aspects.

According to our personal judgment, the main performances/characteristics of the detection methods considered in the present work are listed in Table 7.1.

Table 7.1: Performances/characteristics of the methods

Features	Performances/characteristics of the methods		
	WT	SOBI	KPCA
Discrimination of close frequencies	medium	high	
Ability to describe the nonlinearity	high	low	
Nonlinearity sensitivity	high	medium	high
Ease of implementation	medium	high	high
Computation load	medium	low	medium
Detection by limited number of sensors	medium (only frequencies)	high	high
User-defined parameters	- wavelet properties ω_0, σ - physical modes for the detection	- physical modes for the detection	parameter of the kernel function

Once the detection problem has been solved using one of the three methods described above, the problem of damage localization and quantification may be studied using sensitivity analysis of Principal Component Analysis. In this technique, localization is based on output-only measurements and it does not require recording the complete FRF matrix as a subset of this matrix due to a single input may be adequate. For the sake of quantification, an analytical model is required. A weighting matrix can be used for model parameter estimation in order to accelerate convergence and increase accuracy, particularly when several elements are concerned in the updating process.

To the author's opinion, the main original contributions of the thesis are the following.

- From subspaces spanned by deformation modes (WT, SOBI) or kernel principal components (KPCA), detection was achieved through the concept of subspace angle. The performance of the WT in analyzing nonlinear systems has been reported in Nguyen *et al.* (2010)[87]. Regarding to the SOBI method, it is commonly applied in the literature for the purpose of modal identification using stationary data while in this work, SOBI is proposed to process non-stationary responses and to detect damage (Section 3.6). An extension of SOBI called BMID is also exploited and looks very promising for damage detection. Regarding KPCA, it is used in the literature essentially for image processing and in the chemical domain. In Chapter 4, we have taken advantage of KPCA to perform detection in mechanical systems.
- It has been shown on numerous examples that detection may be considerably enhanced by performing SOBI /BMID and KPCA on block Hankel matrices (the so-called E-methods) rather than on observation matrices. Hankel matrices facilitate the

detection of slight changes in dynamical systems thanks to the increase of sensitivity obtained by exploiting temporal correlations of measurements. Furthermore, the proposed E-methods give the possibility to solve detection problems using one sensor only (Nguyen and Golinval (2010)[91]). Additionally, in the KPCA method, the difficulty related to the large size of the eigenvalue problem when using directly the raw time responses can be avoided by processing the covariance-driven Hankel matrix (Nguyen *et al.* (2010)[92]).

- Sensitivity computation of principal components in the frequency domain has been proposed to solve damage localization and evaluation [Nguyen and Golinval (2010)[88-90]. If experimental FRFs are used, input may be introduced at some or even at only one position; excitation applied to every DOF is not necessary. Localization can be based on several proposed detection indexes. The analytical model is not required for the purpose of localization but it is the basis of the parameter evaluation procedure through model updating. One feature which appears as very important in the model updating procedure is the choice of the weighting matrix.

Among the possible perspectives of the work, let us suggest the following ideas.

- As illustrated in the corresponding chapters, Blind Modal Identification and Kernel Principal Component Analysis show a very good potential to detect damage effectively and more particularly if they are combined with Hankel matrices. The methods could be further applied to more complex systems and the influence of environmental and/or operational factors should be investigated.
- Damage localization has been achieved on the basis of FRF measurements in the present work. The development of a localization method using directly time domain data could be also an interesting alternative.
- In the model updating procedure presented in Chapter 6, the weighting matrix plays an important role in the optimal evaluation of the updating parameters, particularly if the number of parameters is high. A deeper study on the choice of the weighting matrix could be an interesting subject to develop.
- It would be useful to build a wavelet toolbox which makes the choice of ridges more automatically. A step for de-noising signals would be to consider.

Appendix A

Examples on the resolution of WT instantaneous frequency and amplitudes

Figure A1 shows identification results of ridge 2 using the WT of the signal measured at DOF 4 of the beam. In order to improve the resolution of the instantaneous frequency shown in Figure A1*a*, the scale vector was divided by five times to obtain the results presented in Figure A1*b*. It is observed that, although the instantaneous frequency is now better modulated, the instantaneous amplitude remains the same.

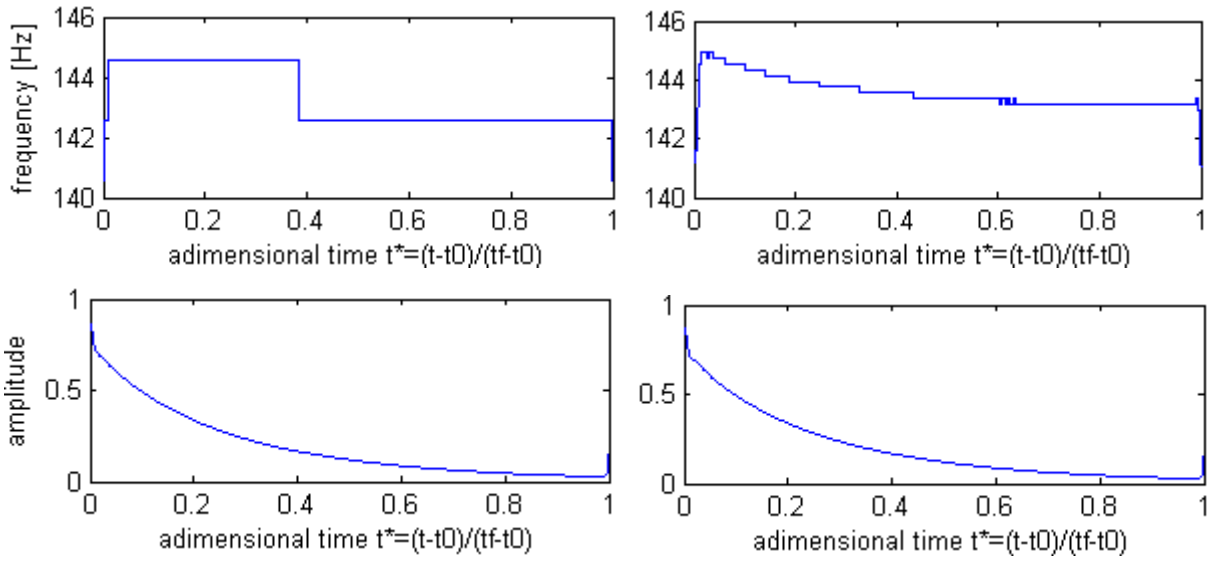

a) by a raw scale vector *b) by a fine scale vector*

Figure A1: Instantaneous frequency and amplitude using a raw scale vector (*a*) and a much finer scale vector (*b*)

Bibliography

[1] Adams D.E., Allemang R.J., "A frequency domain method for estimating the parameters of a nonlinear structural dynamic model through feedback", Mechanical System and Signal Processing 14, 2000, pp. 637-656.

[2] Argoul P. and Le T. P., "Instantaneous indicators of structural behaviour based on the continuous Cauchy wavelet analysis", Mechanical Systems and Signal Processing, 17(1), 2003, pp. 243-250.

[3] Arquier R, Bellizzi S., Bouc R., Cochellin B., "Two methods for the computation of nonlinear modes of vibrating systems at large amplitudes", Computers and Structures, 84, 2006, pp. 1565-1576.

[4] Bakir P. G., Reynders E., De Roeck G., "Sensitivity-based finite element model updating using constrained optimization with a trust region algorithm", Journal of Sound and Vibration 305, 2007, pp. 211-225.

[5] Bakir P. G., Reynders E., De Roeck G., "An improved finite element model updating method by the global optimization technique 'Coupled Local Minimizers'", Computers and Structures, 2008, pp. 1339-1352.

[6] Bayissa W.L., Haritos N., Thelandersson S., "Vibration-based structural damage identification using wavelet transform", Mechanical System and Signal Processing 22, 2008, pp. 1194-1215.

[7] Bellizi S. and Defilippi M., "Nonlinear mechanical system identification using linear system with random parameters", Proceedings of the International Conference on Structural System Identification, Kassel, Germany 2001, pp. 377-386.

[8] Belouchrani A., Meraim K.A., Cardoso J.-F. and Moulines E., "Second-order blind separation of correlated sources", Proceedings International Conference on Digital Signal Processing, Cyprus, 1993, pp. 346–351.

[9] Belouchrani A., Meraim K.A., Cardoso J.F., Moulines E., "A blind source separation technique using Second - order statistics", IEEE transactions on signal Processing 45, 1997, pp. 434-444.

[10] Cao M., Qiao P., "Novel Laplacian scheme and multiresolution modal curvatures for structural damage identification", Mechanical System and Signal Processing 23, 2009, pp. 1223-1242.

[11] Carmona R. A., Hwang W. L., Torrésani B., "Multiridge detection and time-frequency reconstruction", IEEE transactions on Signal processing, vol. 47, n° 2, February 1999, pp. 480-492.

[12] Chang K. O., Sohn H., "Damage diagnosis under environmental and operational variations using unsupervised support vector machine", Journal of Sound and Vibration 325, 2009, pp. 224-239.

[13] Chelidze D., Zhou W., “Smooth orthogonal decomposition-based vibration mode identification”, Journal of Sound and Vibration, 292, 2006, pp. 461-473.

[14] Cui P., Li J., Wang G., “Improved kernel principal component analysis for fault detection”, Expert Systems with Applications 34, 2008, pp. 1210-1219.

[15] Da Silva S., Cogan S., Foltête E., “Nonlinear identification in structural dynamics based on Wiener series and Kautz filters”, Mechanical Systems and Signal Processing 24, 2010, pp. 52-58.

[16] De Boe P., Golinval J.-C., “Principal component analysis of a piezosensor array for damage localization”, Structural Health Monitoring, 2003, pp.137-144.

[17] De Boe P., “Les éléments piézo-laminés appliqués à la dynamique des structures”, PhD dissertation, University of Liège, 2003.

[18] Deraemaeker A., Preumont A., “Vibration based damage detection using large array sensors and spatial filters”, Mechanical Systems and Signal Processing 20, 2006, p. 1615-1630.

[19] Deraemaeker A., Reynders E., De Roeck G., Kullaa J., “Vibration-based structural health monitoring using output-only measurements under changing environment”, Mechanical Systems and Signal Processing 22, 2008, pp. 34-56.

[20] D’Souza K., Epureanu B. I., “Multiple augmentation of nonlinear systems and generalized minimum rank perturbations for damage detection”, Journal of Sound and Vibration 316, 2008, pp. 101-121.

[21] Erlicher S., Argoul P., “Modal identification of linear non-proportionally damped systems by wavelet transform”, Mechanical Systems and Signal Processing 21, 2007, pp. 1386-1421.

[22] Fang S.E., Perera R., De Roeck G., “Damage identification of a reinforced concrete frame by finite element model updating using damage parameterization”, Journal of Sound and Vibration, 313, 2008, pp. 544-559.

[23] Farooq U., Feeny B. F., “Smooth orthogonal decomposition for modal analysis of randomly excited systems”, Journal of Sound and Vibration, 316, 2008, pp. 137-146.

[24] Farrar C., Jauregui D., “Damage Detection Algorithms Applied to Experimental and Numerical Modal Data from the I-40 Bridge”, Los Alamos National Laboratory, 1996.

[25] Farrar C. R., Worden K., Todd M. D., Park G., Nochols J., Adams D. E., Bement M. T., Farinholt K., 2007, “Nonlinear System Identification for Damage Detection”, Los Alamost National Laboratory 11, 2007.

[26] Feeny B. F., Kappagantu R., “On the physical interpretation of proper orthogonal modes in vibrations”, Journal of Sound and Vibration, 211(4), 1998, pp. 607-616.

[27] Feeny B. F., Liang Y., “Interpreting proper orthogonal modes of randomly excited vibration systems”, Journal of Sound and Vibration, 265, 2003, pp. 953-966.

[28] Flandrin P., Gonçalvès P., Rilling G., “EMD equivalent filter banks, from interpretation to applications”, in Hibert-Huang Transform: Introduction and

Application, eds. N.E.Huang and S.S.P. Shen (World Scientific, Singapore), 2005, pp. 67-87.

[29] Friswell M., "Calculation of Second and higher order eigenvector derivatives", Journal of Guidance, Control and Dynamics, Volume 18, No 4, 1994, pp. 919-921.

[30] Friswell M.I. and Mottershead J.E., "Finite Element Model Updating in Structural Dynamics", Kluwer Academic Publishers, 1995.

[31] Friswell M.I., Mottershead J.E., Ahmadian H., "Finite-element model updating using experimental test data: parametrization and regularization", Transactions of the Royal Society of London, Series A, Special Issue on Experimental Modal Analysis, 359(1778), 2001, pp. 169-186.

[32] Ge Z., Yang C., Song Z., "Improved kernel PCA-based monitoring approach for nonlinear process", Chemical Engineering Science 74, 2009, pp. 2245-2255.

[33] Géradin M., Rixen D., Mechanical Vibrations, "Theory and Application to structural dynamics", Masson, Paris, 1994.

[34] Golinval J.-C., Kerschen G., Lenaerts V., Thouverez F. and Argoul P., "European COST action F3 on structural dynamics. Working group 3: identification of non-linear systems. Introduction and Conclusions", Mechanical System and Signal Processing 17, 2003, pp. 177-178; pp. 251-254.

[35] Golub G.H., Van Loan C.F., "Matrix computations" (3rd ed.), Baltimore, The Johns Hopkins University Press, 1996.

[36] Gomes H. M., Silva N. R. S., "Some comparisons for damage detection on structures using genetic algorithms and modal sensitivity method", Applied Mathematical Modelling, 2008, pp. 2216-2232.

[37] Gurley K., Kareem A., "Applications of wavelet transforms in Earthquake, Wind and Ocean Engineering", Engineering Structures 21, 1999, pp. 149-167.

[38] Hadjileontiadis L.J., Douka E., Trochidis A., "Fractal dimension analysis for crack identification in beam structures", Mechanical System and Signal Processing 19, 2005, pp. 659-674.

[39] Hazra B., Narasimhan S., "Wavelet-based Second-order Blind Identification of Structures", Joint ASCE-ASME-SES Conference on Mechanics and Materials, 2009.

[40] He Q., Kong F., Yan R., "Subspace-based gearbox condition monitoring by kernel principal component analysis", Mechanical Systems and Signal Processing 21, 2007, pp. 1755-1772.

[41] Hot A., Kerschen G., Foltête E., Cogan S., Buffe F., Buffe J., Behar S., "Detection and Quantification of nonlinear dynamic behaviours in space structures", Proceedings of the IMAC-XXVIII, Florida USA, 2010.

[42] http://institute.lanl.gov/ei/software-and-data/data

[43] http://perso.telecom-paristech.fr/~cardoso/jointdiag.html

[44] Huang N. E., Shen Z., Long S. R., Wu M. C., Shih H. H., Zheng Q., Yen N.-C., Tung C. C., and Liu H. H., "The empirical mode decomposition and Hilbert

spectrum for nonlinear and nonstationary time series analysis", Proceedings of the Royal Society of London, 1998, Series A, vol. 454, pp. 903-995.

[45] Huang N., Wu Z., Long S.R., Arnold K.C., Chen X., Blank K., "On instantaneous frequency", Advances in Adaptive Data Analysis, Vol. 1, No. 2, 2009, pp. 177-229.

[46] Huynh D., He J., Tran D., "Damage location vector: A non-destructive structural damage detection technique", Computers and Structures 83, 2005, pp. 2353-2367.

[47] Jiang L. J., "An optimal sensitivity-enhancing feedback control approach via eigenstructure assignment for structural damage identification", Journal of Vibration and Acoustics, 129(6), 2007, pp. 771-783.

[48] Jiang L. J. and Wang K. W., "An experiment-based frequency sensitivity enhancing control approach for structural damage detection", Smart Materials and Structures 18, 2009, online at stacks.iop.org/SMS/18/065005.

[49] Jianping J., Guang M., "A novel method for multi-fault diagnosis of rotor system", Mechanism and machine theory, 2009, vol. 4, n° 4, pp. 697-709.

[50] Junkins J.L. and Kim Y., "Introduction to Dynamics and Control of Flexible Structures", AIAA Education Series, Reston, VA, 1993.

[51] Kerschen G., Golinval J.-C., Worden K., "Theoretical and experimental identification of a non-linear beam", Journal of Sound and Vibration 244, 2001, pp. 597-613.

[52] Kerschen G., "On the Model Validation in Nonlinear Structural Dynamics", Ph.D. Thesis, University of Liège, 2003.

[53] Kerschen G., Worden K., Vakakis A. F., Golinval J.-C., "Past, present and future of nonlinear system identification in structural dynamics", Mechanical Systems and Signal Processing 20, 2006, pp. 505-592.

[54] Kerschen G., Poncelet F., Golinval J.-C., "Physical interpretation of independent component analysis in structural dynamics", Mechanical Systems and Signal Processing, 2007, pp. 1561-1575.

[55] Kijewski T. and Kareem A., "On the presence of end effects and their melioration in wavelet-based analysis", Journal of Sound and Vibration, 256(5), 2002, pp. 980-988.

[56] Kijewski T., Kareem A., "Wavelet transforms for system identification in civil engineering", Computer-aided civil and Infrastructure Engineering 18, 2003, pp. 339-355.

[57] Kim J.-T. and Stubbs N., "Improved damage identification method based on modal information", Journal of Sound and Vibration, 252(2), 2002, pp. 223-238.

[58] Kim K. I., Franz M. O. and Schölkopf B., "Iterative Kernel Principal Component Analysis for Image Modeling", IEEE Transactions on Pattern Analysis and Machine Intelligence 27(9), 2005, pp. 1351-1366.

[59] Koh B. H. and Ray L. R., "Localisation of damage in smart structures through sensitivity enhancing feedback control", Mechanical Systems and Signal Processing, 17(4), 2003, pp. 837-855.

[60] Koh B. H. and Ray L. R., “Feedback controller design for sensitivity-based damage localization”, Journal of Sound and Vibration 273, 2004, pp. 317-335.

[61] Koo K.Y, Lee J.J, Yun C.B and Brownjohn J.MW, “Damage detection in beam-like structures using deflections obtained by modal flexibility matrices”, Proceedings of the IMAC-XXVII, Orlando, Florida, USA, February 9-12, 2009.

[62] Kramer M.A., “Nonlinear principal component analysis using autoassociative neural networks”, A.I.Ch.E. Journal 37 (2), 1999, pp. 233-243.

[63] Krzanowski W.J., “Principles of Multivariate Analysis – A User’s Perspective”, Revised ed., Oxford University Press, Oxford, 2000.

[64] Lenaerts V., “Identification de modèles structuraux en dynamique non linéaire”, PhD dissertation, University of Liège, 2002.

[65] Lenaerts V., Kerschen G., Golinval J.-C., “Identification of a continuous structure with a geometrical non-linearity, part II: proper orthogonal decomposition”, Journal of Sound and Vibration 262, 2003, pp. 907-919.

[66] Le Riche R., Gualandris D., Thomas J.J., Hemez F.M., “Neural identification of nonlinear dynamic structures”, Journal of Sound and Vibration 248, 2001, pp. 247-265.

[67] Le T. P., “Auscultation dynamique des structures à l’aide de l’analyse continue en ondelettes”, PhD dissertation, Ecole nationale des ponts et chaussées, Paris, 2003.

[68] Le T. P., Argoul P., “Continuous wavelet transform for modal identification using free decay response”, Journal of Sound and Vibration 277, Issues 1-2, 6, 2004, pp. 73-100.

[69] Lee J. M., Yoo C.K., Choi S. W., Vanrolleghem P. A., Lee I.-B., “Nonlinear process monitoring using kernel principal component analysis”, Chemical Engineering Sciences 59, 2004, pp. 223-234.

[70] Lilien J.- L., Guérard S., Godard B., Feiereisen J.- M., Destiné J., “Power lines real time monitoring”, Proceedings of the 11th ICPVT conference, Vancouver, BC, Canada, 2006.

[71] Link M., “Updating of analytical models-basic procedures and extensions”, in: J.M.M. Silva, N.M.M. Maia (Eds.), Modal Analysis and Testing, Kluwer Academic Publishers, London 1999, pp. 281-304.

[72] Liu J.J., Cheng S.J., Kung I C., Chang H.C., Billings S.A., “Nonlinear system identification and fault diagnosis using a new GUI interpretation tool”, Mathematics and Computers in Simulation 54, 2001, pp. 425-449.

[73] Liu X., Lieven N.A.J., Escamilla-Ambrosio P.J., “Frequency response function shape-based methods for structural damage localization”, Mechanical System and Signal Processing 23, 2009, pp. 1243-1259.

[74] Maeck J., “Damage Assessment of Civil Engineering Structures by Vibration Monitoring”, Ph.D. dissertation, Katholieke Universiteit Leuven, 2003.

[75] Maia, Silva, He, Lieven, Lin, Skingle, To, Urgueira, “Theoretical and Experimental Modal Analysis”, Research Studies Press, Taunton, Somerset, UK, 1997.

[76] Mallat, “A wavelet tour of signal processing”, Academic press, 1999.

[77] Marchesiello S., Garibaldi L. and Fasana A., “CRP application to the non-linear beam benchmark of the COST F3 action”, Proceedings of the International Conference on Structural System Identification, Kassel, Germany 2001, pp. 139-150.

[78] Marchesiello S., Garibaldi L., “A time domain approach for identifying nonlinear vibrating structures by subspace methods”, Mechanical Systems and Signal Processing 22, 2008, pp. 81-101.

[79] McNeil S.I., Zimmerman D.C., “A framework for blind modal identification using joint approximate diagonalization”, Mechanical Systems and Signal Processing 22, 2008, pp. 1526-1548.

[80] McNeil S.I., Zimmerman D.C., “Blind modal identification applied to output-only building vibration”, Proceedings of the IMAC-XXVIII, Florida, USA, February 2010.

[81] Mevel L., Basseville M., Benveniste A. and Goursat M., “Merging sensor data from multiple measurement setups for nonstationary subspace-based modal analysis”, Journal of Sound and Vibration 249, 2002, pp. 719–741.

[82] Messina A., Williams E. J. and Contursi T., “Structural damage detection by a sensitivity and statistical-based method”, Journal of Sound and Vibration, 216 (5), 1998, pp. 791-808.

[83] Messina A., “Detecting damage in beams through digital differentiators filters and continuous wavelet transforms”, Journal of Sound and Vibration, 271, 2004, pp. 385-412.

[84] Meyer S., Weiland M. and Link M. “Modelling and updating of local nonlinearities using frequency response residuals”, Proceedings of the International Conference on Structural System Identification, Kassel, Germany 2001, pp. 151-160.

[85] Michels J., Waldmann D., Maas S., Zürbes A., “Bearing capacity of SFRC flat slabs with opening in the column area: experimental and numerical investigation”, Proceedings of the 7th RILEM-Symposium on Fibre Reinforced Concrete: Design and Applications, 2008, pp. 921-930.

[86] Nelson R. B., “Simplified calculation of eigenvector derivatives”, AIAA Journal, Vol. 14, No. 9, September 1976, pp. 1201-1205.

[87] Nguyen V. H., Peeters M., Golinval J.-C., “Detection of nonlinearity in a dynamic system using deformation modes obtained from the Wavelet transform of measured responses”, Shock and Vibration 17, number 4-5, 2010, pp. 491-506.

[88] Nguyen V. H., Golinval J.-C., “Damage diagnosis of Beam-like Structures based on Sensitivities of Principal Component Analysis Results”, Proceedings of the IMAC-XXVIII, Jacksonville, Florida, USA, February 1-4, 2010.

[89] Nguyen V. H., Golinval J.-C., “Damage localization and quantification for Beam-like Structures using Sensitivities of Principal Component Analysis Results”, Mechanical Systems and Signal Processing 24, 2010, pp. 1831-1843.

[90] Nguyen V. H., Golinval J.-C., “Damage localization in Linear-Form Structures Based on Sensitivity Investigation for Principal Component Analysis”, Journal of Sound and Vibration 329, 2010, pp. 4550-4566.

[91] Nguyen V. H., Golinval J.-C., “Detection of nonlinearity onset based on Kernel Principal Component Analysis”, Engineering Structures 32, 2010, pp. 3683-3691.

[92] Nguyen V. H., Rutten C., Golinval J.-C., “Fault detection in mechanical systems based on subspace features”, to be presented at ISMA 2010 International Conference on Noise and Vibration Engineering, September, 2010.

[93] Nomikos P., MacGregor J.F., “Multivariate SPC charts for monitoring batch processes”, Technometrics 37, 1995, pp. 41-59.

[94] Overschee P. V., De Moor B., “Subspace identification for linear systems-Theory-Implementation-Applications”, Kluwer Academic Publishers, 1997.

[95] Pai P. F., Palazotto A. N., “Detection and identification of nonlinearities by amplitude and frequency modulation analysis”, Mechanical System and Signal Processing 22, 2008, pp. 1107-1132.

[96] Pandey A. K., Biswas M. and Samman M. M., “Damage detection from changes in curvature mode shape”, Journal of Sound and Vibration, 142, 1991, pp. 321-332.

[97] Pascual Jimenez R., “Model Based Structural Damage Assessment Using Vibration Measurements”, PhD Thesis, University of Liège, 1999.

[98] Peeters B., De Roeck G., “Stochastic System Identification for Operational Modal Analysis: A Review”, Journal of Dynamic Systems, Measurement and Control, Transaction of the ASME, vol 123, December 2001, pp. 659-667.

[99] Peeters M., Viguié R., Sérandour G., Kerschen G., Golinval J.C., “Nonlinear Normal Modes, Part II: Toward a practical computation using numerical continuation techniques”, Mechanical Systems and Signal Processing, 23, 2009, pp. 195-216.

[100] Pei J.S., Smyth A.W., Kosmatopoulos E.B., “Analysis and modification of Volterra/Wiener neural networks for the adaptive identification of nonlinear hysteretic dynamic systems”, Journal of Sound and Vibration 275, 2004, pp. 693-718.

[101] Poncelet F., Kerschen G., Golinval J.-C., Verhelst D., “Output-only modal analysis using blind source separation techniques”, Mechanical Systems and Signal Processing 21, 2007, pp. 2335-2358.

[102] Pontoppidan N. H., Sigurdsson S. and Larsen J., “Condition monitoring with mean field independent components analysis”, Mechanical Systems and Signal Processing 19, 2005, pp. 1337-1347.

[103] Popescu T.D., Manolescu M., “Blind Source Separation of Traffic-Induced Vibrations in Building Monitoring”, IEEE International Conference on Control and Automation, ICCA 2007, pp. 2101-2106.

[104] Qiao P., Cao M., “Waveform fractal dimension for mode shape-based damage identification of beam-type structures”, International Journal of Solids and Structures 45, 2008, pp. 5946-5961.

[105] Rainieri C., Fabbrocino G., “Automated output-only dynamic identification of civil engineering structures”, Mechanical Systems and Signal Processing 24, 2010, pp. 678-695.

[106] Ray L. R. and Tian L., “Damage detection in smart structures through sensitivity enhancing feedback control”, Journal of Sound and Vibration, 227(5), 1999, pp. 987-1002.

[107] Reynders E., De Roeck Guido, Bakir P.G. and Sauvage C., “Damage Identification on the Tilff bridge by Vibration Monitoring Using Optical Fiber Strain Sensors”, Journal of Engineering mechanics – ASCE, Volume 133, Issue 2, 2007, pp. 185-193.

[108] Rizzo P., Sorrivi E., Lanza di Scalea F., Viola E., “Wavelet-based outlier analysis for guided wave structural monitoring: Application to multi-wire strands”, Journal of Sound and Vibration, 307, 2007, pp. 52-68.

[109] Rytter A., “Vibration based inspection of civil engineering structures”, PhD dissertation, Aalborg University, Denmark, 1993.

[110] Romdhani S., Gong S. and Psarrou A., “A multi-view nonlinear active shape model using kernel PCA”, Proceedings of BMVC, Nottingham, UK, 1999, pp. 483-492.

[111] Rucka M., Wilde K., “Application of continuous wavelet transform in vibration based damage detection method for beam and plates”, Journal of Sound and Vibration, 2006, pp. 536-550.

[112] Rutten C., Loffet C., Golinval J.-C., “Damage detection of mechanical components using null subspace analysis”, 2th International Symposium ETE’2009 – Brussels, Belgium.

[113] Sampaio R. P. C, Maia N. M. M. and Silva J. M. M., “Damage detection using the frequency – response – function curvature method”, Journal of Sound and Vibration, 226(5), 1999, pp. 1029-1042.

[114] Sanz J., Perera R., Huerta C., “Fault diagnosis of rotating machinery based on auto-associative neural networks and wavelet transforms”, Journal of Sound and Vibration, 302, 2007, pp. 981-999.

[115] Schölkopf B., Smola A., Müller K.-R., “Nonlinear component analysis as a kernel eigenvalue problem”, Neural Computation 10, 1998, pp. 1299-1319.

[116] Schölkopf B., Mika S., Burges C.J.C., Knirsch P., Müller K.-R., Smola A., “Input space vs feature space in kernel-based methods”, IEEE Transaction on Neural Networks 5, 1999, pp. 1000-1017.

[117] Sohn H., Worden K., Farrar C.F, “Novelty detection under changing environmental conditions”, SPIE’s Eight Annual International Symposium on Smart Structures and Materials, Newport Beach, CA (LA-UR-01-1894), 2001.

[118] Staszewski W. J., “Identification of non-linear systems using multi-scale ridges and skeletons of the Wavelet transform”, Journal of Sound and Vibration, 214 (4), 1998, pp. 639-658.

[119] Sun R., Tsung F., Qu L., “Evolving kernel principal component analysis for fault diagnosis”, Computers & Industrial Engineering 53, 2007, pp. 361-371.

[120] Tang A. C., Sutherland M. T. and J.McKinney C., "Validation of SOBI components from high-density EEG", NeuroImage, volume 25, issue 2, 2005, pp. 539-553.

[121] Teughels A. and De Roeck G., "Structural damage identification of the highway bridge Z24 by FE model updating", Journal of Sound and Vibration 278, 2004, pp. 589-610.

[122] Thouverez F., Jezequel L., "Identification of NARMAX models on a modal base", Journal of Sound and Vibration, 189 (2), 1996, pp. 193-213.

[123] Thouverez F., "Presentation of the ECL benchmark", Mechanical Systems and Signal Processings, 17(1), 2003, pp. 195-202.

[124] Titurus B., Friswell M. I., Starek L., "Damage detection using generic elements. Part I. Model updating", Computers and Structures 81, 2003, pp. 2273-2286.

[125] Titurus B., Friswell M.I., Starek L., "Damage detection using generic elements. Part II. Damage detection", Computers and Structures 81, 2003, pp. 2287-2299.

[126] Todd Griffith D., "Analytical sensitivities for Principal Components Analysis of Dynamical systems", Proceedings of the IMAC-XXVII, Orlando, Florida, USA, February 9-12, 2009.

[127] Vapnik V., "The nature of statistical learning theory", New York: Springer Verlag, 1995.

[128] Waltering M., Bungard V., Maas S., Zuerbes A., Waldmann D., De Roeck G., "Damage assessment of a gradually damaged prestressed concrete bridge using static load tests and non-linear vibration characteristic", International Conference on Noise and Vibration Engineering, ISMA 2008.

[129] Wei Z., Yam L.H., Cheng L., "NARMAX model representation and its application to damage detection for multi-layer composites", Computers Structures 68, 2005, pp. 109-117.

[130] Widodo A., Yang B.-S., "Application of nonlinear feature extraction and support vector machines for fault diagnosis of induction motor", Expert Systems with Applications 33, 2007, pp. 241-250.

[131] Wu Z., Huang N., "Ensemble empirical mode decomposition: a noise-assisted data analysis method", Advances in Adaptive Data Analysis, Vol. 1, No. 1, 2009, pp. 1-41.

[132] Yan A.-M., De Boe P. and Golinval J.-C., "Structural Damage Diagnosis by Kalman Model Based on Stochastic Subspace Identification", Structural Health Monitoring, 3, 103, 2004, pp. 103-119.

[133] Yan A.-M. and Golinval J.-C., "Structural damage localization by combining flexibility and stiffness methods", Engineering Structures 27, 2005, pp. 1752-1761.

[134] Yan A.-M., Kerschen G., De Boe P., Golinval J.-C., "Structural damage diagnosis under varying environmental conditions – Part I: A linear analysis", Mechanical Systems and Signal Processing 19, 2005, pp. 847-864.

[135] Yan A.-M., Kerschen G., De Boe P., Golinval J.-C., "Structural damage diagnosis under changing environmental conditions – Part II: local PCA for

nonlinear analysis", Mechanical System and Signal Processing 19(4), 2005, pp. 865-880.

[136] Yan R., Gao R. X., "An efficient approach to machine health diagnosis based on harmonic wavelet packet transform", Robotics and Computers-Integrated Manufacturing 21, 2005, pp. 291-301.

[137] Yan A.-M., Golinval J.-C., "Null subspace-based damage detection of structures using vibration measurements", Mechanical Systems and Signal Processing 20, 2006, pp. 611-626.

[138] Yan B.F., Miyamoto A., Brühwiler E., "Wavelet transform-based modal parameter identification considering uncertainty", Journal of Sound and Vibration 291, 2006, pp. 285-301.

[139] Yang J. N., Lin S. and Pan S., "Damage identification of structures using Hilbert-Huang spectral analysis", Proc. 15th ASCE Engineering Mechanics Conference, New York, 2002.

[140] Yang J.N., Lei Y., Lin S., Huang N., "Hilbert-Huang based approach for structural damage detection", Journal of Engineering Mechanics, No. 1, January 2004.

[141] Zang C., Friswell M.I., Imregun M., "Structural damage detection using independent component analysis", Structural Health Monitoring 3, 2004, pp. 69-83.

[142] Zhou W., Chelidze D., "Blind source separation based vibration mode identification", Mechanical System and Signal Processing 21, 2007, pp. 3072-3087.